Structure of the Hot Intracluster Medium in the Virgo Cluster of Galaxies

Ken'ichi KIKUCHI

Department of Physics, Tokyo Metropolitan University

Abstract

We present the ASCA results of spatially resolved X-ray spectra of the Virgo cluster of galaxies. The northwest and south regions of the Virgo cluster of galaxies have been extensively investigated from ASCA, with the total exposure time and the covered area ~ 500 ksec and ~ 10 deg^2, respectively. Based on the imaging and spectroscopic capability of ASCA, we excluded the contaminating sources other than the ICM, and successfully derived the temperature distribution in the Virgo cluster.

The temperature of the intracluster medium (ICM) in the south region of M87 are generally higher than those in the northwest region, and exhibit significant variation from position to position. We performed detailed analysis for the data in the linking region between M87 and M49 along the X-ray "bridge", and discovered a remarkable hot region. This region has an angular extent of $\sim 4 \times 10^3$ arcmin^2 and a temperature of $kT = 4.38^{+1.60\ +0.61}_{-1.08\ -0.83}$ keV, significantly hotter than the surrounding temperature of ~ 2 keV.

The observed features indicate that the hot region occupies a small angular size compared with the whole extent of the Virgo cluster, and it is surrounded by a cool gas of about 2 keV. The X-ray luminosity of the hot component is about 4×10^{41} erg s^{-1} in 2–10 keV. Based on the spectrum and emission measure of the hot component, its internal thermal energy is estimated to be $\sim 10^{60}$ ergs and the gas density is $\sim 10^{-4}$ cm^{-3}. However, we could not distinguish the spectrum to be either thermal bremsstrahlung or non-thermal (power-law) from the fitting. It is possible to explain that the 'hot' component is produced by inverse Compton scattering of the cosmic microwave background by relativistic electrons with $\gamma \approx 2000$. Another possibility of an origin of the hard emission is non-thermal bremsstrahlung due to suprathermal electrons with energies grater than several keV. The total amount of the non-thermal electron in the region is estimated as $\sim 9.0 \times 10^{68}$. In either thermal or non-thermal case, the presence of the hot component strongly suggests that the shock is created in this region probably due to the motion of the gas associated with M49, approaching M87 with a velocity of $\gtrsim 1000$ km s^{-1}.

Contents

1 Introduction **1**

2 Review of Clusters of Galaxies **3**

2.1 Overview . . . 3

2.2 X-ray Properties . . . 4

2.2.1 Historical Overview . . . 4

2.2.2 Temperature Structure . . . 4

2.2.3 Metal Abundance . . . 6

2.2.4 Mass Distribution . . . 6

2.2.5 X-ray Emission from Elliptical Galaxies . . . 7

2.2.6 Hard X-ray Emission from Clusters of Galaxies and Galaxies . . . 7

2.3 Theoretical Background . . . 9

2.3.1 X-ray Emission from Hot Plasma . . . 9

2.3.2 Heating and Cooling of the ICM . . . 14

2.3.3 Distribution of the ICM . . . 16

3 Review of The Virgo Cluster of Galaxies **19**

3.1 Optical Properties . . . 19

3.2 X-ray Properties . . . 23

3.3 M87 and M49 . . . 27

4 Instrumentation **30**

4.1 The ASCA Satellite . . . 30

4.2 X-ray Telescope (XRT) . . . 32

4.3 Solid-state Imaging Spectrometer (SIS) . . . 34

4.4 Gas Imaging Spectrometer (GIS) . . . 36

5 Response Construction and Background Estimation **39**

5.1 XRT Response for Extended Sources . . . 39

5.1.1 Point Spread Function (PSF) . . . 39

5.1.2 Stray Light . . . 42

5.1.3 Formulation of the ASCA Response . . . 45

5.1.4 SimARF . . . 46
5.2 Background Estimation and Data Reduction . . . 48
5.2.1 Non X-ray Background (NXB) . . . 48
5.2.2 Cosmic X-ray Background (CXB) . . . 55

6 Observation and Analysis **58**
6.1 ASCA Mapping Observation of the Virgo Cluster . . . 58
6.2 Contaminating Sources . . . 64
6.2.1 Source Finding . . . 64
6.2.2 Nearby Bright Sources . . . 70
6.2.3 The North Polar Spur . . . 76
6.3 ROSAT Image as a Model of Surface Brightness Distribution . . . 78
6.4 Temperature Distribution . . . 81
6.4.1 Hardness Ratio . . . 81
6.4.2 Spectral Fitting . . . 83
6.5 Hot Region between M87 and M49 . . . 86
6.5.1 Angular Extent of the Hot Region . . . 86
6.5.2 Spectral Fit above 2 keV . . . 87
6.5.3 Estimation of Systematic Errors on the Temperature . . . 91
6.6 Temperature Distribution in the M49 Subcluster . . . 94
6.6.1 Temperature and Abundance Distribution near M49 . . . 94
6.6.2 Large Scale Temperature Distribution . . . 96
6.7 Summary of the Results . . . 99

7 Discussion **100**
7.1 Physical Conditions of the Hot Component . . . 100
7.1.1 Geometrical Assumption . . . 100
7.1.2 Emission Measure . . . 102
7.1.3 Density and Line-of-Sight Depth . . . 104
7.1.4 Internal Thermal Energy of the Hot Region . . . 105
7.1.5 Pressure Balance . . . 107
7.1.6 Non-thermal Emission . . . 108
7.2 Origin of the Hot Region . . . 111
7.2.1 LMXBs . . . 111
7.2.2 Supernovae . . . 111
7.2.3 AGN . . . 111
7.2.4 Subcluster Merger . . . 112

8 Conclusion **115**

A The ROSAT Satellite **117**
A.1 Overview 117
A.2 Position Sensitive Proportional Counter (PSPC) 117
A.3 ROSAT All-Sky Survey 120

B Detected Source Candidate List in the Virgo Field **122**

C The GIS Spectra Fitted with R-S Model **129**

List of Figures

2.1 Temperature map of the Coma cluster superposed on the contours of X-ray surface brightness in the energy range 0.7–10 keV obtained with GIS 5
2.2 X-ray spectrum of the Virgo cluster (M87) obtained with HEAO-1 8
2.3 Temperature dependence of the cooling function 9
2.4 Electron spectrum of A401 cluster 11
2.5 The non-thermal bremsstrahlung spectra 13
2.6 Schematic representation of the transition region for a shock wave measured in the rest frame of the shock wave 15

3.1 Plot of member and possible member galaxies of the Virgo cluster 20
3.2 Distribution of different galaxy types in the Virgo cluster 21
3.3 A map of the velocity dispersion of the galaxies in Virgo cluster 22
3.4 X-ray surface brightness obtained with Ginga 23
3.5 ICM temperature distribution obtained with Ginga 23
3.6 X-ray contour plot of the Virgo cluster obtained with ROSAT 24
3.7 Azimuthally averaged surface brightness profile and ICM temperature around M87 obtained with ROSAT 25
3.8 Temperature and abundance distribution of the Virgo cluster obtained with ASCA 26
3.9 Contour plot of M49 obtained with ROSAT 29
3.10 Density profiles of the subclusters in the Virgo cluster 29

4.1 In orbit configuration of the ASCA satellite 31
4.2 Onboard instruments of the ASCA satellite 31
4.3 Walter type I optics 32
4.4 Effective area of the ASCA XRT compared with that in previous missions 34
4.5 Cross section view of the SIS camera 35
4.6 Detection efficiency and energy resolutions of the SIS 36
4.7 Schematic view of the GIS sensor system 37
4.8 Detection efficiency and energy resolutions of the GIS 38
4.9 Schematic view of the 6 monitor data in the PH vs. RT plane 38

5.1 Examples of the XRT PSF taken by GIS2 40

5.2 The temperature and abundance profiles of simulated clusters with uniform temperature and metal abundance . . . 41
5.3 Example of radial profile of ray-tracing compared with Cyg X-1 . . . 41
5.4 The Crab stray light images by GIS . . . 42
5.5 Spectra of the Crab stray observations and simulated spectra . . . 43
5.6 Counting rates of the Crab stray observations and the simulations . . . 44
5.7 Plot of the GIS2 ARF for a point source and uniformly extended source . . . 47
5.8 Integrated spectra of the day-earth, the CXB, and the night-earth . . . 48
5.9 Distribution map for three types of phenomena on the Earth surface . . . 50
5.10 COR-H02 correlation during the night-earth observations . . . 50
5.11 H02 sorted spectra during the night-earth observations . . . 53
5.12 Long term variations of the counting rate during the night-earth observations . . . 53
5.13 Figures to check the NXB reproducibility by H02-sorting method . . . 54
5.14 Example of GIS image and mask image . . . 56
5.15 Spectra of the Draco, Nep, QSF3, and SA57 fields . . . 57

6.1 ASCA observed regions superposed on the RASS contour . . . 61
6.2 ASCA observed regions superposed on the contours of number density of galaxies . . . 62
6.3 X-ray image of the Virgo cluster field with the GIS . . . 63
6.4 Example of the image fitting result for nw_p05 . . . 65
6.5 Distribution of the 0.7–7 keV significance for detected 224 source candidates . . . 66
6.6 Radial profile of Cyg X-1 image at 1 CCD nominal position taken by GIS2 . . . 67
6.7 The source-mask for the Virgo cluster . . . 68
6.8 The 0.7–7 keV significance vs. $r_{\rm mask}$ for 224 source candidates . . . 69
6.9 Log N - Log S relation of detected sources candidates in the Virgo cluster . . . 69
6.10 0.7-7 keV GIS surface brightness of A1553, NGC 4325, and s_p11 . . . 73
6.11 The radial brightness profile of A1541 and NGC 4325 obtained with PSPC . . . 74
6.12 GIS spectra of four bright sources . . . 75
6.13 X-ray spectra from the NPS and the Virgo cluster around M49 . . . 76
6.14 X-ray image in the 1/4 keV band around the Virgo cluster obtained with ROSAT . . . 77
6.15 Comparison of projected surface brightness profile of RASS data with the model template . . . 79
6.16 Comparison of surface brightness profile of GIS data with simulation . . . 79
6.17 Relative fraction of the emission . . . 80
6.18 Gray scale plot of the 2 dimensional distribution of the hardness ratio in the Virgo region . . . 81
6.19 The hardness ratio distribution . . . 82
6.20 Temperature distribution for the entire regions of the Virgo from the spectral fitting in 0.7–8 keV band . . . 85
6.21 The 2 dimensional hardness ratio map at s_p05_07_09 and s_p06_08_10 . . . 87

6.22 Contaminating spectrum from four bright sources at s_p05_07_09 and s_p06_08_10 . 88
6.23 GIS spectra of s_p05_07_09 and s_p06_08_10 89
6.24 Confidence contours of single temperature R-S model fitting for s_p05_07_09 and s_p06_08_10 89
6.25 Fitting result by a R-S with a thermal bremsstrahlung model 90
6.26 Confidence contours of R-S temperature vs. thermal bremsstrahlung temperature . 90
6.27 Confidence contours of the corrected kT vs. emission measure for s_p05_07_09 . . . 93
6.28 Confidence contours of the photon index vs. number of photons at 1 keV 93
6.29 GIS image around M49 in 0.7–10 keV 94
6.30 Integrating regions for M49 95
6.31 Temperature and heavy element abundance profiles for M49 95
6.32 Simulation result of the contaminating flux from the annular sky regions to individual regions observed with the GIS 96
6.33 Temperatures for the regions s_p12, s_p13, s_p14, s_p16, and s_p17 97
6.34 Relative fraction of the emission around M49 98
6.35 Combined plot of the temperature profile around M49 subcluster 98

7.1 Schematic view of s_p05_07_09 and s_p06_08_10 101
7.2 Confidence contours of $kT_{\rm hot}$ vs. $EM_{\rm hot}$, $kT_{\rm hot}$ vs. $EM_{\rm cool}$, and $kT_{\rm hot}$ vs. $EM_{\rm cool}/EM_{\rm hot}$.103
7.3 Allowed regions of the gas density shown as a function of the line-of-sight depth for the cool and hot components 105
7.4 Relations given by various values of $E_{\rm th}$ 106
7.5 Curves show relations with fixed α values plotted on the $EM_{\rm cool}/EM_{\rm cool}$ vs. $kT_{\rm hot}$ plane 107
7.6 Confidence contours of the photon index vs. number of photons at 1 keV for the hot component 108
7.7 Electron spectrum for the hot region 109
7.8 Relation between $EM_{\rm cool}/EM_{\rm hot}$ and $kT_{\rm hot}$ for fixed values of α 113

A.1 Schematic view of the ROSAT spacecraft 118
A.2 The ROSAT PSPC-C entrance window transmission and effective area of the ROSAT XRT as a function of energy 119
A.3 The PSF of the ROSAT XRT and PSPC 119
A.4 The exposure map of RASS around the Virgo cluster 121
A.5 RASS image of the Virgo cluster 121

List of Tables

2.1 General properties of clusters of galaxies 4

3.1 General properties of M87 and M49 28
3.2 Masses of the subclusters around M87 and M49 28

4.1 Design parameters and performance of the ASCA XRT. 33
4.2 Design parameters and performance of the SIS 35
4.3 Design parameters and performance of the GIS 38

5.1 Summary of the coordinates 45
5.2 Summary of factors constituting the response function 46
5.3 Summary of the flare-cut conditions 51
5.4 Blank sky observations used for the CXB database 55

6.1 Log of ASCA mapping observation of the Virgo cluster. 59
6.2 Log of ASCA observation around the Virgo cluster 60
6.3 Best fit parameters with 90% errors for 4 bright sources 72
6.4 Contaminating photon fraction from the four bright sources 72
6.5 Comparison of X-ray emission from Virgo and NPS around M49 along with 90% errors. 76
6.6 The best fit parameters and confidence limits with $\Delta\chi = 2.706$ from a R-S model fitting in 0.7–8 keV band 84
6.7 The best fit temperature, statistical error, and systematic error for s_p05_07_09 and s_p06_08_10, determined from a R-S model fitting in 2–8 keV band 92

A.1 Design parameters and performance of the PSPC 118

B.1 Detected Source Candidate List in the Virgo Field 123

Chapter 1

Introduction

Clusters of galaxies are one of the most important objects in the recent observational and theoretical astrophysics. They are the largest virialized system in the universe, and their physical conditions are closely related to the nature of the dynamical and chemical evolution of the universe.

The intracluster medium (ICM) usually comprises the dominant fraction of the visible matter in rich clusters with the mass 1–10 times larger than that of optically detectable galaxies. X-ray observations are the most effective way of investigating the properties of the ICM, since its temperature lies in 2–10 keV. The gravitational structure and evolution of clusters are for the most part controlled by the dark matter, which occupies some 80% of the total cluster mass. The ICM is thought to have been heated up through the gravitational collapse in the formation process of the cluster. Therefore, the ICM is the best tool to probe the gravitational potential well created by the invisible dark matter.

One expects to observe a smooth temperature distribution in a fully virialized system. However, recent X-ray observations are revealing significant large-scale temperature and surface brightness variation in many clusters. These clusters might not be relaxed, but undergoing evolution. Under a framework of hierarchical structure formation, the clusters are thought to often undergo merging with other clusters or subclusters in the process of growth. This creates complex temperature structures. Hydrodynamic simulations show that clusters recently formed by merging should have a complex temperature structure, and becomes more regular with time (e.g. Roettiger et al. 1993; Schindler & Müller 1993). Thus, spatial distribution of the ICM temperature is important as an indicator of the dynamical evolution and present state of the cluster. The main purpose of this thesis is to investigate the temperature structure in the cluster of galaxies, the Virgo cluster, with the best sensitivity ever achieved.

The ICM is a mixture of primordial and metal-rich gases. Since the metals must have been synthesized through nuclear reactions in stars and injected into the intracluster space, galaxies are considered to be the source of the metals. Some part of the metals are thought to be injected into the intracluster space by galactic winds, caused by a number of supernovae occurred just after the formation epoch of galaxies. This means that the galaxies contained in clusters could

also be the heat sources for the ICM (e.g. White 1991). Therefore, the past supernova history of galaxies can be traced not only by the distribution of heavy elements in the ICM, but also by the associated extra heat. New assessment of the role of galaxies in the thermal and chemical history of the ICM is also the aim of this thesis.

ASCA (Tanaka et al. 1994) has a superior energy resolution and a high sensitivity over a wide energy band 0.5–10.0 keV. These properties bring us a considerable jump in the observational knowledge on the hot ICM in clusters. Spatially resolved temperature and metal abundance can be obtained in a reliable manner for the first time. In this thesis, we perform detailed investigation on the temperature structure of the ICM in the Virgo cluster, based on extensive mapping observations with ASCA. Since the Virgo cluster is the nearest cluster ($\sim$ 20 Mpc from us), spatially-resolved spectroscopy can be performed in the most unambiguous way considering the moderate angular resolution of ASCA. We can study the hot-gas properties both by focusing on the vicinities of prominent galaxies ($\lesssim$100 kpc) and by averaging over a large scale in the whole cluster ($\gtrsim$1 Mpc). Furthermore, the Virgo cluster is thought to be a dynamically young system as recognized from its irregular structure in the optical and X-ray bands. Thus the Virgo cluster should provide us with a valuable opportunity to investigate the on-going heating process in the ICM.

We assume the distance to the Virgo cluster to be 20 Mpc (e.g. Federspiel et al. 1998), hence $1'$ angular separation at the cluster corresponds to 5.8 kpc. We also assume $H_0 = 50$ km s^{-1} Mpc^{-1}, and $q_0 = 0.5$. The 1 solar number abundance of Fe relative to H is taken as 4.68×10^{-5} (Anders & Grevesse 1989) throughout this thesis.

Chapter 2

Review of Clusters of Galaxies

2.1 Overview

Clusters of galaxies are gravitationally bound systems including large number of galaxies. They are known as the largest structure in the universe, with typical dimensions of roughly 1–5 Mpc across.

Optically, clusters of galaxies are classified according to the number of member galaxies. Clusters containing many galaxies (up to thousands) are called rich, while those with fewer members (down to ten or so) are called poor. Galaxy distribution in rich clusters is usually smooth and centrally peaked at cluster center. On the other hand, poor clusters usually show asymmetric and poorly condensed galaxy distribution. Although the Virgo cluster, which is the nearest cluster from the Sun, contains more than 1000 galaxies (Binggeli et al. 1985), it is often classified as poor cluster due to its irregular appearance.

At the central region, clusters often have the largest elliptical galaxies in the universe, called cD galaxies. Clusters with and without cD galaxies are referred to as cD clusters and non-cD clusters, respectively. The characteristic of the cD galaxy is the presence of a largely extended envelope of diffuse stellar light around the nucleus. In the visible light, cD galaxies are $10 - 100$ times larger than normal galaxies, hence the total luminosity associated with cDs is extremely large. The fact that many cDs have multiple nuclei suggests the cDs would be created by merging of smaller galaxies.

The luminous objects in clusters of galaxies are primarily divided into two components: visible galaxies and intracluster medium (ICM). The ICM is a hot ($kT \sim 10^8$ K) and tenuous ($n \lesssim 10^{-3}$ cm^{-3}) plasma, and fills the whole region of a cluster of galaxies. Because of its high temperature, the ICM emits the most of energy in X-ray band. Previous X-ray observations revealed that total mass of the ICM is 3–10 times larger than that of visible member galaxies in rich clusters, and at least comparable even in poor clusters. In short, the most of the visible matter in clusters can be observable only in the X-ray band. In the following sections, the X-ray properties of clusters are briefly reviewed General properties of clusters of galaxies are summarized in table 2.1.

Table 2.1: General properties of clusters of galaxies

ICM Temperature	$1 - 10$ keV
Central density of ICM	$\sim 10^{-3}$ cm^{-3}
Luminosity	$10^{42} - 10^{45}$ ergs s^{-1} cm^{-2}
Gravitational mass	$10^{14} - 10^{15}\ M_{\odot}$
ICM mass	$10^{13} - 10^{14}\ M_{\odot}$
Galaxy mass	$10^{12} - 10^{13}\ M_{\odot}$

2.2 X-ray Properties

2.2.1 Historical Overview

Based on the all-sky survey with Uhuru, the world's first X-ray astronomical satellite launched in 1970 (Giacconi et al. 1971), it has been recognized that clusters of galaxies are generally strong X-ray emitters, and the emission was suggested to be extended. The discovery of iron K emission line in the X-ray spectra by OSO-8 experiment has established the X-rays from clusters to be of thermal origin (Serlemitsos et al. 1977).

The X-ray study of clusters has made a big advance with the Einstein observatory (Giacconi et al. 1979), the world's first imaging X-ray mission. The imaging capability of the Einstein allows us to measure rather accurately the distribution of the ICM, revealed the presence of substantial dark matter in the halo of galaxy M87, the cD galaxy of the Virgo cluster (Fabricant et al. 1983). The subsequent ROSAT mission (Trümper 1983), with superior angular resolution, has detected substructure in many clusters, and discovered many new X-ray clusters through the all-sky survey.

Spectroscopic information on the cluster X-rays has been progressively deepened by HEAO-1 (Peterson 1975), EXOSAT (Taylor et al. 1981) and Ginga (Makino et al. 1987; Turner et al. 1989), through determinations of the ICM temperature and measurements of equivalent width of the Fe K line. Furthermore, the high energy resolution of ASCA (Tanaka et al. 1994) has made possible to determine the temperature more precisely, and measure not only Fe abundance but also those of other elements such as O, Si, and S.

2.2.2 Temperature Structure

Heating mechanisms of the ICM is still unclear. Since the sound crossing time across the cluster, $\sim 10^9$ yr (see equation 2.37), is considerably shorter than the age of the Universe, the ICM should achieve isothermality if clusters have reached hydrodynamic equilibrium long time ago. However, theoretical studies indicate that the cluster formation processes are very slow and are still in progress. Therefore, the temperature structure in the ICM could be a powerful clue to investigate the history of cluster formation.

A clear correlation has been found between the X-ray luminosity of cluster ($L_{\rm x}$) and the ICM

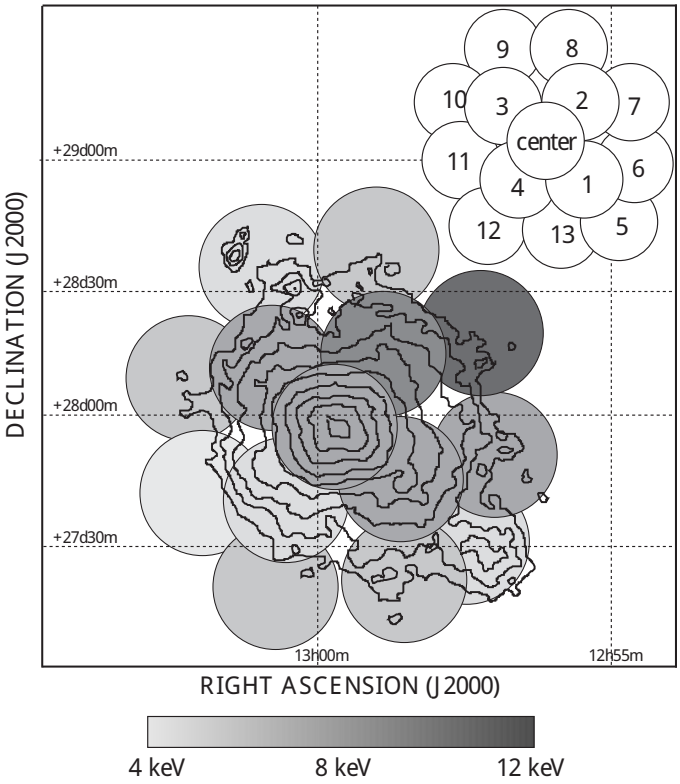

Figure 2.1: Temperature map of the Coma cluster superposed on the contours of X-ray surface brightness in the energy range 0.7–10 keV obtained with GIS. Each circle indicates $20'$ arcmin radius which corresponds to the GIS field of view (Honda et al. 1997).

temperature (kT) as $L_{\rm x} \propto T^{\alpha}$ (Mushotzky 1984; Edge & Stewart 1991; David et al. 1993; Markevitch 1998b), and observations indicate $\alpha \sim 3$. The Virgo cluster, characterized by $kT = 2.4$ keV and $L_{\rm x} = 1.16 \times 10^{43}$ ergs s^{-1} (David et al. 1993), also satisfies this relation. However, self-similar models of cluster evolution predicts $L_{\rm x} \propto f^2(1+z_{\rm f})^{3/2}T^2$, where f is the mass fraction of the cluster and $z_{\rm f}$ is the redshift of formation of the cluster (e.g. Kaiser 1991). To cope with this discrepancy, some explanations are proposed (e.g. Kaiser 1991; David et al. 1993; Cavaliere et al. 1997; Allen & Fabian 1998).

Recent experiments made it possible to obtain spatially resolved spectra of clusters, and are revealing the temperature structure. Markevitch et al. (1998) analyzed spatially resolved X-ray spectra of 30 nearby clusters with ASCA and ROSAT. They reported that most of them show a similar temperature decline at large radii, and about a half of the sample shows signs of merging. Determination of the dynamical structure of the clusters can constrain cosmological models because clusters should be dynamically more relaxed in a low-density universe than in a high-density one (e.g. Richstone et al. 1992). Comparing the temperature profiles with the results of cluster hydrodynamic simulations, Markevitch et al. (1998) found the low Ω ($\lesssim 0.3$) cosmological models are suitable to explain the temperature profiles.

Recent ASCA and ROSAT observations revealed complex temperature variation in some clusters (e.g. Briel & Henry 1994 for A2256; Henriksen & Markevitch 1996 for A754; Henry & Briel 1996 for A2142; Honda et al. 1996 for Coma; Davis et al. 1998 for A2255; Donnelly et al. 1998 for

A1367). Figure 2.1 shows the temperature map of the Coma cluster (Honda et al. 1996; Honda et al. 1997). These variations are usually explained as a result of a recent or ongoing merger by comparing with theoretical simulations (e.g. Roettiger et al. 1993; Schindler & Müller 1993; Roettiger et al. 1995; Evrard et al. 1996). Ishizaka & Mineshige (1996) performed N-body + hydrodynamic simulations and successfully created temperature variation like in the Coma cluster.

2.2.3 Metal Abundance

Since heavy elements can be produced only by thermonuclear reactions in stars and supernovae, the presence of the emission lines found in the spectra from the ICM implies that heavy elements processed in galaxies largely contaminate the ICM.

Koyama et al. (1991) discovered Fe abundance increases at the center of the Virgo cluster with Ginga. From the ASCA observation, similar central abundance increases were found in several clusters (Fukazawa et al. 1994; David et al. 1996; Matsumoto et al. 1996; Xu et al. 1997; Kikuchi et al. 1998). On the other hand, a large scale gradient in the metal abundance (over 500 kpc) is detected in AWM7 (Ezawa et al. 1997a) and Perseus cluster (Ezawa 1998). The authors discuss that the metals injected from individual galaxies are not effectively mixed in the ICM and hold the original galaxy distribution.

Fukazawa et al. (1998) investigated the abundance of Fe and Si as a function of the ICM temperature. The Fe abundance is almost constant to be 0.3 solar, while the Si abundance increases in clusters with higher ICM temperature. Since the ICM temperature would be proportional to the depth of the gravitational potential of the cluster, this fact indicates that the larger fraction of Si (type II supernovae products) has escaped from a shallower potential of poor systems due to galactic wind during early phase of cluster formation. On the other hand, Fe would be more recently supplied by type Ia supernovae, with little contribution from the galactic wind.

2.2.4 Mass Distribution

Previous X-ray observations of clusters established that the ICM mass is larger by a factor of 3–10 than the total mass contained in the optically visible galaxies. Therefore the ICM is the dominant form of baryon in the universe. Moreover, the X-ray emission from the ICM serves as a good tracer of the gravitational potential of matter in clusters of galaxies, both visible and invisible. Assuming a hydrostatic equilibrium, the distribution of the gravitational mass can be calculated from density and temperature distribution of the ICM (see section 2.3.3). Since the total gravitating mass is generally larger by a factor of 3–10 than the baryonic mass (total masses of the ICM and galaxies), there still remains a significant amount of missing mass, or dark matter.

Many clusters exhibit central emission in excess of that expected from β model (see equation 2.50) (e.g. Jones & Forman 1984). These excesses are considered to be caused by cooling flows in the central region, because the flow is expected to make the ICM density high, hence to push the X-ray flux higher than that given by a simple β model. Ikebe et al. (1997), however, analyzed the ROSAT and ASCA data for Hydra-A cluster, and found a central excess even in the high

energy band (> 4 keV). It suggests that the central excess emission is not only due to the dense cool ICM, but also due to the structure of gravitational potential of the cluster. Almost identical structure is found in the Centaurus and Fornax clusters (Ikebe 1994; Ikebe et al. 1996). The potential structure must have an additional central dimple which may be associated with the cD galaxy, and suggests that the dark matter exhibits a hierarchical structure.

2.2.5 X-ray Emission from Elliptical Galaxies

Elliptical galaxies are known as a luminous soft X-ray emitter. Typical temperature and density of ISM (interstellar medium) are ~ 1 keV and ~ 0.01 cm^{-3}, respectively. The soft X-ray luminosities ($10^{39} - 10^{42}$ ergs s^{-1}) are systematically higher than those of late-type galaxies with the same optical luminosities (Fabbiano et al. 1988).

Elliptical galaxies are thought to be important sources of metals in the ICM. Matsushita (1997) analyzed about 30 elliptical galaxies observed with ASCA, and found that the metal abundances in luminous elliptical galaxies are ~ 1 solar, which is nearly consistent with metal abundances of stars in elliptical galaxies derived from optical observations (Arimoto et al. 1997).

Matsushita (1997) and Matsushita et al. (1998) found the evidence of hierarchical surface brightness structure in NGC 4636 and other X-ray luminous ($L_{\rm X} > 10^{41}$ ergs s^{-1}) elliptical galaxies. The X-ray emission around NGC 4636 extends $\gtrsim 300$ kpc, and the gravitational mass reaches $9 \times 10^{12}\ M_{\odot}$. Furthermore, they found the metal abundance decreases from ~ 1 solar within ~ 30 kpc, to ~ 0.2 solar beyond ~ 50 kpc to a typical value of galaxy groups and clusters of galaxies. These suggest that the X-ray luminous elliptical galaxies sit at the bottom of a large potential well, which is as massive as those of galaxy groups or poor clusters.

2.2.6 Hard X-ray Emission from Clusters of Galaxies and Galaxies

Hard X-ray emission (> 10 keV in terms of temperature) from clusters of galaxies has been reported (e.g. Lea et al. 1981 for Virgo and A2142; Primini et al. 1981 for Perseus; Rephaeli & Gruber 1988 for A401, A2255, and A2256; Fusco-Femiano et al. 1999 for Coma; Kaastra et al. 1999 for A2199;). Since the clusters which emit strong hard X-rays tend to contain strong radio sources (Owen 1974), which are known to emit synchrotron radiation from relativistic electrons in a weak magnetic field, inverse Compton (IC) scattering by the relativistic electrons of the 3 K microwave background photons is proposed as the origin of the hard X-rays. Figure 2.2 shows 0.2–100 keV spectrum of the Virgo cluster (M87) obtained with HEAO-1 (Lea et al. 1981). Recent EUVE (Bowyer & Malina 1991) observations showed the presence of a diffuse EUV emission component in clusters of galaxies (e.g. Lieu et al. 1996 for Virgo; Mittaz et al. 1998 for A1795). Sarazin & Lieu (1998) suggest that these extreme-ultraviolet emission is inverse Compton scattering by electrons which have Lorentz factors $\gamma \sim 300$.

Although inverse Compton scattering is an attractive model to explain the hard X-ray emission from ICM, it requires implausible conditions at least some clusters. Recent observation with BeppoSAX has detected hard X-ray emission from A2199 (Kaastra et al. 1999). If the hard

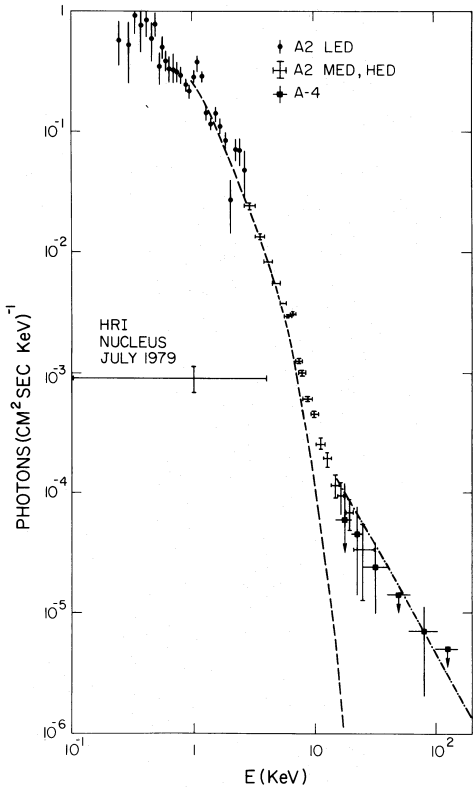

Figure 2.2: X-ray spectrum of the Virgo cluster (M87) obtained with HEAO-1. Dashed line shows a 2.05 keV thermal bremsstrahlung spectrum, and Dot-dashed line shows the predicted IC spectrum for a 5×10^{-7} gauss field (Lea et al. 1981).

X-ray emission is a result of inverse Compton scattering, the same electrons should produce diffuse radio synchrotron emission, as long as the ICM contains a magnetic field. Indeed, the lower limits of strength of the magnetic field in ICM imposed by Faraday rotation are typically larger than μGauss. The diffuse radio flux from A2199 is quite small, however, implausible weak magnetic field of $\lesssim 0.07$ μGauss is required if the hard X-ray is produced by inverse Compton scattering (Kempner & Sarazin 2000). To overcome such difficulties, non-thermal bremsstrahlung is proposed for an origin of the hard X-ray emission from ICM (e.g. Kaastra et al. 1999; Enßlin et al. 2000; Kempner & Sarazin 2000).

Elliptical galaxies also emit hard X-rays. The most dominant contribution of the hard X-rays is thought to come from low-mass X-ray binaries (LMXBs) (Canizares et al. 1987; Matsushita et al. 1994). The integrated LMXB emission exhibits a hard spectrum ($kT \sim 10$ keV in the equivalent temperature, Makishima et al. 1989; Matsushita et al. 1994), and its luminosity is inferred to be proportional to the optical luminosity of the host galaxy (Canizares et al. 1987): for example $L_{\rm X} \approx 3 \times 10^{40}$ ergs s^{-1} in 2–10 keV band for M49.

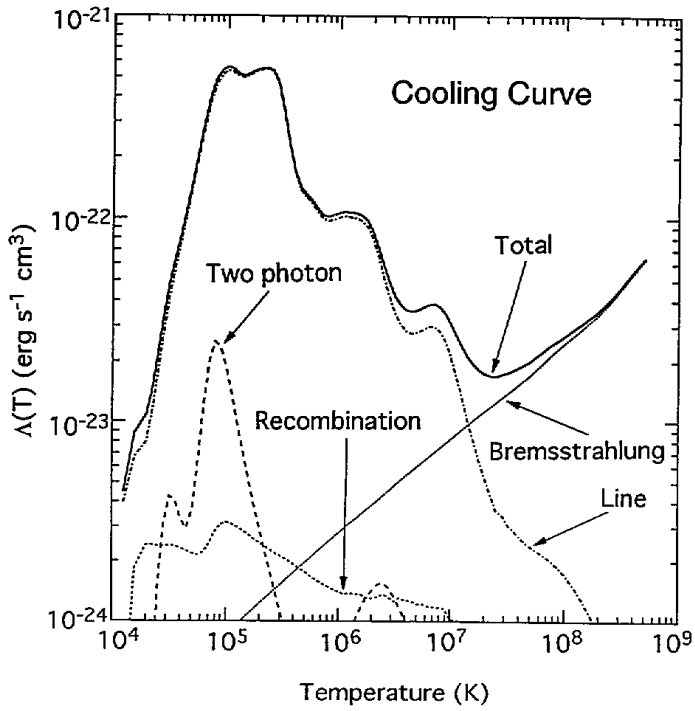

Figure 2.3: Temperature dependence of the cooling function with its components for optically thin plasma containing cosmic abundances of elements (Allen 1973).

2.3 Theoretical Background

2.3.1 X-ray Emission from Hot Plasma

Thermal Bremsstrahlung

The ICM, having low gas density ($\sim 10^{-3}$ cm^{-3}) and a high temperature ($\sim 10^{8}$ K) radiates predominantly in the X-ray band. The emitted X-rays consist of thermal Bremsstrahlung continuum and various atomic emission lines.

The plasma volume emissivity, i.e. X-ray radiation energy emitted from a unit volume in a unit time, is given as

$$\epsilon = n_{\rm g}^2 \Lambda(T, Z). \tag{2.1}$$

The quantity $n_{\rm g}$ is number density of the gas, and $\Lambda(T, Z)$ is called cooling function, with T and Z representing the plasma temperature and the heavy element abundance, respectively. Figure 2.3 shows the cooling function as a function of the plasma temperature assuming the cosmic abundances. The contribution of the bremsstrahlung continuum to Λ increases as $\propto T^{0.5}$. In contrast, the line contribution to Λ monotonously decreases with temperature above $T \sim 10^7$ K.

We can obtain the total X-ray luminosity by integrating equation 2.1. It is useful to define the emission integral as

$$EI = \int n_{\rm g}^2 \, dV, \tag{2.2}$$

where V is the volume of the cluster. If we assume that the ICM has a spatially-uniform temperature and abundance in the volume V, and that the ICM density is constant over the projected sky area S, then the luminosity is given as

$$L_{\rm X} = \int \epsilon \, dV = EM \times S \times \Lambda(T, Z). \tag{2.3}$$

The EM is the emission measure defined as

$$EM = \int n_{\rm g}^2 \, dl, \tag{2.4}$$

where l is the depth of the plasma along the line of sight. The emission integral determines the normalization of the spectrum (the overall intensity or luminosity), and the shape of the spectrum depends only on the temperature T and the heavy element abundance Z. Thus, by spectral fittings performed in the following sections, we can obtain T, Z, and EI (or EM if S is known) from the observed X-ray spectra.

Inverse Compton and Synchrotron Radiation

Several observations suggest the presence of magnetic fields and relativistic electrons in clusters of galaxies (see section 2.2.6). Due to these electrons, X-ray emission by the Inverse Compton scattering on the 3 K background photon is expected. In this section, the method to estimate the magnetic field strength in the clusters based on the X-ray and radio observations are summarized.

The number spectrum of relativistic electrons can be approximately expressed in the form

$$N(E)dE = KE^{-p}dE, \tag{2.5}$$

where K is an amplitude coefficient. We can expect the observed radiation flux as

$$f = \frac{V}{4\pi D^2} \int N(E)\dot{E}dE \propto \int \nu^{-\alpha} d\nu, \tag{2.6}$$

where V is the volume of the source, D is the distance to the source, and $p = 2\alpha + 1$ (e.g. Rybicki & Lightman 1979). The energy loss rate, $\dot{E}$, for the X-ray inverse Compton emission is

$$\dot{E}_{\rm c} \equiv \left(\frac{dE}{dt}\right)_{\rm c} = \frac{4}{3}\sigma_{\rm T} c \beta^2 \gamma^2 U_{\rm ph}, \tag{2.7}$$

and for the radio synchrotron emission is

$$\dot{E}_{\rm s} \equiv \left(\frac{dE}{dt}\right)_{\rm s} = \frac{4}{3}\sigma_{\rm T} c \beta^2 \gamma^2 U_{\rm B} \tag{2.8}$$

(e.g. Rybicki & Lightman 1979), where $\sigma_{\rm T} = 6.65 \times 10^{-25}$ cm^2 is the cross section for Thomson scattering, β is the velocity of relativistic electrons normalized by the speed of light, γ is the Lorentz factor of the relativistic electrons, $U_{\rm ph} = 4.0 \times 10^{-13}$ ergs cm^{-3} is the energy density of 3 K photons, and $U_{\rm B} = B^2/8\pi$ is the energy density of the magnetic field. Then, energy loss time scale due to inverse Compton scattering of 3 K microwave background photon is

$$\begin{aligned} t_{\rm c} = \frac{E}{(dE/dt)_{\rm c}} &\approx 2.4 \times 10^9 \left(\frac{\gamma}{10^3}\right)^{-1} \ {\rm yr} \\ &\approx 2.0 \times 10^9 \left(\frac{E}{10^{-3} \ {\rm erg}}\right)^{-1} \ {\rm yr}, \end{aligned} \tag{2.9}$$

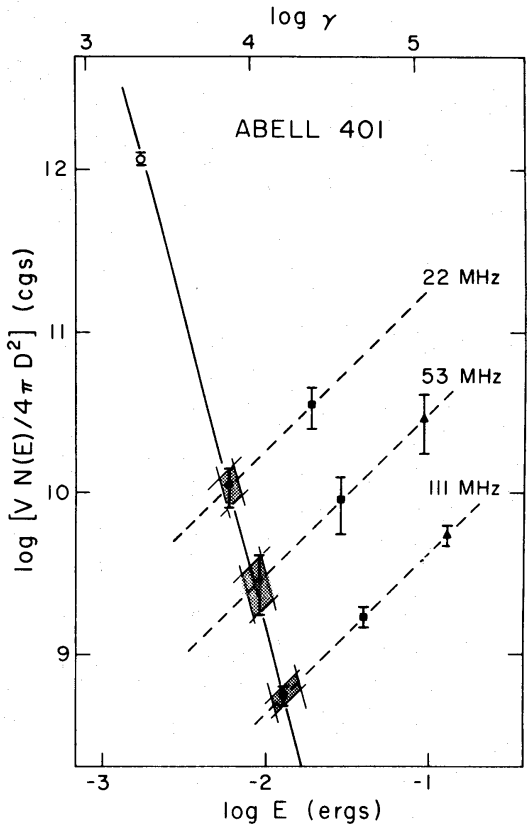

Figure 2.4: Electron spectrum of A401 cluster. The open circle is determined by X-ray observation, and the solid line shows a spectrum with an index p (see equation 2.5). The dashed lines are calculated from equation 2.15 and 2.14, based on the radio observations. Magnetic field strengths are indicated by filled-circles (10^{-7} gauss), filled-rectangles (10^{-8} gauss), and filled-triangles (10^{-9} gauss) (Harris & Romanishin 1974).

and that due to synchrotron emission is

$$t_{\rm s} = \frac{E}{(dE/dt)_{\rm s}} \approx 2.5\times10^{10}\left(\frac{\gamma}{10^3}\right)^{-1}\left(\frac{B}{10^{-6}\ {\rm gauss}}\right)^{-2}\ {\rm yr}$$
$$\approx 2.0\times10^{10}\left(\frac{E}{10^{-3}\ {\rm erg}}\right)^{-1}\left(\frac{B}{10^{-6}\ {\rm gauss}}\right)^{-2}\ {\rm yr}, \quad (2.10)$$

where $E=\gamma m_{\rm e}c^2$ is used. Thus the inverse Compton loss is more important than synchrotron losses when $B \lesssim 3\times10^{-6}$ gauss.

The characteristic frequency of inverse Compton emission due to an electron of energy E is

$$\nu_{\rm c} \approx 4\times10^{23}E^2\ {\rm Hz}, \quad (2.11)$$

while the frequency of synchrotron emission from an electron of energy E is

$$\nu_{\rm s} \approx 10^{18}BE^2\ {\rm Hz}, \quad (2.12)$$

where E is in ergs, and B is in gauss.

Harris & Romanishin (1974) introduced "normalized number of electrons" to determine the magnetic field strength based on X-ray and radio observations. The X-ray luminosity, produced by the inverse Compton process, in a bandpass width of 1 Hz is given as

$$L_{{\rm x},\nu} = 4\pi D^2 f_{{\rm x},\nu} = V\dot{E}_{\rm c}N(E)dE, \quad (2.13)$$

where $f_{\mathrm{x},\nu}$ is the X-ray flux in 1 Hz. Based on the X-ray observations, we measure the flux in a certain energy band. Using the above equations, we obtain

$$\left[\frac{VN(E)}{4\pi D^2}\right]_{\mathrm{x}} = 1.89\times10^{23}\frac{(1-\alpha)f_{\mathrm{x}}}{\epsilon_{\mathrm{c}}^{1.5}[(\epsilon_2/\epsilon_{\mathrm{c}})^{1-\alpha}-(\epsilon_1/\epsilon_{\mathrm{c}})^{1-\alpha}]}\ \text{electrons cm erg}^{-1}, \tag{2.14}$$

where f_{x} is the X-ray flux (ergs s^{-1} cm^{-2}) in the energy band from ϵ_1 to ϵ_2 keV, and ϵ_{c} is the energy in keV of the center of the band. This "normalized number of electrons" $[VN(E)/4\pi D^2]_{\mathrm{x}}$ should be plotted at an energy

$$E = 8.75\times10^{-4}\epsilon_{\mathrm{c}}^{1/2}\ \text{ergs},\ \text{ or }\ \gamma = 1069\epsilon_{\mathrm{c}}^{1/2}. \tag{2.15}$$

We can consider the radio data as a monochromatic flux. Then we obtain in the same manner as the X-ray case,

$$\left[\frac{VN(E)}{4\pi D^2}\right]_{\mathrm{r}} = 1.32\times10^{8}\frac{f_{\mathrm{r},\nu}}{(\nu_{\mathrm{r}}B)^{1/2}}\ \text{electrons cm erg}^{-1}, \tag{2.16}$$

where $f_{\mathrm{r},\nu}$ is the radio flux (Jy = 10^{-23} erg s^{-1} cm^{-2} Hz^{-1}) at ν_{r} Hz. This $[VN(E)/4\pi D^2]_{\mathrm{r}}$ should be plotted at

$$E = 4\times10^{-10}\left(\frac{\nu_{\mathrm{r}}}{B}\right)^{1/2}\ \text{ergs},\ \text{ or }\ \gamma = 4.88\times10^{-4}\left(\frac{\nu_{\mathrm{r}}}{B}\right)^{1/2}, \tag{2.17}$$

where B is the magnetic field strength in gauss. Figure 2.4 shows the electron spectrum of the A401 cluster as an example (Harris & Romanishin 1974).

Non-Thermal Bremsstrahlung

Alternatively, non-thermal bremsstrahlung, which caused by suprathermal electrons in ICM, is proposed as an emission process of the hard X-ray detected in some clusters. These sub-relativistic non-thermal particles might recently be accelerated up to higher energies either by shocks or turbulent acceleration, because they will quickly lose energies by interactions with the thermal plasma (Sarazin 1999).

We assume the differential spectrum of the suprathermal electrons can be expressed as a power-law in the momentum

$$N(p) = N_0\, p^{-\mu} \qquad p \gtrsim p_{\mathrm{l}}, \tag{2.18}$$

where p is the momentum of the non-thermal electrons normalized to $m_{\mathrm{e}}c$, and minimum momentum p_{l} is also assumed. For shock acceleration, the exponent μ is represented as

$$\mu \approx \frac{r+2}{r-1}, \tag{2.19}$$

where r is the shock compression ratio (e.g. Bell 1978). The luminosity of non-thermal bremsstrahlung emitted at photon energies from ϵ to $\epsilon + d\epsilon$ is is given by the integral

$$L_\epsilon d\epsilon = \epsilon d\epsilon \int_{p_{\mathrm{l}}}^{\infty} N(p)dp\, v(p)\ \sum_Z n_Z \frac{d\sigma}{d\epsilon}, \tag{2.20}$$

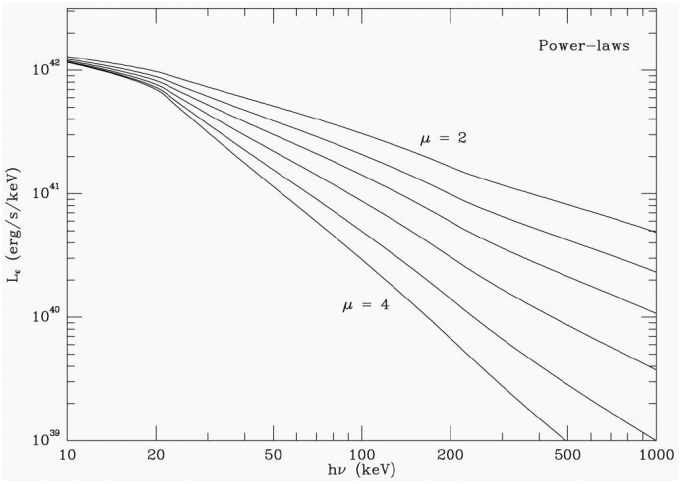

Figure 2.5: The non-thermal bremsstrahlung spectra modeled with power-law momentum distribution. The exponent values are $\mu = 2, 2.3, 2.6, 3, 3.5, and 4$ from upper to lower (Sarazin & Kempner 2000).

where $\epsilon = h\nu$ (ν is the photon frequency), $v(p)$ is the velocity of an electron with a momentum p, Z is the various thermal particles in the plasma, n_Z is the number densities of these thermal particles, and $d\sigma/d\epsilon$ gives the cross-section for the collision between a non-thermal electron and a thermal particle, to emit a photon with an energy range of ϵ to $\epsilon + d\epsilon$ (Sarazin & Kempner 2000).

Figure 2.5 shows emission model of the non-thermal bremsstrahlung assuming $p_l = [(1 + 3kT/m_e c^2)^2 - 1]^{1/2}$, $kT = 7$ keV, and the total number of non-thermal electron $N_{\rm nt} = 10^{69}$ (Sarazin & Kempner 2000).

For steep power-law momentum distributions ($\mu \gtrsim 3$), the spectrum of non-relativistic bremsstrahlung in the range of $p_1^2 < 2\epsilon/(m_e c^2) \ll 1$ is represented as,

$$L_\epsilon = \frac{32\pi^{3/2}}{3} \frac{e^6}{m_e c^4 h} \left[\frac{\Gamma(\mu/2)}{\mu\Gamma(\mu/2+1/2)}\right] \left(\sum_Z n_Z Z^2\right) N_0 \left(\frac{m_e c^2}{2\epsilon}\right) \tag{2.21}$$

where e is an elemental charge in esu unit, and Γ is a gamma function (Sarazin & Kempner 2000). Thus the photon index is $\Gamma \approx 1 + \mu/2$ in this energy range. At lower photon energies, the spectrum flatten because of the lack of low energy non-thermal electrons. At very low photon energies with $\epsilon \ll [(1 + p_1^2)^{-1/2} - 1] m_e c^2$, the single-particle non-relativistic bremsstrahlung luminosity is given by

$$L_{\epsilon,p} = \frac{32\pi}{3} \frac{e^6}{m_e c^4 h} \left(\sum_Z n_Z Z^2\right) \frac{1}{p} \ln\left(\frac{2p^2 m_e c^2}{\epsilon}\right) \tag{2.22}$$

(Sarazin & Kempner 2000). Thus, the non-thermal bremsstrahlung spectrum only depends on the logarithm of $(1/\epsilon)$ at photon energies below the lowest kinetic energy of non-thermal electrons.

2.3.2 Heating and Cooling of the ICM

If we consider heating of the ICM only due to an infall of the primordial gas into the cluster and the compression, the heating time scale is equal to the free-fall time scale given as

$$t_{\rm heat} \approx 3.1 \times 10^9 \left(\frac{D}{\rm Mpc}\right)^{3/2} \left(\frac{M_{\rm total}}{10^{14}\ M_\odot}\right)^{-1/2} \ {\rm yr}, \tag{2.23}$$

where D is the cluster diameter, and $M_{\rm total}$ is the total mass of the cluster. On the other hand, the primary cooling process for the ICM is radiative cooling due to free-free emission, expressed as

$$t_{\rm cool} \approx 8.5 \times 10^{10} \left(\frac{n_{\rm p}}{10^{-3}\ {\rm cm}^{-3}}\right)^{-1} \left(\frac{T}{10^8\ {\rm K}}\right)^{1/2} \ {\rm yr} \tag{2.24}$$

(Sarazin 1988, p. 149), where $n_{\rm p}$ is the number density of protons. Thus the cooling time is longer than the Hubble time for most of the clusters except for the central region.

If the ICM has a gradient in the temperature, thermal conduction transports the heat from hot to cool regions. The thermal conduction is primarily due to electrons. If the scale length of the temperature gradient $T/|\nabla T|$ is much larger than the electron mean free path (equation 2.29), the heat flux (i.e. erg s^{-1} cm^{-2}) is expressed as

$$Q = -\kappa\, \nabla T, \tag{2.25}$$

where κ is thermal conductivity given as

$$\kappa \approx 4.6 \times 10^{13} \left(\frac{T}{10^8\ {\rm K}}\right)^{5/2} \left(\frac{\ln \Lambda}{40}\right)^{-1} \ {\rm erg\ s^{-1}\ cm^{-1}\ K^{-1}} \tag{2.26}$$

(Sarazin 1988, p. 157), where Λ is the ratio of the largest to the smallest impact parameters for collisions and only weakly depends on temperature and density (Spitzer 1962). The terms $\ln \Lambda$ is often called Coulomb logarithm. The conduction time scale is estimated approximately as

$$\begin{aligned} t_{\rm cond} &\approx \frac{n_{\rm e} k}{\kappa} \left(\frac{T}{|\nabla T|}\right)^2 \\ &\approx 5.6 \times 10^7 \left(\frac{n_{\rm e}}{10^{-3}\ {\rm cm}^{-3}}\right) \left(\frac{T}{10^8\ {\rm K}}\right)^{-5/2} \left(\frac{\ln \Lambda}{40}\right) \left(\frac{T/|\nabla T|}{0.25\ {\rm Mpc}}\right)^2 \ {\rm yr}, \end{aligned} \tag{2.27}$$

where k is the Boltzmann's constant $= 1.38 \times 10^{-16}$ erg K^{-1}. Then, the ICM within ~ 1 Mpc scale would achieve isothermality in the Hubble time. If the mean free path of electrons is larger compared with the scale length of the thermal gradient, the heat flux expressed by equation 2.25 gives an overestimate, because the electrons are implied to diffuse at a speed greater than their thermal speed. General expression for the heat flux, including the correction factor for the mean free path, is approximately expressed as

$$Q \approx -\frac{\kappa T}{T/|\nabla T| + 4.2\lambda_{\rm e}} \frac{\nabla T}{|\nabla T|} \tag{2.28}$$

(Sarazin 1988, p. 158).

Shock Heating

Recent observations revealed statistically significant substructures in X-ray surface brightness in many clusters (e.g. Jones & Forman 1984; Burns et al. 1994). The observed substructures in the ICM argue for remnants or ongoing merger events. The hydro/N-body simulations show that the shocks play important roles to heat up the ICM, if the merging occurs supersonically (see e.g. Ishizaka & Mineshige 1996). We briefly discuss the transition of physical conditions in the upstream to the downstream of the shock.

The mean free path of electrons ($\lambda_{\rm e}$) and ions ($\lambda_{\rm i}$) in a plasma are expressed as

$$\lambda_{\rm e} = \lambda_{\rm i} \approx 23 \left(\frac{n_{\rm e}}{10^{-3}\ {\rm cm}^{-3}} \right)^{-1} \left(\frac{T}{10^8\ {\rm K}} \right)^2\ {\rm kpc} \tag{2.29}$$

(Sarazin 1988, p. 156), where $n_{\rm e}$ is the number density of electrons. If the region of interest has a much larger scale than the mean free path, we may consider that the physical parameters shown in figure 2.6 satisfy the 'jump' condition. It is called as Rankine-Hugoniot jump condition (e.g. Shu 1992). The mass, momentum, and energy conservation equations are expressed as

$$\rho_1 v_1 = \rho_2 v_2, \tag{2.30}$$

$$\rho_1 v_1^2 + p_1 = \rho_2 v_2^2 + p_2, \tag{2.31}$$

$$\frac{1}{2} v_1^2 + \frac{\gamma}{\gamma - 1} \frac{p_1}{\rho_1} = \frac{1}{2} v_2^2 + \frac{\gamma}{\gamma - 1} \frac{p_2}{\rho_2}, \tag{2.32}$$

where ρ, v, and p indicate the density, velocity, and pressure, respectively, measured from the rest frame of the shock. The suffixes of 1 and 2 represent the upstream and downstream of the shock, respectively, and γ is the ratio of specific heats. From the above equations, we find

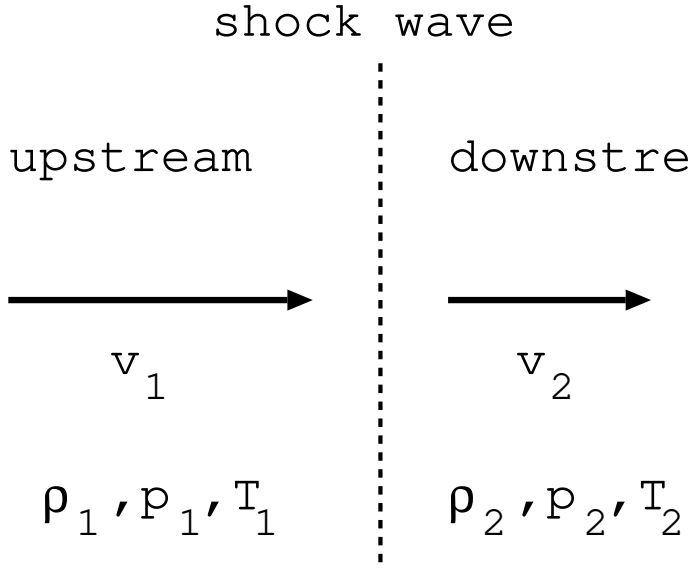

Figure 2.6: Schematic representation of the transition region for a shock wave measured in the rest frame of the shock. Upstream gas properties are transformed to downstream ones.

$$\frac{\rho_2}{\rho_1} = \frac{(\gamma+1)\mathcal{M}_1^2}{(\gamma-1)\mathcal{M}_1^2+2}, \tag{2.33}$$

$$\frac{p_2}{p_1} = \frac{2\gamma\mathcal{M}_1^2-(\gamma-1)}{\gamma+1}, \tag{2.34}$$

$$\frac{T_2}{T_1} = \frac{p_2\cdot\rho_1}{p_1\cdot\rho_2} = \frac{[2\gamma\mathcal{M}_1^2-(\gamma-1)][(\gamma-1)\mathcal{M}_1^2+2]}{(\gamma+1)^2\mathcal{M}_1^2}, \tag{2.35}$$

where $\mathcal{M}$ indicates the Mach number.

In the limit of a weak shock, $p_1 \approx p_2$, the shock wave travels with a velocity which is close to the speed of sound, and is practically the same as an acoustic compression wave (Zel'dovich & Raizer 1966). On the other hand, in the limit of a strong shock, $p_2 \gg p_1$, $\mathcal{M}_2$ approaches a constant value $\mathcal{M}_2 \to [(\gamma-1)/2\gamma]^{1/2}$, and p_2 is expressed as

$$p_2 \approx \frac{2(\gamma-1)}{(\gamma+1)^2}\rho_2 v_1^2. \tag{2.36}$$

Thus, for the strong shock, the gas can be heated up to $kT_2 \approx (3/16)\mu m_{\rm p} v_1^2$, where $\mu \approx 0.6$ is a mean molecular weight and $m_{\rm p}$ is a proton mass, assuming $\gamma = 5/3$.

2.3.3 Distribution of the ICM

Gravitational Mass

The sound crossing time is expressed with the gas temperature T and the cluster diameter D as

$$t_{\rm s} \approx 6.6\times10^8 \left(\frac{T}{10^8\ {\rm K}}\right)^{-1/2}\left(\frac{D}{\rm Mpc}\right)\ {\rm yr} \tag{2.37}$$

(Sarazin 1988, p. 165). The crossing time for a cluster is considerably shorter than the age of the universe, so the ICM can be assumed to be under hydrostatic equilibrium:

$$\nabla P_{\rm g} = -\rho_{\rm g}\nabla\phi \tag{2.38}$$

where $P_{\rm g}$ is gas pressure, ϕ is gravitational potential, and $\rho_{\rm g}$ is mass density of the gas which can be expressed as $\rho_{\rm g} = \mu m_{\rm p} n_{\rm g}$. Here $\mu \approx 0.6$ is a mean molecular weight in terms of the proton mass, $n_{\rm g}$ is the number density of the gas, and $m_{\rm p}$ is a proton mass.

Because of low density and high temperature, the ICM can be treated as an ideal gas. Furthermore, if we assume a spherical symmetry, the above equation reduces to

$$\frac{d\phi(R)}{dR} = -\frac{kT_{\rm g}}{\mu m_{\rm p}}\frac{d\ln(n_{\rm g}T_{\rm g})}{dR}. \tag{2.39}$$

Then combining with the Newton's equation

$$\frac{d\phi(R)}{dR} = -\frac{GM(<R)}{R^2}, \tag{2.40}$$

where $M(<R)$ denotes gravitational mass of the cluster of galaxies, we can express $M(<R)$ as

$$M(<R) = -\frac{kT_{\rm g}R}{\mu m_{\rm p}G}\left(\frac{d\ln T_{\rm g}}{d\ln R}+\frac{d\ln n_{\rm g}}{d\ln R}\right). \tag{2.41}$$

Therefore, measurements of the density distribution $n_{\rm g}(R)$ and the temperature distribution $T_{\rm g}(R)$ gives estimates on the total mass distribution $M(<R)$.

Radial Distribution of the ICM Density

First, we consider a cluster of galaxies to be a self-gravitating system consisting of collision-less particles of a single species, although a cluster is in fact a multi-component system. We assume the particles to have a mass m, density profile $n(R)$, and an isotropic uniform velocity dispersion of $\sigma_{\rm r}^2$. The hydrostatic equation for the particles can be written, in analogy to equation 2.39, as

$$\frac{d\phi(R)}{dR} = -\sigma_{\rm r}^2 \frac{d\ln n(R)}{dR}, \tag{2.42}$$

which may be integrated and solved for $n(R)$ as

$$n(R) = n_0 \exp\left[\frac{\phi(R)}{\sigma_{\rm r}^2}\right]. \tag{2.43}$$

To determine $n(R)$, we may combine above equation with Poisson's equation

$$\nabla^2\phi(R) = 4\pi G m n(R). \tag{2.44}$$

King (1962) found the function

$$n(R) = n_0 \left[1 + \left(\frac{R}{R_{\rm c}}\right)\right]^{-3/2} \tag{2.45}$$

to be a good approximation of the numerical solution (King model). Here $R_{\rm c}$ is a characteristic radius called core radius. In many clusters of galaxies, spatial distribution of the density of member galaxies is known to follow equation 2.45 well. This suggests that the King model is a good approximation of the total mass distribution in clusters.

We next consider the ICM density profile when the potential can be approximated by the King model. For simplicity we assume the ICM to be isothermal. Then, as the ICM and the 'particles' must obey the same gravitational potential $\phi(R)$, we can equate equations 2.39 and 2.42 as

$$\frac{kT_{\rm g}}{\mu m_{\rm p}} \frac{d\ln\left(n_{\rm g}T_{\rm g}\right)}{dR} = -\sigma_{\rm r}^2 \frac{d\ln n(R)}{dR}. \tag{2.46}$$

Substituting equation 2.45 for $n(R)$, we get an approximate expression for the ICM density

$$n_{\rm g}(R) = n_0 \left[1 + \left(\frac{R}{R_{\rm c}}\right)\right]^{-3\beta/2} \tag{2.47}$$

with

$$\beta = \frac{\mu m_{\rm p}\sigma_{\rm r}^2}{kT_{\rm g}}. \tag{2.48}$$

Equation 2.47 is commonly referred to as the β model.

The β model is specified by three parameters; the central density n_0, the core radius $R_{\rm c}$, and β. The parameter β indicates the ratio between specific kinetic energy of the particle representing the cluster potential and the specific thermal energy of ICM particle. When all components of a cluster have the same energy per unit mass, we expect $\beta = 1$.

X-ray Surface Brightness Distribution

When the ICM can be assumed to have a spherically symmetric shape, the X-ray surface brightness $S(r)$ of a cluster is expressed by the integration of emissivity along the line-of-sight, as

$$S(r) = \int_r^{R\mathrm{max}} \frac{2R\,\epsilon(R)\,dR}{\sqrt{R^2 - r^2}} \tag{2.49}$$

where R is as before the three-dimensional distance from the cluster center, R_{max} is the effective boundary of the cluster, and r is the projected radius. If we assume that the ICM is isothermal, with negligible abundance gradient, obeying the β model density profile, and R_{max} being infinity, then we can analytically integrate above equation to obtain

$$S(R) = S_0 \left[1 + \left(\frac{r}{R_{\mathrm{c}}}\right)\right]^{-3\beta+1/2}. \tag{2.50}$$

This expression is known to give a good fit to the observed X-ray surface brightness distribution. Many clusters show $\beta = 0.4-0.8$ from the observed X-ray surface brightness (e.g. Jones & Forman 1984).

Chapter 3

Review of The Virgo Cluster of Galaxies

3.1 Optical Properties

The Virgo cluster of galaxies is the nearest cluster of galaxies ($\sim$ 20 Mpc from the Sun), and has a large angular extent of about 12° in diameter on the celestial sphere. Its general appearance is irregular (Abell et al. 1989), it is classified as Bautz-Morgan type III (Bautz & Morgan 1970), and as Rood-Sastry type F (Rood & Sastry 1971).

The Virgo cluster of galaxies is one of the most important stepping stones to determine the distance to extragalactic objects (e.g. Tully 1988). It's distance has been used to determine the Hubble constant ever since 1920'. Recent determinations of the distance to the Virgo cluster is performed by Hubble Space Telescope (HST) mission by observing the period-luminosity relation of Cepheid variables. Most recently, Ferrarese et al. (1997) observed 52 Cepheids in the Virgo member galaxy M100 (NGC 4321, VCC 0596) with the HST, and determined the distance modulus of the galaxy to be 31.04 ± 0.17 mag, corresponding to a distance of 16.1 ± 1.3 Mpc. They also gives a Hubble constant of $H_0 = 83 \pm 16$ km s^{-1} Mpc^{-1}.

On the basis of the deep Las Campanas survey of the Virgo cluster area over $\sim$ 140 deg^2, Binggeli et al. (1985) (updated in Binggeli et al. 1993) have cataloged 1292 members of galaxies in the Virgo cluster. The survey is complete down to an absolute magnitude limit of $M_{B_T} \approx -13.7$ mag, and contains in addition many faint dE and Im galaxies down to the limit of $M_{B_T} \approx -11.7$ (Virgo Cluster Catalogue, VCC). Figure 3.1 shows the distribution of galaxies in the Virgo cluster (Schindler et al. 1999, based on the VCC). We can see several sub-concentrations. A major subcluster exists around M87 (M87 subcluster or subcluster A), and another smaller, less dense subcluster lies around the M49 (M49 subcluster or subcluster B). Although M87 is often taken as the center of the Virgo cluster, it is 1° away from the density peak of the subcluster A toward the east. With respect to morphological type, early-type member galaxies are concentrated most strongly. On the other hand, late-type galaxies are scattered over the whole region of the cluster (figure 3.2). Furthermore, the late-type galaxies have a larger velocity dispersion of $\sigma_{\rm r} \approx 737$ km

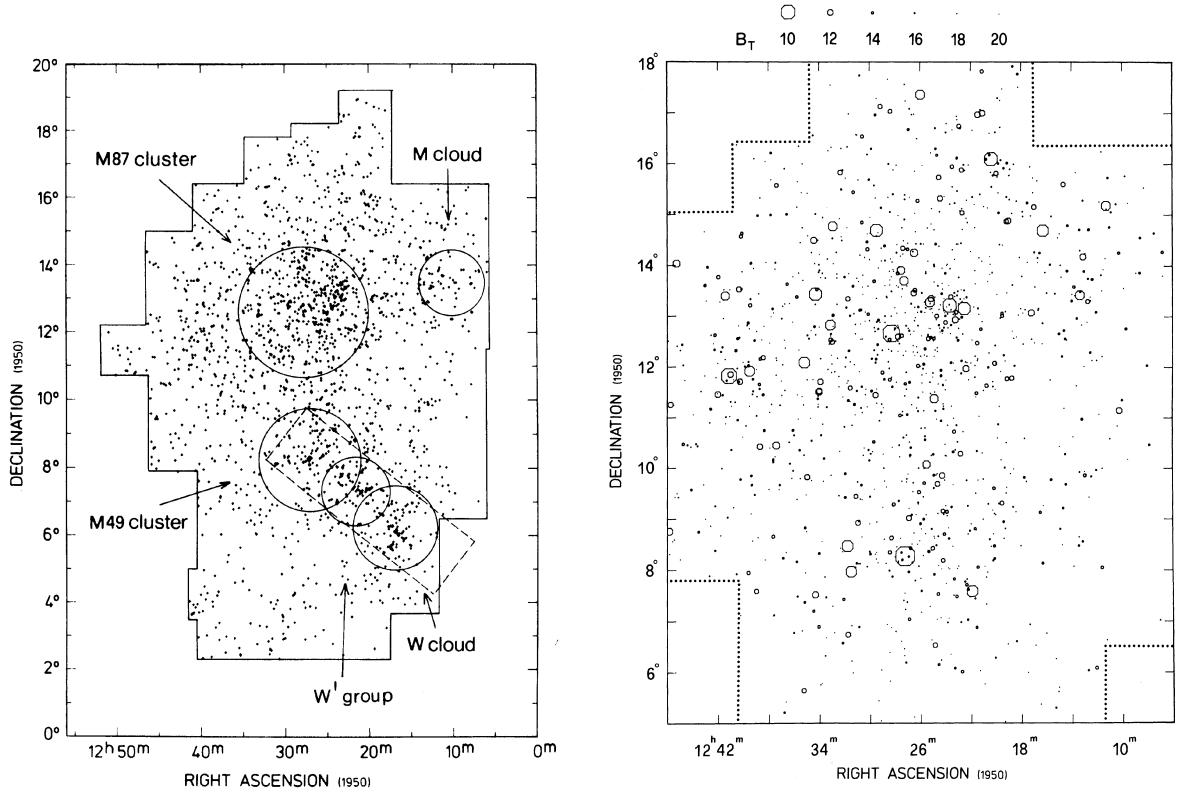

Figure 3.1: Plot of member and possible member galaxies of the Virgo cluster in the Virgo Cluster Catalogue (Binggeli et al. 1985). *left* : Dots show the member and possible member galaxies. Five main concentration indicated by circles. *right* : All cluster members are plotted with Luminosity weighted symbols (Binggeli et al. 1987).

s^{-1} than that of early-type galaxies, $\sigma_r \approx 589$ km s^{-1} (Binggeli et al 1993). These suggest that late-type galaxies have only recently (in the last few Gyr) fallen, or are still falling into the cluster from environment.

From the figure 3.2, we can see that the M87 subcluster is made up predominantly of early-type galaxies, while the M49 subcluster contains mainly late-type galaxies. Though the M49 subcluster has a higher spiral abundance, the velocity dispersion of M49 subcluster is $\sigma_r \approx 500$ km s^{-1} which is lower than that of M87 subcluster $\sigma_r \approx 800$ s^{-1} (figure 3.3).

Fukugita et al. (1993) and Yasuda et al. (1997) carried out a B-band Tully-Fisher analysis for a complete sample of spiral galaxies in the Virgo cluster, and the three dimensional structure was studied. They showed the evidence that spiral galaxies in the Virgo cluster are distributed in an elongated region, like a filament, which extends from 10 to 30 Mpc almost in the line of sight. They also showed that the number density of the galaxies has a peak at a distance 14–18 Mpc, and M49 subclusters is located $15 - 20\%$ farther than the M87 subcluster on average.

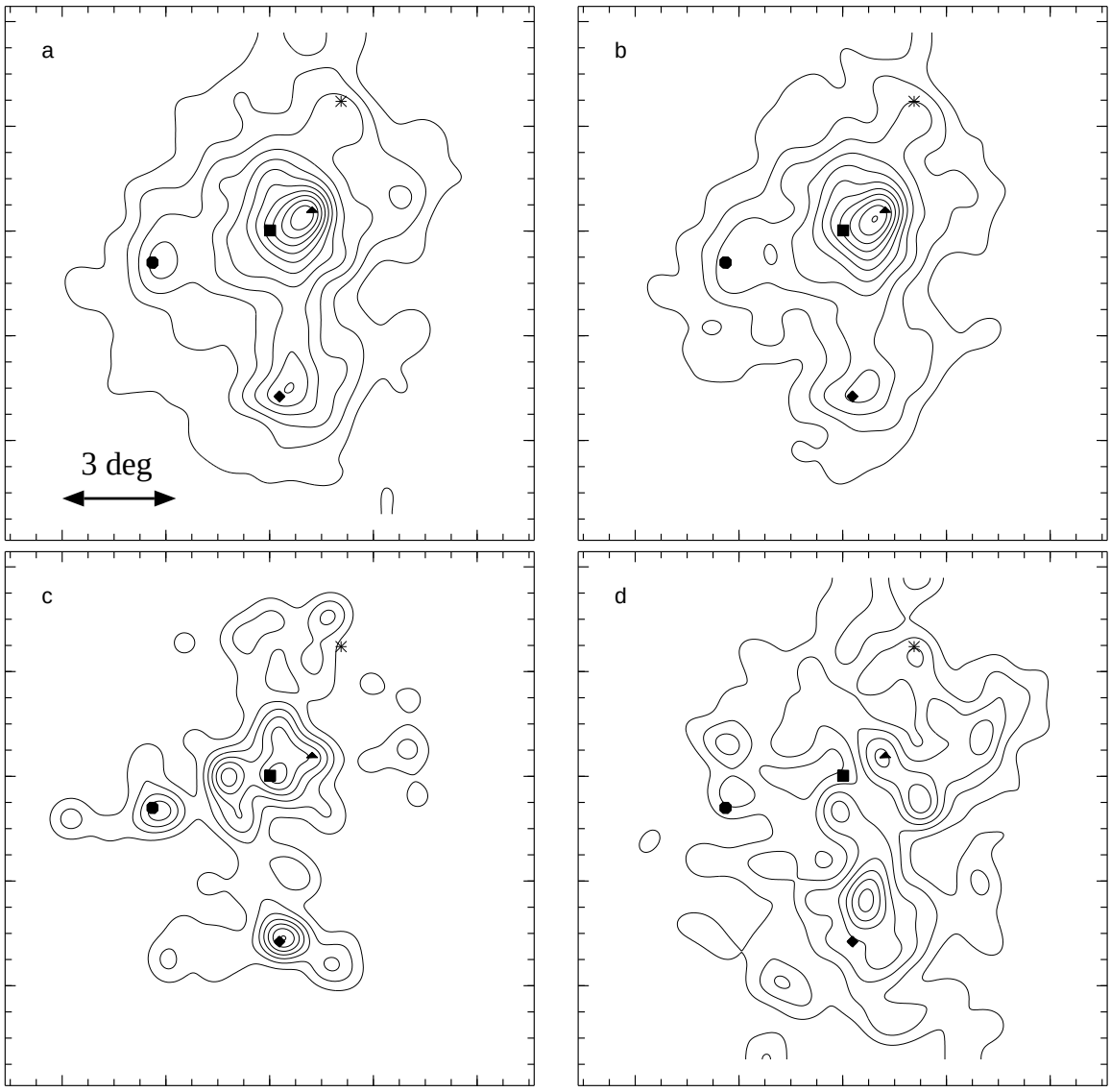

Figure 3.2: Distribution of different galaxy types in the Virgo cluster. (a) all galaxy types, (b) dwarf elliptical and dwarf S0 galaxies, (c) elliptical and S0 galaxies, (d) spiral and irregular galaxies. Number densities smoothed with a Gaussian of $\sigma = 24'$. The distance between two tick marks is $42'$ in each panel. Symbols indicate major galaxies: M87 (square), M49 (diamond), M86 (triangle), M60 (octagon), and M100 (star) (Schindler et al. 1999).

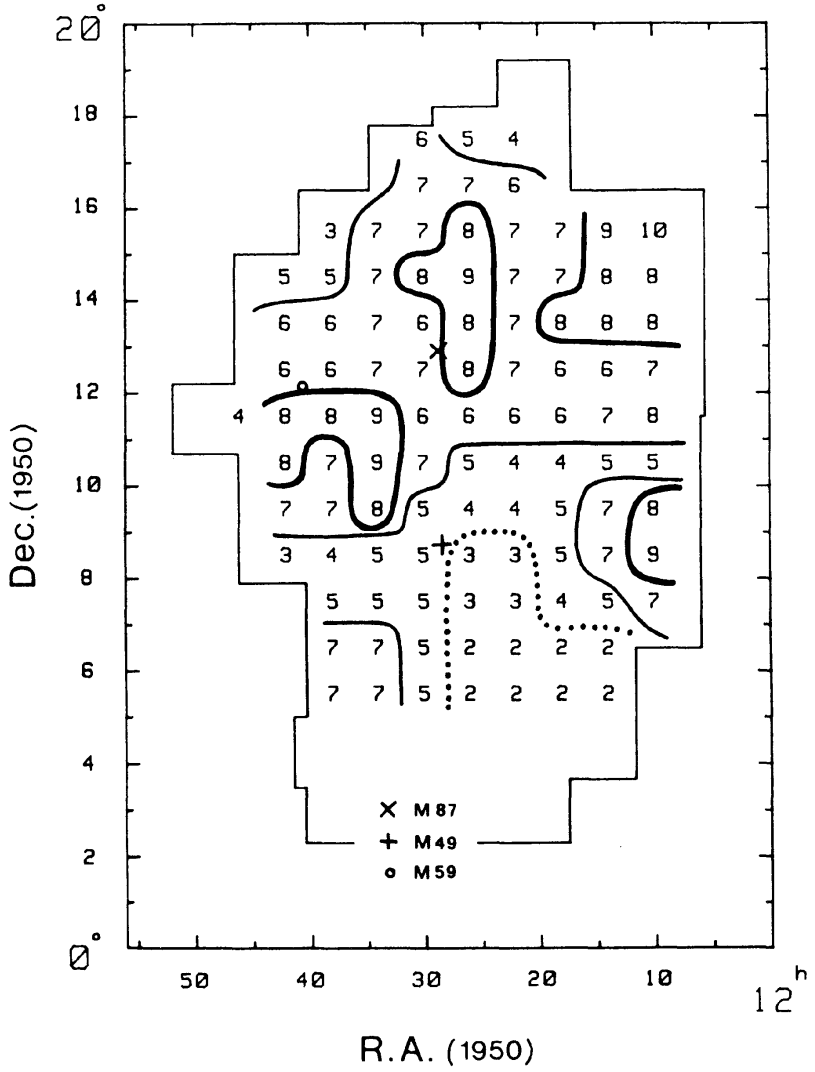

Figure 3.3: A map of the velocity dispersion of the galaxies in Virgo cluster. The number gives the mean $\sigma = (v - \langle v \rangle^2 / 100 \text{ km s}^{-1})$ in $1^\circ \times 1^\circ$ cells, smoothed over nine neighboring cells. Lines of constant velocity dispersion at various levels are also shown (Binggeli et al. 1987).

3.2 X-ray Properties

The Virgo cluster of galaxies is the first extragalactic X-ray source to be identified (Byram et al. 1966; Bradt et al. 1967). The diffuse X-ray emission from the Virgo cluster is strongly concentrated around the dominant elliptical galaxy M87 and is centered on M87 (Malina et al. 1976) rather than the optical center of the cluster which lies about 1° northwest of M87.

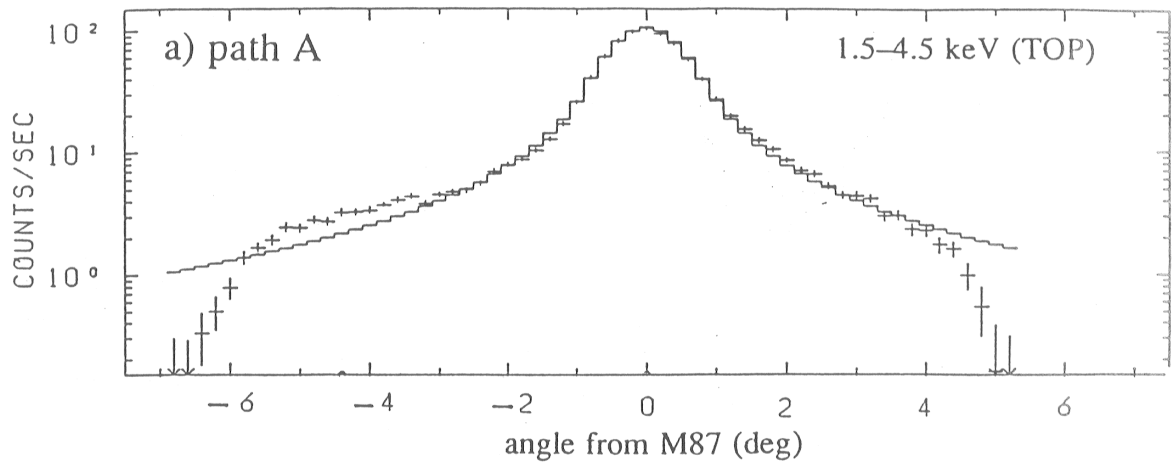

Figure 3.4: X-ray surface brightness obtained with Ginga (Takano 1990). The solid line denotes the expected profiles by extrapolating the X-ray surface brightness distribution independently measured with Einstein IPC within 100′ from M87 (Fabricant et al. 1983).

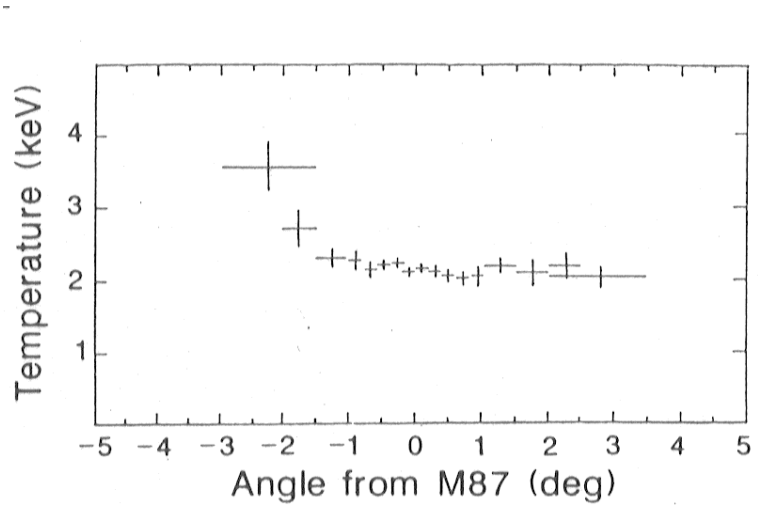

Figure 3.5: ICM temperature distribution obtained with Ginga (Koyama et al. 1991).

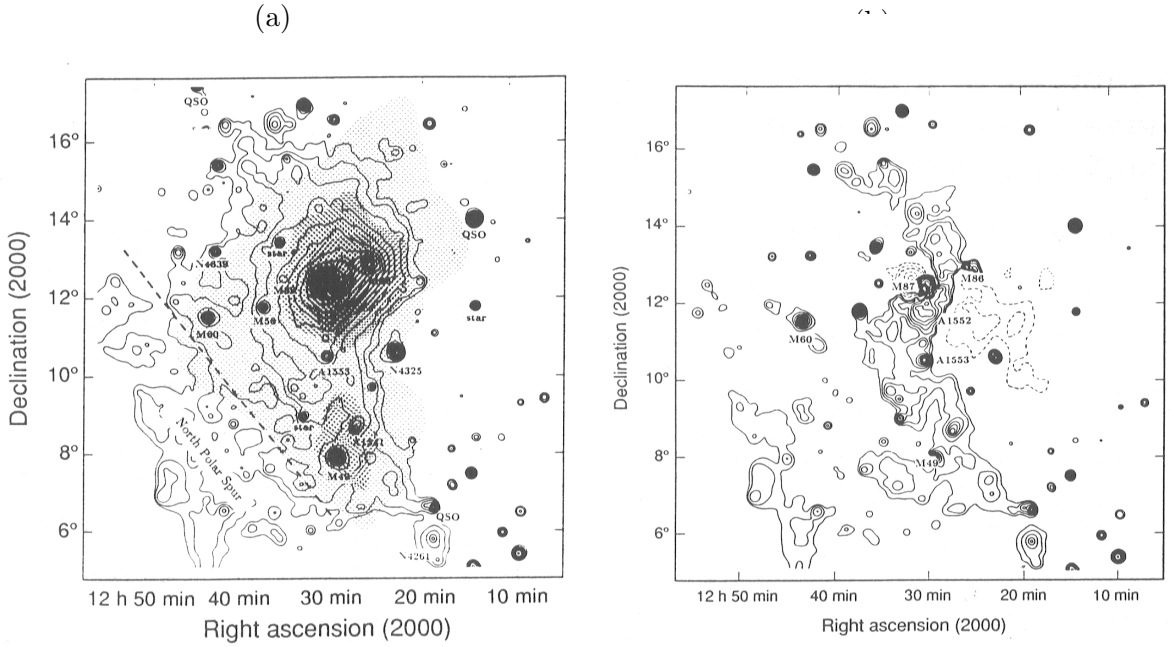

Figure 3.6: (a) X-ray contour plot of the Virgo cluster obtained with ROSAT in the energy range of $0.4 - 2.4$ keV (Böhringer et al. 1994). The first two contour levels correspond to 3σ and 5σ above the background, and following contour levels increase by factors of 1.5. The galaxy density distribution as taken from Binggeli et al. (1987) is shown in gray scales. (b) Contour plot of the residual X-ray surface brightness image that is obtained by subtraction of a model image corresponding the model fit of figure 3.7(a). Negative contours are shown as dashed lines.

A first indication of diffuse emission extending over 10° in the sky was found with the non-imaging collimator detector on board the Ginga satellite (Takano 1990; Koyama et al. 1991). The diffuse X-ray emission is strongly peaked at M87, and is well described by the β model (equation 2.50) with $\beta \approx 0.436$, $R_{\rm c} \approx 1'.62$, except for the south region (figure 3.4), where the X-ray surface brightness distribution shows significant flattening with $\beta \approx 0.357$. Figure 3.5 shows that the gas temperature around M87 is almost constant with $kT \approx 2$ keV, but the temperature is rising to ≈ 4 keV toward M49. These suggests that the ICM of the Virgo cluster consists of at least two components, and the Virgo cluster is not a dynamically relaxed system.

Another important result of the Ginga observation is that the iron abundance increases drastically towards the center of the Virgo cluster. The iron abundance is at least about half of the cosmic value in the innermost region of M87, and significantly decreases at outward region to ~ 0.2 solar.

ROSAT scanned the Virgo cluster region between November 1990 and January 1991 in the energy range 0.1–2.4 keV (Böhringer et al. 1994). Figure 3.6 shows contour map of the X-ray surface brightness of the Virgo cluster. The X-ray morphology is similar to the structure of the galaxy distribution (Schindler et al. 1999). However, the M49 halo is much smaller in the X-ray image compared to the optical appearance of the galaxies around M49. The X-ray surface

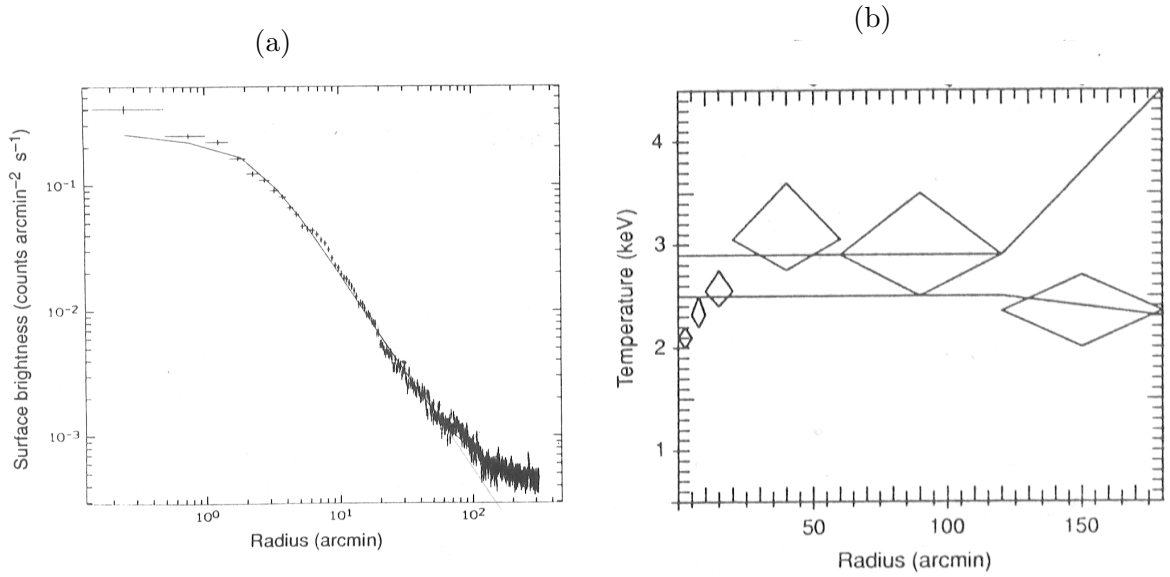

Figure 3.7: (a) Azimuthally averaged surface brightness profile around M87 (data points) and result of a β model fit (line) by Böhringer et al. (1994). The β model parameters are $\beta = 0.45$ and $R_c = 2'.3$. (b). Radial temperature profile of the ICM around M87. The diamonds give the values determined by ROSAT, and the lines show the results of the Ginga. The symbols indicate 1σ errors in the temperature determination.

brightness around M87 can be fitted by the β model with $\beta = 0.45$ and $R_c = 2'.3$ (figure 3.7 a). Although the overall temperature distribution around M87 is consistent with Ginga result within $\sim 1^\circ$ (see figure 3.7 b), ROSAT found no evidence of the temperature increase around M49.

Recently, Matsumoto et al. (1996) and Matsumoto (1998) reported the ASCA results of the observation of M87 and northwest region of M87. They found the spectra of the M87 require at least two temperature components, approximately 2.9 and 1.3 keV, and the cool component is more concentrated toward the center than that of the hot component. Furthermore, the surface brightness profile of the hot component can be extrapolated smoothly to that of the ICM beyond $40'$ from the center. These suggests that the cool component of M87 can be attributed to the interstellar matter of M87, while the hot component is the ICM of the Virgo main body. The abundance of Fe, Si, and S rise towards the center of M87, although the ratio of Si/Fe and S/Si remain constant. The ICM at regions beyond $40'$ from the center of M87 toward northwest can be represented by a single-temperature plasma. The temperature decreases with radius from $0'$ to $50'$, and it becomes almost constant beyond the $50'$ radius. The metal abundances also decrease with radius from $0'$ to $50'$, then become almost constant beyond the radius of $50'$ (Figure 3.8).

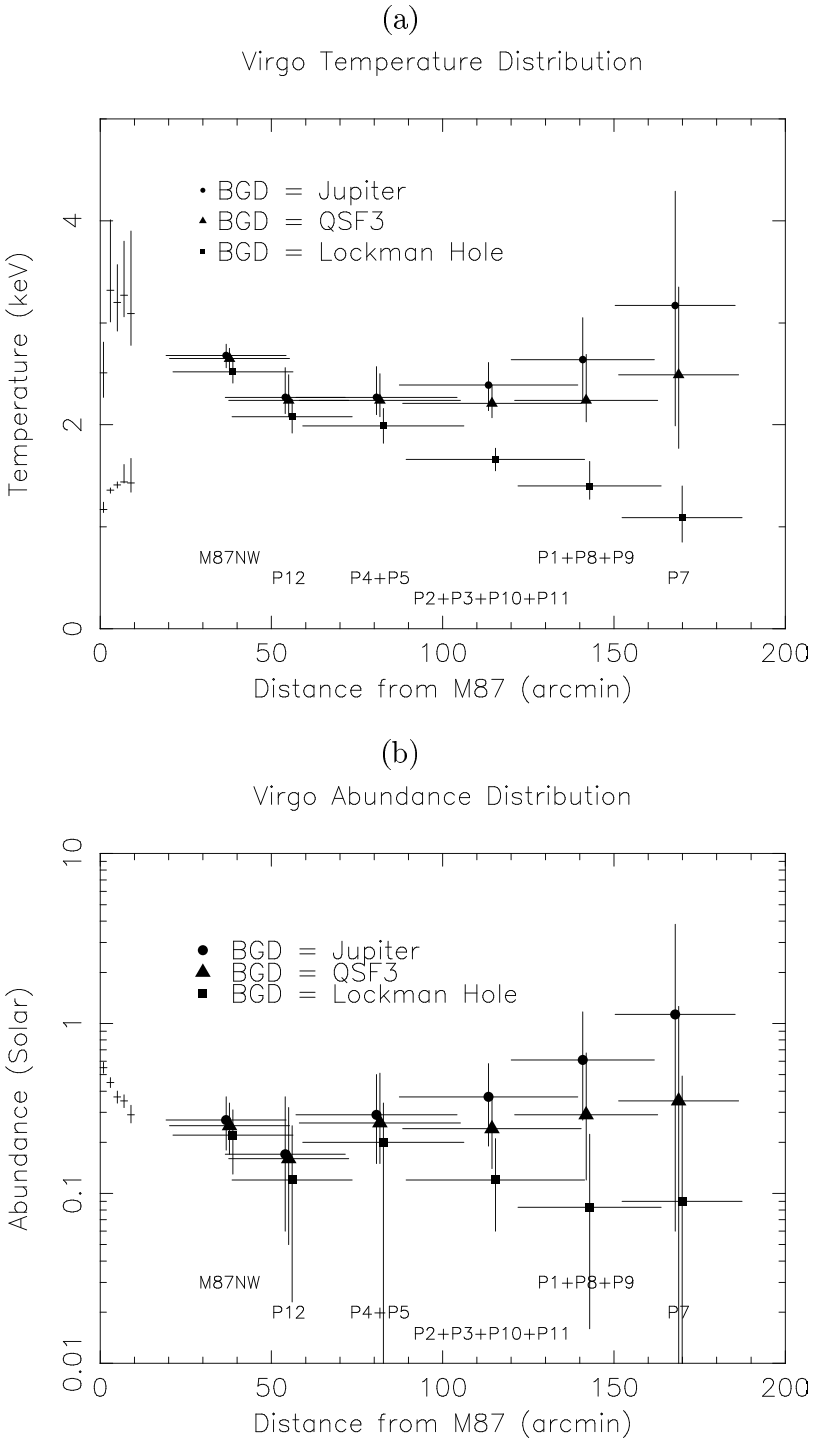

Figure 3.8: Temperature (upper panel) and abundance (lower) distribution of the Virgo cluster obtained with ASCA (Matsumoto 1998). To estimate the ambiguity of the background level, he uses three different observation data sets as the background: observation of Jupiter (dot), QSF3 (triangle), and Lockman hole (square). Labels (such as p1) indicates the observed position of ASCA which corresponds to the position listed in table 6.1 (p1 of above figures corresponds to nw_p1 in table 6.1).

3.3 M87 and M49

In this section, we summarize the properties of M87 (subcluster) and M49 (subcluster). General properties of these galaxies (or subclusters) are summarized in tables 3.1 and 3.2.

M87 is a giant elliptical galaxy at the center of the Virgo cluster. Though it has fairly extended optical emission, it is not classified as a cD galaxy (Schombert 1986). M87 is known as the first galaxy from which a jet was discovered. The jet is seen in radio, IR, optical, UV, and X-ray bands with essentially the same morphology (Biretta et al. 1991). From the ASCA observation, complex temperature structure (at least two components of 2.9 and 1.3 keV are required), and gradient of abundances of Fe, Si, and S were found (Matsumoto et al. 1996; Matsumoto 1998), as shown in section 3.2.

M49 is the brightest object in the Virgo cluster (even brighter than M87) in optical, and is also a strong radio and X-ray emitter. From the ASCA observation, the ISM temperature is ~ 1 keV, and and abundance gradient is clearly seen (Awaki et al. 1994; Matsushita et al. 1994; Matsushita 1997). Matsushita (1997) suggested the presence of a large-scale (a few hundred kpc scale) X-ray halo around M49.

Recent distance determinations to M49 subcluster and M87 subcluster based on Tully-Fisher relation (Fukugita et al. 1993; Yasuda et al. 1997) shows that the distance modulus of the M87 subcluster and M49 subcluster are $(m-M)_{\rm M87\ subcluster} = 31.09$ and $(m-M)_{\rm M49\ subcluster} = 31.48$, respectively. The difference in the distance modulus between M49 subcluster and M87 subcluster is 0.39 mag, which is consistent with the 0.37 mag obtained by de Vaucouleurs et al. (1986), 0.31 mag by Krann-Korteweg et al. (1988), and 0.35 mag by Fouqué et al. (1990). This suggests the M49 subcluster locates at ~ 3 Mpc behind the M87 subcluster. On the other hand, distance determination based on surface brightness fluctuations and planetary nebula luminosity functions implies that M49 galaxy and M87 galaxy are at nearly the same distance of ~ 15 Mpc (Ciardullo et al. 1993, see table 3.1). These suggest that M49 galaxy is not located at the center of M49 subcluster.

From the ROSAT observation, the rapid decrease in the surface brightness in the north side of M49 was found (figure 3.9). This "bow shock" shape is probably caused by ram pressure associated with the motion of M49 through the Virgo cluster ICM. Irwin & Sarazin (1996) shows M49 might to be moving toward the center of the Virgo cluster with velocity $v \approx 1300$ km s^{-1} to balance the pressure at the interface between interstellar gas of M49 and the Virgo ICM.

Figure 3.10 shows normalized density profile of the gas and galaxies for the subclusters in the Virgo system: i.e. M87, M49, and M86 subclusters (Schindler et al. 1999). The M49 subcluster shows more compact profile both in the optical and the X-ray than M87 subcluster. Schindler et al. (1999) also calculate the mass of each component, as summarized in table 3.2. The gas mass fraction ($M_{\rm gas}/M_{\rm tot}$) of the M87 subcluster is $\sim 10\%$ which is almost consistent with these in usual clusters (e.g. Böhringer 1994b; White & Fabian 1995; Kikuchi et al. 1998b), while M49 subcluster exhibits quite low gas mass fraction of $\sim 1\%$.

Table 3.1: General properties of M87 and M49

	M87	M49
Position (RA, Dec)$_{\rm J2000.0}$ [a]	$(12^{\rm h}30^{\rm m}49^{\rm s}.7, +12^\circ23'24")$	$(12^{\rm h}29^{\rm m}46^{\rm s}.5, +7^\circ59'58")$
Morphological type [a]	E0-1 pec	E2
Heliocentric velocity $v_{\rm r}$ (km s^{-1}) [a]	1282 ± 9	983 ± 10
B band magnitude B_T^0 [a]	9.59 ± 0.04	9.37 ± 0.06
Distance modulus $(m-M)$ [b]	30.87(SBF), 30.86(PNLF)	30.78(SBF), 30.84(PNLF)
ISM temperature (keV) [c]	~ 1.2 keV	~ 0.9 keV
X-ray luminosity $L_{\rm X}$ (erg s^{-1}) [c]	1.5×10^{42}	2.6×10^{41}
Subcluster member galaxies	elliptical rich	spiral rich

a : RC3 catalogue (de Vaucouleurs et al. 1991).

b : Ciardullo et al. (1993). SBF: surface brightness fluctuation, PNLF: planetary nebula luminosity function.

c : Matsumoto (1998) for M87 ($r < 4'$), and Matsumoto et al. (1997) for M49($r < 5'$). Luminosities are calculated in 0.5–10 keV band assuming a distance of 20 Mpc.

Table 3.2: Masses of the subclusters around M87 and M49 (Schindler et al. 1999)

	M87 ($r < 1$ Mpc)	M49 ($r < 750$ kpc)
Total mass $M_{\rm tot}$ ($10^{13} M_\odot$)	14	8.7
Gas mass $M_{\rm gas}$ ($10^{13} M_\odot$)	1.9	0.044
Galaxy mass $M_{\rm gal}$ ($10^{13} M_\odot$)	0.51	0.34
$M_{\rm gas}$ / $M_{\rm tot}$	14%	0.5%
$M_{\rm gal}$ / $M_{\rm tot}$	4%	4%
$M_{\rm gal}$ / $M_{\rm gas}$	0.28	7.7
M/L ($M_\odot/L_{\odot,{\rm B}}$)	≈ 500	≈ 600

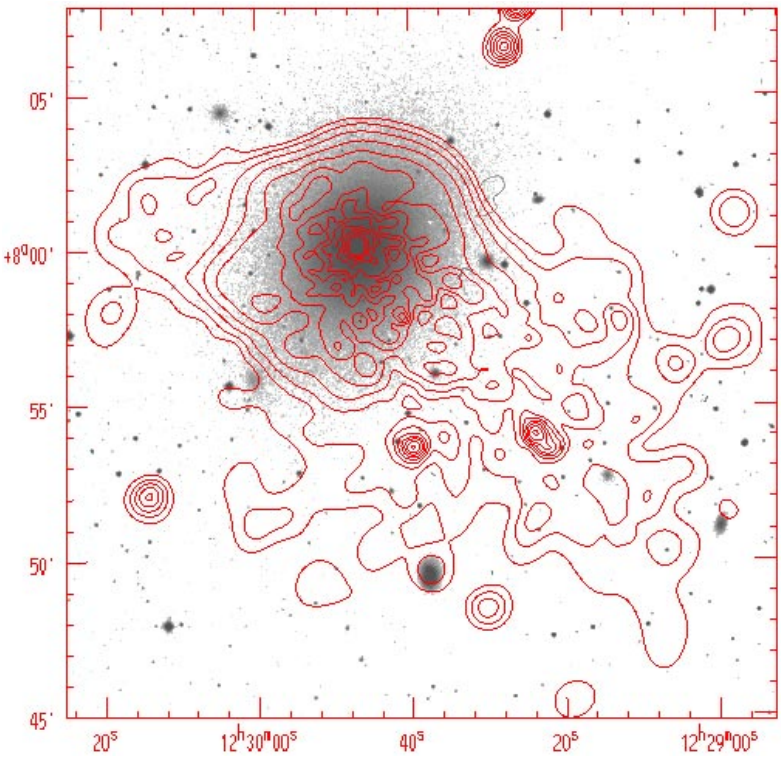

Figure 3.9: Contour plot of M49 obtained with ROSAT superposed on an optical image of the galaxy from the Digitized Sky Survey. The coordinates are RA and Dec (J2000.0) (Irwin & Sarazin 1996).

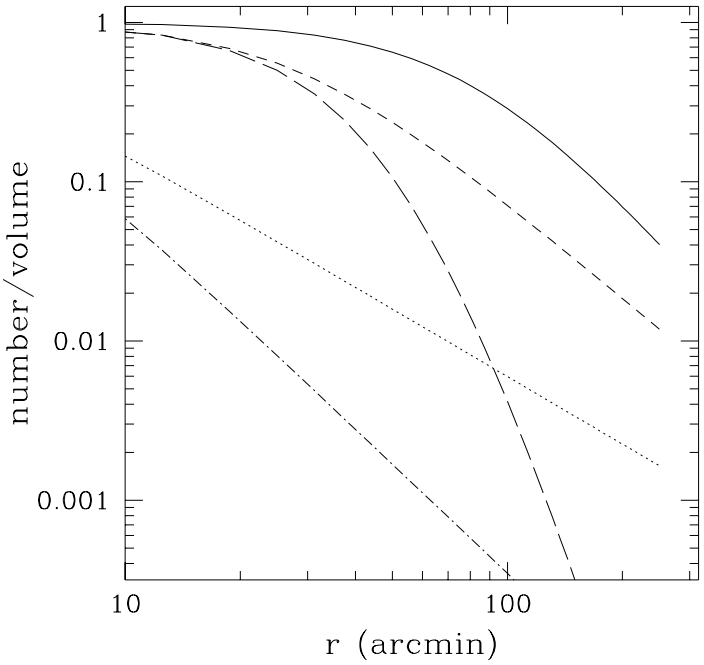

Figure 3.10: Density profiles of the subclusters in the Virgo cluster. All profiles are normalized to a central value of 1. The three upper lines shows the number density of galaxies: M87 subcluster (solid), M49 subcluster (dashed), and M86 subcluster (long dashed). The two lower lines show the 3 dimensional gas density: M87 subcluster (dotted), M49 subcluster (dot-dashed) (Schindler et al. 1999).

Chapter 4

Instrumentation

4.1 The ASCA Satellite

The ASCA (Advanced Satellite for Cosmology and Astrophysics) is a project of the Institute of Space and Astronautical Science (ISAS), developed under a Japan-US collaboration (Tanaka et al. 1994). Following Hakucho (1979), Tenma (1983) and Ginga (1987), ASCA is the fourth Japanese satellite devoted to the cosmic X-ray investigations. ASCA has been launched on 20 February 1993 at 11 a.m. JST, using the three-stage solid-propellant M-3SII-7 rocket, from Kagoshima Space Center (KSC) of ISAS at Uchinoura, Kagoshima. ASCA has achieved a near-circular orbit with a perigee of 520 km, an apogee of 625 km, and an inclination of 31°. ASCA makes about 15 revolutions per day around the Earth, five out of which pass over Japan.

Figure 4.1 shows the in-orbit configuration of ASCA. It weighs 420 kg, and has an octagonal-shaped body of a diameter 1.2 m where six solar panels are attached. The spacecraft has a nested double-cylinder structure, with the outer cylinder serving as the spacecraft body while the inner cylinder serving as an extendible optical bench (EOB). During the launch, the EOB is retracted inside the outer cylinder, and the solar panels are folded around it, so that the entire spacecraft is contained inside the nose fairing of the launch vehicle. Following the launch, the solar panels were deployed on February 25, to ensure the electric power generation up to 490 W. Then the EOB was extended on March 3. Further details of ASCA are given in Tanaka et al. (1994).

At the top of the EOB, four sets of identical imaging X-ray Telescopes (XRTs) are placed. They are all aligned along the satellite Z-axis with a common focal length of 3.5 m. Compared with X-ray telescopes of previous X-ray satellites, the ASCA XRT has a much larger throughput and a drastically wider energy band up to 10 keV (see §4.2). As illustrated in figure 4.2, the focal planes of the XRTs are equipped with four position-sensitive X-ray detectors; two SIS (Solid-state Imaging Spectrometer) detectors called SIS0 and SIS1, and two GIS (Gas Imaging Spectrometer) detectors called GIS2 and GIS3. Each detector is coupled to a fixed XRT, and the four telescope-detector systems acquire data simultaneously for the same target. Both the GIS and the SIS have unprecedent spectral resolutions as well as adequate position resolutions. We describe the XRT, the SIS, and the GIS in §4.2, §4.3 and §4.4, respectively.

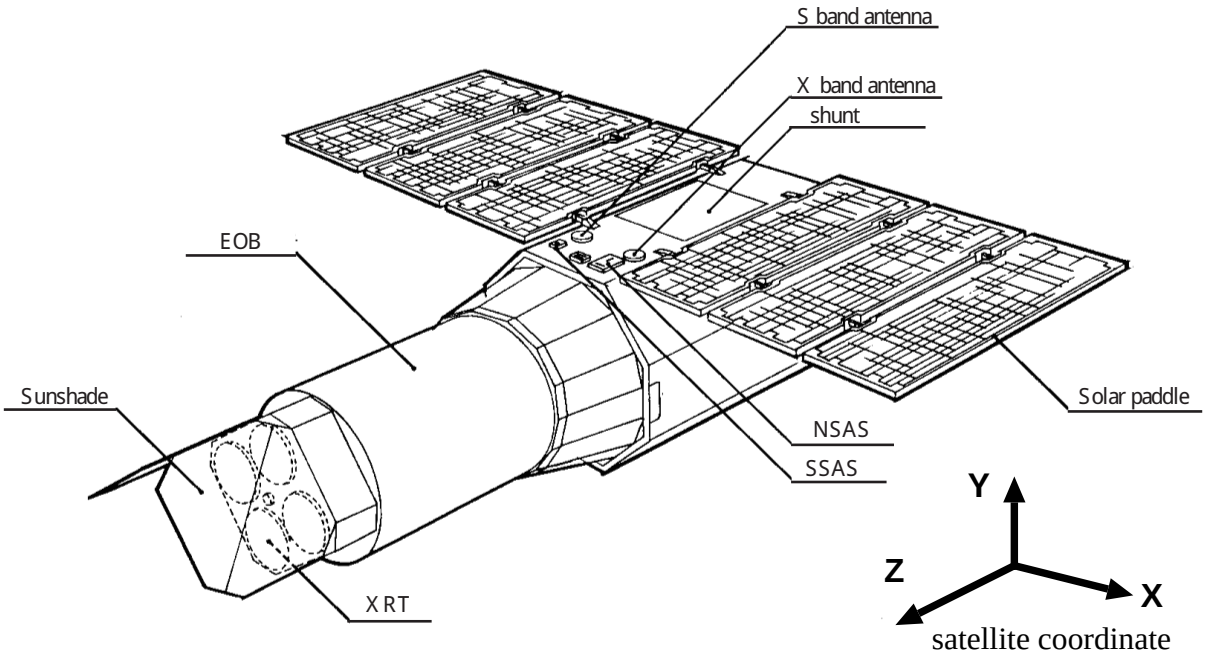

Figure 4.1: In orbit configuration of the ASCA satellite

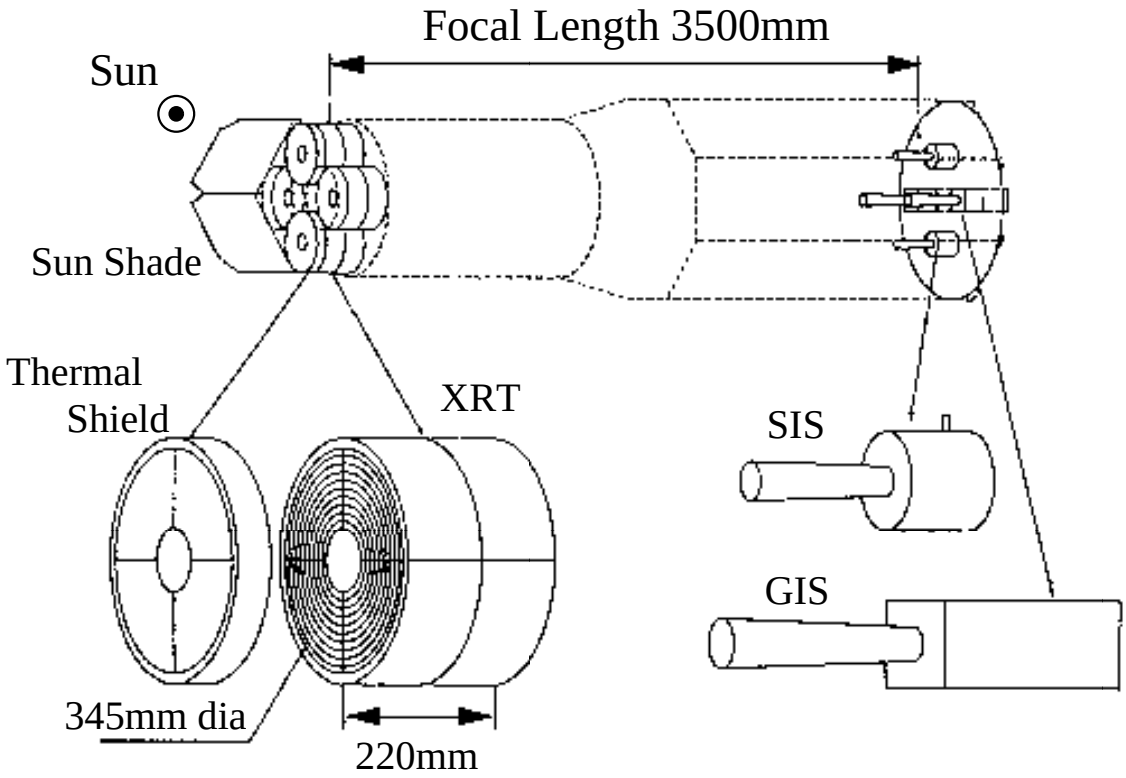

Figure 4.2: Onboard instruments of the ASCA satellite

4.2 X-ray Telescope (XRT)

The X-Ray Telescope (XRT) onboard ASCA has for the first time enabled cosmic X-ray imaging studies above X-ray energies of a few keV up to about 10 keV (Serlemitsos et al. 1995).

Soft X-rays are totally reflected off a smooth surface, when their incident angle measured from the surface is shallower than a certain critical value. This phenomenon is known as grazing-incidence reflection. The critical angle, typically of order 1 degree or so, is inversely proportional to the X-ray energy and increases with increasing free electron density of the reflecting material.

X-ray telescope mirrors use this mechanism usually in so called Wolter type I configuration (figure 4.3), which employs paraboloid and hyperboloid surfaces as the primary and the secondary mirrors so as to remove the first-order aberration. The two mirrors have a common focus and reflect X-rays in series (double reflection). This Walter type I optics have been used for many X-ray astronomy satellites, including the X-ray telescope onboard the Einstein (1978–1981), the Low-Energy Telescope onboard the EXOSAT (1983–1986), the main and sub telescopes onboard the ROSAT (1990–), and the US-made Soft X-ray Telescope onboard the Japanese solar observatory Yohkoh (1991–). These previous X-ray telescopes have all made the reflecting shells from highly polished glass or glass ceramic, on which heavy metal (Ni, Au, etc.) is evaporated to increase the reflectivity. The effective area is usually increased by having multiple nested set of mirrors with a common focus. For example, the Einstein telescope and the ROSAT telescope both use four nesting.

Since the critical angle for the total X-ray reflection decreases with increasing X-ray energy, it becomes more difficult to reflect X-rays at higher energies. In order to ensure a high reflectivity for harder X-rays, we have to operate the mirror shells under a very small incident angle, hence very small projected area. In order to achieve a large effective area up to higher energies, we have to increase the number of mirror nesting. This can be realized by a design called multiple thin-foil

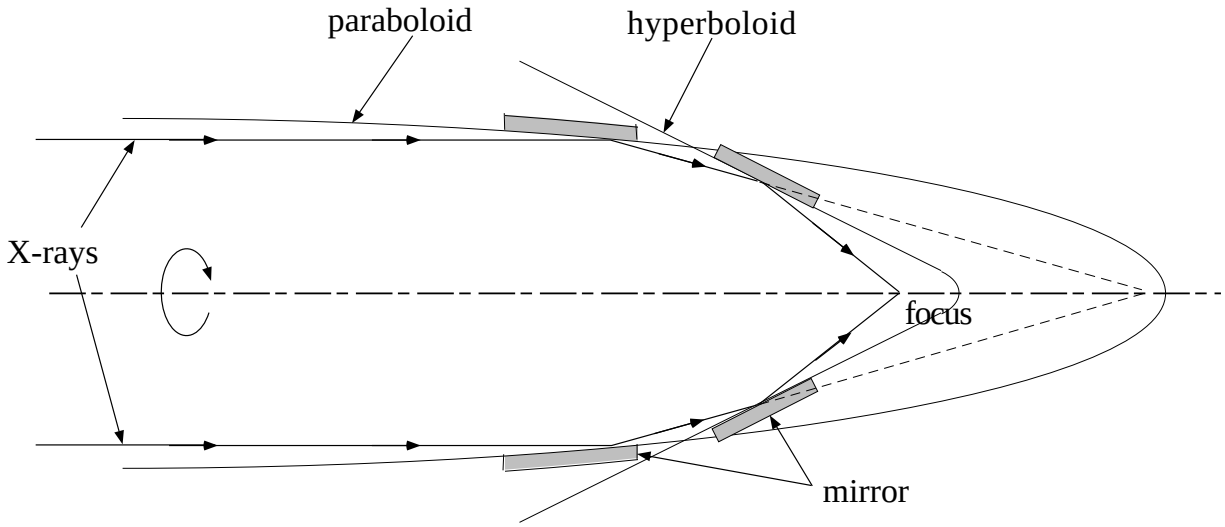

Figure 4.3: Walter type I optics

Table 4.1: Design parameters and performance of the ASCA XRT.

Mirror substrate	Aluminum foil (127 μm)
Mirror surface	Acrylic lacquer (10 μm) + Au (50 nm)
Mirror length	100 mm
Number of foils per quadrant	120 foils
Inner / outer diameter	120 mm / 345 mm
Focal length	3500 mm
Incident angle	0.24° – 0.7°
Total weight of four XRTs	$\sim$ 40 kg
Geometrical area	558 cm^2 / telescope
Field of view	$\sim 24'$ (FWHM at 1 keV) / $\sim 16'$ (FWHM at 7 keV)
Energy range	$\lesssim$ 10 keV
Effective area of four XRTs	$\sim$ 1300 cm^2 (1 keV) / $\sim$ 600 cm^2 (7 keV)
Half power diameter	$\sim$ 3 arcmin

optics, a special version of the Wolter I optics. This design makes each shell extremely thin by using metal foils instead of polished glass, and drastically increase the number of nesting. However it is very difficult to shape a thin foil into a paraboloid or a hyperboloid. Thus, a conical surface is instead used as its approximation, which reduces the imaging quality. A prototype multiple thin-foil mirrors were used successfully in the BBXRT (Broad-Band X-Ray Telescope) experiment flown onboard Space Shuttle mission ASTRO-1 in December 1990. Then the technique has been applied to the ASCA XRT.

The reflector shells of the ASCA XRT are all made of thin (127 μm) aluminum foils, bent in a conical form to approximate paraboloid or hyperboloid. The bent foils are $\sim$ 10 μm lacquer-coated to improve the surface smoothness, and then $\sim$ 50 nm gold-evaporated to increase the reflectivity. The 120 of these foils are closely packed together in an onion-ring configuration with a typical spacing of 1 mm, to cover a large fraction of the mirror aperture. The innermost and the outermost shells have diameters of 120 mm and 345 mm, respectively. In practice, the foils are produced and packed in four quadrants, and aligned by 13 alignment bars into 14 sectors. The first and the last sector is masked because shape error is severe. Four quadrants make up the "paraboloid" section of 100 mm long, and another set of four quadrants make up the "hyperboloid" section. One XRT unit thus fabricated weighs about 9.8 kg. Design parameters and performance of the XRT are shown in table 4.1.

The XRT has successfully achieved a very large effective area and a wide energy range, as shown in figure 4.4. When the four units are summed up, the effective area reaches $\sim$ 1100 cm^2 below $\sim$ 2 keV, almost by a factor of 6 and 2 larger than those of Einstein and ROSAT respectively. A sudden drop in the reflectivity at 2.2 keV is caused by the M-edge of the gold used as reflective coating. The XRT maintains a very large reflecting area towards higher energies, e.g. $\sim$ 600 cm^2 at 7 keV, with the upper energy bound as high as $\sim$ 10 keV. X-ray imagery above 3–4 keV has

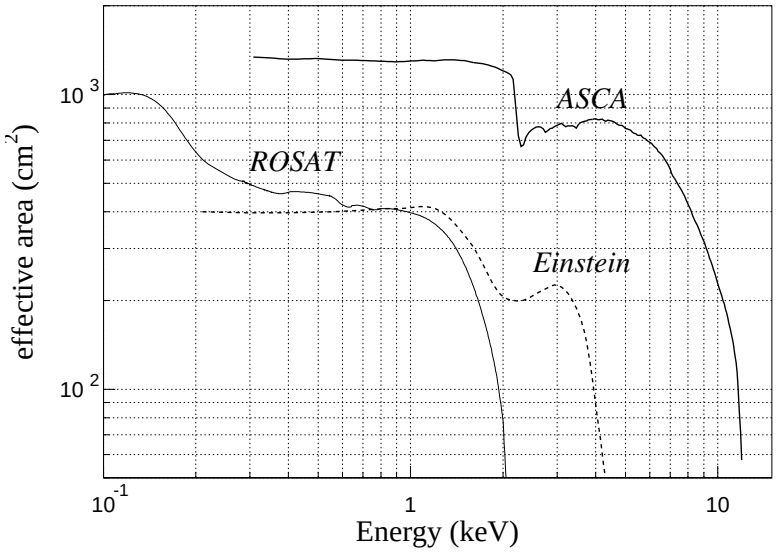

Figure 4.4: Effective area of the ASCA XRT (4 XRTs summed up, on-axis) compared with that of polished mirrors used in previous missions.

never been achieved by polished mirrors used in previous missions.

Although the XRT has a large effective area even at ~ 10 keV, it sacrifices the imaging quality: large-extended point spread function, and stray light which comes from outside of the field of view caused by abnormal reflection. These effects on our analysis are described in section 5.1.

4.3 Solid-state Imaging Spectrometer (SIS)

The Solid State Spectrometer (SIS) experiment is the first X-ray detector in orbit that utilizes CCDs (charge coupled devices) in the photon counting mode (Burke et al. 1991).

The SIS experiment consists of two detectors (SIS camera; SIS0 and SIS1). Figure 4.5 shows a cross section view of the SIS camera. Each SIS detector is made up of four CCD chips of 11 mm square each developed in the MIT Lincoln laboratory, to achieve a 22 mm $\times$ 22 mm square area for X-ray detection. The four CCD chips are aligned in square with narrow gaps to cover about $20' \times 20'$ square region on the sky. Each chip has 4096 by 4096 pixels of 27 μm square each, and a depletion layer of about 40 μm thick which ensures an improved efficiency for harder X-rays than conventional CCDs. Design parameters and performance of the SIS are summarized in table 4.2.

The CCD chip used for the SIS is a frame transfer type CCD and has the same structure as an optical CCD of the same type. Its detection part is made of an Si semiconductor of p-type and n-type connected each other through p-n junction. An insulator layer made of SiO_2 are attached on the front surface of the n-type Si, and electrodes are built on it. By supplying specific patterns of voltages on the electrodes charges in a pixel are transfered from a pixel to a next pixel. An electrode is also attached on the back. A depletion layer is developed in the device by supplying a bias voltage between the electrodes on the front and on the back.

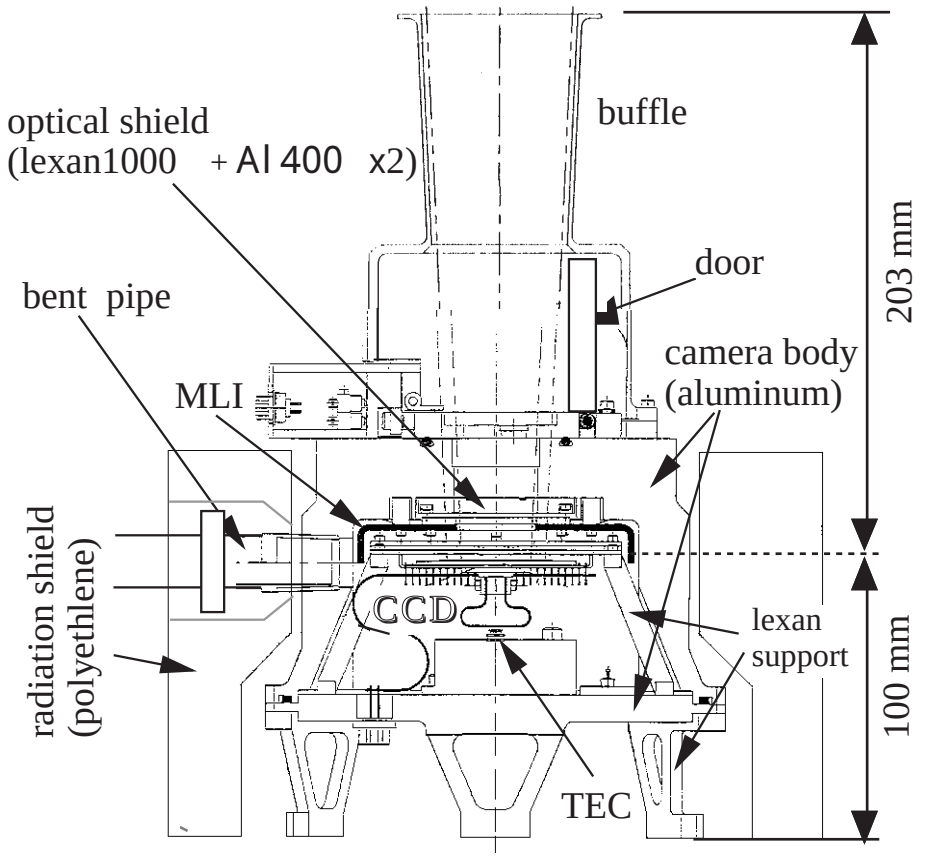

Figure 4.5: Cross section view of the SIS camera

Table 4.2: Design parameters and performance of the SIS

Irradiation Method	Front irradiation
Charge Transfer Method	Frame Transfer
Clock	3-phase drive
Number of pixels in Image Region	420 pixels × 422 lines per chip
Pixel Size	27 μm
Area	11×11 mm square per chip
Field of View	11×11 arcmin square per chip
Thickness of Depletion Layer	$\sim$ 40 μm
Optical Blocking Filter	100 nm Lexan film coated with 40 nm aluminum
Drive temperature	~ -62 °C
Energy Band	0.4–12 keV
Quantum Efficiency	$\sim$ 80% at 5.9 keV
Energy Resolution	2% at 5.9 keV (FWHM)

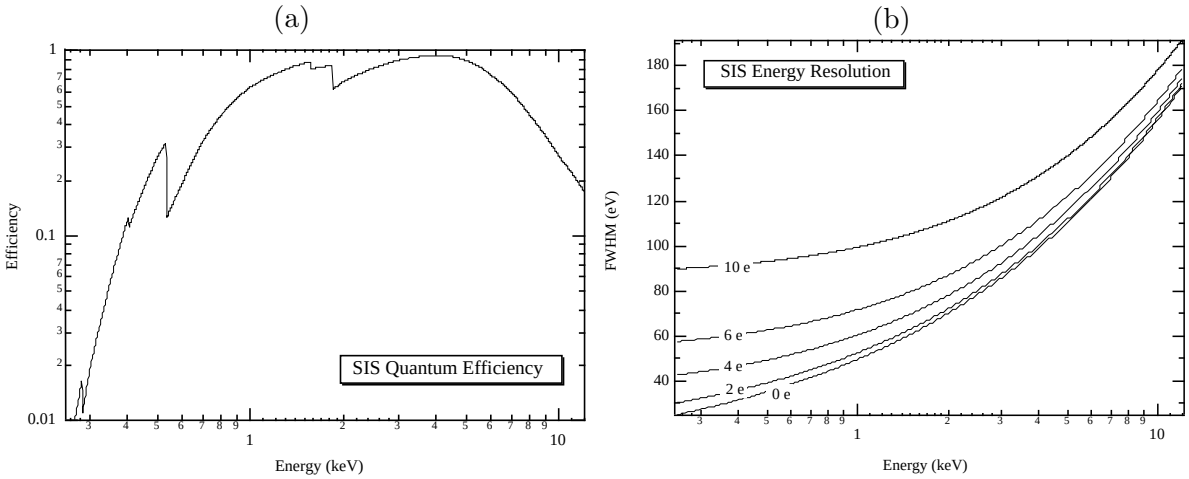

Figure 4.6: (a) Detection efficiency of the SIS as a function of incoming X-ray energy. K-edges of O (0.53keV), Al (1.56keV), and Si (1.84keV) are clearly seen in the figure. This efficiency does not includes optical blocking filter. (b) Energy resolutions of the SIS as a function of incoming X-ray energy for the single event. Energy resolutions with different read-out noise N are plotted ($N \sim 5$ for the SIS). The read-out noise levels are given as the equivalent number of electrons.

The aperture is covered by an optical blocking filter (100 nm Lexan film coated with 40 nm aluminum) in front of the CCD chips, in order to prevent visible lights. The whole CCDs are supported by Lexan supports and shielded from charged particles by poly-ethylene of 4 cm thick and aluminum of 1.9 cm thick at the side, aluminum plate of 3.5 cm thick at the bottom, and aluminum of 2.1 cm thickness at the top except for the aperture. A baffle is attached to shield stray light and high energy X-rays as a background.

Figure 4.6a illustrates the quantum efficiency of the SIS as a function of incoming X-ray energy. Thus the SIS sensitivity covers approximately 0.4–10 keV. The CCD chips and preamplifiers are cooled down to -60 °C with a thermo-electric cooler (TEC) from the backside of the chips in order to reduce thermal noise down to $N \sim 5$ electrons level. Thus the SIS achieves an energy resolution of about 150 eV FWHM over the whole energy range (figure 4.6b); this is the best energy resolution ever achieved by non-dispersive X-ray spectrometers so far put into orbit.

4.4 Gas Imaging Spectrometer (GIS)

The Gas Imaging Spectrometer (GIS) is the imaging gas scintillation proportional counter (Makishima et al 1996; Ohashi et al. 1996). The application of the gas scintillator technique to the Japanese X-ray satellite is the second attempt after the successful operation of the SPC experiment on board Tenma (Tanaka et al. 1984; Koyama et al. 1984).

The GIS is a general-purpose X-ray imaging spectroscopy system. It consists of the two detector assemblies, namely GIS2 and GIS3 serving as X-ray detectors. The GIS2 and GIS3 are coupled to two of the four XRTs, and measure pulse-heights and positions of X-rays reflected by the XRTs, photon-by-photon basis.

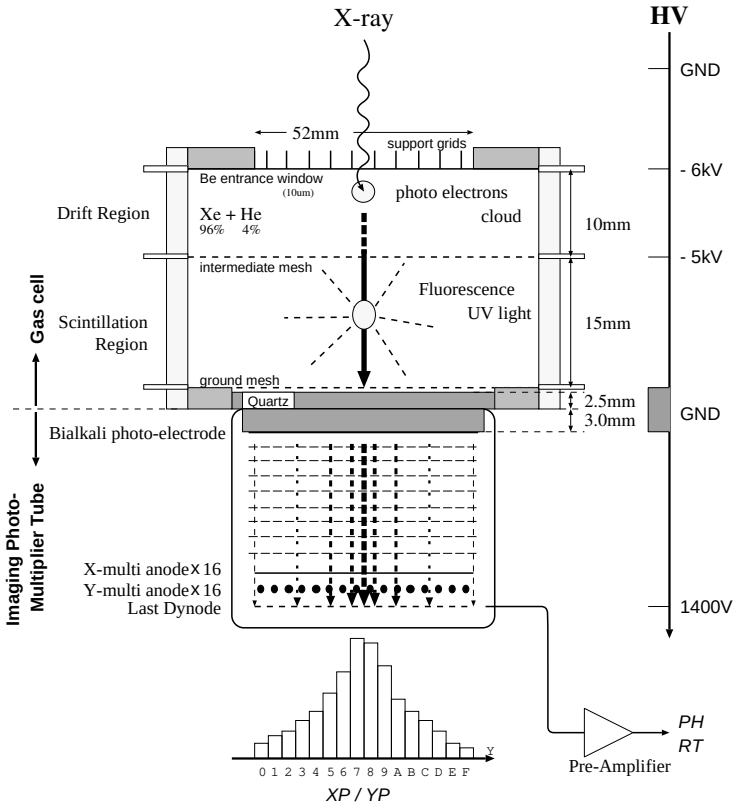

Figure 4.7: Schematic view of the GIS sensor system

Figure 4.7 shows a schematic view of the GIS sensor system. X-rays reflected by the XRT enter through the window, whose electric potential is held at -6000 V, and are absorbed in the drift region. Through photo-ionization, primary electrons are generated on average at the rate of one electron per 21.5 eV. The electron cloud thus created slowly drifts to the intermediate mesh (-5300 keV), and then the cloud is accelerated due to the strong field toward the ground mesh which is placed in front of the quartz window. In this process, the electrons excite Xe and produce a large number of UV photons of ~ 170 nm wavelength. The excitation energy for one UV photon is ~ 10 eV. Through the quartz window, these UV photons are collected by the imaging photo-multiplier tube (IPMT) which measures light distribution and the overall intensity of UV flux, which is proportional to the X-ray energy with accuracy of several %. We can obtain the position information from the anode signals, and derive the pulse-hight (PH) and the rise-time (RT) information from the last dynode. Design parameters and performance of the GIS are summarized in table 4.3, and detection efficiency and energy resolution are shown in figure 4.8.

There are a number of monitor data in the GIS system to support monitoring its proper function and to help estimation such as background and dead time (Ohashi et al. 1996). In the PH vs. RT plane, there are 6 scalers which measure the monitor counts (see figure 4.9). The upper PH discriminator sets one threshold line, and lower and upper RT discriminators make two lines. These discriminators create 6 regions, L0, L1, L2, H0, H1, and H2. The events within the L1 region are allowed as proper X-ray signals by the hard-wired login in the GIS system.

Table 4.3: Design parameters and performance of the GIS

Energy Band	0.7–15 keV
Energy Resolution	8% at 5.9 keV (FWHM) ($\propto E^{-0.5}$)
Effective Area	50 mm diameter
Entrance Window	10 μm beryllium
Absorption Material	Xe (96%) + He (4%), 10 mm depth, 1.2 atm at 0 °C
Positional Resolution	0.5 mm at 5.9 keV (FWHM) ($\propto E^{-0.5}$)
Time Resolution	$\sim$ 61 μsec (Maximum)

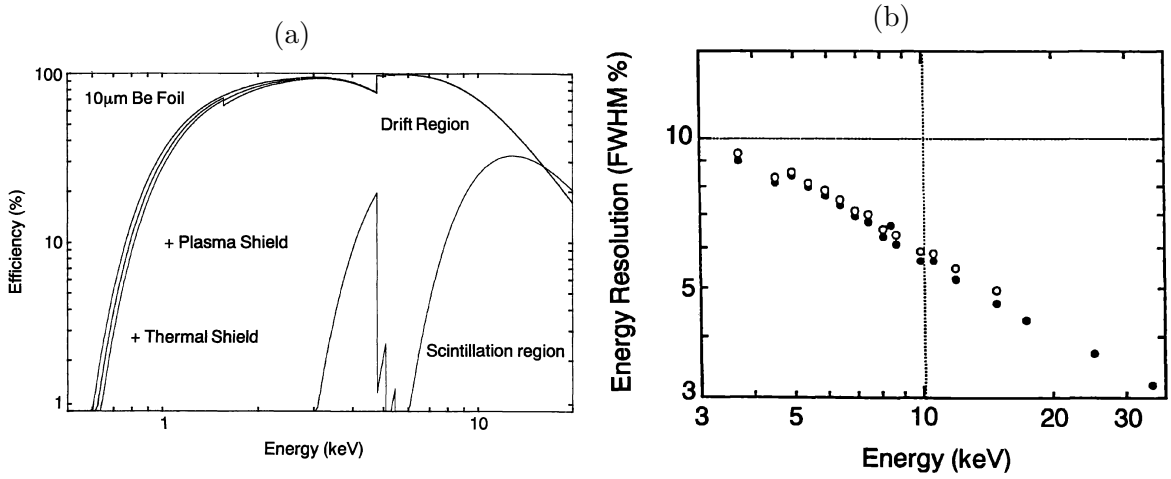

Figure 4.8: (a) Detection efficiency of the GIS as a function of energy. Absorption due to plasma shields in the GIS housing and due to thermal shield in front of the XRT are included in the actual observation. (b) Energy resolutions of the GIS as a function of energy.

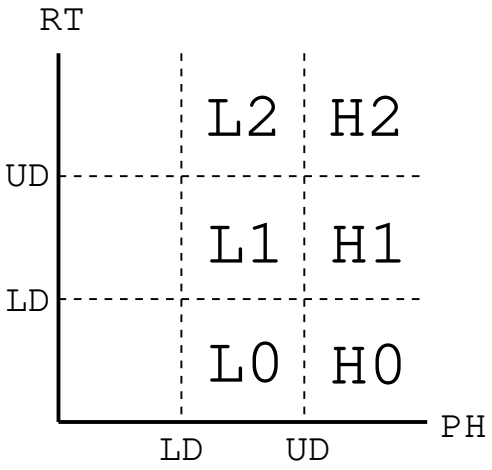

Figure 4.9: Schematic view of the 6 monitor data in the PH vs. RT plane.

Chapter 5

Response Construction and Background Estimation

5.1 XRT Response for Extended Sources

In this thesis, we perform detailed investigations of the Virgo cluster by analyzing the images and the spectra taken with the ASCA GIS. However, ASCA XRT has very complex response, which depend on energy and position of incident X-ray photons, and this makes the analysis of extended sources particularly difficult. Due to the PSF and stray light, the spectrum from extended object accumulated over specified areas on the detector is more or less contaminated by photons which comes from other areas of the object. Furthermore, the PSF cause artificial temperature and abundance increasing in the data of cluster of galaxies toward outer rings.

The imaging capability of the XRT could be divided into two issues: point spread function (PSF) and stray light. In this chapter, we explain the characteristics of the PSF and the stray light, and how the response is built.

5.1.1 Point Spread Function (PSF)

The PSF of the ASCA XRT has largely extended wings, which is due to waving (shape error) of the thin aluminum foils, as well as to the conical approximations of paraboloid (primary mirror) and hyperboloid (secondary mirror) surfaces.

If we observe a point-like source, which has a much less angular extent than the resolution of the XRT, it can be regarded as the PSF of the XRT. We pointed out that the lack of sufficient knowledge of the PSF is a major problem for analysis of the clusters with ASCA (Takahashi et al. 1994), and performed multi-pointing observation of the Cyg X-1 which is one of the brightest point-like source with a hard spectrum (Ikebe 1994; Takahashi et al. 1995; Ikebe et al. 1997). Figure 5.1 show examples of the Cyg X-1 images taken by GIS2. Although the XRT PSF in fact has a more sharply peaked core, it is broadened to some extent in the image by the finite position resolution of the GIS. The XRT PSF has four butterfly-like wings, which reflect the quadrant

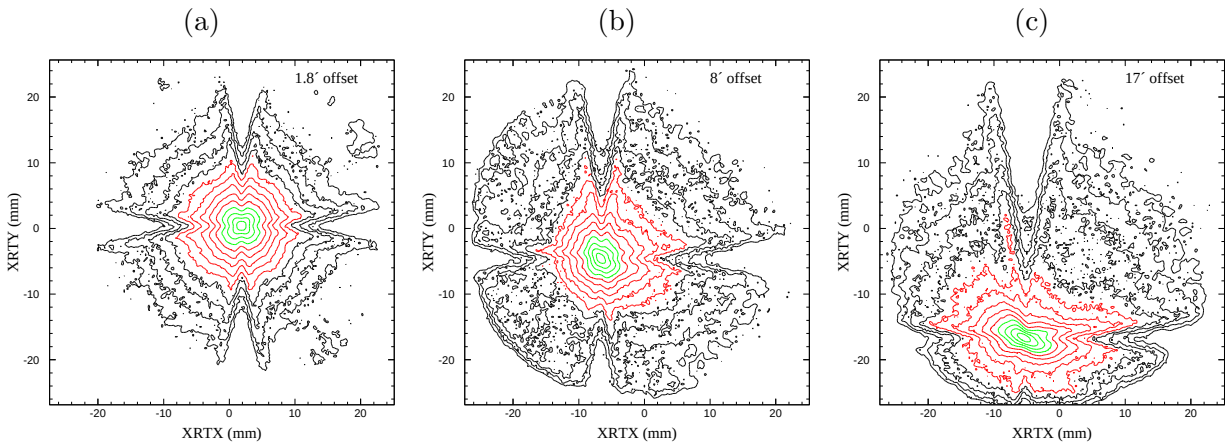

Figure 5.1: Examples of the XRT PSF taken by GIS2. (a) 1.8′ offset, (b) 8′ offset, and (c) 17′ offset Cyg X-1 images in the 0.5 – 12 keV band. Contour levels are every factor of 2, and origins of the coordinates are the optical axis of GIS2.

structure of the XRT, with significant flux extending almost over the whole GIS field of view. Horn like structures seen on the edges of the four wings are caused by the large distortion of the conical shape at the outermost sector of each quadrant. As θ (distance from the optical axis) gets larger, the PSF shape is also distorted, as characterized by a squeezing into the radial direction and an increase in the fraction of wings. Moreover, these effects are all energy-dependent. The PSF has wider outskirts in the higher energy bands. This is mainly due to the scattering of incident X-rays by the micro-roughness of the foil surface, which generally increases with increasing X-ray energy. All these properties of the XRT PSF complicate the analysis of extended X-ray sources. For example, they cause artificial temperature and abundance increase in the data of cluster of galaxies toward outer rings, as shown in figure 5.2.

Now ray-tracing program is available as the simulator of the ASCA XRT (Tsusaka et al. 1995; Kunieda et al. 1995). The ray-tracing calculates the position of X-ray photons on the focal plane by inputting energy and incidence angle of Monte-Carlo photons. Figure 5.3 shows examples of the radial brightness profile simulated by the ray-tracing, compared with the Cyg X-1 profile. It is confirmed that the ray-tracing images agree with the Cyg X-1 data within $\sim 10\%$ level in radial profile (Kunieda et al. 1995). The ray-tracing program is also a reliable tool to estimate the stray light (see section 5.1.2).

In-orbit XRT PSF has been studied mainly based on the multi-pointing observation of Cyg X-1. The image of the Cyg X-1 in low energy band (below 2 keV), however, may be considerably extended possibly due to the X-ray scattering by interstellar dust grains along the line-of-sight to Cyg X-1. Ezawa et al. (1997b) observed Her X-1, which located in a high Galactic latitude with small neutral column density, to calibrate the PSF below 2 keV, and confirmed that the Cyg X-1 images are more extended than the actual PSF in low energies. We compared the radial profile of the cluster simulated by the Her X-1 image as a PSF with the cluster simulated by ray-tracing, and found that the differences between the simulated clusters are almost negligible, as far as the clusters have a extent of $\beta \lesssim 1.0$ and $R_{\rm c} \gtrsim 1.0'$.

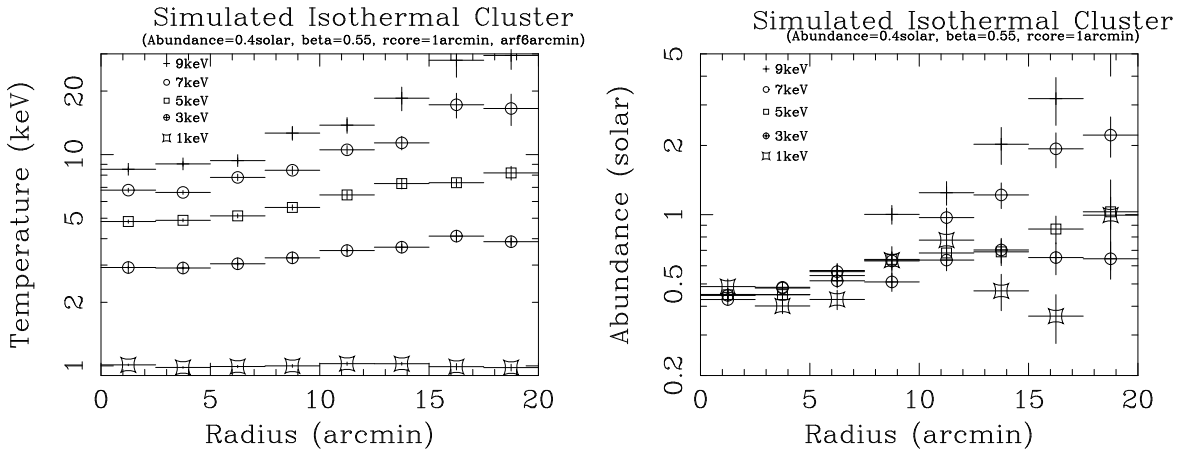

Figure 5.2: The temperature (right) and abundance (left) profiles of simulated clusters with uniform temperature and metal abundance. The spectra are made in the concentric annular regions centered on the cluster, and fitted with conventional procedure which is not taken into account the PSF effect correctly.

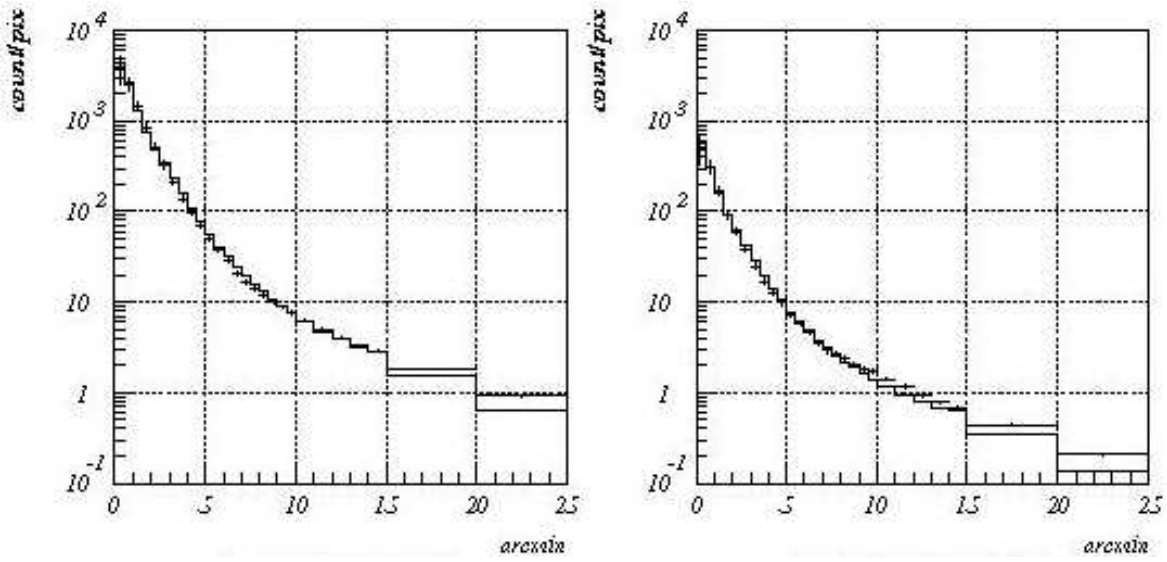

Figure 5.3: Example of radial profile of ray-tracing (line) compared with 8′ offset (1CCD nominal position) Cyg X-1 (cross): 2–6 keV band (left) and 6-12 keV (right) (Kunieda et al. 1995).

5.1.2 Stray Light

The ASCA XRT allows some fraction of the X-rays, which comes from outside of the field of view, to reach the focal plane detector. This phenomenon is somewhat different from the large outskirts of the PSF. The large outskirts of the PSF are mainly due to the waving of the XRT foils, and those photons also undergo the normal sequence of the Wolter type I optics. On the other hand, most of the photons which come from outside of the field of view have gone through abnormal paths, which are not on the assumption of the Wolter type I optics. These X-rays are called stray lights.

The effects of the stray light on the extended source analysis were extensively studied by Ishisaki (1995) for ASCA CXB analysis. Figure 5.4(a) shows an example of stray light images taken by GIS3. The Crab nebula is placed at the position of the filled circle, $60'$ offset from the optical axis in the direction of $\phi = 45^\circ$ / 135° / 225°. A shell-like image is seen spreading over the whole detector plane. The stripes represents the XRT sector structure divided by the alignment bars.

Since the Virgo cluster is extending larger than the GIS field of view, we must take the stray light effect into account for analysis. For example, Honda et al. (1996) shows that the fraction

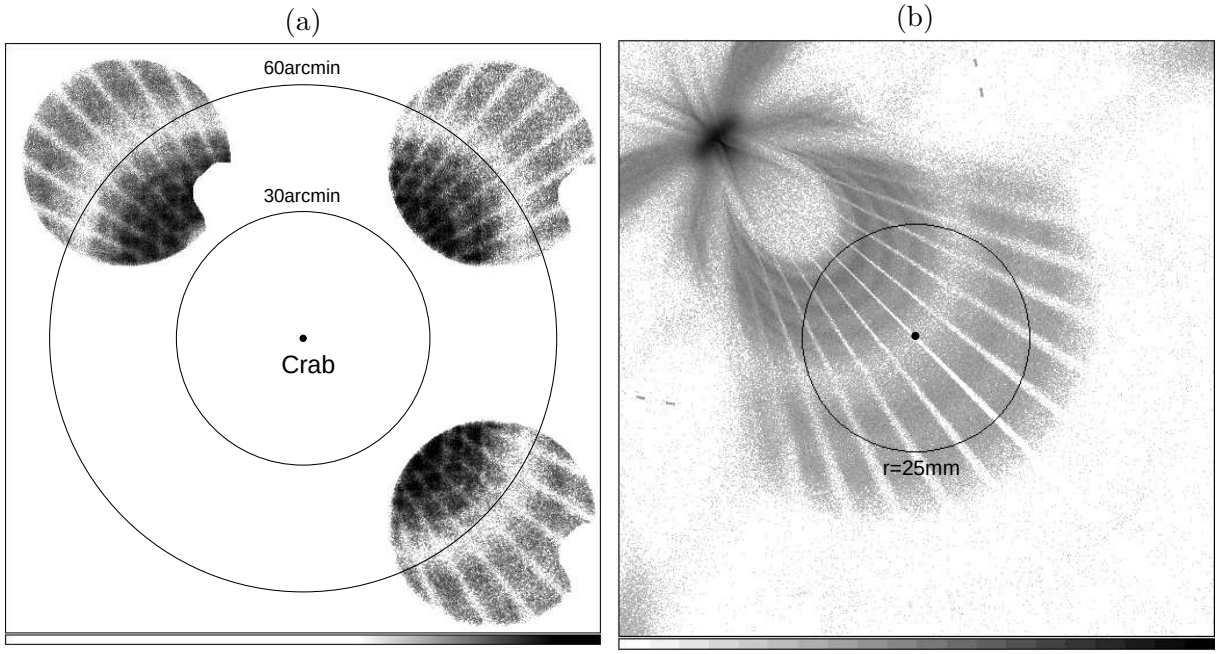

Figure 5.4: (a) Three of the Crab stray light images taken by GIS3 in the 0.7–10 keV band, shifted and superposed on the detector plane so as to reproduce correct angular relations with respect to the Crab nebula. The location of the Crab is indicated with a filled circle, and the optical axis for each observation is offset by $60'$ from the Crab. (b) Ray-tracing image of the stray light pattern at 1 keV for the offset angle $\theta = 60'$ and the azimuthal angle $\phi = 225^\circ$. A filled circle shows a position of the optical axis. A superposed circle of $r = 25$ mm on the image corresponds to the GIS field of view (Ishisaki 1995).

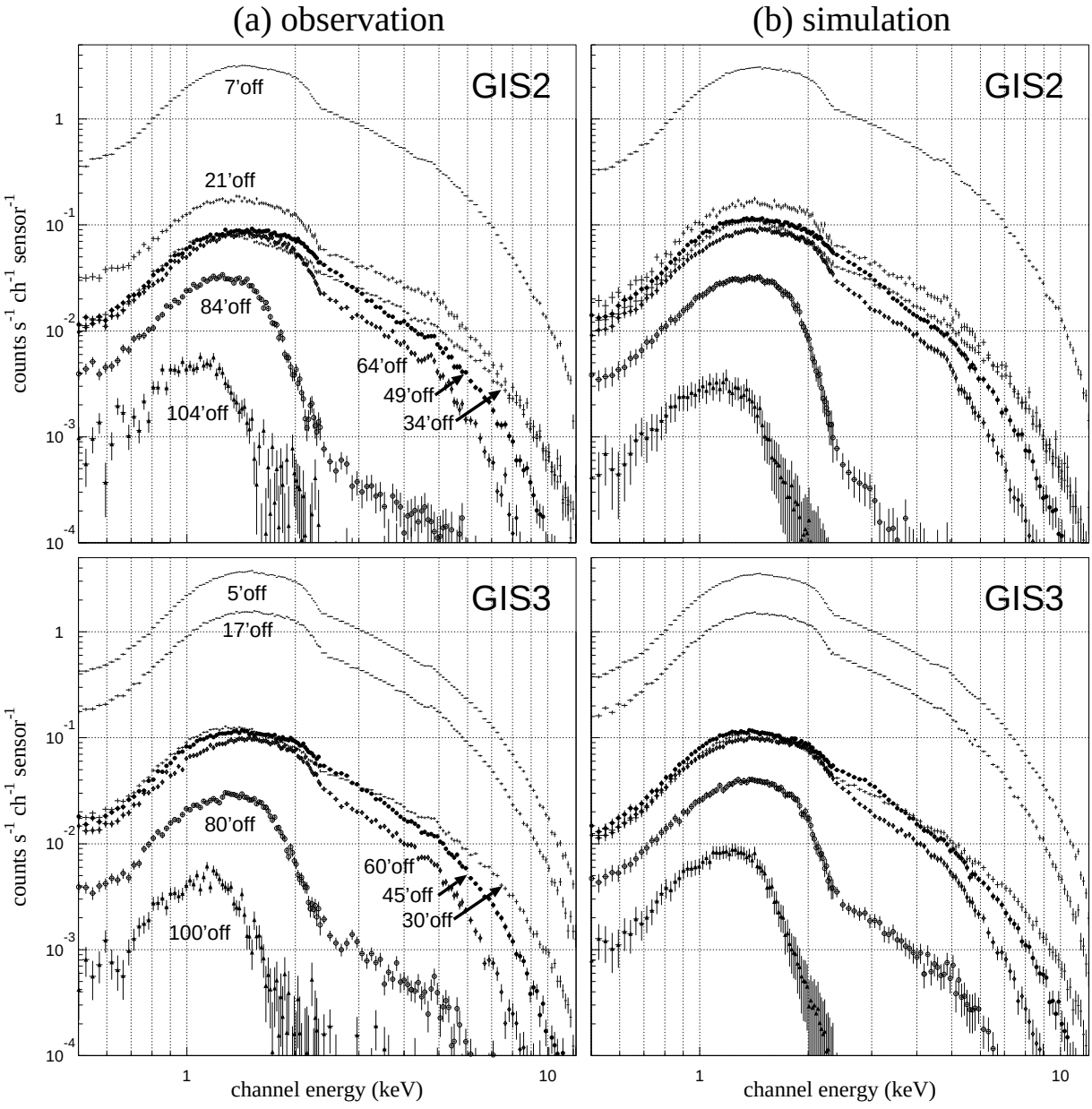

Figure 5.5: (a) Spectra of the Crab stray observations taken by GIS2 (upper panel) and GIS3 (lower panel) integrated in the radius of 20 mm from the optical axis of each sensor. The Crab has been placed at various offset angles as specified in the figure. The CXB+NXB spectra are subtracted after dead time correction. (b) Simulated spectra of the Crab stray observations. The Crab nebula is assumed to have an absorbed power-law spectrum of $\Gamma = 2.10$, $N_{\rm H} = 3.0 \times 10^{21}$ cm^{-2}, and the power-law normalization of 9.7 c s^{-1} cm^{-2} keV^{-1} at 1.0 keV (Ishisaki 1995).

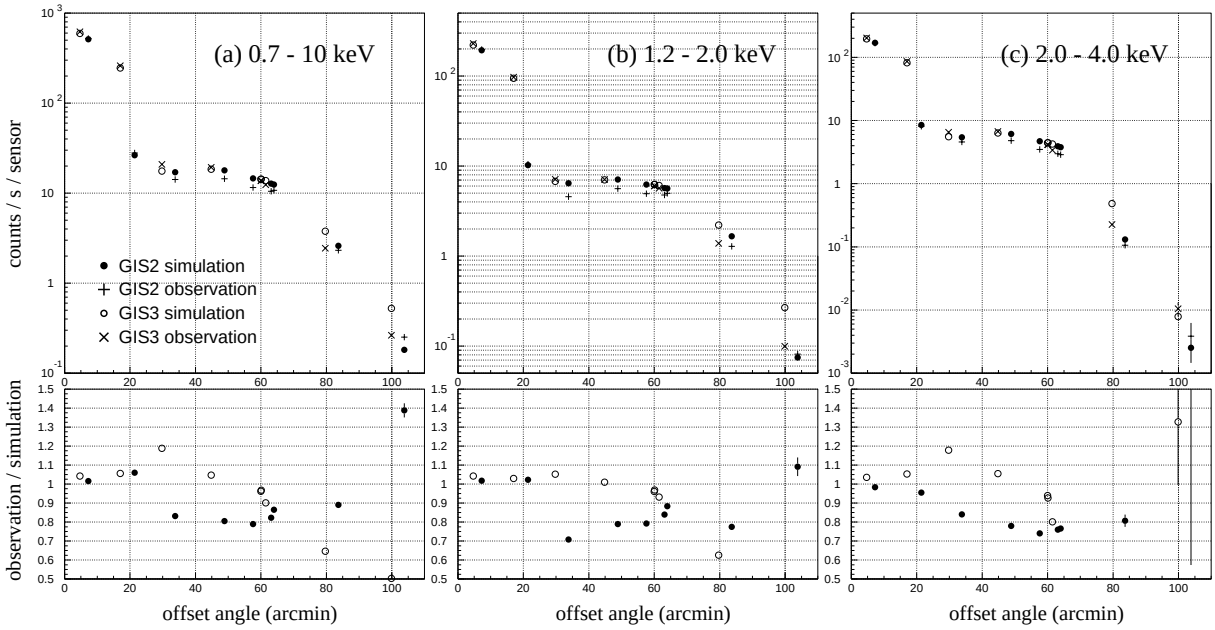

Figure 5.6: Upper panels show counting rates of the Crab stray observations and the ray-tracing simulations in (a) 0.7–10 keV, (b) 1.2–2.0 keV, and (c) 2.0–4.0 keV energy band, plotted versus offset angle of the Crab nebula. Lower panels show the ratios of observation to simulation (Ishisaki 1995).

of the stray light is up to $\sim 50\%$ of the total photons detected at $40'$ offset from the center of the Coma cluster. However, a stray light image has a complex shape as seen in figure 5.4(a), and it is not easy to express it in an analytic formula. Fortunately, stray light patterns are well determined by the foil structure of the XRT. Therefore the ray-tracing program with reliable XRT parameters is expected to reproduce the stray light effects pretty well. Figure 5.4(b) shows a ray-tracing image for $\theta = 60'$ and $\phi = 225^\circ$, which well reproduces the lower right image of figure 5.4(a). Then, using a ray-tracing program, we simulate the effects of stray lights for analysis.

Left panels of figure 5.5 show the observed spectra taken by GIS2 (upper panel) and GIS3 (lower panel). Right panels show the simulated spectra using the ray-tracing. We can say that the simulation roughly reproduces the spectral shape and normalization in the range of as much as five orders of magnitude. Figure 5.6 compares the counting rate from the actual observations with those based on the simulation. There seems to exist a systematic difference between GIS2 and GIS3, although the reason is still unclear. However we are thus confident that the systematic error of the simulation is about -30%–$+10\%$ within $\theta \sim 80'$, where the most part of photons come from for extended source analysis.

5.1.3 Formulation of the ASCA Response

Here we formulate the response of the XRT+GIS system, with some definitions of the coordinates. Let $F(\theta, \phi, E)$ be a source X-ray distribution, where (θ, ϕ) is the two-dimensional position on the sky, and E is the X-ray energy. Angles of θ and ϕ are defined from the optical axis of the XRT as an offset-angle and an azimuth-angle, respectively. Also, let $D(DETX, DETY, PI)$ denote the observed data, i.e. distribution of detected X-ray photons with pulse-invariant PI (gain corrected pulse-height), and detected position ($DETX$,$DETY$). There also is a coordinate called ($XRTX$,$XRTY$), the scale of which is similar to ($DETX$,$DETY$) but centered on the optical axis of the XRT and the Y-axis flipped. Table 5.1 is a summary of these coordinates.

$F(\theta, \phi, E)$ and $D(DETX, DETY, PI)$ are related as

$$\begin{aligned} & D(DETX, DETY, PI) \\ &= \int dE\ R_{\rm GIS}(E, PI) \\ &\times \int dx\, dy\ P_{\rm GIS}(E, x, y; DETX, DETY)\ A_{\rm GIS}(E, x, y) \\ &\times \int d\theta\, d\phi\ P_{\rm XRT}(\theta, \phi, E; x, y)\ A_{\rm XRT}(\theta, \phi, E) \\ &\times A_{\rm T.S.}(E) \\ &\times F(\theta, \phi, E), \end{aligned} \tag{5.1}$$

where (x,y) is the position on the entrance window of the GIS, and the meaning of each factor constituting the response is summarized in table 5.2. In particular, we usually integrate the data $D(DETX, DETY, PI)$ over a specified area Ω on the detector to obtain a spectrum $H(PI; \Omega)$, as

$$H(PI; \Omega) = \int_{\Omega} dDETX\, dDETY\ D(DETX, DETY, PI). \tag{5.2}$$

Table 5.1: Summary of the coordinates

Notation	Figure label	Unit	Comments
E	Energy	keV	Energy of the incident X-ray
PI	channel energy	ch	500 ch = 5.8942 keV, starts from 0 ch
θ	offset angle	arcmin	offset angle from the optical axis
ϕ	azimuth angle	degree	measured clock-wise from X-axis on detector plane
$DETX$ $DETY$	detector coordinates	mm ch	1 mm = 4 ch = 0.9822′, centered the detector center. (0, 0) mm corresponds to (128.5, 128.5) ch
$XRTX$ $XRTY$	XRT coordinates	mm ch	1 mm = 4 ch = 0.9822′, centered the optical axis. Y-axis flipped to the detector coordinate

Table 5.2: Summary of factors constituting the response function

Notation	Description
$A_{\mathrm{T.S.}}(E)$	transmission of the thermal shield
$A_{\mathrm{XRT}}(\theta, \phi, E)$	effective area of the XRT
$P_{\mathrm{XRT}}(\theta, \phi, E; x, y)$	point spread function (PSF) of the XRT
$A_{\mathrm{GIS}}(E, x, y)$	quantum efficiency of the GIS
$P_{\mathrm{GIS}}(E, x, y; DETX, DETY)$	point spread function (PSF) of the GIS
$R_{\mathrm{GIS}}(E, PI)$	energy redistribution matrix for the GIS

The method of spectral fitting is a procedure of finding a set of parameters for $F(\theta, \phi, E)$ which give the most similar model spectrum $H(PI; \Omega)$ to the observed PI spectrum.

If the target is a point source or has a uniform spectral shape even the target extended in the effective integration region on the sky, $F(\theta, \phi, E)$ can be factorized as $F(\theta, \phi, E) = B(\theta, \phi)\, S(E)$, where $B(\theta, \phi)$ is a surface brightness profile and $S(E)$ is a spectrum. Then, equation (5.1) will have a simpler form of

$$H(PI) = \int dE\ R_{\mathrm{GIS}}(E, PI)\ A_{\mathrm{XRT+GIS}}(E)\ S(E) \tag{5.3}$$

where:

$$A_{\mathrm{XRT+GIS}}(E) = \int_{\Omega} dDETX\, dDETY \tag{5.4}$$

$$\times \quad A_{T.S.}(E) \int dx\, dy\ P_{\mathrm{GIS}}(E, x, y; DETX, DETY)\ A_{\mathrm{GIS}}(E, x, y) \tag{5.5}$$

$$\times \quad \int d\theta\, d\phi\ P_{\mathrm{XRT}}(\theta, \phi, E; x, y)\ A_{\mathrm{XRT}}(\theta, \phi, E)\ B(\theta, \phi) \tag{5.6}$$

$R_{\mathrm{GIS}}(E, PI)$ is called an RMF (energy Redistribution Matrix File) and $A_{\mathrm{XRT+GIS}}(E)$ is called an ARF (Auxiliary (or Ancillary) Response File). Note that the RMF is determined only by the elementary process of the detector, and that only one RMF for one detector is sufficient for all the analysis. To be accurate, the RMF of the GIS slightly depend on a position of incoming X-rays, but in most case it is negligible. We should rebuild only ARFs when changing the target position or the integration area.

5.1.4 SimARF

As we have seen in section 5.1.3, we could represent the obtained spectra in the form of equation 5.3 if the target has a uniform spectral shape. To obtain $A_{\mathrm{XRT+GIS}}(E)$ in equation 5.3, we used SimASCA which is an ASCA simulator developed mainly by M. Hirayama, Y. Ishisaki, T. Kotani, and Y. Ogasaka (SimASCA Working Group). We generate a number of Monte-Carlo photons of energy E according to the surface brightness distribution $B(\theta, \phi)$, run the XRT+GIS simulator, and count how many photons come into the integration area on the detector plane. We can expect that $D_{\mathrm{XRT}} \times (N_{\mathrm{detect}}/N_{\mathrm{gen}})$ gives the value of $A_{\mathrm{XRT+GIS}}(E)$ in equation 5.3, where N_{gen} is

number of the generated Monte-Carlo photons, $N_{\rm detect}$ is number of detected photons, and $D_{\rm XRT}$ is geometrical aperture of the XRT. The Monte-Carlo error Δ of this value is expected to be $\Delta/A_{\rm XRT+GIS}(E) = [(N_{\rm gen} - N_{\rm detect})/(N_{\rm gen} \cdot N_{\rm detect})]^{1/2}$. We continue generating the Monte-Carlo photons of energy E, until this error ratio becomes typically less than 5%. M. Hirayama, H. Honda, and R. Shibata (SimARF team) have developed a code doing this procedure, and they named it SimARF. The SimARF has already been used for the analysis of clusters of galaxies, such as Coma, AWM7, 2A 0335+096, etc. (Honda et al. 1996; Ezawa et al. 1997a; Kikuchi et al. 1998b).

The XRT simulator is the key module for making ARFs. We selected the ray-tracing program as the XRT simulator, which can take into account the stray light effects in a natural way. This ray-tracing program is released by the XRT team and also used to make the pre-calculated XRT tables for the effective area and the PSF. As seen in the previous section, the ray-tracing program has sufficient accuracy and reliability in quantifying the stray light effects on the extended source analysis.

Figure 5.7 shows examples of the point source ARFs and the uniformly extended source ARFs created by the SimARF. The main difference is that the extended source ARF has much less effective area in higher energy bands than the ARF at 1CCD nominal position, because of both vignetting and the soft spectra of stray lights. Then, if we fit the spectrum from extended sources using the ARF at 1CCD nominal position, the temperature is underestimated by ~ 0.2 keV for $kT = 2.0$ keV thermal bremsstrahlung, or the photon index is overestimated by ~ 0.2 for $\Gamma = 1.7$ power-law emission.

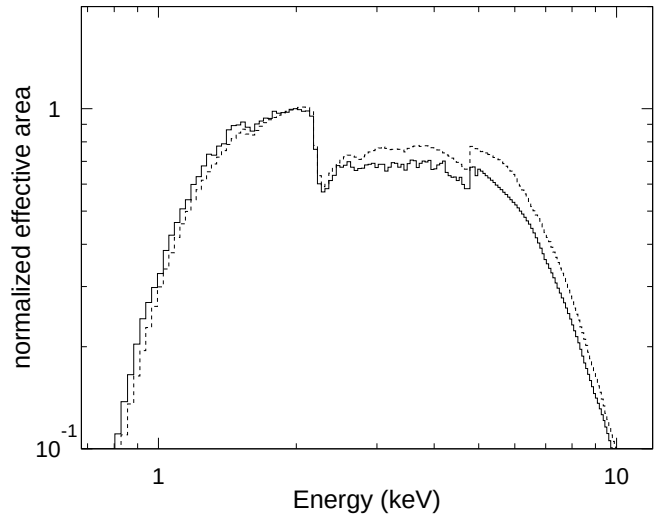

Figure 5.7: Plot of the GIS2 ARF for a point source and uniformly extended source. Solid line shows the uniformly extended source ARF with integration radius 20 mm, and dashed line shows the point source ARFs at 1CCD nominal position with integration radius 6 mm. Both ARFs are normalized to 1.0 at 2.0 keV.

5.2 Background Estimation and Data Reduction

As shown in figure 3.8, the best fit temperature at the nw_p07, where the X-ray emission from the Virgo is the faintest in northwest region, varies from ~ 1 keV to ~ 3 keV with the background estimation. Thus, it is essential to estimate the background precisely to derive physical parameters, such as temperature and abundance, at the region with low surface brightness.

Figure 5.8 shows the average night-earth and the CXB spectrum, presented together with the day-earth spectrum. The count rate and spectrum of the GIS background which includes NXB (non X-ray background) and CXB (cosmic X-ray background) depends on various parameters such as cutoff rigidity, satellite orbit, etc. The properties of the GIS background are extensively studied by many people (Kubo 1994; Ikebe 1994; Ishisaki 1995). By applying these methods, we could estimate the CXB and NXB with the systematic error of ~ 10 %. In following sections, we briefly summarize the background estimation and subtraction methods.

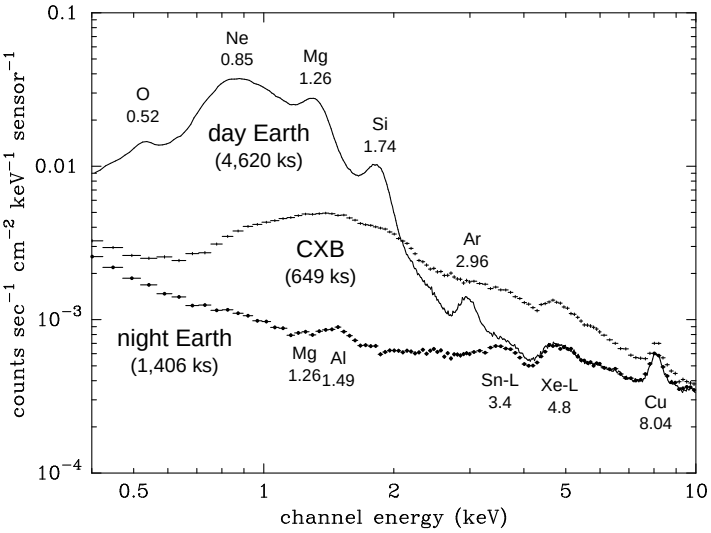

Figure 5.8: Integrated spectra of the day-earth (smooth line), the CXB (crosses), and the night-earth (filled circles) observations taken by the GIS2+3. Each of exposure time is given in the parentheses. The CXB and the day-earth spectra contains NXB. Possible origin of the line feature with the energy in keV are also given in the figure.

5.2.1 Non X-ray Background (NXB)

We cannot distinguish NXB from the real X-ray events. Therefore, we utilize the night-earth data, i.e. events obtained when the XRT was pointing to the night-side of the Earth, to study the NXB properties. Although there is a possibility of oxygen line or harder X-rays from aurora, we assume that the night-side of the Earth emits no X-rays; hence we believe that the night-earth data consist solely of NXB.

The properties of the NXB is well studied by Ishisaki (1995). For the Virgo analysis, we can extract the NXB spectrum based on this method. Since the NXB as a long-term variability, as seen in following section, we reproduced the database of night-earth observation from June 1993 to July 1998 (note that the Virgo cluster was observed before June 1998), and re-calculated scaling factor for the long-term correction for our analysis.

Flare event cut

Time variation of NXB is predominantly correlated with geomagnetic cutoff rigidity (COR) for cosmic rays along the satellite orbit. COR defines the minimum momentum of charged particles that can penetrate against electro-magnetic force due to terrestrial magnetism. Figure 5.10 shows a correlation between COR and H02 counts (sum of H0 and H2 counts, which are GIS monitor counts described in section 4.4) during the night-earth observations. The H02 count is almost free from signal X-rays in the field of view, even during the on-source observations.

Although COR is a good indicator of NXB, there exists a secondary branch below COR $\sim$ 10 GeV/c on the COR vs. H02 correlation. This is probably due to a slight inaccuracy of the COR-map. If we plot the satellite positions on the Earth, those periods which fall on the secondary branch appear only at the north east region of the map above the north Atlantic Ocean (dots in figure 5.9). The H02 is a good indicator of the NXB, however, there are two more issues known as "hard-flares" and "soft-flares".

We can see the hard-flares as a large scatter around COR $\sim 11 - 12$ GeV c^{-1} in figure 5.10. If we plot the satellite positions on the Earth, the hard-flare period are concentrated in the region peripheral to the south Atlantic anomaly (SAA) (filled circles in figure 5.9). SAA is a hole in the geomagnetic field which allows particles trapped in the magnetosphere to come down than usual. The hard-flares are probably caused by particles trapped in SAA. These events can be eliminated by rejecting time intervals when $H02 > 1.5 \times f(COR)$ in figure 5.10.

The soft-flare events appear in two regions: the south west to SAA and above Hawaii (crosses in figure 5.9). During the soft-flares, it is known that the NXB counts increase without an increase of $H02$. The soft-flares show harder profile than the average spectrum for the entire night-earth observations. Although the soft-flares can be eliminated by masking these regions, masking area is a little too large to ignore a decrease of integration time. To cope with this, we use the RBMCNT, i.e. a counting rate of the radiation belt monitor (RBM) to reject the soft-flares.

From these investigations, we have arrived at the conditions to reject the hard- and soft-flares as summarized in table 5.3. To avoid high NXB periods, we usually restrict H02 in the range of 15–45 c/s, too. We call the procedure to apply these conditions "flare-cut".

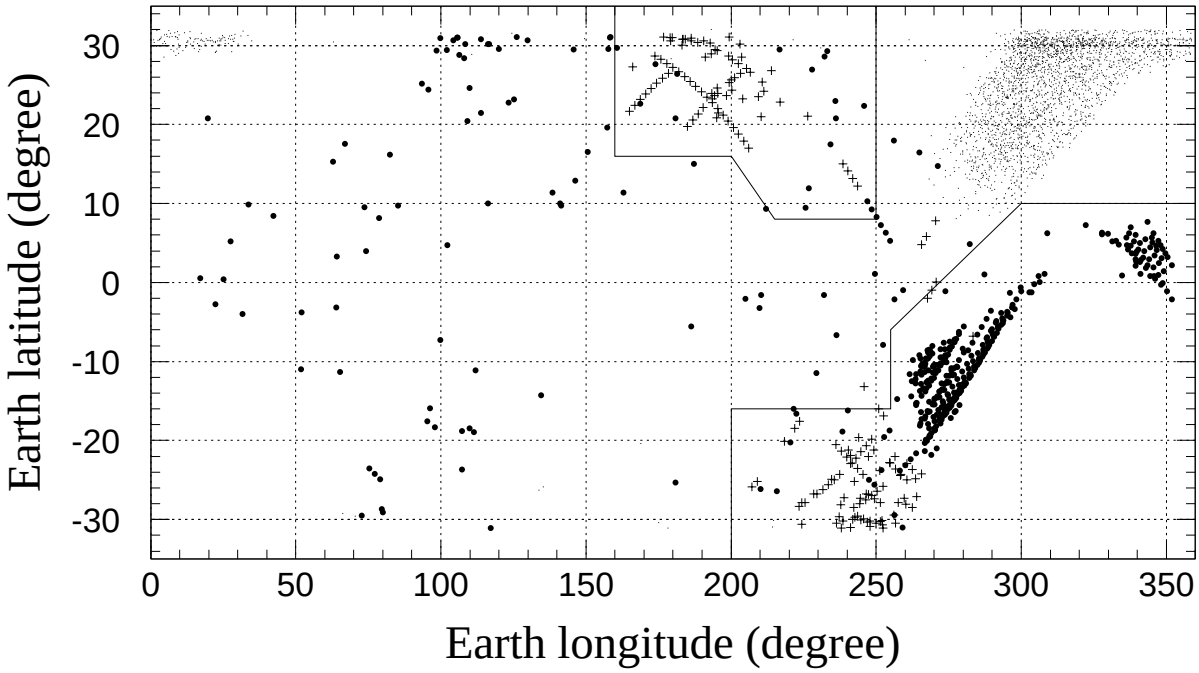

Figure 5.9: Distribution map for three types of phenomena on the Earth surface. The mark "$\cdot$" represents a position when H02 is less than the lower solid line in figure 5.10, where the COR-map is thought to be inaccurate. The mark "$\bullet$" represents a position when H02 is greater than the upper solid line in figure 5.10 (the hard-flares). The mark "+" represents a position when H02 $<$ 1000 c/32 s = 31.25 c/s and NXB $>$ 15 c/32 s = 0.46875 c/s. Two regions surrounded by solid lines define the dangerous areas where we should be cautious of the hard- and the soft-flares.

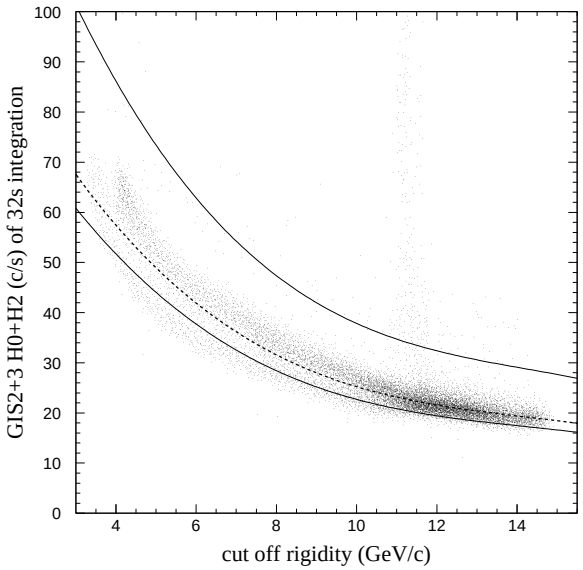

Figure 5.10: Correlation between COR and H02 counts during the night-earth observations. $H02$ is integrated for every 32 s. A dashed line means a function $f(x) = (109.3 - 17.05x + 1.127x^2 - 0.02627x^3)/32$ derived from fitting. Two solid lines below and above show $f(x)$ scaled by 0.9 and 1.5 times, respectively. The flare-cut is not applied.

Table 5.3: Summary of the flare-cut conditions

Condition	Reason
15 c/s $\leq$ H02 $\leq$ 45 c/s	to avoid high NXB
H02 $\leq 1.5 \times f(\mathrm{COR})^{\dagger}$ c/s	for hard flares
RBM $\leq$ 300 c/16 s = 18.75 c/s everywhere	for soft flares
RBM $\leq$ 100 c/16 s = 6.25 c/s in the dangerous areas (figure 5.9)	for soft flares

† $f(x) = 0.5(109.3 - 17.05x + 1.127x^2 - 0.02627x^3)$ c/ 16 s.

H02-Sorting Method

As seen in previous section, H02 can be a good indicator of NXB. Thus we use H02 to predict the NXB variation.

We sort the night-earth data which is applied the flare-cut by H02 in every 5 c/s step, i.e. 15–20 c/s, 20–25 c/s, 25–30 c/s, etc. H02 is counted in the 16 s time interval including the arrival time when the corresponding event is detected. Figure 5.11 shows the residual night-earth spectra corresponding to five H02 intervals. As H02 increases, the spectrum gets softer. We denote each exposure time T_i^{NTE}, and each spectrum $H_i^{NTE}(PI)$, both of which are counted or created on the same condition and in the same detector region as the on-source observations. When T_i^{OBS} is the exposure time in the i-th $H02$ bin during the on-source observation, the NXB spectrum contained in the on-source data is estimated as:

$$H(PI) = \sum_i H_i^{NTE}(PI)\ \frac{T_i^{OBS}}{T_i^{NTE}}. \tag{5.7}$$

We call this method "H02-sorting method".

To check the reproducibility of NXB by the H02-sorting method, we split the entire night-earth data into 340 $\times$ 10 ksec intervals. Then we compared the counting rate of each interval with that estimated by H02-sorting method using the entire night-earth data. The results are shown in figure 5.13. Filled circles in the upper panel show the actual counting rate of each interval, and the middle panel shows the counting rate divided by the prediction. We can see that there is a general trend of increasing counting rate with time, which means that the long-term NXB increase which is seen in figure 5.12 cannot be reproduced by the H02-sorting method.

Correction of the Long-term Variability

A long-term NXB increase by several percent in a year has been seen, as shown in figure 5.12. Although the spectral shape has not changed significantly (figure 5.12), it is probably caused by a gradual build-up of long-term decay radioisotopes.

Therefore, we have to adjust the normalization of the NXB estimated by the H02-sorting method with the formula:

$$scaling\ factor \quad = \quad 1.0$$

$$+1.654475 \times 10^{-9} \cdot (ascatime - 82948010)$$
$$-6.631425 \times 10^{-18} \cdot (ascatime - 82948010)^2 \quad (5.8)$$

where *ascatime* represents the time in second from 00:00:00 (UT) on 1 January 1993, and is calculated from the mean observation time.

Lower panel of figure 5.13 indicates a distribution of the value of observed / predicted NXB ratio after the flare-cut procedure, the H02-sorting method, and the long-term NXB trend correction. The standard deviation is 0.06570, which means ~ 6.6 % rms variation of the NXB counts. This values includes a Poisson error of ~ 3.4 %; therefore, we conclude that we can achieve a ~ 5.6% rms reproducibility in NXB, by a combined use of the standard background rejection, the flare-cut procedure, the H02-sorting method, and the long-term NXB trend correction. In the following, we quote 6 % as a typical systematic uncertainty associated with the NXB estimation.

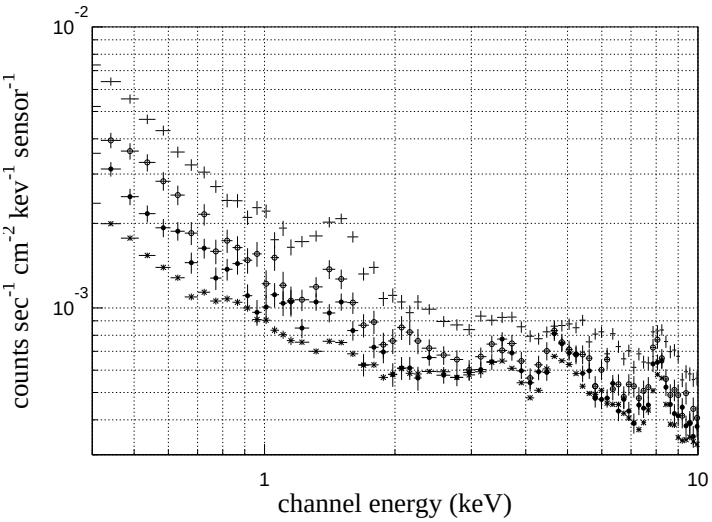

Figure 5.11: H02 sorted spectra during the night-earth observations in the 0.6–7.0 keV energy band. The mark '+' represents the data when H02 is in the range 50–80 c/s, '○' 40–45 c/s, '●' 30–35 c/s, and '×' 20–25 c/s. H02 are integrated for every 16 s. The flare-cut is applied.

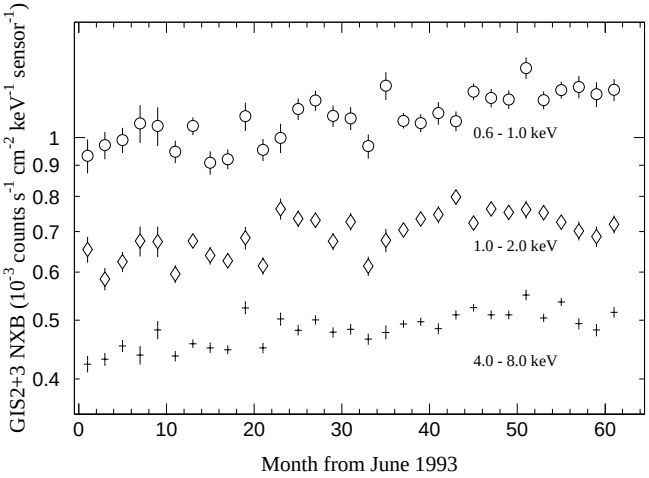

Figure 5.12: Long term (June 1993 – July 1998) variations of the GIS2+GIS3 counting rate during the night-earth observations in the 0.6–1.0 (open circle), 1.0–2.0 (diamond), and 4.0–8.0 (crosses) keV energy bands, integrated within the radius of 20 mm from the optical axis. The flare-cut is applied.

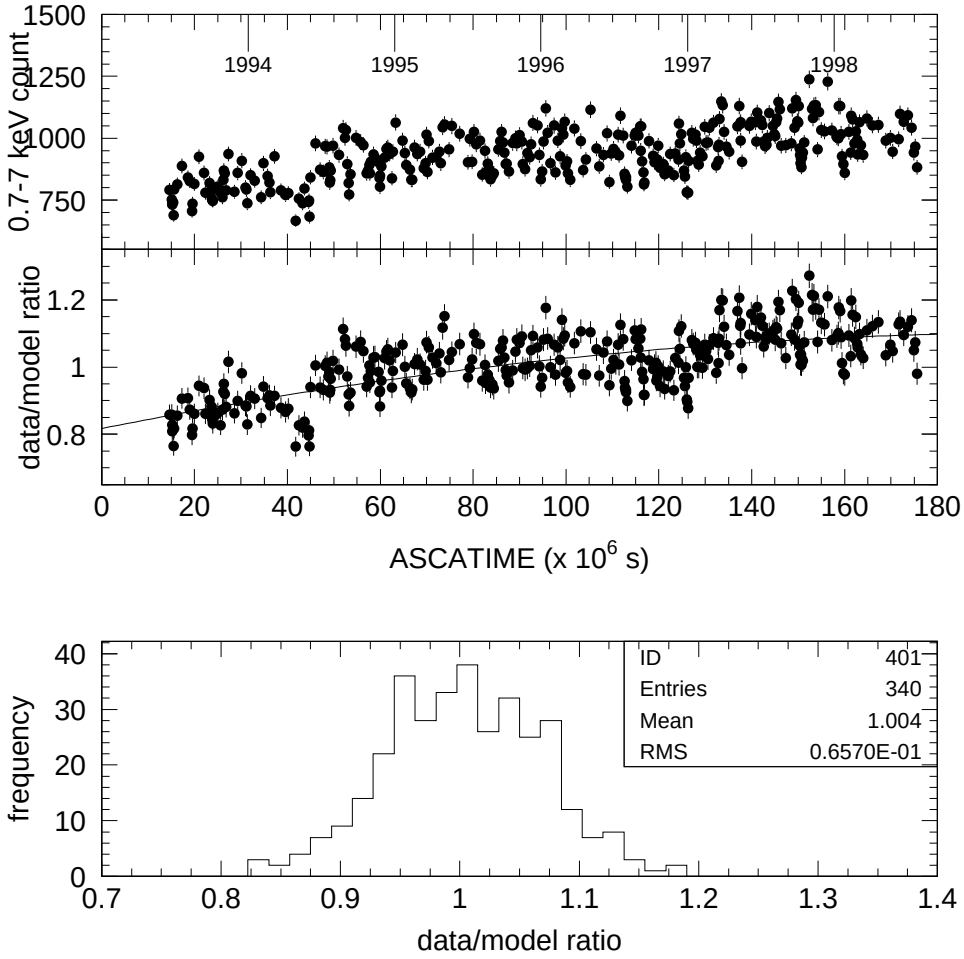

Figure 5.13: Figures to check the NXB reproducibility by H02-sorting method. Upper panel shows the actual NXB (filled circles) in the 0.7–7.0 keV energy band, for every 10 ksec exposure. Filled circles in the middle panel indicate ratios of the NXB to the prediction. The solid line shows the best fit line shown as eq. 5.8. Lower panel shows a distribution of the ratios around the best fit model. The mean value and the standard deviation for the distribution are indicated in the inset.

5.2.2 Cosmic X-ray Background (CXB)

For reproduction of the CXB, we use Master Background Database system (MBDB) described in Ikebe (1994). The MBDB consists of the Master Background Photon File (MBPF) and the Master Background Exposure Map (MBEM), based on observation data sets of 4 different blank sky fields; 'Draco', 'NEP', QSF3, and 'SA57'. Table 5.4 shows the observation log of 18 pointings included in the MBDB. After the data screening described in section 5.2.1, we obtained total exposure time of $\sim$ 476 ksec.

Table 5.4: Blank sky observations used for the CXB database

Field Name	Obs. Date † (UT)	Position ‡ (gl, gb)	Exp. Time § (sec)
Draco	1993.06.04	(102.23, 34.13)	21891
	1993.06.05	(102.28, 33.90)	10715
	1993.06.05	(102.33, 33.67)	24812
NEP	1993.07.20	(96.39, 29.81)	10691
	1993.06.10	(96.39, 29.81)	16120
	1993.10.21	(96.39, 29.82)	14733
	1993.08.16	(96.40, 29.98)	17735
	1993.07.02	(96.39, 29.98)	13329
	1993.09.30	(96.38, 29.98)	16132
QSF3	1993.07.11	(250.85, -51.98)	24133
	1993.09.15	(250.86, -51.99)	12494
	1993.09.10	(250.86, -51.98)	12810
	1993.09.21	(250.86, -51.99)	12225
SA57	1993.12.21	(64.25, 85.56)	54119
	1993.12.24	(65.44, 85.65)	41176
	1993.12.28	(63.00, 85.48)	94438
	1994.01.16	(63.15, 85.66)	44129
	1994.01.18	(65.19, 85.47)	33820
Total			475502

†: The start time of observation in year.month.day

‡: Galactic coordinate of the direction of the GIS3 center.

§: Total exposure time after data screening described in section 5.2.1.

An example of GIS2 image is shown in figure 5.14(a). We can recognize that some faint sources are seen in the image. To eliminate faint sources, we apply the MBEM to the image. The MBEM defines an exposure map over the entire GIS field, and the value of MBEM at pixel

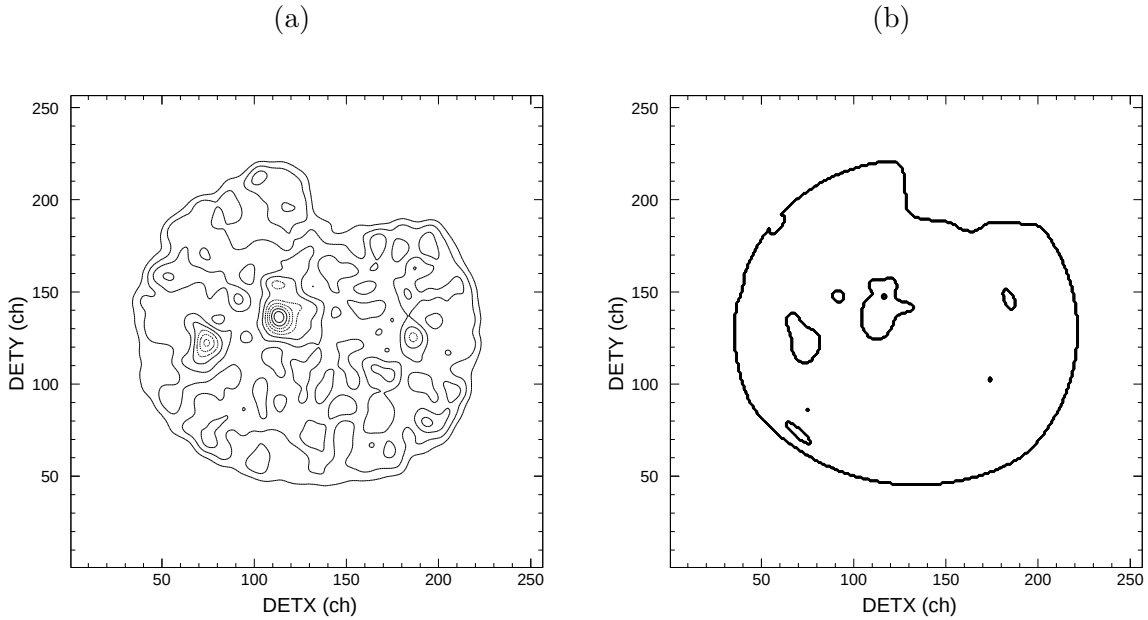

Figure 5.14: Example of GIS image and mask image. (a) 0.7–10 keV GIS2 image of NEP field observed in July 1993. The image is smoothed by Gaussian of $\sigma = 1'$. The NXB is not subtracted. (b) Mask image for (a).

$(DETX, DETY)$ is calculated as;

$$\mathrm{MBEM}(DETX, DETY) = \sum_i T_i \times mask_i(DETX, DETY) \tag{5.9}$$

where T_i is the exposure time of the i-th pointing, and $mask_i$ is the mask image for the i-th pointing. Ikebe (1994) determined the mask image to remove the pixels which have a larger number of counts than a threshold level, considering the PSF of XRT+GIS. Figure 5.14(b) shows an example of the mask image. Although the exposure time varies by position due to the mask, we obtain the CXB with good statistics with minimum value in the summed exposure map is 277 ksec, and maximum is 476 ksec.

Figure 5.15(a) shows the spectra of the four fields, and figure 5.15(b) compares spectrum shape at each fields with Draco spectrum. We can say the spectrum shape dose not vary in the four fields significantly. The fluctuation of the CXB flux is roughly $\sim 10\%$ for the size of GIS field of view (Ishisaki 1995). Thus we estimate the systematic error of 10% for the normalization of the CXB.

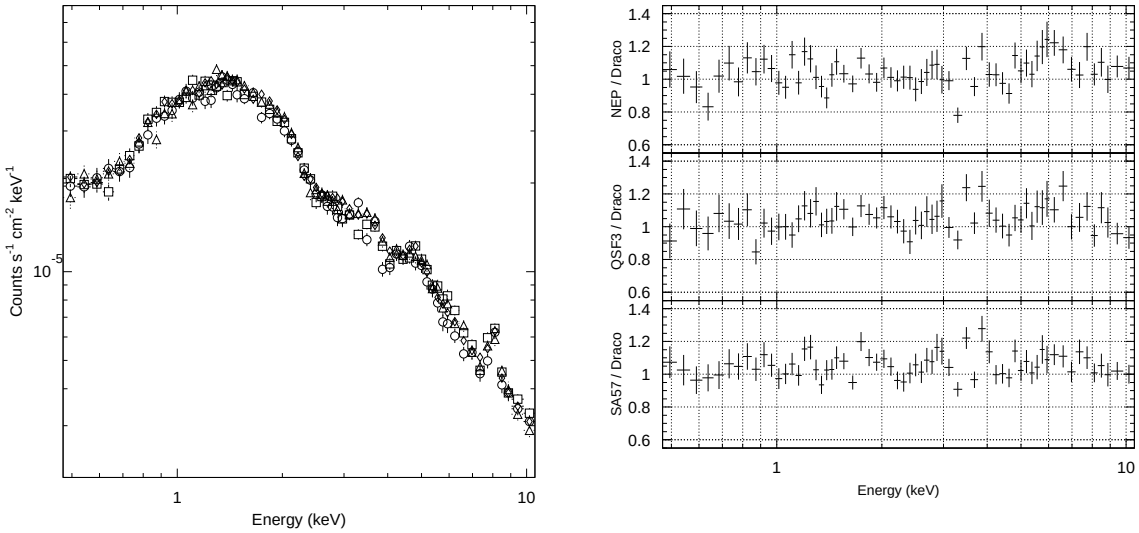

Figure 5.15: Spectra of the Draco, Nep, QSF3, and SA57 fields. The NXB is subtracted. (a) Plot of 4 spectra in counts s^{-1} cm^{-2} keV^{-1}; Draco (circle), NEP (rectangle), QSF3 (triangle), and SA57 (diamond). (b) Comparison of spectrum shape. The spectra of NEP, QSF3, and SA57 are divided by Draco.

Chapter 6

Observation and Analysis

6.1 ASCA Mapping Observation of the Virgo Cluster

We performed mapping observations of the Virgo cluster with ASCA (Kikuchi & Ohashi 1997; Ohashi et al. 1998a; Ohashi et al. 1998b). The observations were carried out in December 1996 and in June 1997 for a total of 200 ksec (northwest region of M87), and in June 1998 for a total of 280 ksec (south region). The observation logs are summarized in table 6.1 and table 6.2, and the observed positions are shown in figure 6.1 and 6.2, compared with the X-ray brightness obtained from RASS and number density of the member galaxies of the Virgo cluster, respectively.

The SIS data were obtained with the 2CCD mode for the northwest region, and 1CCD mode for the south region. However, the energy resolution and dark current of the SIS at the time of the Virgo mapping observation were significantly degraded and increased compared with those just after the launch of ASCA, probably caused by cosmic ray irradiation in orbit. Furthermore, photon statistics of SIS data is poorer than GIS ones, because the effective area of SIS is much smaller than the GIS. Thus, we did not use the SIS data in this thesis, except for the regions around NGC 4472, which were observed in 1993.

The GIS data were obtained with the normal PH mode. We selected the GIS data with the telescope elevation angle from the Earth rim $> 5^\circ$, and with the attitude aberration from the average < 1 arcmin. The flare-cut and H02-sorting methods, which are described in section 5.2.1, are also applied. Figure 6.3 shows the obtained GIS image of the Virgo cluster region listed in table 6.1 and 6.2 in two energy bands. From the figure 6.3, the largely extended emission is clearly seen, and several discrete sources are also recognized.

Table 6.1: Log of ASCA mapping observation of the Virgo cluster.

Field	RA, Dec (J2000)	Distance † (arcmin)	Date ‡ (UT)	Exposure* (sec)	Rate § (c/s)	N_H ¶ 10^{20} cm^{-2}
Northwest:						
nw_p01	185.74, 13.69	142	96/12/25 19:10	14516	0.79	3.01
nw_p02	185.89, 13.12	117	96/12/26 11:20	14896	0.85	2.88
nw_p03	186.32, 13.54	108	96/12/26 22:20	14941	0.98	2.92
nw_p04	186.90, 13.39	77	96/12/27 15:20	7729	1.70	2.78
nw_p05	187.32, 13.81	88	96/12/27 20:30	6775	1.30	2.72
nw_p07	186.00, 14.71	173	97/06/14 22:10	18615	0.64	2.70
nw_p08	186.15, 14.13	140	97/06/15 16:00	13709	0.79	2.87
nw_p09	186.58, 14.56	147	97/06/16 06:20	14331	0.75	2.67
nw_p10	186.73, 13.98	112	97/06/16 20:50	14519	1.04	2.81
nw_p11	187.16, 14.40	125	97/06/17 09:00	(GIS2) 13935	0.86	2.63
				(GIS3) 11557		
nw_p12	187.55, 13.31	56	97/06/14 11:20	7867	2.17	2.65
South:						
s_p01	187.59, 11.81	37	98/06/11 09:30	4753	3.71	2.45
s_p02	187.04, 11.48	68	98/06/11 12:40	10323	1.47	2.39
s_p03	187.58, 11.17	73	98/06/11 19:00	11178	1.42	2.28
s_p04	187.02, 10.85	101	98/06/12 03:00	8867	0.80	2.20
s_p05	187.00, 10.33	130	98/06/12 11:00	19384	0.76	2.05
s_p06	187.58, 10.03	142	98/06/12 22:10	12143	0.77	1.95
s_p07	186.96, 9.83	160	98/06/13 09:20	18804	0.81	1.90
s_p08	187.54, 9.52	172	98/06/13 20:30	14315	0.68	1.83
s_p09	186.93, 9.32	190	98/06/17 04:40	16249	0.67	1.81
s_p10	187.51, 9.00	203	98/06/17 16:00	14809	0.61	1.77
s_p11	186.90, 8.80	221	98/06/18 04:40	14992	0.88	1.75
s_p12	187.46, 8.50	234	98/06/23 14:40	10503	0.65	1.70
s_p13	186.87, 8.21	256	98/06/18 15:10	12650	0.64	1.66
s_p14	186.70, 7.60	293	98/06/19 00:50	9143	0.62	1.60
s_p15	187.34, 7.30	306	98/12/21 08:50	11715	0.59	1.61
s_p16	187.88, 7.56	290	98/06/19 18:20	3525	0.54	1.61
s_p17	187.98, 8.14	256	97/06/20 05:30	12432	0.62	1.66

†: Distance from the center of M87 in arcmin. The position of M87 is $(\mathrm{RA, Dec})_{\mathrm{J2000}} = (187.7065, 12.3901)$.

‡: The start time of observation in year/month/day hour:minutes.

∗: Total Exposure time of the GIS 2 and 3 after the data screening described in section 5.2.1.

§: Counting rate of GIS 2+3 (including the Cosmic X-ray background and Non X-ray background).

¶: Galactic line of sight column density from Einstein On-line Service ($EINLINE$).

Table 6.2: Log of ASCA observation around the Virgo cluster

Field	RA, Dec (J2000)	Distance † (arcmin)	Date ‡ (UT)	Exposure* (sec)	Rate § (c/s)	N_H ¶ 10^{20} cm^{-2}
Other Pointings :						
M87[a]	187.63, 12.44	5	93/06/07 00:50	9184	17.3	2.52
M87 NW[a]	187.10, 12.65	40	93/06/08 07:11	10352	2.84	2.61
NGC 4406[a]	186.47, 12.96	82	93/07/03 15:20	14594	2.20	2.76
NGC 4374[a]	186.32, 12.80	87	93/07/04 15:35	17055	1.85	2.75
NGC 4388[b]	186.37, 12.62	81	95/06/21 09:53	20084	1.59	2.70
NGC 4438 N1[c]	187.03, 13.03	56	95/12/24 21:34	18832	2.30	2.69
NGC 4438 N2[c]	187.03, 13.04	56	96/01/05 17:54	20799	2.32	2.69
A1553[d]	187.59, 10.54	111	96/06/12 09:24	28407	1.14	2.09
NGC 4325[e]	185.84, 10.60	155	97/01/05 15:40	21850	0.77	2.17
M49 NW8.5[a]	187.34, 7.90	270	93/06/30 12:26	17961	1.14	1.63
M49 NW3.5[a]	187.41, 7.96	266	93/07/07 15:37	14495	1.20	1.63
NGC 4365[a]	186.10, 7.33	319	93/06/27 23:43	29153	0.59	1.60

†: Distance from the center of M87 in arcmin. The position of M87 is $(\mathrm{RA, Dec})_{\mathrm{J2000}} = (187.7065, 12.3901)$.

‡: The start time of observation in year/month/day hour:minutes.

$*$: Total Exposure time of the GIS 2 and 3 after the data screening described in section 5.2.1.

§: Counting rate of GIS 2+3 (including the Cosmic X-ray background and Non X-ray background).

¶: Galactic line of sight column density from Einstein On-line Service ($EINLINE$).

$a - e$: Principal Investigator.

a. PV (Observation in the Performance Verification phase.)

b. Cohen, R.

c. Mushotzky, R.

d. McHardy, I.

e. Mulchaey, J. / Fukazawa, Y.

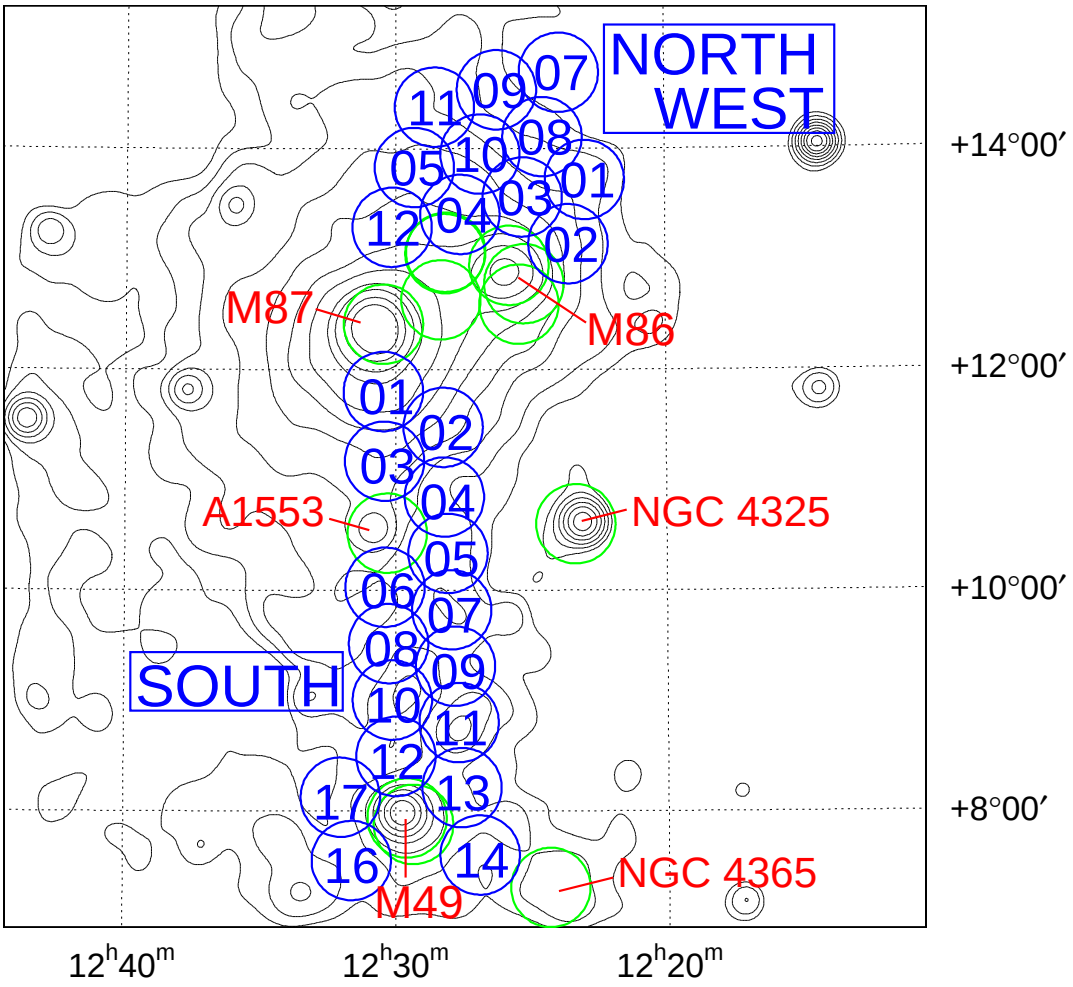

Figure 6.1: ASCA observed regions superposed on the RASS contour (Böhringer et al. 1994) in 0.5–2 keV band. The observed regions are listed in table 6.1 and table 6.2. Radius of each circle is 22′ corresponding to GIS field of view. Contours show the X-Ray intensity observed by the ROSAT All-Sky Survey in a logarithmic scale, as shown in figure A.5.

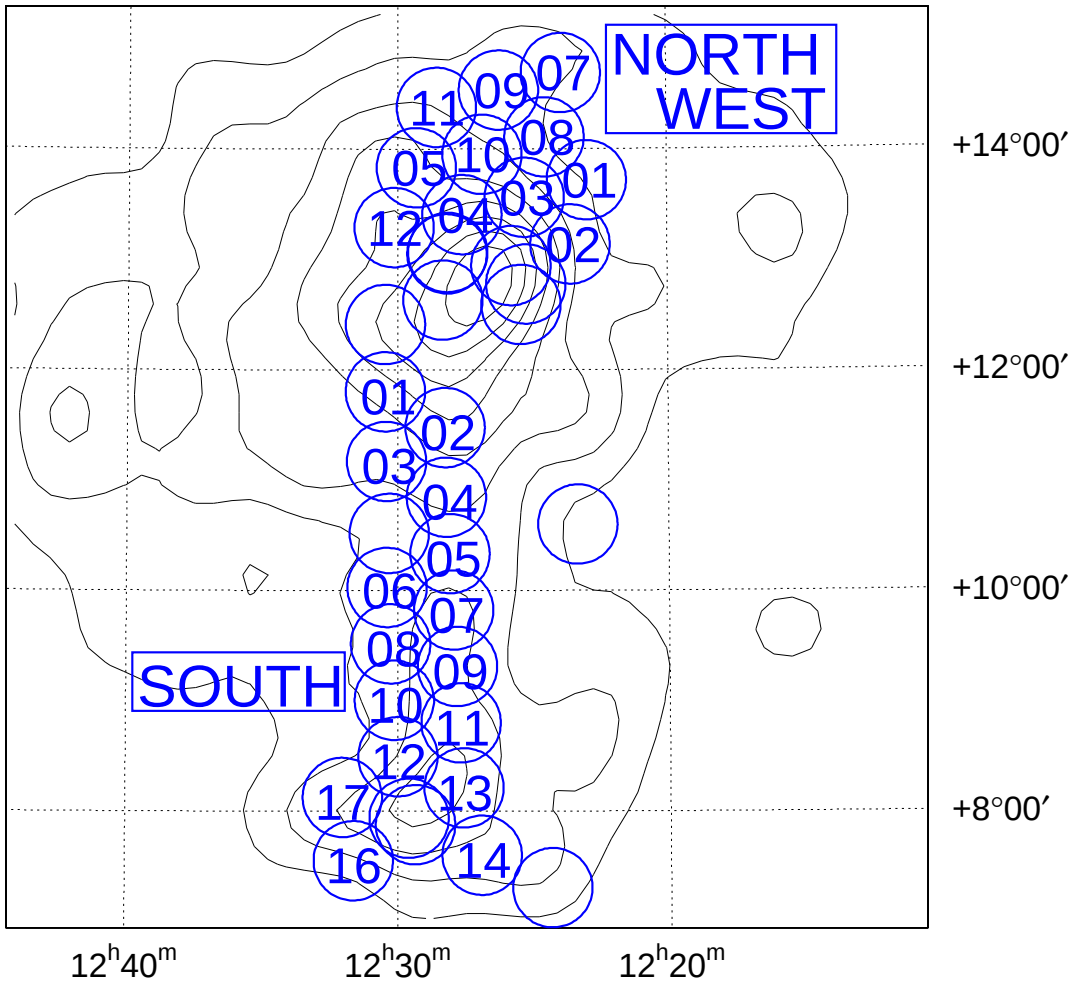

Figure 6.2: ASCA observed regions superposed on the contours of number density of galaxies. The observed regions are listed in table 6.1 and table 6.2. Radius of each circle is $22'$ corresponding to GIS field of view. Contours shows the number density of the Virgo member galaxies of VCC smoothed with a Gaussian of $\sigma = 20.4'$ in linear scale. The lowest contour level is 2.58×10^{-3} galaxies arcmin^{-2}, and the contour spacing is 2.07×10^{-3} galaxies arcmin^{-2}.

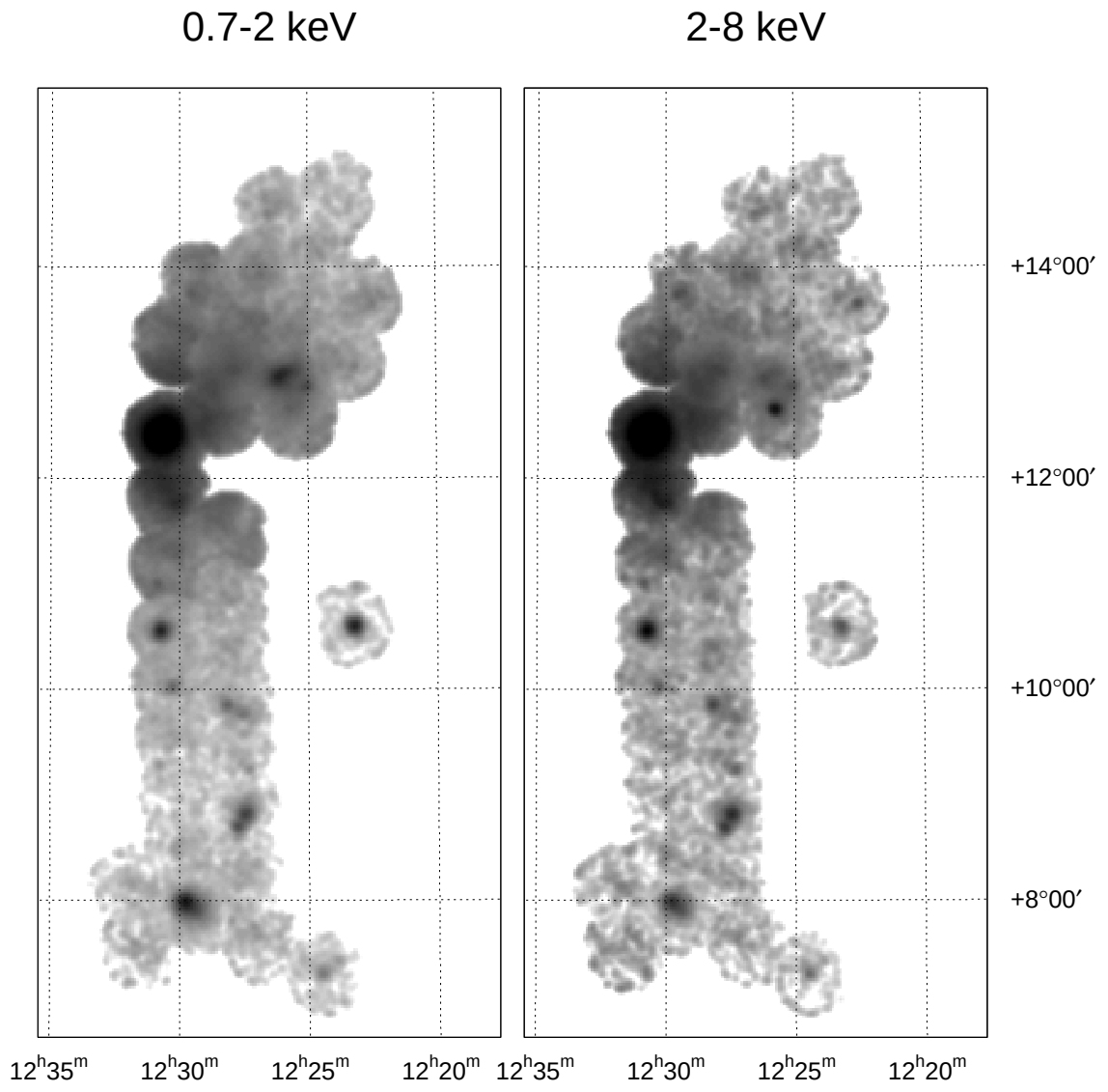

Figure 6.3: X-ray image of the Virgo cluster field with the GIS ($0.7 - 2$ keV band (left panel) and $2 - 8$ keV (right)). XRT vignetting is not corrected but the background (CXB and NXB) is subtracted.

6.2 Contaminating Sources

6.2.1 Source Finding

The observed GIS image of the Virgo cluster is shown in figure 6.3. From the figure 6.1, we can see the largely extended X-ray emission with some discrete peaks. To extract the X-ray spectrum of the ICM in the Virgo cluster, we have to estimate and exclude contamination of X-ray sources other than the ICM. For this purpose, we carried out source detection analysis. Since the faintest region in the Virgo cluster observed with ASCA has a 2–10 keV flux of $\sim 2 \times 10^{-15}$ ergs s^{-1} cm^{-2} arcmin^{-2} ($\sim 6 \times 10^{-3}$ counts s^{-1} in 0.7–7 keV band at 1CCD nominal position within $r < 6$ mm, which corresponds to an energy flux of $\sim 3 \times 10^{-13}$ ergs s^{-1} cm^{-2} in 2–10 keV assuming a point source with a photon index of 1.7), we need to exclude contaminating sources which have at least the same flux level with the Virgo cluster : i.e. $\sim 10^{-13}$ ergs s^{-1} cm^{-2} in 2–10 keV band.

The source detection method has been developed for the CXB study by Ueda (Ueda 1995; Ueda et al. 1998), who dealt with the complicated detector response in a systematic way, including the position dependence of the PSF effect. This procedure consists of three steps: (1) detection of candidates, (2) estimation of statistical significance and flux of the source candidates, and (3) calculation of the spectral information by the spectral fitting. In the second step, fitting for a 2 dimensional image is performed. The model function for a certain pointing data is expressed as

$$\mathrm{Model}(X,Y) = A_{\mathrm{bgd}}\, t\, BGD(X,Y) + \sum_{i=1}^{n} A_i\, t\, f(x_i,y_i)\, PSF(x_i,y_i;X,Y) \tag{6.1}$$

where (X,Y) is position coordinate, A_{bgd} is normalization of background, t is exposure time, $BGD(X,Y)$ is count rate of the background at (X,Y), (x_i,y_i) is position of the i-th source candidate detected in the first step, A_i is normalization of the i-th source candidate in unit of flux, $f(x_i,y_i)$ is conversion factor from flux to count rate, and $PSF(x_i,y_i;X,Y)$ is PSF intensity at a position (X,Y) from a point source located at (x_i,y_i). Free parameters are A_{bgd} and A_i, while others are fixed. The background (CXB+NXB) is reproduced from a template which is constructed in a similar way as in Ikebe (1994) (see section 5.2.2). Although the long-term variability of NXB is not considered, it matters little for the present image fitting because CXB component dominates the total photons in 0.7–7 keV band, which we will use for the source detection, even at 20 mm offset from the optical axis. However, we have to pay attention that the image, which have a significant gradient in the surface brightness, may not be fitted well by this method, because it uses CXB(+NXB) image as the template of the surface brightness. Fortunately, the Virgo cluster is extended much larger than the GIS field of view, so gradient of the surface brightness in a field of view is negligible in almost all regions. Also, in applying this method to the Virgo cluster, we simply exclude the regions which contain bright extended sources such as background clusters of galaxies.

Thus, we used the following 28 fields for the source detection (see table 6.1 and 6.1):

nw_p01, nw_p02, nw_p03, nw_p04, nw_p05, nw_p07, nw_p08, nw_p09, nw_p10,
nw_p11, nw_p12, s_p01, s_p02, s_p03, s_p04, s_p05, s_p06, s_p07, s_p08, s_p09,

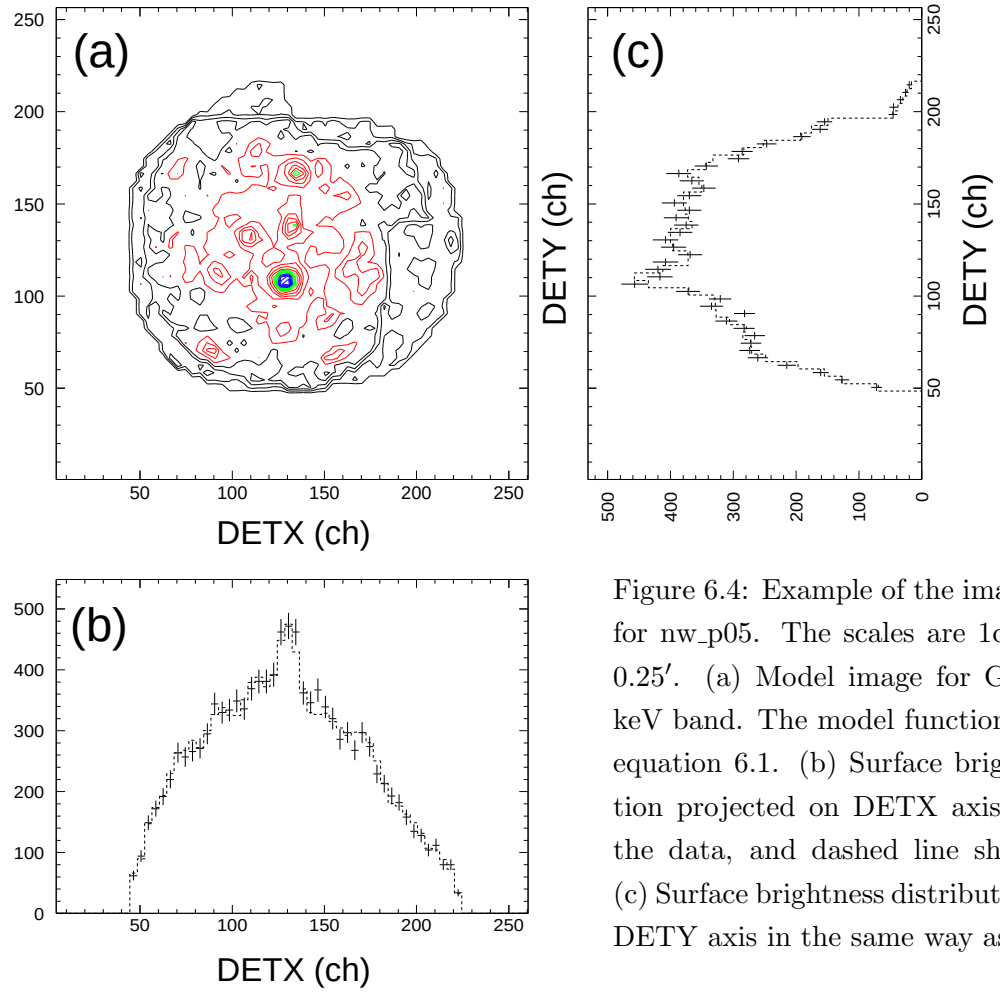

Figure 6.4: Example of the image fitting result for nw_p05. The scales are 1ch = 0.25mm ≈ 0.25′. (a) Model image for GIS2+3 in 0.7–7 keV band. The model function is expressed in equation 6.1. (b) Surface brightness distribution projected on DETX axis. Crosses show the data, and dashed line shows the model. (c) Surface brightness distribution projected on DETY axis in the same way as (b).

s_p10, s_p12, s_p13, s_p14, s_p16, s_p17, M87 NW, NGC 4365.

We adopt rather low level of criterion to find source candidates for our purpose: i.e. the detection significance greater than 3σ in $0.7-7$ keV band. The definition of the significance is,

$$\text{Detection Significance } (\sigma) = \frac{\text{Best fit Flux}}{1\ \sigma \text{ Error of the Flux}}.$$

The error represents the statistical error for a single parameter obtained by the fitting. As the result, we detected 224 source candidates as listed in table B. Figure 6.4 shows an example of the image fitting for the region nw_p05. We found the surface brightness obtained by GIS is well described by the model (equation 6.1).

Figure 6.5 shows the distribution of the 0.7–7 keV significance for all candidates. Note that fraction of 'fake' sources, which are produced by statistical fluctuation of the background, in detected candidates increases as the threshold level goes down. Ueda (1995) studied that the fraction of the fake sources in the total number of detected sources in the ASCA LSS (Large Sky

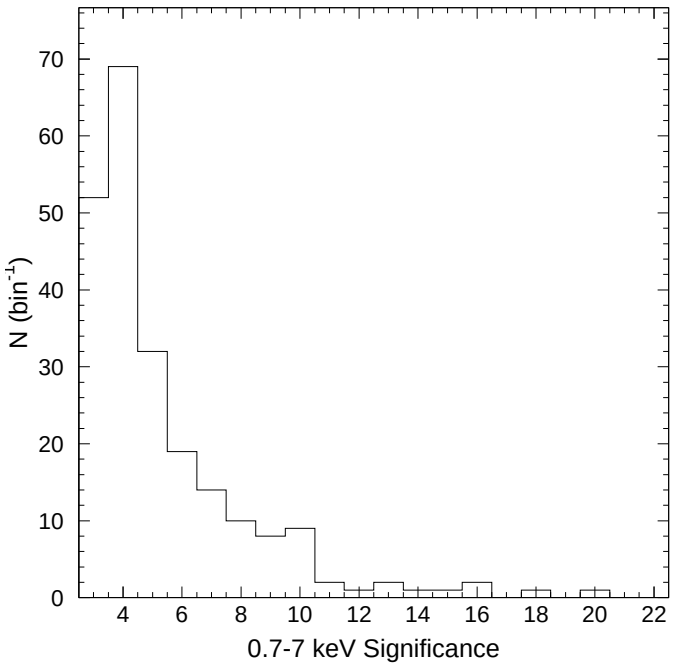

Figure 6.5: Distribution of the 0.7–7 keV significance for detected 224 source candidates.

Survey) fields becomes about 10% if we adopt $\sigma = 3.0$. Since the exposure time of each observed point in the Virgo is nearly the same as that in the LSS (typically ~ 20 ksec), we can assume the fraction to be about 10% for our criterion.

In order to remove the point sources thus detected, we decided to mask the regions centered on the point sources within an appropriate radius depending on the source flux, because a brighter source affects a wider region around it than a fainter one. We have created the source-mask which is utilized to mask out the point sources. We chose the mask radius $r_{\rm mask}$ where the surface brightness due to the point source drops to less than 5% of the ICM level. Figure 6.6 shows an example of the azimuthally averaged XRT + GIS PSF (Ishisaki 1995). Although the XRT + GIS PSF has energy- and position dependence (figure 5.1), they matter little for the present purpose. The observed radial surface brightness profile of the PSF can be roughly expressed by a double exponential form (Ishisaki 1995),

$$f(x) = 528.5\ \exp(-0.96\ x) + 4.95\ \exp(-0.16\ x). \tag{6.2}$$

We assume the surface brightness of the Virgo cluster is constant in an angular scale of $\sim 10'$.

Then, the radial surface brightness distribution around detected source candidates can be represented by a formula:

$$a\ f(x) + b, \tag{6.3}$$

where a represents the normalization of the flux of the point source, and b is the flux of the Virgo ICM. CXB and NXB are subtracted here. We calculated a and b by fitting for the detected 224 source candidates to obtain $r_{\rm mask}$ which could be calculated as $a\ f(r_{\rm mask}) = 0.05\ b$. We also set

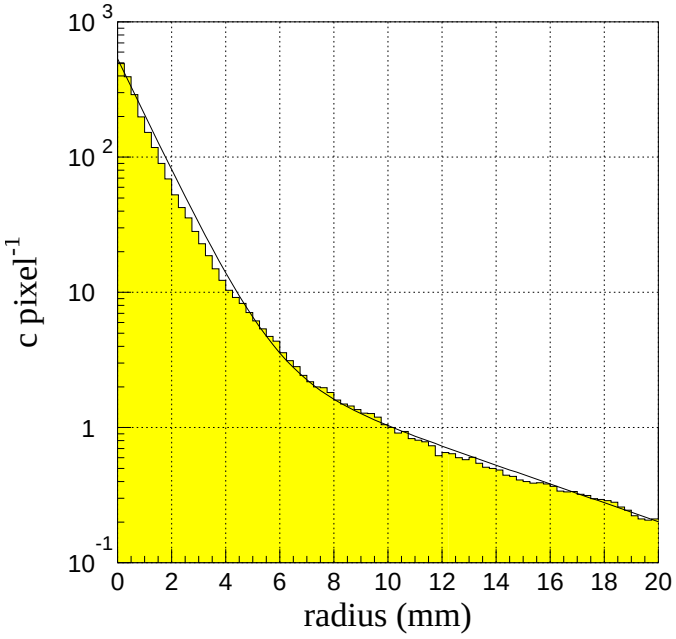

Figure 6.6: Hatched histogram shows a radial profile of Cyg X-1 image at 1 CCD nominal position taken by GIS2 in the $5 - 6$ keV energy band. Smooth solid line superposed on the histogram shows the function of $f(x) = 528.5\ \exp(-0.96\ x) + 4.95\ \exp(-0.16\ x)$ (Ishisaki 1995).

the minimum value of $r_{\rm mask}$ as 3 mm ($\approx 3'$). This ensures that the remaining source flux outside of the mask is always fainter than 5% of the ICM flux in the Virgo cluster.

Figure 6.7 shows the source masks as black circles superposed on the ASCA observed regions. In this figure, we can see the positions of detected source candidates near M87, namely positions nw_p12, M87 NW, s_p01, s_p02 and s_p03, are distributed predominantly in the near side of M87 in each field. Furthermore, some candidates found near M87 exhibits extremely higher count rate than others. These are possibly 'fake' sources due to strong stray light from M87. Figure 6.8 shows $r_{\rm mask}$ of 224 candidates plotted against its significances. Filled circles indicates the candidates near M87 (in nw_p12, M87 NW, s_p01, s_p02, and s_p03), and open circles are others. We can see that $r_{\rm mask}$ is nearly proportional to the significance for open circles. Most of the filled circles do not follow this relation, suggesting that they are fake sources.

Based on the above results, we derived the Log N - Log S relation for the detected sources. It is calculated as

$$N(>S) = \frac{\text{Number of Sources (flux} > S)}{\Omega(S)}. \tag{6.4}$$

Here $N(>S)$ represents the number of sources with its flux higher than S, and $\Omega(S)$ is the net sky area where the sensitivity limit is achieved to be less than S. We have to estimate the completeness of the source detection in the area $\Omega(S)$ to calculate the accurate Log N - Log S relation. Since the sensitivity limit depends on the parameters such as the exposure, effective area, and background level, elaborated works are required to estimate $\Omega(S)$ accurately (Ueda 1995). For simplicity, we assume the whole observed area as $\Omega(S)$. In this case, $N(>S)$ is regarded to be a lower limit because our sensitivity is poorer than S in most of the regions. Excluding the regions near M87, nw_p12, M87 NW, s_p01, s_p02, and s_p03, due to heavy contamination from

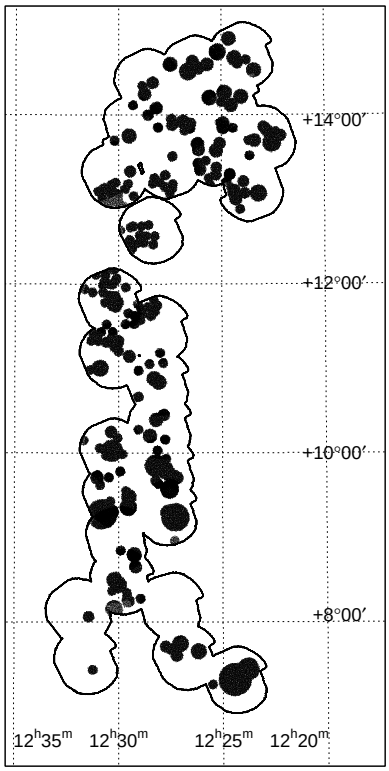

Figure 6.7: The source-mask for the Virgo cluster (filled circle) superposed on the GIS field of views. We applied the source finding method to the following fields: nw_p1, nw_p2, nw_p3, nw_p4, nw_p5, nw_p7, nw_p8, nw_p9, nw_p10, nw_p11, nw_p12, s_p1, s_p2, s_p3, s_p4, s_p5, s_p6, s_p7, s_p8, s_p9, s_p10, s_p12, s_p13, s_p14, s_p16, s_p17, M87 NW, NGC 4365. List of the source candidates are in appendix B.

M87, the value of $\Omega(S)$ is estimated to be 8.5 deg^2 (northwest region is 3.6 deg^2 and south region is 4.9 deg^2).

The calculated Log N - Log S relation is shown in figure 6.9. In this calculation, we employed the significance level greater than $\sigma = 4$ to eliminate fake sources produced by the statistical fluctuation of the background. In this case, the expected number of fake sources is estimated to be ~ 0.5 deg^{-2} (Ueda 1995). Although we have some information about the energy spectrum for each source, we calculate the flux from the count rate assuming a power-law spectrum with a photon index of 1.7 to compare with previous analysis. Furthermore, we treat any pair of candidates as identical if their positions coincide within $2'$ due to the uncertainty of position determination (Ueda 1995).

Figure 6.9 shows the Log N - Log S relation for the northwest and south regions of the Virgo cluster, as compared with the result from the ASCA CXB study (Ueda 1995; Ueda et al. 1998). Our result for the northwest region is almost consistent with Matsumoto (1997) who independently calculated the Log N - Log S relation. Although our result is a lower limit, it is almost the same as that of the CXB above $\sim 1 \times 10^{-13}$ ergs cm^{-2} s^{-1}. Since our $\Omega(S)$ is expected to approach the true $\Omega(S)$ as S increases, our $N(> S)$ is considered to be a good approximation of the true $N(> S)$ in the high flux region.

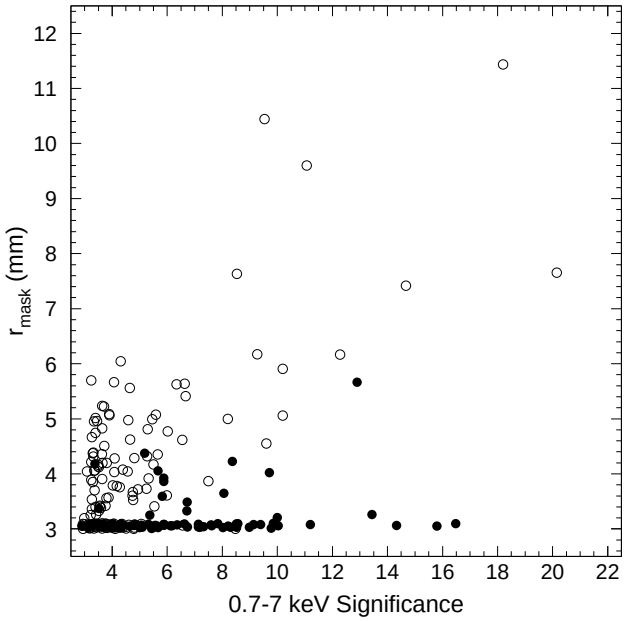

Figure 6.8: The 0.7–7 keV significance vs. $r_{\rm mask}$ for 224 source candidates. Filled circles indicate the candidates found in the regions nw_p12, M87 NW, s_p01, s_p02, and s_p03, and open circles are in others.

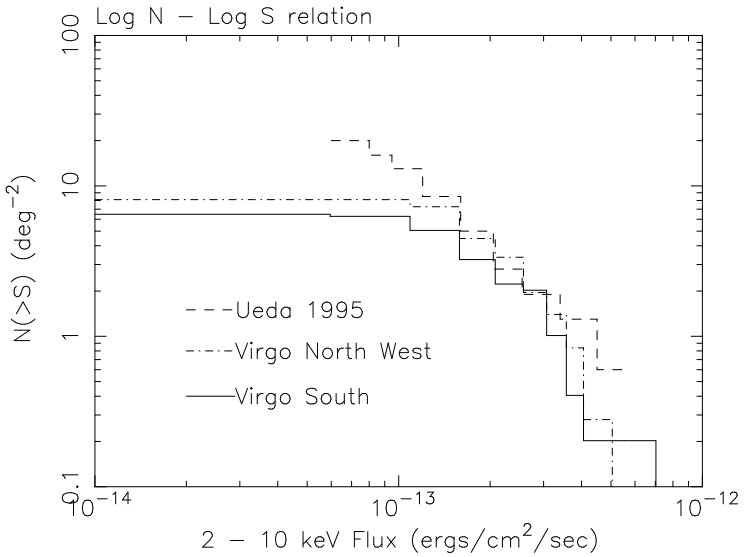

Figure 6.9: Log N - Log S relation of detected sources candidates in the Virgo cluster: for the northwest region (dot-dashed line) and the south region (solid line). Note that these lines indicate lower limits. Dashed line shows the result from ASCA CXB analysis (Ueda 1995).

6.2.2 Nearby Bright Sources

In this section, we look into the properties of bright X-ray sources in the Virgo area. As seen in the RASS image shown in figure A.5, there are four bright sources in the south region of the Virgo cluster, which are not associated with the Virgo cluster: A1553, NGC 4325, A1541, and RX J1227.7+0841. Although we exclude these four regions in the study of the Virgo ICM, we have to estimate the effect of stray light originating from these sources.

A1553

A1553 [$(\mathrm{RA, Dec})_{\mathrm{J2000.0}} = (12^{\mathrm{h}}30^{\mathrm{m}}.8, 10^{\mathrm{d}}34^{\mathrm{m}})$, Abell et al. 1989] is a cluster of galaxies behind the Virgo, at a redshift of $z = 0.1652$. Ebeling et al. (1996) reported the X-ray luminosity of this cluster to be 7.05×10^{44} erg s^{-1} in $0.1 - 2.4$ keV band based on the ROSAT observation.

ASCA observed A1553 in June 1996 (PI: I. McHardy, see table 6.2). Figure 6.10(a) shows the 0.7–7 keV image and projected surface brightness profile of A1553 obtained with GIS. We fit the radial surface brightness profile with the β model. Unfortunately, no pointing observation was carried out by ROSAT, so we extract the β model parameters from the GIS data using Image Response Matrix (IRM) method which includes the complicated detector response as described in detail in Ikebe et al. (1997) and in Markevitch et al. (1996). To determine the image and spectral parameters for the A1553, we also included the Virgo emission, as indicated with a dashed line in figure 6.10(a), assuming the emission from the Virgo to be $kT = 2.0$ keV, $Z/Z_{\odot} = 0.2$ (Koyama et al. 1991; Matsumoto 1998). The GIS spectrum of A1553 is shown in figure 6.12, and obtained parameters are summarized in table 6.3. The temperature and the luminosity show good agreement with the $L_{\mathrm{x}} - kT$ relation (e.g. David et al. 1993).

NGC 4325

NGC 4325 is a bright E4 galaxy, with B band magnitude $B_T = 14.4$. Although this galaxy is also cataloged by Binggeli (1985) as VCC 616, it's not a member galaxy of the Virgo cluster because of a large radial velocity of 7709 ± 39 km s^{-1}.

NGC 4325 was observed in July 1993 with ROSAT, and January 1997 with ASCA (see table 6.2). For the first step, we fit the PSPC radial brightness profile with the β model (emission from NGC 4325) and a constant (emission from the Virgo and the background). The radial profile is shown in figure 6.11(a) with the best fit model. Lower panel of figure 6.10(b) shows the projected surface brightness of NGC 4325 obtained with GIS. Dotted line in 6.10(b) indicates the best fit β model profile, which is obtained by the PSPC data, convolved with the ASCA response. Thus PSPC-determined β model represent the GIS data well. Using this β model, we fitted the GIS spectrum by the SimARF method. Since we have obtained the β model parameters from the ROSAT, we do not use the IRM for the spectral analysis. We also included the Virgo emission in the same way for A1553. The GIS spectrum is shown in figure 6.12, and the obtained parameters are summarized in table 6.3. The temperature indicates a typical spectrum for an early-type galaxy.

A1541 and RX J1227.7+0841

We can see two bright X-ray peaks in the region s_p11, which are A1541 [$(\mathrm{RA, Dec})_{\mathrm{J2000.0}} = (12^{\mathrm{h}}27.4^{\mathrm{m}}, 8^{\mathrm{d}}50^{\mathrm{m}})$, Abell et al. 1989] and RX J1227.7+0841 [$(\mathrm{RA, Dec})_{\mathrm{J2000.0}} = (12^{\mathrm{h}}27^{\mathrm{m}}45.1^{\mathrm{s}}, 8^{\mathrm{d}}41^{\mathrm{m}}47^{\mathrm{s}})$, Voges et al. 1996]. A1541 is a cluster of galaxies at the background of the Virgo, with a redshift $z = 0.08956$. RX J1227.7+0841 is identified as an AGN from optical observation (Bade et al. 1998), with B magnitude $B_T = 16.8$. Although there is a source [HB89] 1225+089 which is a seyfert I galaxy with a redshift $z = 0.085$ (Hewitt & Burbidge 1989), the catalogued position is $1.2'$ apart from RX J1227.7+0841. The X-ray luminosity of [HB89] 1225+089 is reported as $L_{\mathrm{X}} \approx 7 \times 10^{43}$ ergs s^{-1} in 0.5–4.5 keV band (Stephens 1989, we converted the value assuming $H_0 = 50$ km s^{-1} Mpc^{-1} and $q_0 = 0.5$).

ROSAT PSPC observed A1541, namely with RX J1227.7+0841 in the same field of view, in December 1992. We fit the PSPC radial brightness profile of A1541 with the β model and a constant in the same way as for NGC 4325. The PSPC radial profile is shown in figure 6.11(b) with the best fit model. Lower panel of figure 6.10(c) shows the projected brightness profile of A1541 and RX J1227.7+0841 obtained with GIS. The profile of A1541 is well described by the β model obtained by PSPC (dotted line), even in the ASCA energy band. We assume RX J1227.7+0841 is point-like, at least for the GIS spatial resolution, as indicated with dot-dashed line in 6.10(c). Then we can carry out spectrum fitting of the GIS data, based on the information of the surface brightness distribution. In this fit, we have to deal with the contaminating photons from the other sources, in addition to the photons from the Virgo, since the projected distance of these two sources are only $\sim 10'$. From the figure 6.10(c), we can estimate that photons originating from A1541 occupies $\sim 17\%$ of the total photons in a radius of $3'$ centering RX J1227.7+0841. However, photons from RX J1227.7+0841 contaminates only $\sim 1\%$ in the radius of $3'$ from the center of A1541. Therefore, for the first step, we determine the spectral parameter of A1541 neglecting the photons from RX J1227.7+0841. Then the latter spectrum is obtained by excluding the contaminating region around RX J1227.7+0841. The GIS spectra are shown in figure 6.12, and fitting results are summarized in table 6.3. The temperature and the luminosity of A1541 agree with the $L_{\mathrm{x}} - kT$ relation (e.g. David et al. 1993).

Estimation of the Stray Light from the Four Sources

Based on the results shown in table 6.3, we carried out the ray-tracing simulation, and estimated the fraction of contaminating photons in the other Virgo regions due to the four bright sources. Results are summarized in table 6.4. 'Fraction' in table 6.4 means,

$$\mathrm{Fraction} = \frac{\text{Photons from 'Photon origin' detected in each 'Region'}}{\text{Total photons in the 'Region'}}.$$

We can see that the contaminations due to A1553 and A1541 are significant ($\sim 10\%$) in several regions. Thus, to derive physical parameters of the Virgo ICM, we have to take into account the effect of these contaminating photons.

Table 6.3: Best fit parameters with 90% errors for 4 bright sources

Target	Image Parameter	Spectrum Parameter	$F_{\rm x}^{\dagger}$, $L_{\rm x}^{\ddagger}$
A1553	β model	Raymond-Smith	$F_{\rm x} = 5.7 \times 10^{-12}$
	$\beta = 0.73(0.69 - 0.79)$	$kT = 7.3(6.6 - 8.2)$ keV	$L_{\rm x} = 1.5 \times 10^{45}$
	$R_{\rm c} = 1.0$ (fixed) arcmin	$Z/Z_{\odot} = 0.13(0.01 - 0.25)$	
NGC 4325	β model	Raymond-Smith	$F_{\rm x} = 3.8 \times 10^{-13}$
	$\beta = 0.62(0.60 - 0.64)$	$kT = 0.85(0.81 - 0.88)$ keV	$L_{\rm x} = 1.4 \times 10^{43}$
	$R_{\rm c} = 0.44(0.40 - 0.47)$ arcmin	$Z/Z_{\odot} = 0.23(0.16 - 0.33)$	
A1541	β model	Raymond-Smith	$F_{\rm x} = 3.4 \times 10^{-12}$
	$\beta = 0.48(0.45 - 0.52)$	$kT = 4.0(3.4 - 4.8)$ keV	$L_{\rm x} = 2.2 \times 10^{44}$
	$R_{\rm c} = 0.97(0.78 - 1.19)$ arcmin	$Z/Z_{\odot} = 0.22(< 0.64)$	
RX J1227.7+0841	Point-like	Power-law	$F_{\rm x} = 9.3 \times 10^{-13}$
		Photon index $= 2.0(1.8 - 2.2)$	$L_{\rm x} = 7.1 \times 10^{43}$

†: $2 - 10$ keV flux in erg s^{-1} cm^{-2}.
‡: $0.5-10$ keV luminosity in erg s^{-1} assuming $H_0 = 50$ km s^{-1} Mpc^{-1} and $q_0 = 0.5$. For RX J1227.7+0841, $z = 0.085$ is assumed as the redshift.

Table 6.4: Contaminating photon fraction from the four bright sources

Photon origin	Region	Fraction (0.7–7 keV) †
A1553	s_p03	4.5 %
	s_p04	1.1 %
	s_p05	8.3 %
	s_p06	10.0 %
NGC 4325	s_p04	3.3 %
	s_p05	1.3 %
A1541	s_p09	8.1 %
	s_p10	6.5 %
	s_p12	6.7 %
	s_p13	6.2 %
RX J1227.7+0841	s_p09	1.0 %
	s_p10	1.1 %
	s_p12	1.0 %
	s_p13	1.1 %

†: (Photons from 'Photon origin' in 'Region') / (Total photons in 'Region') in 0.7–7 keV band.

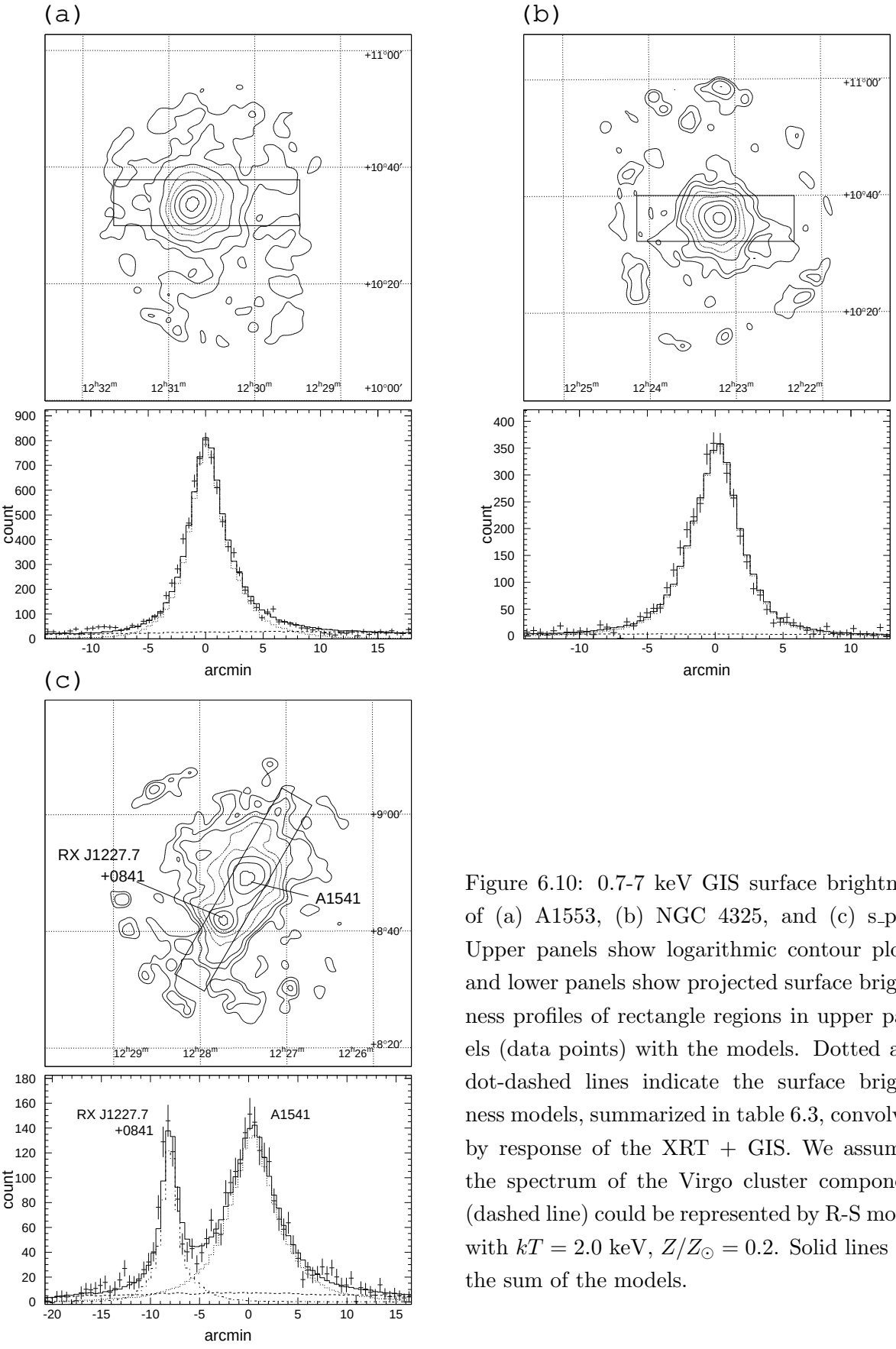

Figure 6.10: 0.7-7 keV GIS surface brightness of (a) A1553, (b) NGC 4325, and (c) s_p11. Upper panels show logarithmic contour plots, and lower panels show projected surface brightness profiles of rectangle regions in upper panels (data points) with the models. Dotted and dot-dashed lines indicate the surface brightness models, summarized in table 6.3, convolved by response of the XRT + GIS. We assumed the spectrum of the Virgo cluster component (dashed line) could be represented by R-S model with $kT = 2.0$ keV, $Z/Z_{\odot} = 0.2$. Solid lines are the sum of the models.

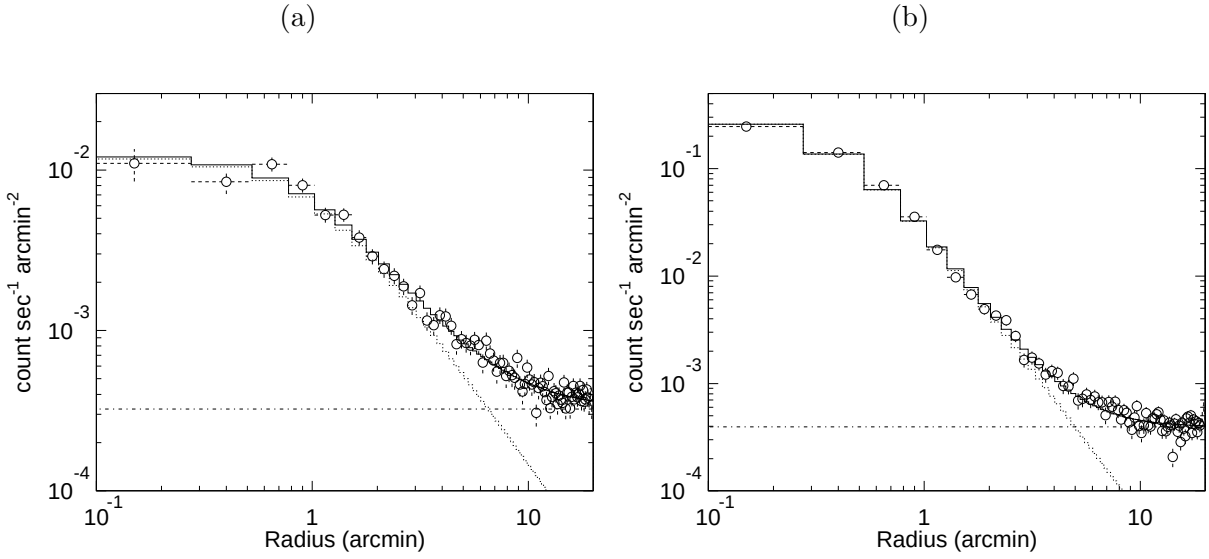

Figure 6.11: The radial brightness profile of (a) A1541 and (b) NGC 4325 obtained with PSPC. Data points are indicated by open circles, and fitting models (β model and a constant) are indicated by broken lines.

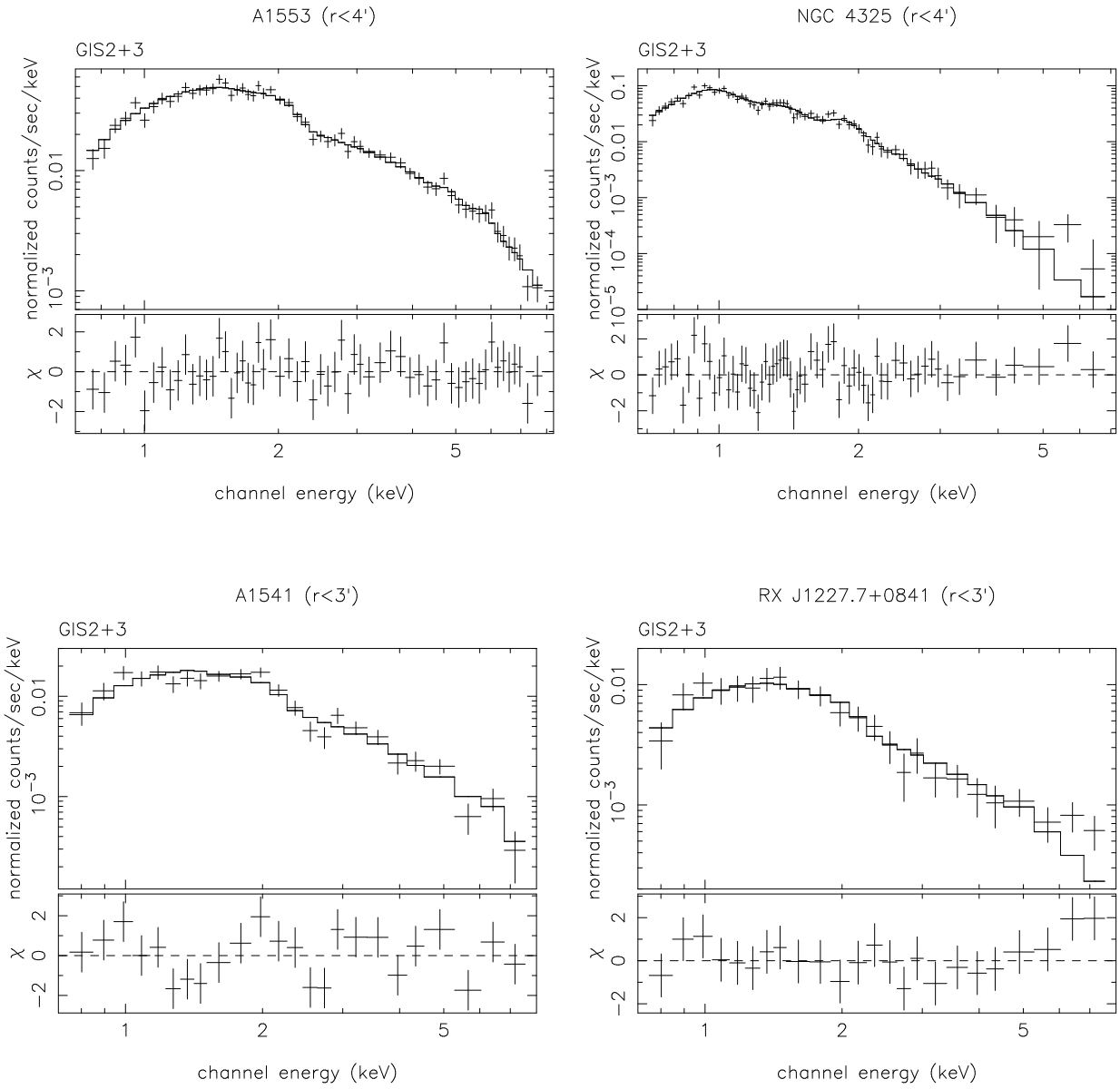

Figure 6.12: GIS spectra of four bright sources: A1553 (upper left), NGC 4325 (upper right), A1541 (lower left) and RX J1227.7+0841 (lower right). The parameters of fitting models (solid lines) are shown in table 6.3

6.2.3 The North Polar Spur

The edge of North Polar Spur (NPS), believed to be the rim of a hot Galactic superbubble (Berkhuijsen et al. 1971; Raymond 1984; Egger & Aschenbach 1995), is located toward the direction of the Virgo cluster. The NPS is the most prominent part of Loop I, which is a Galactic giant superbubble of $58^\circ \pm 4^\circ$ radius centered at $l = 329^\circ.0 \pm 1^\circ.5$, $b = 17^\circ.5 \pm 3^\circ.0$ (Berkhuijsen et al. 1971). Based on the ROSAT observation, Egger (1993) modeled the Loop I as a 2×10^7 years old superbubble produced by a supernova in the Sco-Cen association, and the center of the shell is at a distance of ~ 170 kpc from the Sun. Several observations indicate that the NPS has a temperature of $1 - 4 \times 10^6$ K (Hayakawa et al. 1977; Schnopper et al. 1982; Egger 1993), and strong line emission from C, N, O, Ne, and Fe are seen (Inoue et al. 1980; Rocchia et al. 1984).

Based on the ROSAT observation, Irwin & Sarazin (1996) found the NPS component in the spectra around M49. Figure 6.13 shows comparison of X-ray emission from the NPS with the Virgo cluster based on the parameters obtained by Irwin & Sarazin (1996). These parameters are shown in table 6.5. Figure 6.14 shows the 1/4 keV image around the Virgo obtained with RASS (Snowden et al. 1994). Although the strong soft X-ray emission from the NPS is seen in the southeast region of the Virgo cluster, it is weakened in the north region of M49. Thus we can neglect the emission from the NPS above ~ 1 keV band in the whole Virgo cluster region.

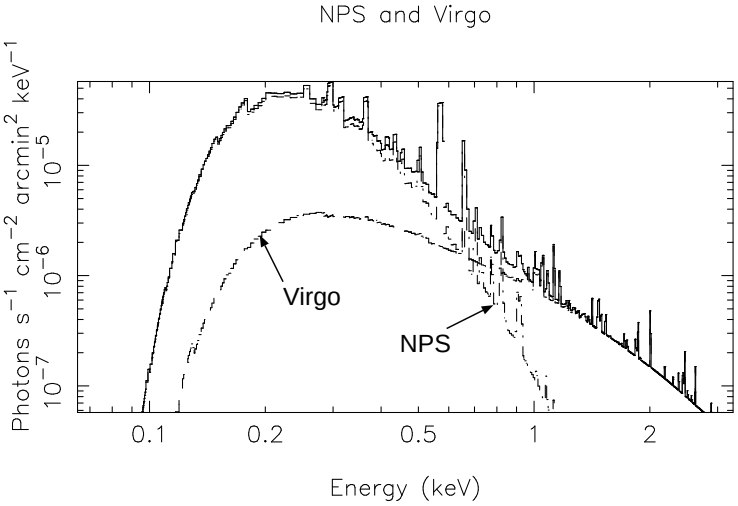

Figure 6.13: X-ray spectra from the NPS (dash-dotted line) and the Virgo cluster (dashed line) around M49. Solid line shows the sum of two component. These spectra are calculated by R-S model, with the parameters listed in table 6.5.

Table 6.5: Comparison of X-ray emission from Virgo and NPS around M49 along with 90% errors.

Parameter	Virgo Component	NPS Component
Temperature (keV)	$1.4(> 1.1)$	$0.15(0.10 - 0.21)$
Abundance ($Z/Z_\odot$)	0.1 (fixed)	0.03 (unconstrained)
Column density (10^{20} cm^{-2})	1.64 (fixed)	$1.44(0.85 - 2.46)$
$F_{\mathrm{X}\ 0.2-2.48}$ (10^{-15} erg s^{-1} cm^{-2} arcmin^{-2})	$2.4(1.8 - 2.7)$	$5.3(4.9 - 6.6)$

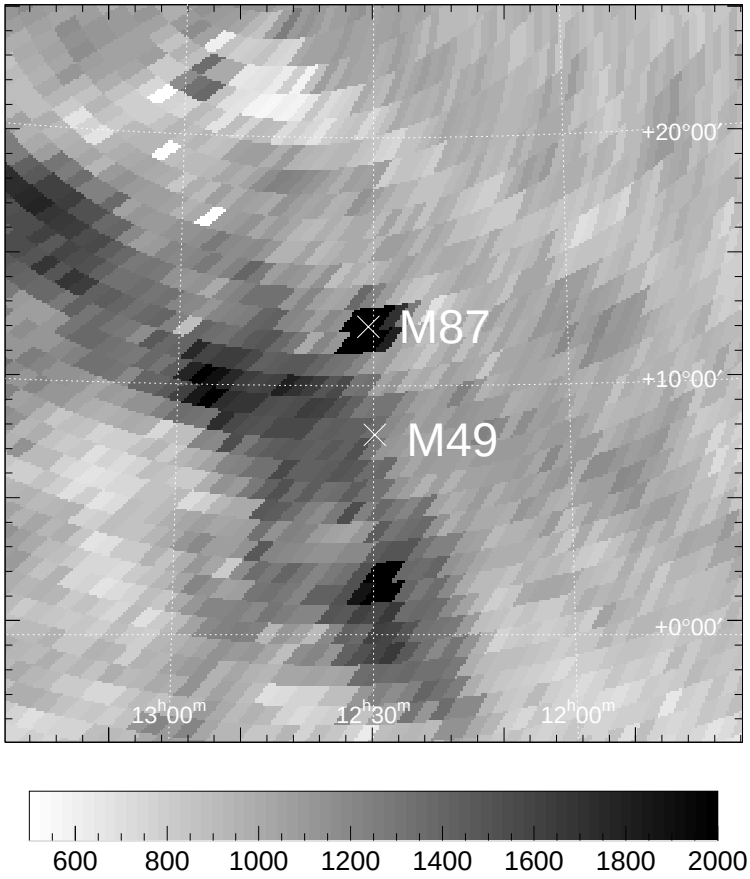

Figure 6.14: X-ray image in the 1/4 keV band around the Virgo cluster obtained with ROSAT (Snowden et al. 1995). Lower panel shows scale of the counting rate in 10^{-6} counts s^{-1} $pixel^{-1}$.

6.3 ROSAT Image as a Model of Surface Brightness Distribution

The discrete source contributions have been masked out based on the analysis in the previous section. The next task is to obtain spatially resolved spectral information for the ICM in the Virgo cluster. To perform this, we have to know the surface brightness distribution all over the Virgo cluster to estimate the amount of the stray light at each observed point.

Fortunately, the RASS (ROSAT All-Sky Survey, see section chapter A.3) data is available for this purpose. We decided to use the data only above 0.9 keV (channel 91 to 201) to exclude emission from the NPS. Spatially uniform background of 1.4×10^{-4} counts s^{-1} $arcmin^{-2}$ is subtracted from the data at first, which has been calculated from the count rate for a blank sky region in the north of M87: $RA_{J2000.0} = 12^h21^m.4 - 12^h38^m.6$, $Dec_{J2000.0} = 13°21' - 14°2'$. Next, we smoothed the RASS image by a Gaussian with $\sigma = 20'$ for the faintest flux level and decreasing the size of σ with increasing surface brightness in 6 steps. Thus, we made a template of the surface brightness distribution from the RASS data. Figure 6.15 shows the comparison of projected surface brightness profile between the data and this template. Note that small-scale structures smaller than $\sim 1'$ may not be reproduced by the template because of the above smoothing.

To check the quality of this template, we simulate the GIS observation using this template as a surface brightness distribution. Figure 6.16(a) shows comparison of count rate profile for GIS data with the simulation in 0.7–2 keV band which is almost the same as the ROSAT band. We assumed the Virgo ICM has a uniform spectrum given by the Raymond-Smith model (Raymond & Smith 1977, hereafter R-S) with $kT = 2.0$ keV, $Z/Z_\odot = 0.2$ (Koyama et al. 1991; Matsumoto 1998) for the simulation. We can see that the simulation reproduces the GIS data very well with the discrepancy less than $\sim 20\%$, which corresponds to the systematic error of the ray-tracing results, except for the regions around M87 and M49. The large discrepancy around M87 and M49 is likely to be due to deviation in temperature. M87 has a higher temperature of ~ 3.0 keV (Matsumoto et al. 1996; Matsumoto 1998), and M49 has a lower temperature of ~ 1.0 keV (Awaki et al. 1994; Matsushita et al. 1994; Irwin & Sarazin 1996). The fact that the discrepancy is larger in higher energy band is consistent with this possibility (figure 6.16(b)). If this is the case, the discrepancy between the GIS data and the simulation at the linking region between M87 and M49 ($\sim -3°$ from M87 in figure 6.16(b)) suggests a temperature variation in this region.

It is important to know the contribution of X-ray flux from outside of the field of view, to obtain the 'true' temperature and abundance in each region. The above simulation helps us to estimate where the detected photons originate from. Figure 6.17 shows relative fractions of the emission in 0.7–10 keV band from the observed sky region (bar chart), contribution from M87 within $10'$ radius (circle), and that from M49 within $10'$ radius (rectangle) for each region. Almost half of the photons come from the pointed sky for each region except for the regions on M87 and M49 (NGC 4472). The middle region between M87 and M49 is almost free from the stray photons from M87 and M49, where complex spectral structures (such as temperature and abundance gradients) are seen. This helps the analysis for this region easier and ensures reliable results.

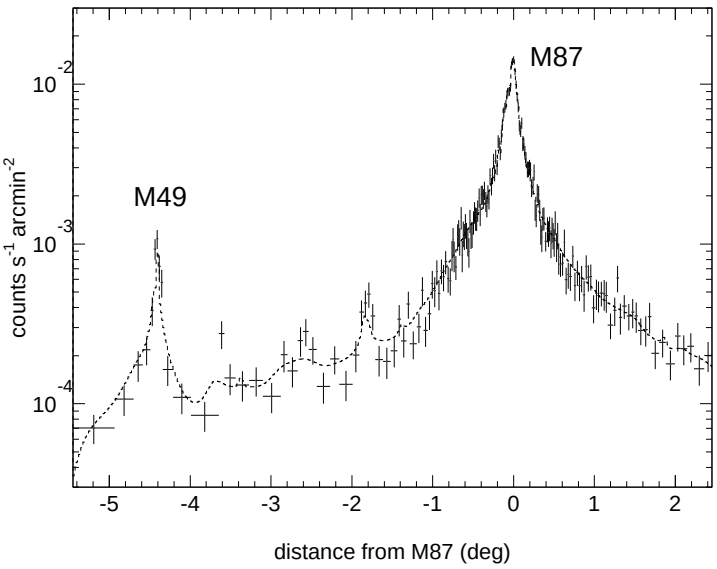

Figure 6.15: Comparison of projected surface brightness profile of RASS data (data points) with the model template (dotted line) (see section 6.3). The background (CXB and NXB) is subtracted.

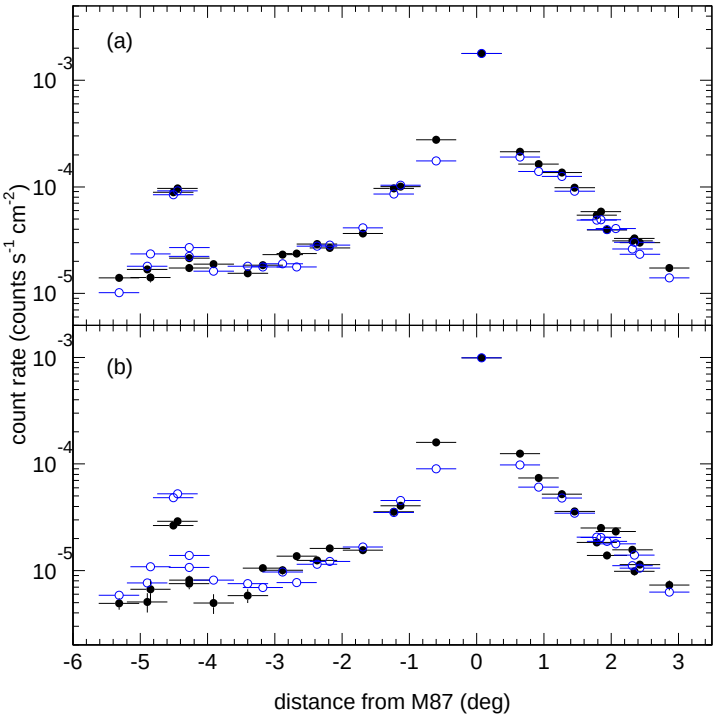

Figure 6.16: Comparison of surface brightness profile of GIS data with simulation: for (a) 0.7–2 keV, and (b) 2–10 keV band. The filled circles indicate the GIS data, and open circles are simulation. The simulation data are normalized to have the same value as the data at M87. The temperature and heavy element abundance of the Virgo ICM are estimated to be 2 keV and 0.2 solar, respectively.

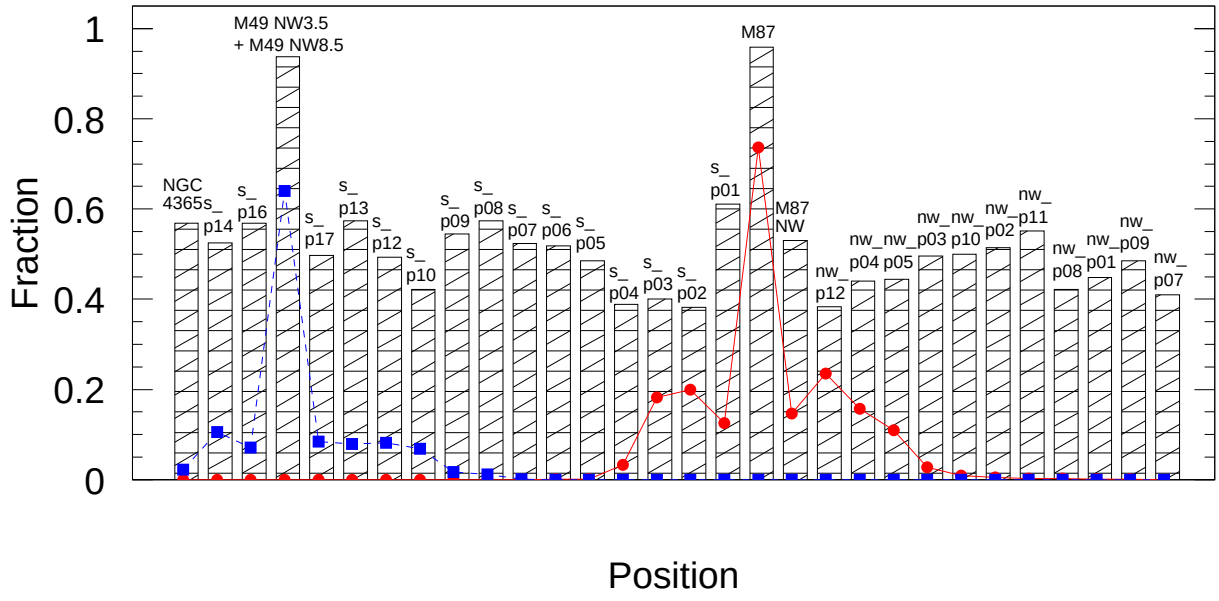

Figure 6.17: Relative fraction of the emission in 0.7–10 keV band estimated by the ray-tracing simulation: fraction of region's own emission (bar chart), emission from the M87 within 10′ radius (circles), and emission from the M49 within 10′ radius (rectangles). We assumed the temperature and heavy element abundance of the Virgo are 2 keV and 0.2 solar, respectively, and used the surface brightness model made from RASS data described in section 6.3. The regions are displayed in the south to north order (see table 6.1 and 6.2).

6.4 Temperature Distribution

In this section, we estimate the temperature distribution of the Virgo ICM in a simple manner. We first look into the hardness ratio of the spectrum (section 6.4.1), and then perform spectrum fitting with single temperature R-S model (section 6.4.2). Here only the GIS data after exclusion of discrete sources as described in section 6.2.1, are analyzed. In this section, we do not consider the stray light from the four bright sources (section 6.2.2) or the NPS (section 6.2.3). More detailed analysis will be carried out in section 6.5 and 6.6.

6.4.1 Hardness Ratio

As the first attempt to study the temperature distribution in the Virgo ICM, we calculate the hardness ratio, defined as the ratio of count rates between two energy bands 2–7 keV and 0.7–2 keV, for the regions where discrete sources are eliminated. Figure 6.18 shows a two dimensional map of the hardness ratio. We divide the regions into $20' \times 20'$ cells, and sum up the data of neighboring regions where the S/N ratio is lower than 4. The cell positions are also indicated in the left panel of figure 6.18. The systematic error of the hardness ratio is due to the ambiguity in the background (CXB and NXB) and typically $\sim 15\%$. In the figure 6.18, we can see significant variation of the hardness in the Virgo cluster ranging between 0.3 and 0.7. There is a concentration of hard regions at half way between M87 and M49, and the hardness ratio is generally high in the south regions compared with the northwest region.

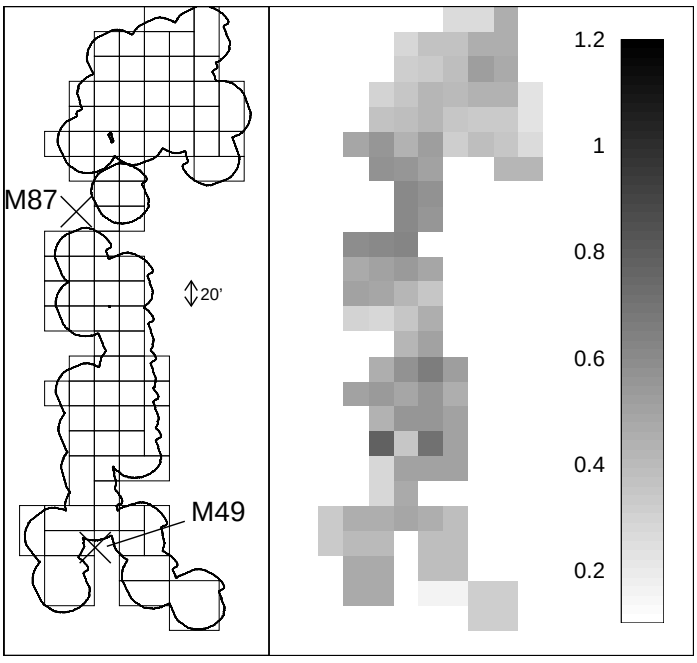

Figure 6.18: Gray scale plot of the 2 dimensional distribution of the hardness ratio in the Virgo region. Energy bands are 2–7 keV and 0.7–2 keV. Left panel shows rectangle mesh regions where the hardness are calculated superposed on the observed regions, and the right panel indicates the hardness. The contaminating sources which detected by the source finding technique described in section 6.2.1 are removed.

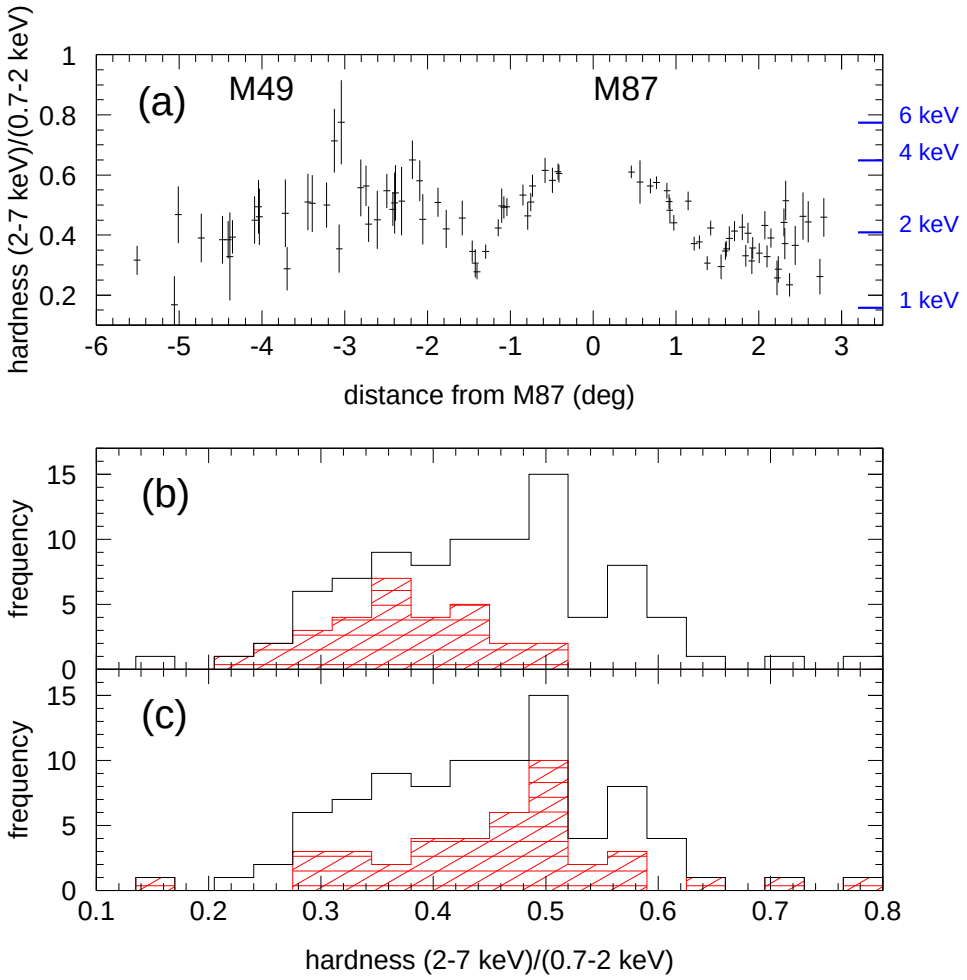

Figure 6.19: (a) The hardness ratio distribution as a function of distance from M87. The error bars indicate statistical errors. The systematic error of the hardness caused by the ambiguity of the background (CXB and NXB) is typically $\sim 15\%$. The values indicated right side of the panel show the temperature assuming R-S model with heavy element abundances 0.2 solar. (b) Solid line shows the frequency distribution of the hardness ratio in (a). Hatched region shows the distribution for the northwest region (distance from M87 is 1° to 3°) only. (c) Same as (b), but hatched region shows the distribution for the south region (distance from M87 is -6° to -1°) only.

Figure 6.19(a) again shows the hardness ratio as a function of angular distance from M87. The right side of M87 shows the northwest region and the left side is the south region, respectively. A broad enhancement of the hardness over a scale of a few degrees (corresponding to ~ 1 Mpc) is seen between M87 and M49. Two 'V'-shaped structures are seen at $\sim 80'$ from M87 in both south and northwest regions. However, it is possibly an artificial feature caused by the stray light from M87, because the fraction of hard photons in the stray light sharply drops when the pointing

direction is $\sim 80'$ offset (see figure 5.5).

We compare the hardness ratio distribution in the south region with that in the northwest one. The solid line in figure 6.19(b) shows the distribution for the data in (a), and the hatched part is for the northwest region (distance from M87 is 1° to 3°). Figure 6.19(c) is the same as (b), but the hatched part indicates the south region (distance from M87 is -6° to -1°). In the northwest region, the hardness values distribute around ~ 0.35 (corresponding to the temperature of ~ 2 keV, if we assume the R-S spectrum with metal abundance of 0.2 solar), while in the south region, the peak of the hardness is ~ 0.50 (~ 3 keV) and the values widely scatter from 0.15 to 0.8. This suggests presence of a complex temperature structure in the south region.

6.4.2 Spectral Fitting

As the next step, we performed spectral fitting with R-S models. Because of the limited statistics, we do not divide the regions into small cells, but derive one spectrum for each GIS pointing. Again, we use only the data in which discrete sources are eliminated by the source finding. The ARF for each pointing is produced by the SimARF method, using the surface brightness template made from the RASS image as described in section 6.3. Then we fit the X-ray spectrum for each pointed region in 0.7–8 keV band with a R-S model modified by interstellar absorption. The interstellar absorption is fixed to the Galactic value as shown in table 6.1. Thus the free parameters are the plasma temperature, metal abundance, and normalization. Results of the spectral fits are summarized in table 6.6.

Since the temperatures are around 2 keV, the metal abundance is primarily determined by the Fe L lines. Therefore we should regard the metal abundance in this fit to be that of Fe. However, the abundances are poorly constrained in many regions because of poor photon statistics. We only mention that the best-fit values suggest that the metal abundances in the general cluster regions are around 0.2 solar.

If we fitted the spectra with free absorption, the data often require the absorption to be zero. This suggests existence of an additional soft component below ~ 1 keV, which may be the emission from the NPS even in northwest region.

Temperature distribution as a function of distance from M87 is shown in figure 6.20. The distribution is similar to that of the hardness ratio, as shown in figure 6.19. We can see that the temperature around M87 is ~ 2.5 keV, and slightly decreases to ~ 2.0 keV at $\sim 2^\circ$ away from M87 in the northwest region (right side of figure 6.20). In the south region (left side of figure 6.20), the average temperature at a distance of -2° from M87 is still ~ 2.5 keV, with a large scatter from 1.8 keV to 3.4 keV. If we only look at the regions s_p05, s_p07 and s_p09, which are located along the "emission bridge" between M87 and M49, the ICM temperature around -2° to -3° rises up to ~ 3 keV. This feature is partly consistent with the Ginga's result (Takano 1990; Koyama et al. 1991; see figure 3.5). However, the ICM temperature decreases toward M49 to ~ 1.5 keV. This drop of temperature is inconsistent with the Ginga one, and we suspect that the non-imaging data of Ginga may have some contamination by hard X-ray sources. Our results

Table 6.6: The best fit parameters and confidence limits with $\Delta\chi = 2.706$ from a R-S model fitting in 0.7–8 keV band

Region	Temperature (keV))	Abundance (solar)	χ^2/ν
nw_p01	$1.40(1.25-1.70)$	$0.04(<0.20)$	45.7/28
nw_p02	$1.65(1.48-1.82)$	$0.27(0.11-0.53)$	27.2/28
nw_p03	$1.66(1.50-1.83)$	$0.17(0.05-0.35)$	28.5/28
nw_p04	$2.01(1.87-2.15)$	$0.15(0.06-0.27)$	54.5/44
nw_p05	$2.02(1.84-2.19)$	$0.31(0.16-0.53)$	72.6/44
nw_p07	$2.07(1.56-2.77)$	$0.33(<1.54)$	18.7/10
nw_p08	$2.57(2.15-3.06)$	$0.12(<0.45)$	67.1/44
nw_p09	$1.82(1.58-2.14)$	$0.00(<0.13)$	20.8/23
nw_p10	$2.10(1.92-2.28)$	$0.40(0.21-0.69)$	45.1/28
nw_p11	$2.21(2.01-2.45)$	$0.26(0.09-0.50)$	45.4/28
nw_p12	$2.38(2.20-2.54)$	$0.31(0.17-0.47)$	80.8/57
M87 NW	$2.57(2.48-2.67)$	$0.20(0.12-0.28)$	199.0/118
s_p01	$2.49(2.36-2.62)$	$0.24(0.13-0.36)$	56.9/57
s_p02	$2.05(1.90-2.20)$	$0.28(0.16-0.45)$	70.4/57
s_p03	$1.79(1.67-2.01)$	$0.14(0.05-0.28)$	71.2/57
s_p04	$2.46(2.05-2.92)$	$0.16(<0.53)$	33.2/28
s_p05	$3.14(2.71-3.58)$	$0.46(0.14-0.89)$	46.3/28
s_p06	$2.34(1.97-2.78)$	$0.25(<0.69)$	37.8/28
s_p07	$2.80(2.36-3.35)$	$0.65(0.21-1.36)$	46.1/28
s_p08	$1.80(1.51-2.26)$	$0.08(<0.44)$	40.1/28
s_p09	$3.17(2.46-3.90)$	$0.71(0.08-1.88)$	26.7/23
s_p10	$2.15(1.58-2.88)$	$1.42(0.17-14.92)$	9.2/10
s_p12	$1.30(1.00-1.66)$	$0.04(<0.28)$	16.3/23
s_p13	$1.79(1.54-2.18)$	$0.15(<0.51)$	32.8/23
s_p14	$1.33(1.00-1.78)$	$0.04(<0.28)$	32.2/23
s_p15	$1.07(0.75-1.38)$	$0.13(<0.99)$	15.5/19
s_p16	$2.17(1.42-3.11)$	1.10 (unconstrained)	14.31/10
s_p17	$1.34(1.17-2.12)$	$0.21(0.06-0.53)$	43.1/23

are consistent with those by pointing Ginga observation (Awaki et al. 1991), by ROSAT (Irwin & Sarazin 1996), and by ASCA (Matsushita 1997), which all report the temperature in the M49 region to be $\sim 1.0-1.9$ keV. We will analyze the temperature structure of these region in detail in the following section.

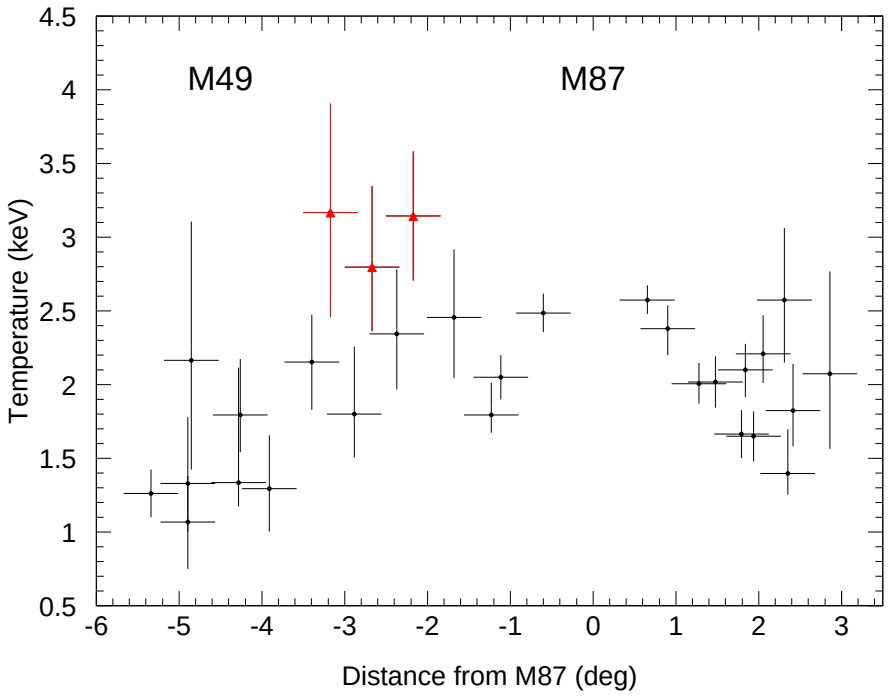

Figure 6.20: Temperature distribution for the entire regions of the Virgo from the spectral fitting in 0.7–8 keV band. Triangles show the positions s_p05, s_p07, and s_p09, which exhibit the hardest spectra (see section 6.5.

6.5 Hot Region between M87 and M49

In the previous section, we found a complex temperature structure in the south region of M87 by the hardness ratio analysis and the spectral fitting. In this section, we perform more detailed analysis for the middle region between M87 and M49, where an unusual high temperature is suggested. We will derive the temperature structure in more detail, and estimate systematic errors on the temperature caused by stray light and background uncertainty.

6.5.1 Angular Extent of the Hot Region

In section 6.4.2, we found unusually high temperatures in the regions s_p05, s_p07 and s_p09, as indicated by triangles in figure 6.20. All three regions show $kT > 2.8$ keV, higher than the surrounding regions. Important information is the spatial distribution of the hot region, which is useful to estimate the physical condition or origin of the region. It is difficult to estimate it, however, because the statistical errors on temperature become too large if we divide the regions into small cells. Since, as we have shown in 6.4.2, errors on the temperature in the middle region are $\sim 20\%$ when integrating the whole GIS field of view ($\sim 20'$ radius), they may increase to $\sim 70\%$ if we use the cell size of $10' \times 10'$.

Therefore, we can only estimate the rough shape and the angular extent of the hot region. First, we calculate the hardness ratio in the same way as in section 6.4.1, but use smaller cells of $10' \times 10'$. We then perform a Gaussian smoothing with $\sigma = 10'$ for the hardness map. Figure 6.21(a) shows the (2–7 keV) / (0.7–2 keV) hardness map thus obtained. To look at the deviation from the isothermal case, we also perform a simulation assuming isothermal emission with $kT = 2.0$ keV and $Z/Z_\odot = 0.2$ over the whole cluster with almost the same photon statistics with the actual data, and calculated the hardness ratio just in the same manner (figure 6.21(b)). The contour level of 0.42 and 0.56 roughly correspond to 2.0 keV and 3.0 keV, respectively, if we assume the R-S model spectrum with 0.2 solar abundance, modified by interstellar absorption with $N_{\rm H} = 2.0 \times 10^{20}$ cm^{-2}. The figure shows that the isothermal simulation exhibits almost flat distribution of the hardness in this region. On the other hand, the actual data indicates significant hardness variation with the highest hardness value > 0.6. This 'hot region' is extended in the north–south direction along the west side of the observed region: connecting s_p05, s_p07, and s_p09. On the contrary, the east side, s_p06, s_p08, and s_p10, exhibit softer spectra than in the west side.

Although we can not tell whether the hot region further extends towards west where no ASCA observation exists, it seems that the hot region is almost confined in s_p05, s_p07, and s_p09, and does not extend to the north of s_p05 or south of s_p09. We can point out that in these regions the elongated structure in the soft X-rays is seen in the ROSAT image, and the surface brightness in the west side (s_p05, s_p07, and s_p09) is slightly brighter than that in the east side (s_p06, s_p08, and s_p10) (see figure 6.1). Furthermore, the west region also shows some concentration in the galaxy distribution than the east (see figure 6.2).

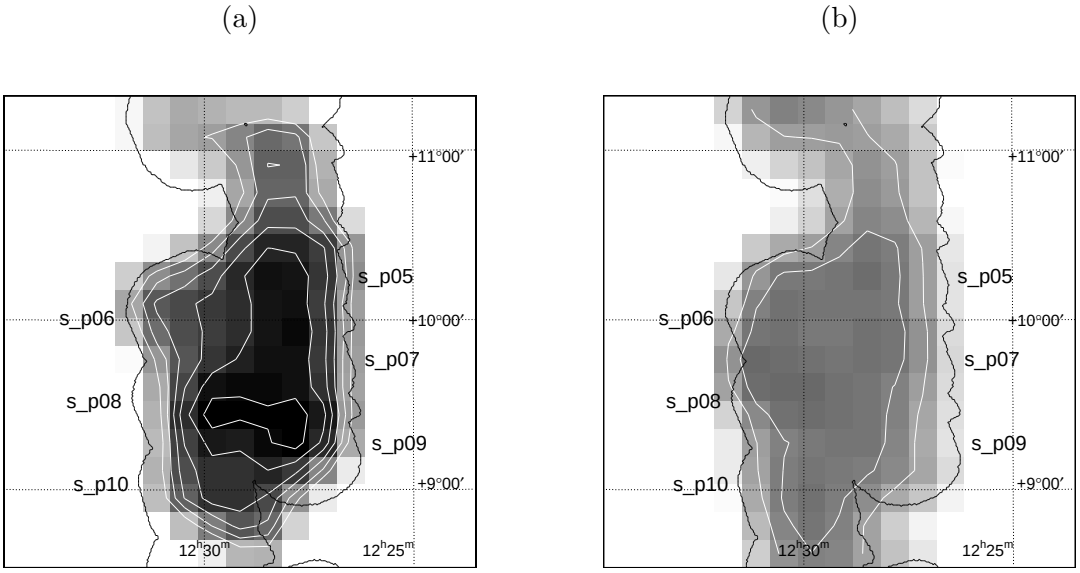

Figure 6.21: The two dimensional hardness ratio map at s_p05_07_09 and s_p06_08_10: (a) data, and (b) simulation for an isothermal case. The hardness ratio between 2–7 keV and 0.7–2 keV are calculated in each $10' \times 10'$ cell, and smoothed by a Gaussian with $\sigma = 10'$. The lowest contour level is 0.34, and the contour spacing is 0.5 for both (a) and (b). We assumed X-ray spectrum of the Virgo as $kT = 2.0$ keV and $Z/Z_\odot = 0.2$ solar for the simulation indicated in panel (b).

6.5.2 Spectral Fit above 2 keV

In the previous section, we investigated the angular extent of the hot region, and found that the hot region is mainly located on the west side of the observed region: s_p05, s_p07, and s_p09. To improve the statistics, we sum up the spectra of these regions: s_p05, s_p07 and s_p09 (hereafter s_p05_07_09). For comparison, we also combine the spectra of s_p06, s_p08 and s_p10 (hereafter s_p06_08_10), which are located just east of the s_p05_07_09. Both s_p05_07_09 and s_p06_08_10 are parallel to the 'emission bridge' between M87 and M49, and the distance from M87 and M49 is almost the same.

Before the fitting, we subtract the contaminating flux from the four bright sources as estimated in section 6.2.2. Figure 6.22 shows the spectra of s_p05_07_09 and s_p06_08_10, and the contaminating spectrum from the four sources.

Then we fit the X-ray spectra for each region in 0.7–8 keV band with a R-S model in the same manner as in section 6.4.2. We fix the interstellar absorption to 1.9×10^{20} cm^{-2} which is the average value of the Galactic column density for s_p05 – s_p10 (see table 6.1). Thus the free parameters are the plasma temperature, metal abundance, and normalization. Upper panels of figure 6.23 show the spectra of two regions and the best fit model of a R-S model, and lower panels show the ratio of the data to model. The best fit parameters from the R-S model for s_p05_07_09 and s_p06_08_10 are $kT = 3.1 \pm 0.4$ keV, $Z/Z_\odot = 0.66 \pm 0.38$, $\chi^2/\nu = 42.2/21$, and $kT = 2.0 \pm 0.3$

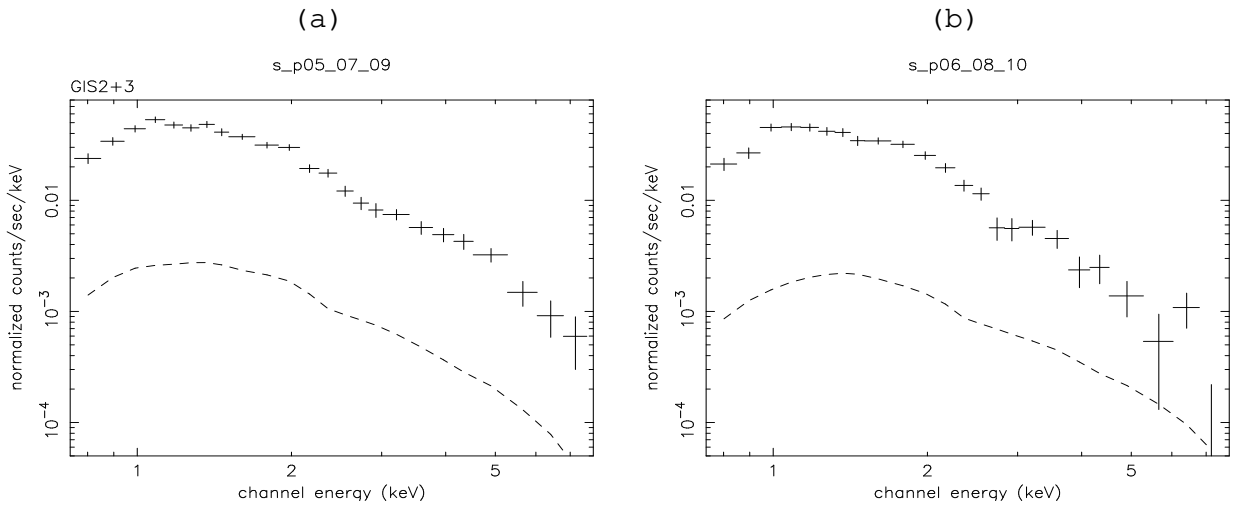

Figure 6.22: Cross shows CXB+NXB subtracted spectrum, and dashed line shows contaminating spectrum from four bright sources: (a) s_p05_07_09 (the hot region) and (b) s_p06_08_10.

keV, $Z/Z_{\odot} = 0.27 \pm 0.26$, $\chi^2/\nu = 30.5/21$, respectively. Thus the isothermal model gives a poor fit especially for the spectrum for s_p05_07_09. As shown in figure 6.23(a), we can see an excess emission above 4 keV, suggesting a high temperature component in s_p05_07_09.

The excess emission is also seen below 1 keV in both two regions, possibly due to the emission from the NPS. We, therefore, neglect the energy range below 2 keV, and try to quantify the ICM temperature in s_p05_07_09 and s_p06_08_10 with the hard-band data. Since the metal abundance is primarily determined by the Fe L lines for $kT \sim 2$ keV ICM, we can not constrain the abundance. Fixing the abundance to 0.2 solar, we carry out spectral fitting with a R-S model. Free parameters are the plasma temperature and normalization. Acceptable fits are obtained with $\chi^2/\nu = 10.3/11$ for s_p05_07_09, and $\chi^2/\nu = 13.0/11$ for s_p06_08_10. Figure 6.24 shows the confidence contours of temperature vs. emission measure (see equation 2.4). In calculating the emission measure, we assume the sky area (S in equation 2.3) to be 4×10^3 arcmin$^2 \approx 0.13$ kpc^2 which corresponds to the area covered either with s_p05_07_09 or s_p06_08_10. As shown in figure 6.24, the temperature difference between s_p05_07_09 and s_p06_08_10 is significant at more than 90% confidence. However, we have not yet included the systematic errors due to the ray-tracing and the background uncertainties. These systematics will be estimated in the next section.

If we fit the 0.7–8.0 keV spectra by a two-component (R-S model and thermal bremsstrahlung) model, the fit improves to $\chi^2/\nu = 21.0/19$ and $\chi^2/\nu = 26.5/19$ for s_p05_07_09 and s_p06_08_10, respectively. Figure 6.25 shows 0.7–8.0 keV spectra with the best fit models, and figure 6.26 shows confidence contours of R-S temperature vs. thermal bremsstrahlung temperature. The additional thermal bremsstrahlung component indicates the best fit value of $kT = 0.2 - 0.3$ keV with $F_{\mathrm{X},0.5-2} \sim 0.8 \times 10^{-15}$ ergs s^{-1} cm^{-2} arcmin^{-2} for both s_p05_07_09 and s_p06_08_10 spectra. Irwin & Sarazin (1996) reported that the temperature of the X-ray emission from the NPS around

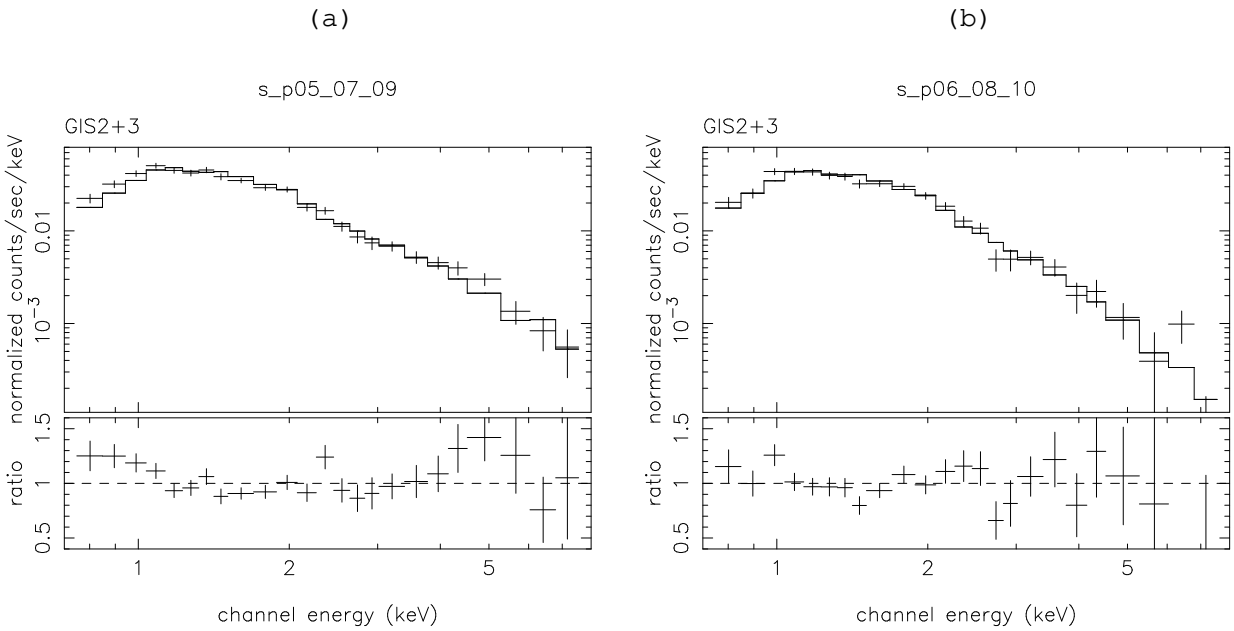

Figure 6.23: GIS spectra of (a) s_p05_07_09, and (b) s_p06_08_10. Upper panels show the spectra (data points) with the best fit single R-S model (line), and lower panels show ratio of the data to model.

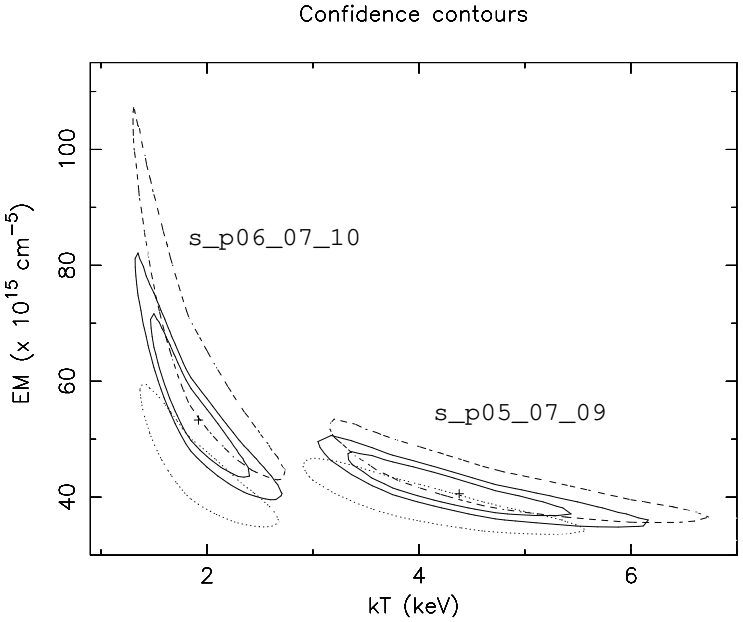

Figure 6.24: Confidence contours with single temperature R-S model for s_p05_07_09 and s_p06_08_10. Only the data above 2 keV are used. The heavy element abundances are fixed to 0.0 (dashed), 0.2 (solid), and 0.5 (dotted) solar. Two solid contours show 1σ and 90% confidence levels, and dashed and dotted ones show 90% confidence level.

M49 is ~ 0.15 keV (see table 6.5). If we estimate the X-ray flux from the NPS using the parameters listed in table 6.5, it becomes 0.63×10^{-15} ergs s^{-1} cm^{-2} arcmin^{-2} in 0.5–2 keV band. This is almost consistent with our result for the additional thermal bremsstrahlung component.

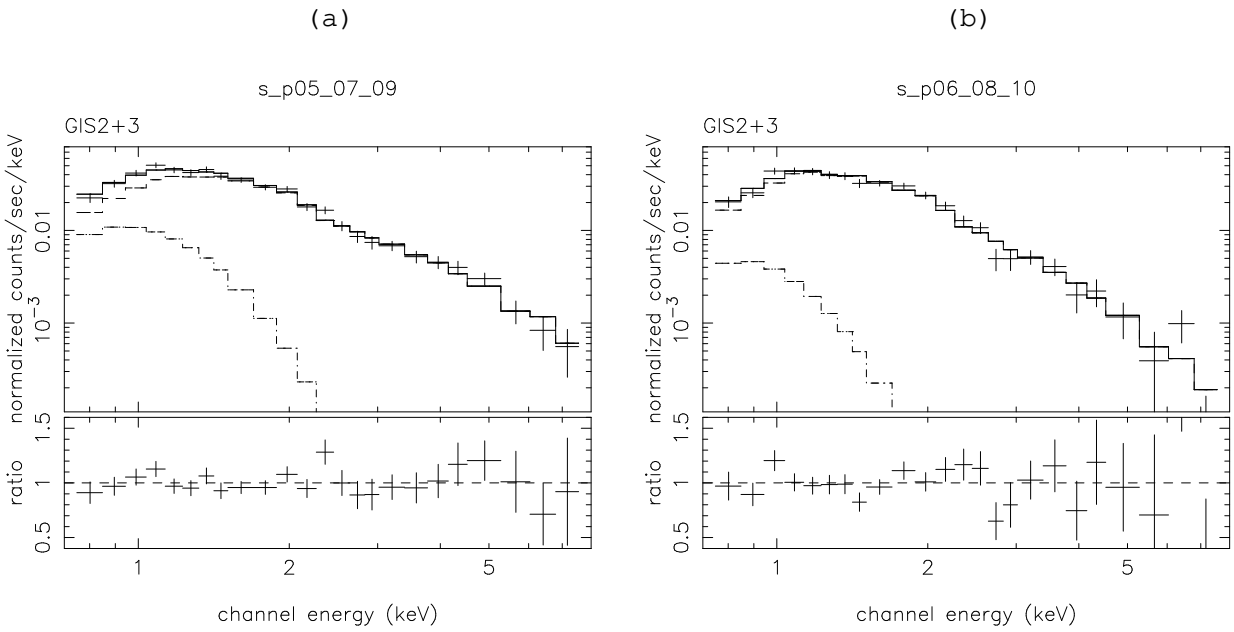

Figure 6.25: Fitting result by a two component (R-S and thermal bremsstrahlung) model; (a) s_p05_07_09, and (b) s_p06_08_10. Upper panels show the spectra (data points) with the best fit R-S model (dashed) and thermal bremsstrahlung model (dash-dotted). The sum of the two components is also indicated by solid lines. Lower panels show the ratio of data to the two component model.

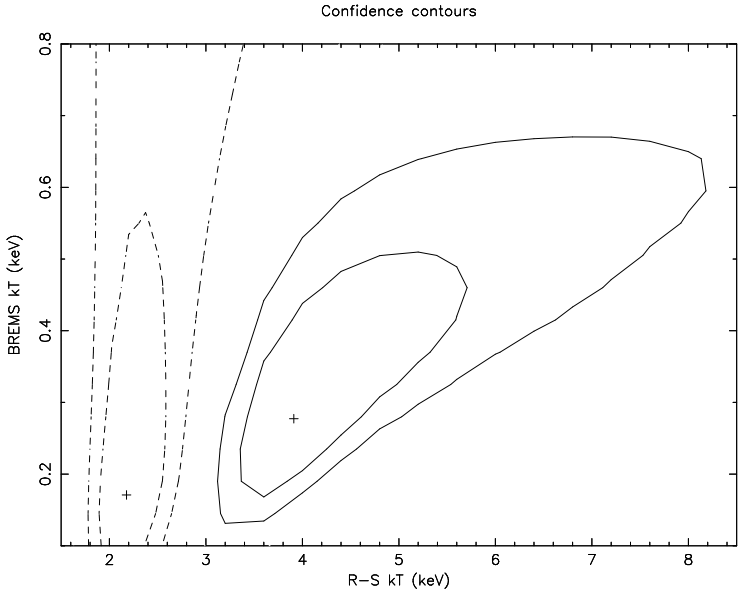

Figure 6.26: Confidence contours of R-S temperature vs. thermal bremsstrahlung temperature: s_p05_07_09 (solid) and s_p06_08_10 (dashed). 1σ and 90% confidence levels are shown.

6.5.3 Estimation of Systematic Errors on the Temperature

In this section, we estimate the following systematic errors on the temperatures, which are determined in the previous section.

a. Systematic errors due to the contaminating flux from the four bright sources:
We estimated the amount of the contaminating photons from the four bright sources (A1553, NGC 4325, A1541, and RX J1227.7+0841) by the ray-tracing method (section 6.2.2). We also estimated that the systematic error on the stray light contribution in the ray-tracing simulation was −30%–+10% (section 5.1.2). Based on this we calculate the error on the best fit temperature by changing the fraction of the contaminating flux from the four sources (see table 6.4) between −30% and +10%.

b. Systematic errors in the contaminating spectra:
We determined the spectral parameters for the four bright sources (section 6.2.2) with statistical errors. We calculate the systematic errors on the best fit temperatures by changing the contaminating spectra from the four sources between the 'softest' case and the 'hardest' case within the 90% error (see table 6.3). We also determined the source mask regions for detected source candidates (section 6.2.1), by defining the boundaries where the surface brightness due to the point source drops to less than at most 5% of the ICM level. This process leaves 5% of the total flux of the ICM not removed by the masks.

- The softest case for the contaminants: $kT_{\rm A1553} = 6.6$ keV, $kT_{\rm NGC4325} = 0.81$ keV, $kT_{\rm A1541} = 3.4$ keV, and $\Gamma_{\rm RXJ1227.7+0841} = 2.2$.
- The hardest case: $kT_{\rm A1553} = 8.2$ keV, $kT_{\rm NGC4325} = 0.88$ keV, $kT_{\rm A1541} = 4.8$ keV, $\Gamma_{\rm RXJ1227.7+0841} = 1.8$, and 5% of the total flux of the ICM level.

c. Systematic error due to the CXB fluctuation:
We calculated the best fit temperature when the CXB flux was changed by ±10% (see section 5.2.2).

d. Systematic error due to the NXB uncertainty:
We did the same analysis by changing the NXB flux by ±6% (see section 5.2.1).

In calculating the above systematic errors, we fitted the X-ray spectra for s_p05_07_09 and s_p06_08_10 in the 2–8 keV band with the R-S model. We fixed the interstellar absorption to 1.9×10^{20} cm^{-2}, thus the free parameters are the plasma temperature, metal abundance, and normalization. The result are summarized in table 6.7. We found that the temperature in s_p05_07_09 is still higher than that in s_p06_08_10 with more than 90% confidence.

Note that the temperature thus determined using the SimARF is an 'averaged' value, because this method assumes that the target has uniform spectral parameters (such as temperature and abundance). To obtain the true temperature, we have to know all spectral parameters in the

Table 6.7: The best fit temperature, statistical error, and systematic error for s_p05_07_09 and s_p06_08_10, determined from a R-S model fitting in 2–8 keV band

Region	Best fit temperature (keV)	Statistical error (keV)	Systematic error (keV)				
			a	b	c	d	total†
s_p05_07_09	4.38	$^{+1.60}_{-1.08}$	$^{+0.01}_{-0.02}$	$^{+0.02}_{-0.39}$	$^{+0.59}_{-0.71}$	$^{+0.14}_{-0.19}$	$^{+0.61}_{-0.83}$
s_p06_08_10	1.92	$^{+0.53}_{-0.41}$	$^{+0.02}_{-0.10}$	$^{+0.02}_{-0.27}$	$^{+0.49}_{-0.48}$	$^{+0.07}_{-0.17}$	$^{+0.50}_{-0.58}$

a–d: See section 6.5.
†: Total systematic error defined as $\sqrt{a^2+b^2+c^2+d^2}$.

surrounding regions, including the regions where ASCA has not observed, since the contaminating photons come from the even 1° offset. From the previous observation, it is known that the Virgo ICM has an average temperature of ~ 2 keV (e.g. Koyama et al. 1991; Böhringer et al. 1994) which is consistent with that of s_p06_08_10 determined above. We can assume that the hot region has a much smaller angular size than the 'cool' region where the temperature is ~ 2 keV, and consider that the hard spectrum of s_p05_07_09 is heavily contaminated by the stray light coming from the surrounding 'cool' regions. The temperature of s_p05_07_09 obtained above is, therefore, likely to be underestimated. To simplify the case, we consider that the regions surrounding s_p05_07_09 have a uniform temperature of 2 keV, and estimate the true temperature. Figure 6.27 shows confidence contours of the 'true' kT vs. emission measure for s_p05_07_09. We used the energy range of 2–8 keV, and subtracted the contaminating photons from the surrounding 2 keV regions. In this case, the best temperature of s_p05_07_09 rises up to 5.3 keV, and is allowed to be ~ 20 keV at 99% confidence. In chapter 7, we will again discuss the ICM temperature in the region s_p05_07_09.

So far, we have treated the hot emission to have a thermal spectrum. However, we could not distinguish the spectrum between thin thermal bremsstrahlung and non-thermal (power-law) from the spectral fitting. Indeed, hard X-ray ($kT \gtrsim 10$ keV) emission from galaxies and clusters of galaxies were reported from previous observations (e.g. Lea et al. 1981 for Virgo and A2142; Primini et al. 1981 for Perseus; Bazzano et al. 1991 for Coma; Canizares et al. 1987 and Matsushita et al. 1994 for early-type galaxies). In these cases, possibilities for non-thermal emission, such as by inverse Compton scatterings of the cosmic microwave background, collection of binary X-ray sources, or AGNs etc., have been suggested. If we fit the spectrum for the region s_p05_07_09 with a power-law model, we could obtain an acceptable result with $\chi^2/\nu = 9.9/11$. Figure 6.28 shows the confidence contours of the photon index vs. number of photons at 1 keV. We used the energy range of 2–8 keV, and the stray photons are subtracted assuming that the surrounding regions have a uniform temperature of 2 keV. Non-thermal emission will be discussed in section 7.1.6 in more detail.

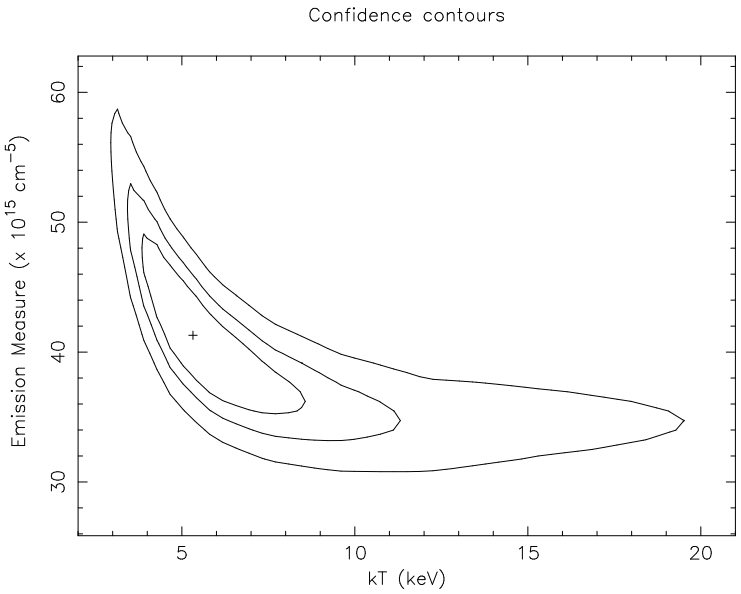

Figure 6.27: Confidence contours of the corrected kT vs. emission measure for s_p05_07_09. Each contour shows 1σ, 90%, and 99% confidence levels. Heavy element abundances are fixed to 0.2 solar. Isothermal emission of 2.0 keV is assumed for the surrounding region of the s_p05_07_09, and we subtracted stray photons from the surrounding region.

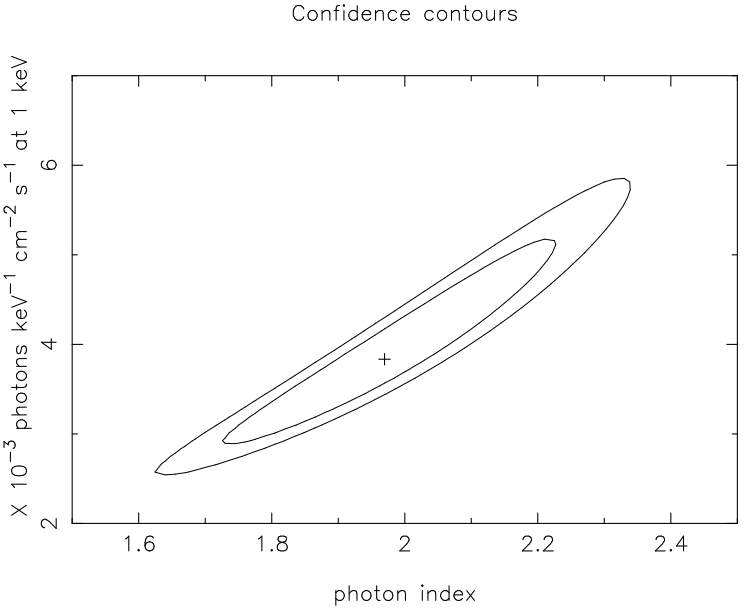

Figure 6.28: Confidence contours of the photon index vs. number of photons at 1 keV. Contours show 1σ and 90% confidence levels. We fitted the spectrum of the region s_p05_07_09 with a power-law model after subtracting the stray light from surrounding regions. We assumed that the temperature and heavy element abundances in the surrounding regions are 2.0 keV and 0.2 solar, respectively.

6.6 Temperature Distribution in the M49 Subcluster

In this section, we will derive temperature distribution around M49. Figure 6.29 shows the surface brightness distribution around M49 obtained with ASCA. Irwin & Sarazin (1996) found a bow shock shape at $\sim 4'$ north of M49 from the X-ray surface brightness obtained by ROSAT. We will look for an indication of the interaction between the M49 subcluster and the M87 subcluster based on the X-ray spectra obtained with ASCA.

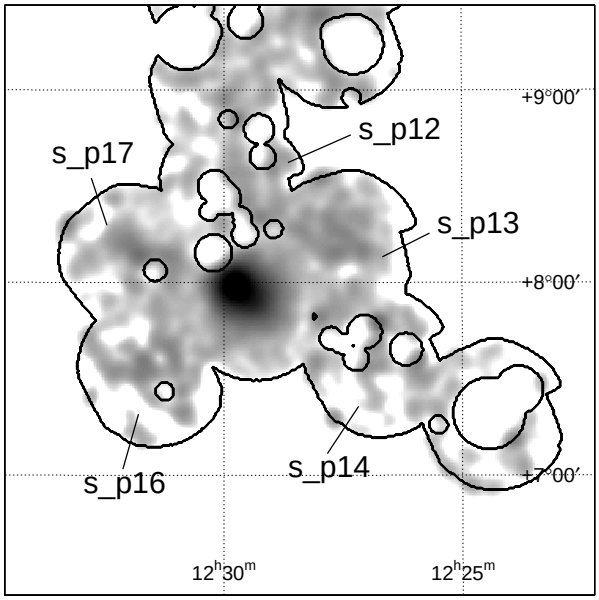

Figure 6.29: GIS image around M49 in 0.7–10 keV. The image is smoothed by a Gaussian with $\sigma = 2'$ after applying the source masks (see section 6.2.1).

6.6.1 Temperature and Abundance Distribution near M49

In this section, we analyze only two data sets pointed on M49 (M49 NW8.5 and M49 NW3.5 in table 6.2), and perform the spectral analysis for the combined GIS and SIS data. Since the observations of M49 were carried out in 1993, just after the launch, there is no degradation in the performance of SIS in these data.

ASCA observed the regions M49 NW8.5 and M49 NW3.5 with the the 4 CCD mode. We screened the SIS data with the nominal selection criteria in order to exclude the data affected by the South Atlantic Anomaly, Earth occultation, together with the exclusion of data taken in the regions of geomagnetic rigidity less than 6 GeV c^{-1}. We also excluded any data contaminated by the stray light from the bright Earth. The ARFs for the SIS are constructed by the SimARF method in the same way as for the GIS. The GIS data are screened by the flare-cut and H02-sorting method described in section 5.2.1.

After the above screenings, the GIS and SIS data are accumulated in eight regions as shown

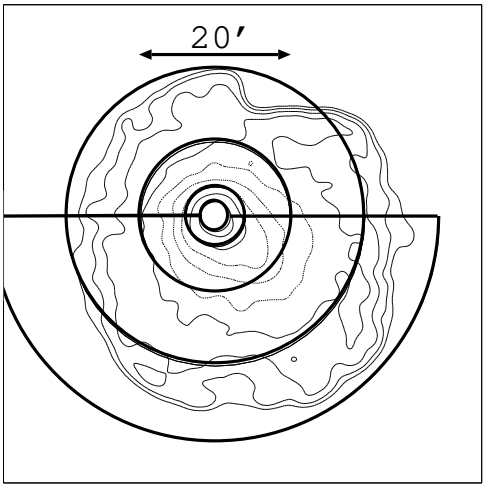

Figure 6.30: Integrating regions for M49. Contours show 0.7–10 keV GIS surface brightness smoothed by a Gaussian with $\sigma = 1'$.

(a) (b)

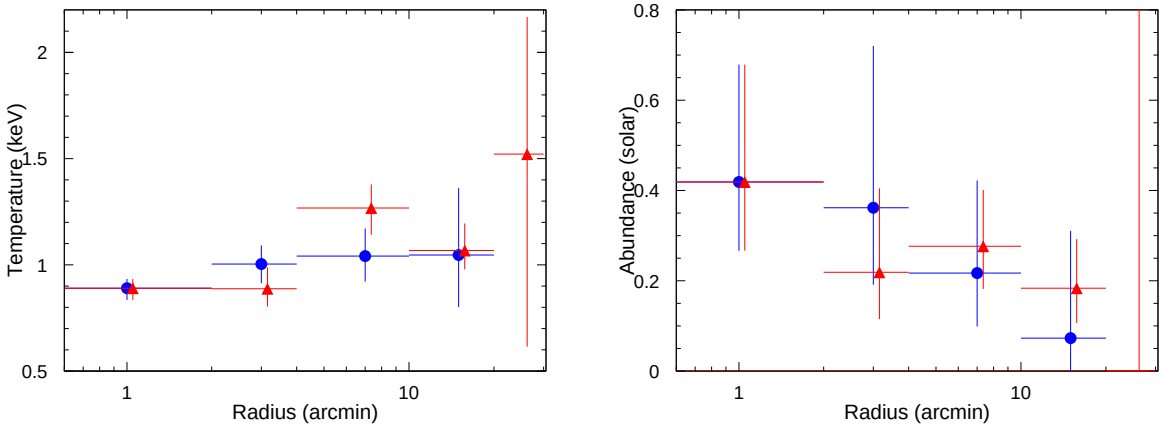

Figure 6.31: (a) Temperature and (b) heavy element abundance profiles for M49. Filled circles show the north region of M49, and filled triangles show the south region. Error bars indicate the single-parameter 90% confidence limits.

in figure 6.30: four concentric regions with $r = 0'$–$2'$, $2'$–$4'$, $4'$–10', and $10'$–$20'$. The three rings in $r = 2'$–$4'$, $4'$–10', and $10'$–$20'$ are also divided into north and south regions. We could obtain data in $r = 20'$–$30'$ only with GIS because of the small field of view of SIS. Then all GIS and SIS spectra in each region are fitted simultaneously. We neglect the energy range below 1.2 keV to avoid the soft X-ray emission from the NPS, although the X-ray flux in the inner regions ($\lesssim 15'$) of M49 are much higher than that from the NPS. Since hard X-rays from LMXBs are contained in the spectra of elliptical galaxies (Canizares et al. 1987; Matsushita et al. 1994),

we fitted the data with a double component model: the R-S model for the hot gas in M49 and the thermal bremsstrahlung model with the temperature fixed at 10 keV. The latter spectrum is known to be a good approximation to the LMXB spectra (Makishima et al. 1989; Matsushita et al. 1994). Interstellar absorption is fixed to the Galactic value as shown in table 6.1. Although an excess absorption is reported in the spectra for the central region (Irwin & Sarazin 1996; Matsushita 1997), it does not matter in our fit because the data below 1.2 keV are ignored. Thus, free parameters are temperature, metal abundance, normalization of the R-S component, and normalization of the bremsstrahlung model.

The obtained temperature and abundance of the R-S component are plotted in figure 6.31. We can not find any significant difference in the profiles between the north and the south regions. Both regions show temperature increase and abundance decrease toward the outer region. These are almost consistent with azimuthal-averaged temperature and abundance profiles obtained by Irwin & Sarazin (1996) and Matsushita (1997).

In this analysis, we did not correct the contaminating photons from the near-by regions caused by the extended tail of the PSF. Figure 6.32 shows relative fractions of the contaminating flux from the other concentric regions compared with the region's own emission for each ring, calculated from the ray-tracing simulation. In particular, the bright inner regions cause significant effect to outer regions. This means that the 'true' gradient of the temperature and abundance gradient should be steeper than the feature shown in figure 6.31.

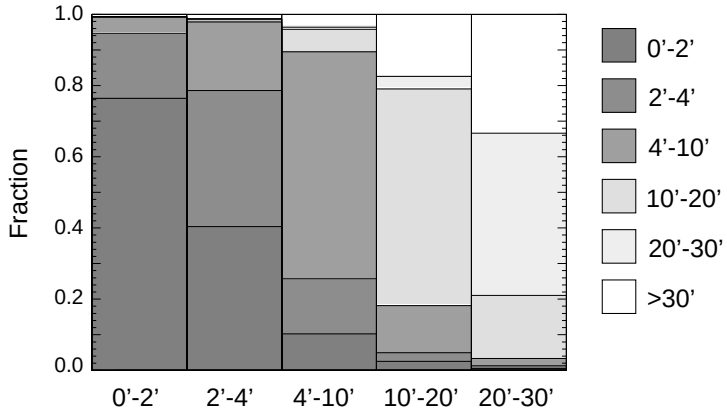

Figure 6.32: Simulation result of the contaminating flux from the annular sky regions to individual regions observed with the GIS. The horizontal axis shows the radius ranges of the GIS data, and the vertical axis shows the fraction of photons originated in different sky regions. We assumed that M49 has a uniform temperature and abundance of $kT = 1.0$ keV and $Z/Z_{\odot} = 0.5$, respectively.

6.6.2 Large Scale Temperature Distribution

In the next, we derive the temperature around M49: i.e. for the regions s_p12, s_p13, s_p14, s_p16, and s_p17 (see figure 6.29). In this section, we again use only the GIS data.

Before the fitting, we subtract the contaminating flux from the four bright sources from the

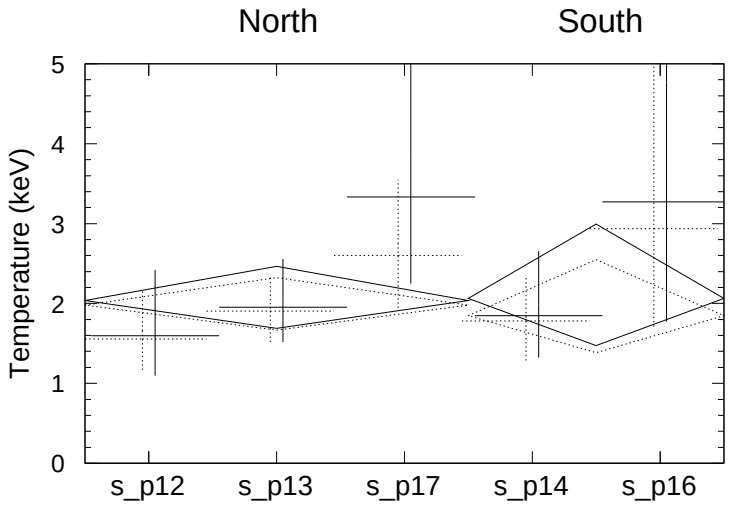

Figure 6.33: Temperatures for the regions s_p12, s_p13, s_p14, s_p16, and s_p17. The dotted/solid lines show the fitting results before/after subtracting the emission from $r < 20'$ region of M49. Errors show the single-parameter 90% confidence region.

data in s_p12 and s_p13, as estimated in section 6.2.2. Then we fitted the data with a R-S model. In this case, we did not introduce the 10 keV thermal bremsstrahlung model. The spectral fits with the two component R-S and the bremsstrahlung model indicate that the normalization of the bremsstrahlung component becomes zero or much smaller than the R-S component. We also neglected the energy range below 1.2 keV in the same way as in the previous section. Interstellar absorption is fixed to the Galactic value, then free parameters are temperature, metal abundance, and normalization. The results are plotted by dotted lines in figure 6.31.

The data in these regions are significantly contaminated by photons coming from M49. To estimate the fraction of the contaminating photons, we again carried out the ray-tracing simulation assuming $kT = 1.0$ keV and $Z/Z_{\odot} = 0.5$ for the spectrum of M49. Figure 6.34 shows relative fractions of the emission from the observed sky region (bar chart), contribution from M49 within $20'$ radius (circles) for each region. We found that half of the photons come from the pointed sky, and $\sim 20\%$ come from M49 within $20'$ for each region. Based on this simulation, we subtracted the contaminating photons from M49 for each region, and again fitted the spectra. The results are plotted by the solid lines in figure 6.33.

As the result, we found that the temperatures in these regions are almost constant with the average value of ~ 2 keV, which is consistent with that in the Virgo ICM. Although about 20% of the total photons should come from the extended ICM for each region, these contamination may not change the obtained temperatures significantly. Thus we can conclude that no significant temperature increase, such as that seen in the middle region between M87 and M49, exists either in the north or south direction of M49. Figure 6.35 shows the same results as in figure 6.31(a) and 6.33, but plotted as a function of distance from M49. It is interesting to point out that the

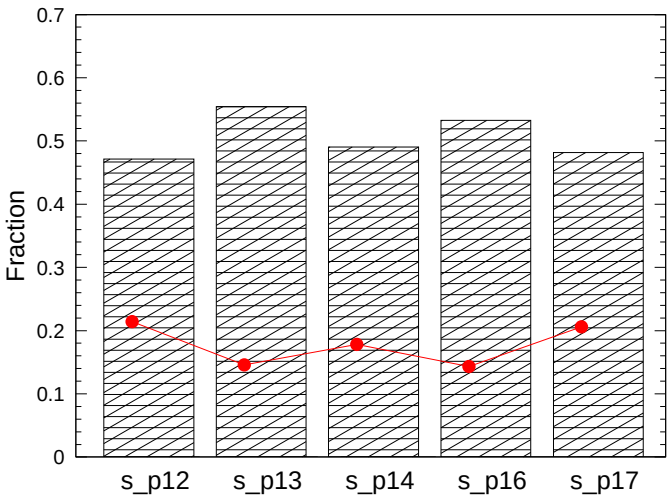

Figure 6.34: Relative fraction of the emission around M49: fraction of the emission from the integrated region (bar chart), and emission from the M49 within 20′ radius (filled circles). We assume the temperature and metal abundance around M49 are 1.0 keV and 0.5 solar. We use the surface brightness model made from the RASS data described in section 6.3.

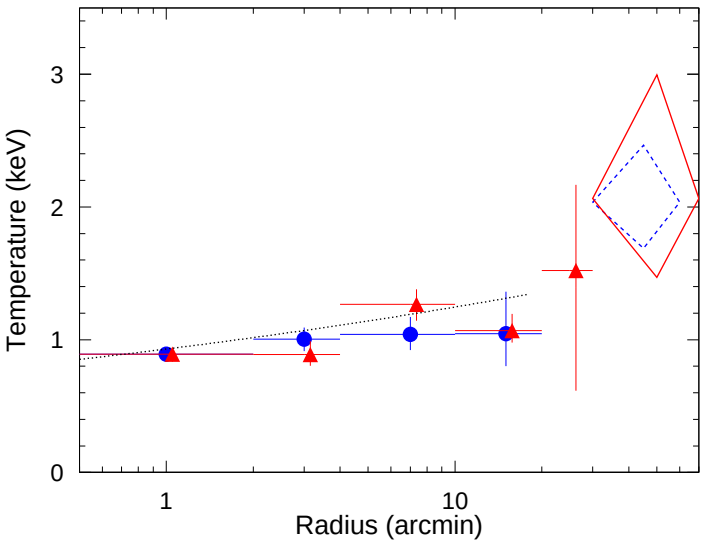

Figure 6.35: Combined plot of the temperature profile around M49 subcluster. Filled triangles and solid diamond indicate the temperature in the north direction from M49, and filled circles and dashed diamond are for the south regions. Errors show the 90% confidence limits. Dotted line is a function $T(r) = 0.93(r/\mathrm{arcmin})^{0.127}$ keV, showing the azimuthal average of the temperature obtained with ROSAT (Irwin & Sarazin 1996).

temperature rises to the south of M49 as shown in figure 6.35. This is a clear evidence that the hot ICM of the Virgo cluster is enshrouding the cool ISM of M49. In other words, the territory of the Virgo cluster is extended further south of M49, and the hot gas down there is heated with the cluster potential.

6.7 Summary of the Results

We have analyzed the ASCA data of the Virgo cluster of galaxies, with appropriate reference to the ROSAT data when detailed morphological information was needed. Based on the imaging and spectroscopic capability of ASCA, we successfully excluded the contaminating sources other than the ICM, and derived the temperature distribution in the Virgo cluster. We summarize our results concerning the south region of the Virgo cluster of galaxies.

1. We have revealed a significant temperature variation in the south region of the Virgo cluster in comparison with the northwest region based on the hardness ratio analysis (figure 6.18 and 6.19 in section 6.4.1) and the spectral fitting (figure 6.20 in section 6.4.2).

2. In the region between M87 and M49 on the X-ray "bridge", the west side of the ASCA observed region (s_p05_07_09) exhibits a temperature $\gtrsim 4$ keV, which is higher by $\gtrsim 2$ keV than that in the east side (s_p06_08_10) (figure 6.21 and table 6.7 in section 6.5). Since the average temperature of the Virgo cluster reported from the previous observations is consistent with that in the region s_p06_08_10 (~ 2 keV), we can assume that the hot region should have a small angular extent and is surrounded by the ~ 2 keV component.

3. We also found that temperature at $\sim 30' - 60'$ from M49 is the about 2 keV in both north and south directions. (figure 6.33 and 6.35 in section 6.6). This fact also supports the above estimation on the angular extent of the hot region.

Chapter 7

Discussion

The results on the temperature structure of the ICM provide important clues in considering the dynamical evolution of clusters of galaxies. In the following sections, we perform quantitative discussion about the physical condition of the hot component which has been discovered with the present observations, assuming a simple geometrical model for the X-ray "bridge" between M87 and M49.

7.1 Physical Conditions of the Hot Component

7.1.1 Geometrical Assumption

Observations of clusters of galaxies from the Earth give only the projected surface brightness on the sky. We usually assume spherically symmetric distribution for the ICM of the clusters, such as applying the β model approximation. However, the Virgo cluster has an irregular shape, suggesting that it is not a relaxed system. Furthermore, recent optical observations reveal that the spiral galaxies in the Virgo cluster distribute along a large-scale filament, which extends from 10 to 30 Mpc almost in the line of sight (Fukugita et al. 1993; Yasuda et al. 1997). Thus, the assumption of a spherical symmetry is not appropriate in our interpretation.

In the following discussion, we will approximate the geometry of the hot gas containing the hard region as shown in figure 7.1. We assume that the region s_p05_07_09 is surrounded by the 'cool' gas. The gas in the directions of both s_p05_07_09 and s_p06_08_10 has the same line-of-sight depth of d, and the hot component included in s_p05_07_09 has a line-of-sight depth of αd ($0 < \alpha \leq 1$). Physical parameters, such as temperature, abundance, and density, in both 'cool' and 'hot' regions are assumed to be uniform. In this assumption, d represents a sort of 'effective' depth of the X-ray emitting volume. We further assume that the hot component occupies the projected area just covered in s_p05_07_09. The direction s_p05_07_09, therefore, contains both hot and cool components.

This geometry is quite simple and considered to be appropriate because both regions s_p05_07_09 and s_p06_08_10 occupy small angular sizes in comparison with the whole scale of the Virgo: the

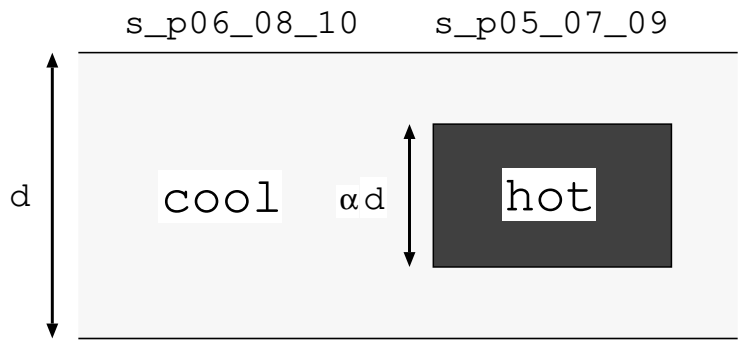

Figure 7.1: Schematic view of s_p05_07_09 and s_p06_08_10.

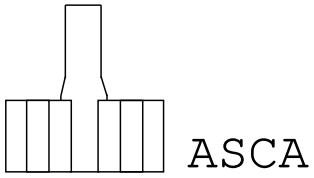

X-ray surface brightness changes by only less than a factor of 2 in each region. Moreover, the hot region which appears in the direction of s_p05_07_09 should occupy a quite small part of the cluster, because previous Ginga and ROSAT observations reported $\sim$ 2 keV as the global ICM temperature of the Virgo cluster. Since we cannot separate the hot and cool components contained in s_p05_07_09 by the surface brightness distribution, we assume that both components have the same projected shape; namely we use an identical ARF, made by the SimARF method using the ROSAT surface brightness in the spectral fitting of the hot and cool components in s_p05_07_09. Note that the obtained temperature changes by less than 10% even if we use an ARF for a uniformly extended source as the hot component.

Each component is designated with the suffix either hot or cool in the following discussion. Parameters of the cool component in the direction s_p06_08_10 is specified with the suffix s_p06_08_10.

7.1.2 Emission Measure

In this section, we constrain the gas density and volume of the hot and cool components using the spectral information. Since the angular extent of the hot component is defined by the ASCA observation, we can express the constraint in terms of emission measure (equation 2.4) based on the geometrical assumption introduced in the previous section.

The projected area on the sky for the cool and hot components in the direction s_p05_07_09 is estimated from our analysis as

$$S_{\rm s_p06_08_10} \approx S_{\rm cool} \approx S_{\rm hot} \approx 4 \times 10^3 \ {\rm arcmin}^2. \tag{7.1}$$

The emission measure (equation 2.4) for each component is obtained as

$$EM_{\rm s_p06_08_10} = n_{\rm cool}^2 \, d, \tag{7.2}$$

$$EM_{\rm cool} = n_{\rm cool}^2 \, (1-\alpha) d, \tag{7.3}$$

$$EM_{\rm hot} = n_{\rm hot}^2 \, \alpha d. \tag{7.4}$$

Then we performed spectral fitting with two component (hot and cool) R-S models in the 1.2–8.0 keV band where the emission from the NPS is negligible. The temperature of the cool component ($kT_{\rm cool}$) is fixed to 1.2, 2.0, or 2.7 keV, which are the confidence limits and the best-fit value for the temperature derived for the data in s_p06_08_10 (table 6.7). Contaminating photons coming from outside of s_p05_07_09 are subtracted assuming that the surrounding region has uniform temperature of $kT_{\rm cool}$. We also fixed heavy element abundances to 0.2 solar for both hot and cool emission, assuming a common interstellar absorption at 1.9×10^{20} cm^{-2}. So the free parameters are temperature of the hot component ($kT_{\rm hot}$), normalization of the hot component ($\propto EM_{\rm hot}$), and normalization of the cool component ($\propto EM_{\rm cool}$).

Figure 7.2(a), (c), and (d) show confidence contours in the parameter spaces of $kT_{\rm hot}$ vs. $EM_{\rm hot}$, $kT_{\rm hot}$ vs. $EM_{\rm cool}$, and $kT_{\rm hot}$ vs. $EM_{\rm cool}/EM_{\rm hot}$, based on the analysis in the previous chapter. The contours indicate the cases with fixed cool-component temperatures: $kT_{\rm cool} = 1.2, 2.0$, and 2.6 keV. We also show the effect of the uncertainty in the contaminating flux from the surrounding cool region by changing its level between -30% and $+10\%$. The lower limit of $EM_{\rm hot}$ and the upper limit of $EM_{\rm cool}$ can be determined. Figure 7.2(b) shows the relations for various constant fluxes of hot component plotted on the $kT_{\rm hot}$ vs. $EM_{\rm hot}$ plane. Figure 7.2(a) shows the allowed regions based on the spectral fit in the same plane. Therefore, by comparing (a) and (b), we can estimate that the hot component has a 2–10 keV flux of $3 \sim 12 \times 10^{-12}$ erg s^{-1} cm^{-2} at a 90% confidence ($L_{\rm x} \sim 1 - 6 \times 10^{41}$ ergs s^{-1}, assuming a distance of 20 Mpc).

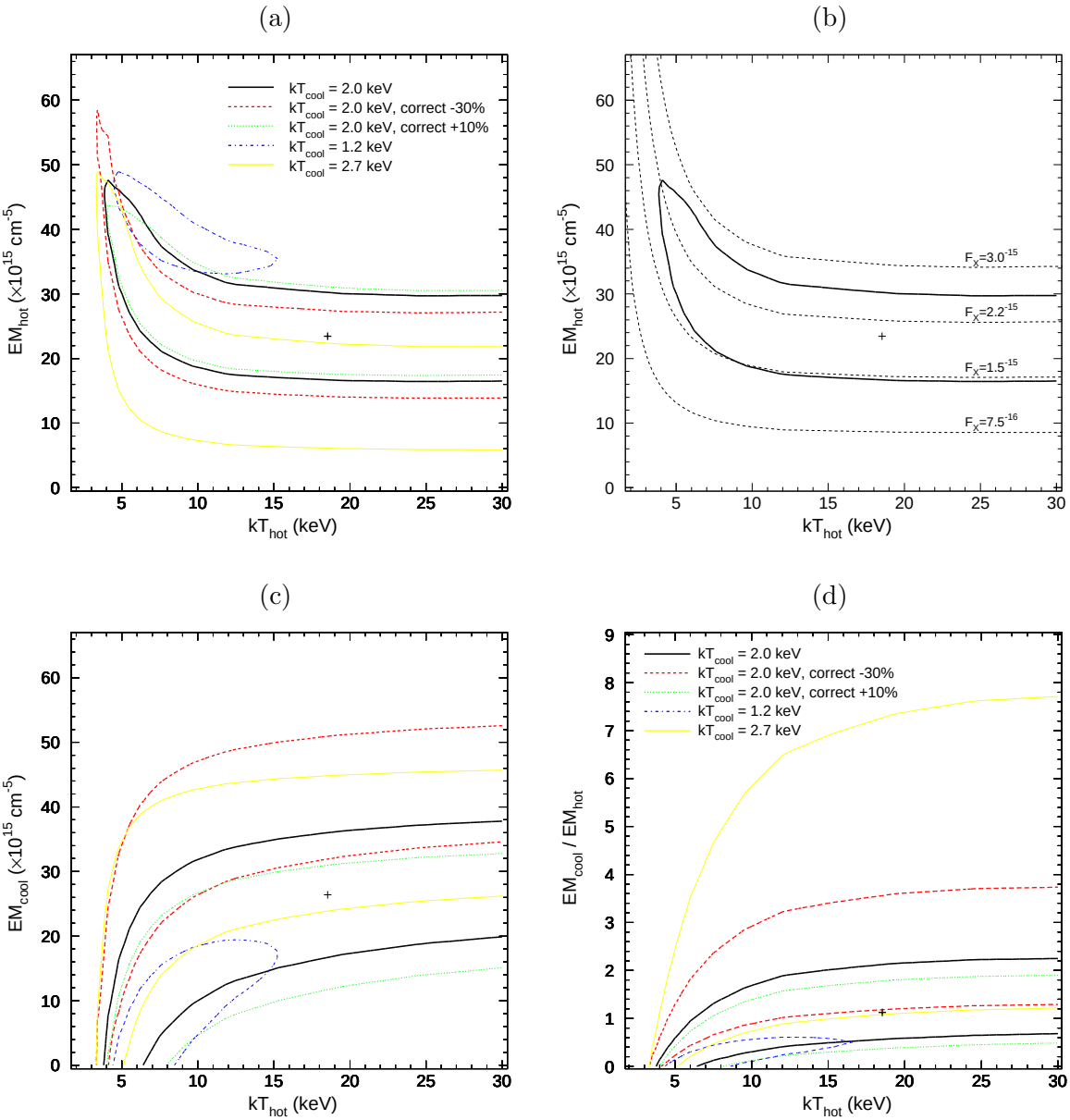

Figure 7.2: Confidence contours for various sets of parameters: (a) $kT_{\rm hot}$ vs. $EM_{\rm hot}$, (c) $kT_{\rm hot}$ vs. $EM_{\rm cool}$, and (d) $kT_{\rm hot}$ vs. $EM_{\rm cool}/EM_{\rm hot}$. Each contour shows the 90% confidence level. In all panels, the contours indicate the cases for $kT_{\rm cool} = 1.2, 2.0, 2.6$ keV with different lines. We also indicate the confidence contours when the contaminating flux from the surrounding cool region is varied between -30% and $+10\%$, corresponding to the systematic error in the ray-tracing code. In the panel (b), relations given by constant X-ray fluxes of hot region in ergs s^{-1} cm^{-2} arcmin^{-2} are also shown.

7.1.3 Density and Line-of-Sight Depth

Using the equation 7.2, 7.3, and 7.4, we can estimate the relation between the gas density and the line-of-sight depth of the cool and hot components. The allowed range of the emission measure can be determined from the figures 6.24, 7.2(a), and (c). The constraint on the emission measure immediately gives a relation between the gas density and the depth of the emission region. Figures 7.3(a), (b), and (c) show allowed regions on the density vs. line-of-sight depth plane for the cool component in the region s_p06_08_10 (a), for the hot component in s_p05_07_09 (b), and for the cool component in s_p05_07_09 (c), respectively. To estimate the line-of-sight depth d, we tentatively assume that the gas has a spherically symmetric distribution around the cluster center. Integrating the density along the line-of-sight, by an analogy with the equation 2.49, we can obtain the column density of the gas, expressed with an average gas density $\overline{n}_{\rm g}$ multiplied by the effective line-of-sight depth $d_{\rm eff}$;

$$\int_r^{R\rm max} \frac{2R\, n_{\rm g}(R)\, dR}{\sqrt{R^2 - r^2}} \equiv \overline{n}_{\rm g}\, d_{\rm eff} \tag{7.5}$$

where $n_{\rm g}$ is the gas density, R is the three-dimensional distance from the cluster center, $R_{\rm max}$ is the effective boundary of the cluster, and r is the projected radius, respectively.

To constrain the geometry of the emission region, we will further assume that $n_{\rm g}$ obeys the β model. Böhringer et al. (1994) shows that β and the core radius for the Virgo cluster are $\beta = 0.45$ and $R_{\rm c} = 2'.3$, respectively, and Matsumoto (1998) derives the central density of the Virgo ICM to be $\sim 3.0 \times 10^{-2}$ cm^{-3}. Assuming these β model parameters and a cut-off radius $R_{\rm max} = 5{\rm Mpc} = 860'$, we can obtain the column density at $r = 172'$, i.e. at the position of s_p08, to be $\overline{n}_{\rm g}\, d_{\rm eff} = 0.16$ cm^{-3} kpc. If we may simply assume $d_{\rm eff} \approx d$, we can plot the constraint given by this column density on the density vs. line-of-sight depth relation for the region s_p06_08_10 [figure 7.3(a)]. This additional constraint from the β model assumption is indicated with a dotted line. Taking the cross points in this plot, the line-of-sight depth is estimated as $d \sim 1$ Mpc. Although the density is ~ 10 times lower than that in the center of the Virgo cluster, it is dense enough to achieve an equilibrium between electrons and protons in the Hubble time. Note that this β model approximation is a very crude one. As mentioned earlier, the X-ray morphology of the south region is very extended like a bridge, and there is no way that the whole Virgo cluster can be approximated by a single β model. The above values should, therefore, be regarded as an order-of-magnitude estimation.

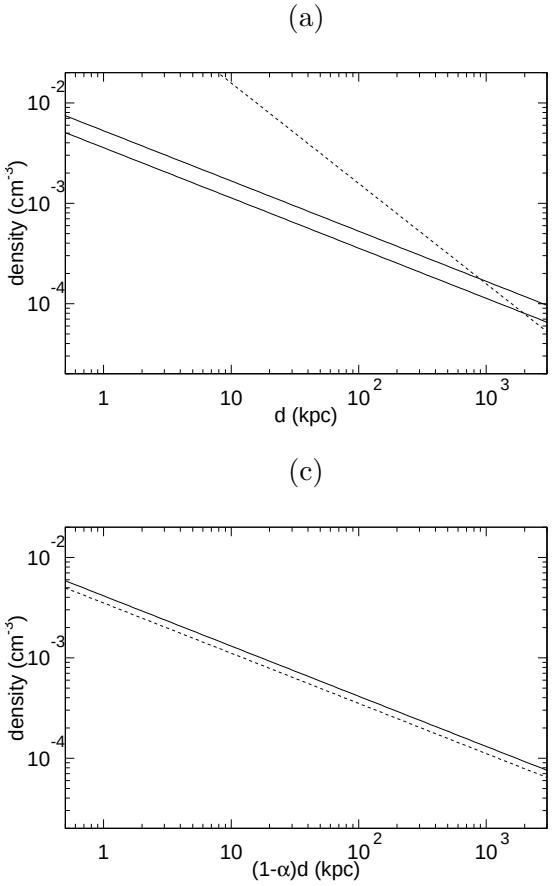

Figure 7.3: Allowed regions of the gas density shown as a function of the line-of-sight depth for (a) the cool component in the region s_p06_08_10, (b) the hot component in s_p05_07_09, and (c) the cool component in s_p05_07_09. Calculations are based on the equations 7.2, 7.3, and 7.4. Solid lines indicate the 90% confidence range in (a) and (b), and the upper limit in (c). Dashed line in (a) shows the density profile derived from the β model assumption (see section 7.1.3). Dashed lines in (b) and (c) indicate the density profile in the case of $kT_{\rm cool} = 2.0$ keV.

7.1.4 Internal Thermal Energy of the Hot Region

In this section, we estimate the internal thermal energy in the hot component, which is excesses of that in the surrounding cool region. The thermal energy can be expressed as

$$E_{\rm th} = V_{\rm hot}\, n_{\rm hot}\, kT_{\rm hot}, \tag{7.6}$$

where $V_{\rm hot}$ is the total volume of the hot component. We may combine this with the equation 7.4 to obtain

$$E_{\rm th} = S_{\rm hot}\, (EM_{\rm hot}\, \alpha d)^{1/2}\, kT_{\rm hot}. \tag{7.7}$$

We can constrain $E_{\rm th}$ by comparing the error regions of $EM_{\rm hot}$ shown in figure 7.2(a). Since we now assume $S_{\rm hot} \approx 4 \times 10^3$ arcmin^2 (i.e. we regard that the hot component is confined in the region s_p05_07_09), we may underestimate $E_{\rm th}$ if the hot component is more extended than the ASCA observed region. However, our estimation on the angular extent of the hot region may be correct within a factor of a few, as discussed in section 7.1.1.

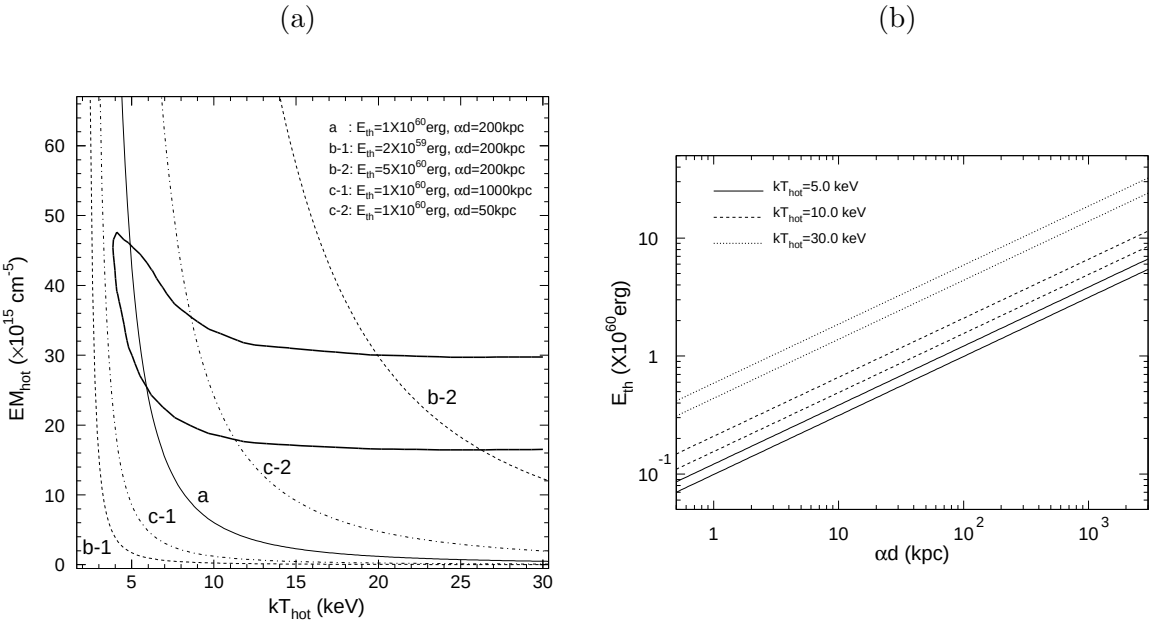

Figure 7.4: (a) Relations given by various values of $E_{\rm th}$ (the internal thermal energy of the hot component) are shown on the $kT_{\rm hot}$ vs. $EM_{\rm hot}$ plane calculated from the equation 7.7. The $kT_{\rm cool}$ is fixed to 2.0 keV, and other parameters for each line (a, b-1, b-2, c-1, and c-2) are indicated at the upper right in the panel. The thick line shows the 90% confidence contour as shown in figure 7.2(a). (b) $E_{\rm th}$ plotted as a function of αd (the line-of-sight depth of the hot component). Lines show 90% confidence range for various values of $kT_{\rm hot}$, calculated from the relation in figure (a). The $kT_{\rm cool}$ value is again fixed to 2.0 keV.

Figure 7.4(a) shows the $kT_{\rm hot}$ vs. $EM_{\rm hot}$ relation for various values of $E_{\rm th}$ with αd also fixed to certain values. The allowed region (thick solid line) on this diagram, determined from the spectral data, indicates the possible range of $E_{\rm th}$. To express the constraint on $E_{\rm th}$ more directly, figure 7.4(b) shows allowed regions of $E_{\rm th}$ as a function of αd for different values of $kT_{\rm hot}$.

For a crude estimation, the line-of-sight depth αd can be assumed to be the same as the projected width of the region: $\sim$ 100 kpc. Figures 7.4(a) and (b) indicate that the internal energy of the hot component is an order of 10^{60} ergs and proportional to the hot component temperature $kT_{\rm hot}$. This energy is comparable to the kinetic energy of a typical galaxy having a mass of $10^{11} M_{\odot}$ moving with a velocity of 1000 km s^{-1}.

7.1.5 Pressure Balance

Since the sound crossing time across ~ 300 kpc is less than 1 Gyr, it is reasonable to assume that the pressure balance is achieved between the hot and cool components in the direction s_p05_07_09,

$$n_{\rm hot} T_{\rm hot} = n_{\rm cool} T_{\rm cool}. \tag{7.8}$$

With equations 7.3 and 7.4, we can express α as

$$\alpha = \left[1 + \frac{EM_{\rm cool}}{EM_{\rm hot}} \left(\frac{kT_{\rm cool}}{kT_{\rm hot}} \right)^2 \right]^{-1}. \tag{7.9}$$

This relation can be used to restrict the α value from the allowed region shown in figure 7.2(d). Figure 7.5(a) shows the $EM_{\rm cool}/EM_{\rm hot}$ vs. $kT_{\rm hot}$ relation for fixed α values, given by the above equation. Figure 7.5(b) also shows the confidence region in the $\alpha - kT_{\rm hot}$ plane for different values of $kT_{\rm cool}$. Thus we can determine the lower limit of α to be ~ 0.6. This estimation suggests that the hot component occupies a large fraction in the depth.

(a) (b)

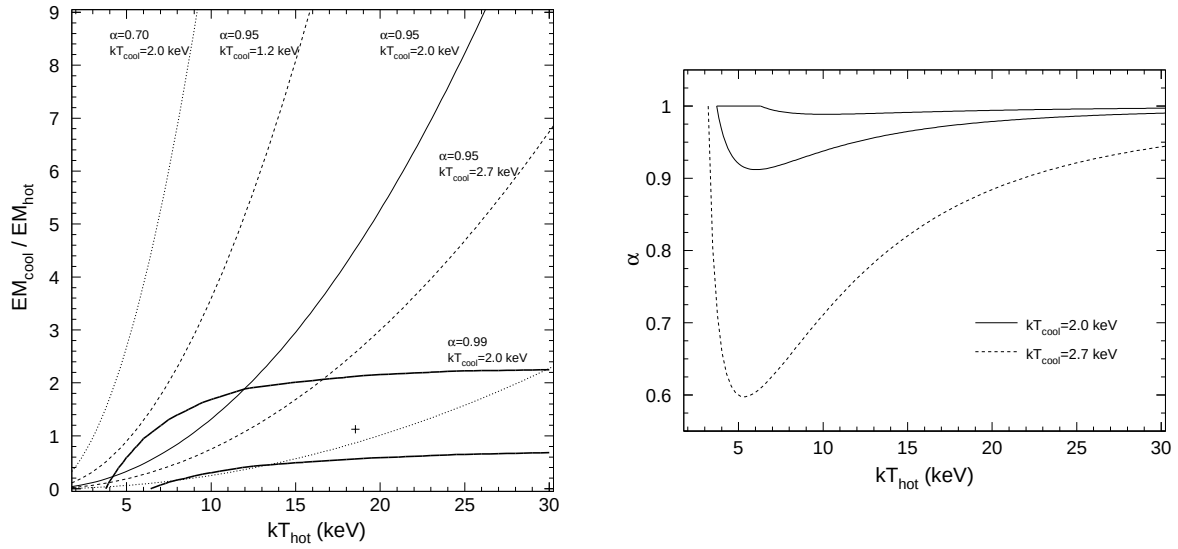

Figure 7.5: (a) Curves show relations with fixed α values plotted on the $EM_{\rm cool}/EM_{\rm cool}$ vs. $kT_{\rm hot}$ plane calculated from the equation 7.9. (b) Solid lines show 90% confidence range plotted in the $\alpha - kT_{\rm hot}$ plane assuming $kT_{\rm cool} = 2.0$ keV. This is the same confidence region shown in (a), and dashed line shows 90% lower limit assuming $kT_{\rm cool} = 2.7$ keV.

7.1.6 Non-thermal Emission

There is a possibility that the hot component has a power-law spectrum, since no significant Fe-K emission line is seen, and the data cannot constrain the thermal or non-thermal nature of the emission. Previous observations have detected hard X-ray ($E \gtrsim 10$ keV) emission from several clusters of galaxies (e.g. Lea et al. 1981 for Virgo and A2142; Primini et al. 1981 for Perseus; Fusco-Femiano et al. 1991 for Coma; Kaastra et al. 1999 for A2199; Canizares et al. 1987 and Matsushita et al. 1994 for early-type galaxies). Theoretically, existence of non-thermal emission in clusters has been suggested, probably produced by inverse Compton scattering of the cosmic microwave background by relativistic electrons, or by non-thermal bremsstrahlung emission due to suprathermal electrons, as shown in section 2.2.6. We, therefore, fit the spectrum for the s_p05_07_09 region with a R-S (for the cool component) and power-law models (for the hot component), and obtained an acceptable fit. Figure 7.6 shows the confidence contour for the photon index against normalization (number of photons at 1 keV) for the hot component. The luminosity of the power-law component is about 4×10^{41} ergs s^{-1} in 2–10 keV.

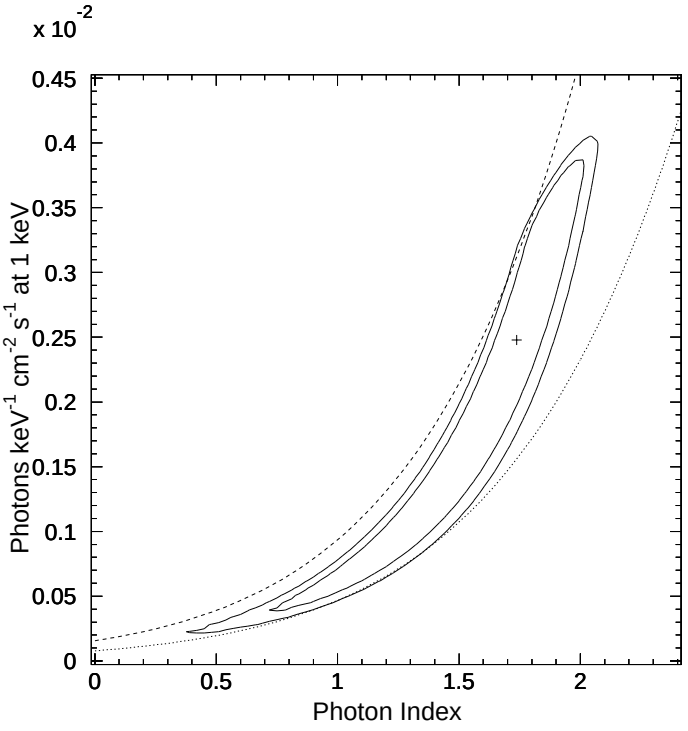

Figure 7.6: Confidence contours of the photon index vs. number of photons at 1 keV for the hot component. Contours show 1σ and 90% confidence levels. The spectrum for the region s_p05_07_09 is fitted with a R-S model (for the cool component) plus power-law model (for the hot component). The temperature and heavy element abundances of the R-S model are fixed to 2.0 keV and 0.2 solar, respectively. The dotted and dashed lines indicate the relation for a fixed 2–10 keV flux at 6.0×10^{-12} ergs s^{-1} cm^{-2} and 1.2×10^{-11} ergs s^{-1} cm^{-2}, respectively.

Inverse Compton Scattering

As described in Harris & Romanishin (1974) (see section 2.3.1), we can use our data to constrain the electron spectrum and magnetic fields in the radio emitting region, considering that the hard X-ray emission is produced by the inverse Compton scattering on the 3 K microwave background. We have obtained the X-ray flux of 8×10^{-12} ergs s^{-1} cm^{-2} in 2–10 keV, and the best-fit photon

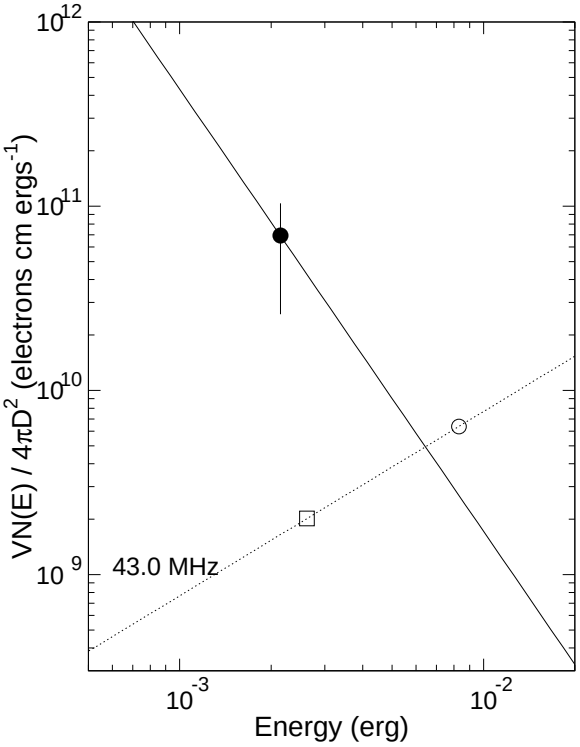

Figure 7.7: Electron spectrum for the hot region. Filled circle is determined from ASCA observation, and solid line shows the spectral index $p = 2\alpha + 1 = 2.4$ of the electron spectrum (equation 2.5). Dotted line represents loci of solutions for the 43.0 MHz observation around M87 (Hanisch & Erickson 1980). Magnetic field strengths are indicated by open circle (10^{-7} gauss) and open rectangle (10^{-6} gauss).

index of 1.7 (energy index of 0.7) for the hot component. Then the "normalized number of electrons" (see equation 2.14) is calculated as $VN(E)/4\pi D^2 = 6.9 \times 10^{10}$ electrons cm erg^{-1}.

This value is plotted on the power-law energy spectrum of electrons in figure 7.7 with a filled circle. The error bar shows the 90% confidence range determined by the X-ray flux. The solid line shows the electron spectrum with the spectral index $p = 2\alpha + 1 = 2.4$ (equation 2.5), normalized to pass through the filled circle. Unfortunately, no radio data with good sensitively is available for this region. Hanisch & Erickson (1980) obtained a radio flux profile near M87 at 43.0 MHz. Based on this result, we roughly estimate that the radio flux at $\sim 2^\circ$ offset from M87 is less than 100 Jy at this frequency. Assuming a flux of 100 Jy, we plot the constrains on the electron density imposed by radio data in figure 7.7. To explain both the hard X-ray emission and the 43.0 MHz radio flux, the magnetic field in this region is inferred to be $\sim 2 \times 10^{-7}$ gauss from the cross point in figure 7.7. Our rough estimate gives a consistent number with the result by Lea et al. (1981), who derived 4.7×10^{-7} gauss.

As shown in 7.7, we expect the presence of relativistic electrons with $E \sim 10^{-3} - 10^{-2}$ erg ($\gamma \sim 10^3 - 10^4$). If the magnetic field strength is $B \sim 2 \times 10^{-7}$ gauss, the energy loss due to inverse Compton process always dominates over the synchrotron loss (see equation 2.9 and 2.10). In the low energy end of the electron spectrum, the energy loss due to Coulomb collisions between relativistic electrons and thermal electrons in the ICM becomes dominant. The time scale of the

energy loss for a relativistic electron with energy E by Coulomb collisions is expressed as

$$t_{\rm Coulomb} \approx 3 \times 10^{11} \left(\frac{E}{10^{-3}\ {\rm erg}} \right) \left(\frac{n}{10^{-4}\ {\rm cm^{-3}}} \right)^{-1}\ {\rm yr} \tag{7.10}$$

(Rephaeli 1979). The energy loss times due to inverse Compton and Coulomb collisions become equal at an energy

$$E_{\rm eq} \approx 8 \times 10^{-5} \left(\frac{n}{10^{-4}\ {\rm cm^{-3}}} \right)^{1/2}\ {\rm erg}, \tag{7.11}$$

and the inverse Compton loss dominates at $E > E_{\rm eq}$. The life time of the relativistic electrons with $E \sim 10^{-3} - 10^{-2}$ erg ($\gamma \sim 10^3 - 10^4$) can be estimated by the equation 2.9 as $\sim 0.1 - 1$ Gyr. Therefore, unless there is a continuous supply of relativistic electrons, the hard X-ray emission cannot persist over the Hubble time.

Non-thermal Bremsstrahlung

If we consider that high-energy electrons are produced by first-order Fermi acceleration, the momentum spectrum of the electrons is described as $N(p) = N_0 p^{-\mu}$. Here, $\mu = (r+2)/(r-1)$ and r is a ratio of the shock compression (see section 2.3.1). For the shock with a Mach number ~ 2, the exponent is implied as $\mu \approx 3.3$. In such a steep spectra, an energy loss due to non-thermal bremsstrahlung possibly dominates the inverse Compton loss (Sarazin & Kempner 2000). The electrons quickly lose their energy through Coulomb loss, whose time scale is $t_{\rm Coulomb} \lesssim 3 \times 10^8\, \gamma$ yr, so that the non-thermal electrons might be recently produced.

The spectral index of the non-thermal bremsstrahlung emission is approximately $1 + \mu/2$ at the range $p_{\rm l}^2 < 2\epsilon/(m_{\rm e}c^2) \ll 1$, where $p_{\rm l}$ is the lowest normalized momentum of the non-thermal electrons, and flatten at lower photon energies (Sarazin & Kempner 2000). This is consistent with the photon index of the hot component obtained by the fitting with power-law model (figure 7.6).

Let we estimate the total number of non-thermal electrons $N_{\rm nt}^{\rm tot}$ in the hot region. The obtained flux by fitting with power law model for the 'hot' component is 2.5×10^{-3} photons cm^{-2} s^{-1} keV^{-1} at 1 keV (see figure 7.6), which corresponds to the luminosity at 1 keV $L_{\rm 1keV} = 1.9 \times 10^{41}$ ergs s^{-1} keV^{-1}, assuming a distance of 20 Mpc. If we assume the non-thermal population consists of electrons with kinetic energies exceeds $3kT$ (i.e. $p_{\rm l} = [(1+3kT/m_{\rm e}c^2)^2 - 1]^{1/2}$), where $kT = 2$ keV is the temperature of the thermal ICM, we can use equation (2.22) to calculate the luminosity of non-thermal bremsstrahlung emission at 1 keV. Then $N_0 \approx 2.8 \times 10^{67}$ is obtained, assuming the index of non-thermal electron $\mu = 3.3$ and the number density of thermal plasma $\Sigma n_{\rm Z} = 1.0 \times 10^{-4}$ cm^{-3}. By integrating equation (2.18) from $p_{\rm l}$ to ∞, we obtain $N_{\rm nt}^{\rm tot} \approx 9.0 \times 10^{68}$, which is order $\sim$ several factors smaller than that in the Coma and A2199 (Kempner & Sarazin 2000; Sarazin & Kempner 2000).

7.2 Origin of the Hot Region

In the previous sections, we restricted the physical parameters such as emission measure, density, and internal energy of the hot component. We also discussed about the inverse Compton scattering of the 3 K radiation and non-thermal bremsstrahlung by suprathermal electrons. Based on these considerations, we will discuss the origin of the hard component.

7.2.1 LMXBs

Elliptical galaxies are known as hard X-ray emitters due to LMXBs. Most luminous elliptical galaxies, such as NGC 4472, show a hard X-ray luminosity of $\sim 10^{41}$ ergs s^{-1}, with $kT \sim 10$ keV if approximated in terms of temperature (Canizares et al. 1987; Matsushita et al. 1994). However, there are no luminous elliptical galaxies in s_p05_07_09 region, and the hot region extends in the north–south direction over several hundred kpc. Therefore the hard X-ray emission from LMXBs is considered as an unlikely source of the hot component.

7.2.2 Supernovae

The supernovae associated with the stellar population in galaxies are known as the sources of high-energy particles. However, high-energy electrons have to survive under Coulomb or adiabatic losses to reach the intracluster space. Furthermore, the intracluster pressure is so large ($nkT \sim 10^{-13}$ dyns cm^{-2}) that the galactic wind would be difficult to develop, expect in the starburst phase (e.g. Breitschwerdt et al. 1991). Although the galaxies in clusters may have experienced the starburst phase in $z \gtrsim 2$, the high-energy electrons have to suffer a strong inverse Compton loss: the electrons with $\gamma \gtrsim 2000$ should lose their energy within 1 Gyr. These points indicate supernovae to be unlikely sources of energy.

7.2.3 AGN

There are some evidences about the evolution of active galactic nuclei (AGNs): that luminous AGNs are inferred to have turned into fainter AGNs or non-AGN objects (e.g. Padovani et al. 1990), probably due to a decrease in the mass accretion rate onto the central black hole. Then the life time of the AGNs can be roughly estimated by the Eddington time scale,

$$t_{\rm E} = \frac{c\sigma_{\rm T}}{4\pi G m_{\rm p}} = 4.5 \times 10^8 \text{ yr}. \tag{7.12}$$

Extragalactic radio sources often reveal jets probably driven by a central black hole, with a kinetic energy of $\sim 10^{44} - 10^{46}$ ergs s^{-1} (e.g. Rawlings & Saunders 1991). If the jet keeps its activity over the Eddington time, they may deposit the energy to the intergalactic space with a total amount of $\sim 10^{60} - 10^{62}$ ergs.

The time scale to achieve equipartition between electrons and protons is expressed as

$$t_{\rm eq(e-p)} \approx 6.4 \times 10^8 \left(\frac{n}{10^{-3}\text{ cm}^{-3}}\right)^{-1} \left(\frac{T}{10^8\text{ K}}\right)^{3/2} \text{ yr} \tag{7.13}$$

(Spitzer 1962). Thus, it takes about 1 Gyr to equilibrate through electron-proton collisions in the hot region ($n \sim 1 \times 10^{-4}$ cm^{-3}, $kT \sim 4$ keV). If the jets heat up some volume in the ICM, thermal conduction transports the heat to surrounding regions. The thermal conduction time scale (see equation 2.27, 2.28) for the hot component (i.e. $n \sim 1 \times 10^{-4}$ cm^{-3}, $kT \sim 4$ keV, and a scale length $T/|\nabla T| \sim 300$ kpc) is an order of 10^8 yr, which is almost the same as the life time of the AGN. Furthermore, galaxies should be moving in the ICM with a typical velocity $v \sim 500$ km s^{-1}, comparable to the velocity dispersion in the Virgo cluster. This process may work to spread the energies injected by the jets over the intracluster space with a scale of ~ 100 kpc scale within 0.2 Gyr.

However, given the lack of strong candidate for the AGN or an ex-AGN in the Virgo cluster, the hypothesis of the energy injection by the jets would have to remain highly speculative.

7.2.4 Subcluster Merger

The estimated internal thermal energy $E_{\rm th}$ in the hot component in the Virgo cluster is orders of magnitude lower than the total kinetic energy involved in such a subcluster merger (10^{63-64} ergs). This means that if there is a bulk motion of gas in this region, caused by an infall or collision of galaxies or a small group of galaxies, then it would be enough in terms of energetics to heat up the gas to the observed temperatures.

Honda et al. (1996) reported temperature variation of the ICM in the Coma cluster, and found a remarkable hot region ($\gtrsim 11$ keV) which is distinct from the average temperature of the whole cluster (~ 8 keV). This hot region is located at $40'$ (1.6 Mpc) offset from the cluster center, and has an angular extent of $\sim 20'$ radius. On the other hand, Briel et al. (1992) obtained the β model parameters of the Coma cluster from the ROSAT observation: $\beta = 0.75 \pm 0.03$, $R_{\rm c} = 10.5 \pm 0.6$ arcmin, and the central density is $2.89 \pm 0.04 \times 10^{-3}$ cm^{-3}. With these parameters, we can roughly estimate the increase in the internal energy at the hot region in the Coma cluster as $\sim 8 \times 10^{61}$ ergs. Ishizaka & Mineshige (1996) performed N-body + Hydrodynamic simulations for a subcluster collision with a main cluster, and successfully created a temperature variation as observed in the Coma cluster. In their model, the subcluster initially holds 1/8 of the mass of the main cluster and the colliding velocity is 2000 km s^{-1}, the kinetic energy of the subcluster is up to 9×10^{63} ergs if we assume the total gravitating mass of the Coma cluster to be $1.8 \times 10^{15} M_\odot$ (Briel et al. 1992).

Following the considerations so far made, we look into a specific possibility that the gas in the hot component has been heated by the shocks. Since typical velocities of the subclusters are ~ 1000 km s^{-1} which is the same order of the speed of sound in the ICM, we can treat the shock wave as an acoustic compression wave (Zel'dovich & Raizer 1966). Using the Rankine-Hugoniot jump condition (see equation 2.33 and 2.35) and the equations 7.3 and 7.4, we obtain the following relations,

$$\frac{EM_{\rm cool}}{EM_{\rm hot}} = \left[\frac{(\gamma-1)\mathcal{M}^2_{\rm cool}+2}{(\gamma+1)\mathcal{M}^2_{\rm cool}}\right]^2 \frac{1-\alpha}{\alpha}, \tag{7.14}$$

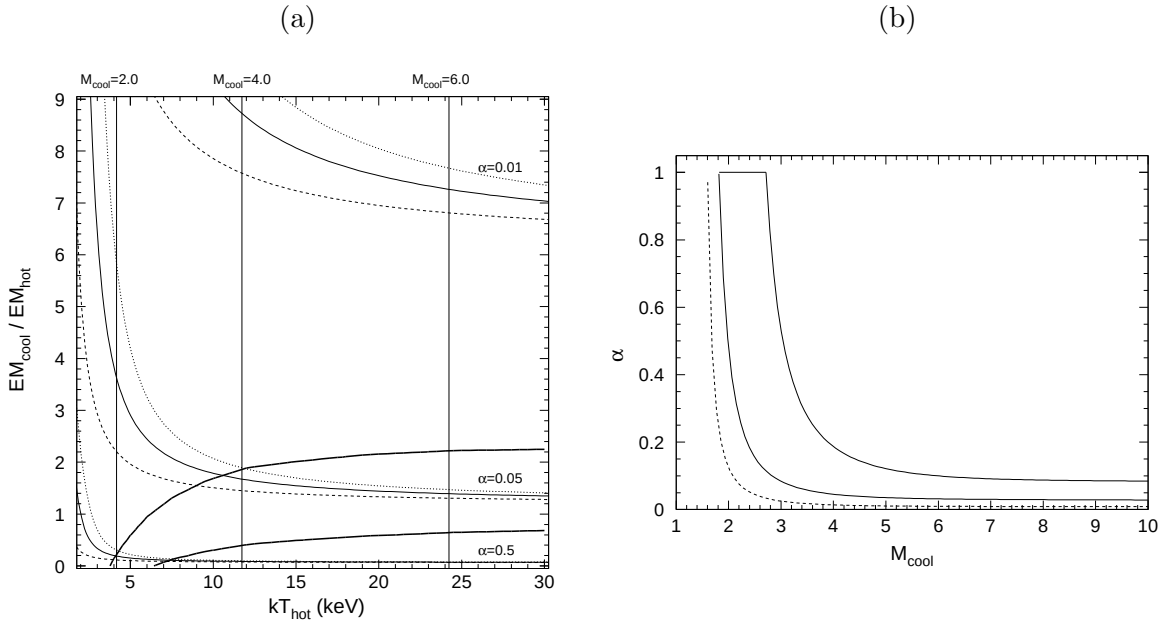

Figure 7.8: (a) Relation between $EM_{\rm cool}/EM_{\rm hot}$ and $kT_{\rm hot}$ for fixed values of α calculated from equations 7.14 and 7.15. The ratio of specific heats γ is fixed to 5/3. Solid lines show the case of $kT_{\rm cool} = 2.0$ keV, dashed lines are for $kT_{\rm cool} = 1.2$ keV, and dotted lines are for $kT_{\rm cool} = 2.7$ keV. Thick line shows the 90% confidence contour for $kT_{\rm cool} = 2.0$ keV as shown in figure 7.2(d). (b) Lines show 90% confidence range in the $\alpha - \mathcal{M}_{\rm cool}$ (Mach number of the shock wave) plane, assuming $kT_{\rm cool} = 2.0$ keV. This is the same confidence region shown in (a). Dashed line shows 90% lower limit for $kT_{\rm cool} = 2.7$ keV.

$$kT_{\rm hot} = \frac{[2\gamma\mathcal{M}^2_{\rm cool} - (\gamma-1)][(\gamma-1)\mathcal{M}^2_{\rm cool} + 2]}{(\gamma+1)^2\mathcal{M}^2_{\rm cool}}\, kT_{\rm cool}, \tag{7.15}$$

where γ is the ratio of specific heats, and $\mathcal{M}_{\rm cool}$ is the Mach number of the shock wave in the cool region. Since figure 7.2(d) shows the allowed region for $EM_{\rm cool}/EM_{\rm hot}$ as a function of $kT_{\rm hot}$, we can use this to constrain α which is the fraction in the line-of-sight depth of the hot region. In figure 7.8(a), relation between $EM_{\rm cool}/EM_{\rm hot}$ and $kT_{\rm hot}$ is plotted for various values of α calculated from the above equations. The allowed region (between thick solid lines) is then plotted as a relation between α and $\mathcal{M}_{\rm cool}$ in figure 7.8(b), where the 90% confidence region is shown. In both figures, we assume γ to be 5/3 for a monoatomic ideal gas.

Irwin & Sarazin (1996) discuss that M49 is moving supersonically ($v \approx 1300$ km s^{-1}) in the Virgo ICM toward the direction of M87, based on the X-ray morphology of the hot halo around the galaxy. Since the sound speed in the 2 keV gas is ~ 700 km s^{-1}, $\mathcal{M}_{\rm cool} \approx 2$ is a reasonable estimate if the shock wave is created by the motion of the gas associated with M49. In this case $kT_{\rm hot}$ should be ~ 4 keV, and the fraction of the hot component α is restricted as $\gtrsim 0.1$ from the figures 7.8(a) and (b). Furthermore, the density compression ratio for $\mathcal{M}_{\rm cool} \approx 2$ shock is given as $\rho_{\rm hot}/\rho_{\rm cool} \approx 2.3$ (equation 2.33), which constrains the upper limit of α as $\lesssim 0.3$ from figures

7.3(a) and (b). Using this α value and $d = 1$ Mpc as discussed in section 7.1.3, we can estimate the internal energy of the hot region, $E_{\rm th}$, to be an order of 10^{60} ergs. This is consistent with the value obtained in section 7.1.4.

The shock and turbulence created in the ICM associated with the merging can accelerate electrons as they traverse the ICM (e.g. Tribble 1993; Röttgering et al. 1997). Furthermore, the mergers will gradually build up the magnetic field. We can assume that the time scale for the magnetic field reconnection is very slow expect when the energy density of the field reaches an equipartition with the thermal energy of the ICM. The magnetic field strength to achieve an equipartition with the ICM ($n \approx 1 \times 10^{-4}$ cm^{-3}, $kT \approx 2$ keV) is $B_{\rm eq} \approx 3 \times 10^{-6}$ gauss, which is about 10 times larger than that estimated in section 7.1.6. Even when $B \gtrsim B_{\rm eq}$, the reconnection proceeds with an average velocity of $\sim 0.1 v_{\rm A}$ (Soker & Sarazin 1990), where $v_{\rm A}$ is the Alfvén speed:

$$v_{\rm A} \approx 300 \left(\frac{B}{10^{-6}\ {\rm gauss}} \right) \left(\frac{n}{10^{-4}\ {\rm cm}^{-3}} \right)^{-1/2} {\rm km\ s}^{-1}. \tag{7.16}$$

This ensures that the compression of the magnetic field can take place effectively, without the field dissipation due to reconnection. Therefore we can assume that the mergers can supply both high-energy electrons and magnetic fields if the subclusters move through the ICM with a supersonic velocity.

Chapter 8

Conclusion

The northwest and south regions of the Virgo clusters of galaxies have been extensively investigated with ASCA. The total observation time and the covered area are $\sim$ 500 ksec and $\sim$ 10 deg^2, respectively. This is the first attempt to study the spatially-resolved 0.5–10 keV spectra in this cluster over $\sim$ 1 Mpc scale.

Analyzing the X-ray image with ASCA, all possible spurious sources have been eliminated from the data. We also estimate the intensities of the stray light for each observed region, based on the calibration observation and the ray-tracing simulation of the XRT. As the result, we successfully obtained large-scale temperature distribution in the ICM in the Virgo cluster.

The hardness ratios of the spectra in the south region of M87 are generally higher than those in the northwest region, and exhibit significant variation from position to position. In particular, a remarkable 'hot' region is discovered in the linking region between M87 and M49 along the X-ray "bridge". This region has an angular extent of $\sim 4 \times 10^3$ arcmin^2 and a temperature $kT = 4.38^{+1.60\ +0.61}_{-1.08\ -0.83}$ keV. The temperature is significantly higher than that in the near-by 'cool' region which is just on the east side of the hot region: $kT = 1.92^{+0.53\ +0.50}_{-0.41\ -0.58}$ keV.

We detect no significant temperature variation around M49. The temperature of the gas within $\gtrsim 20'$ from M49 is about 1keV, and smoothly increases to the surrounding level of 2 keV, which is the average temperature of the Virgo cluster, at $\sim 60'$.

The observed feature indicates that the hot region occupies a small angular size compared with the whole extent of the Virgo cluster, and it is surrounded by a cool gas of about 2 keV. The X-ray luminosity of the hot component is very roughly 4×10^{41} erg s^{-1} in 2–10 keV. Based on the spectrum and emission measure of the hot component, its internal thermal energy is estimated to be $\sim 10^{60}$ ergs and the gas density is $\sim 10^{-4}$ cm^{-3}. Also, the scale of the hot component is likely to be $\sim$ 100 kpc both in the projected plane and in the line-of-sight depth. With these features, we discuss the possible origin of the hot component along three basic pictures.

1. Subcluster mergers can produce temperature variations in the ICM. Since the kinetic energy of the M49 subcluster is estimated to be $\sim 1 \times 10^{63}$ ergs ($M = 8.7 \times 10^{13}$ by Schindler et al. 1999; $v = 1300$ km s^{-1} by Irwin & Sarazin 1996), it would be enough to heat up the ICM. If the shock is produced in the 2 keV ICM by the gas motion with $v = 1300$ km s^{-1}

($\mathcal{M} \sim 2$), the ICM would be heated up to 4 keV.

2. The internal energy of the hot component is comparable to the total energy emitted by a typical AGN in its life time of the activity. The heated ICM by jets from an AGN will spread into the intracluster space over several hundred kpc within 1 Gyr by heat conduction and motion of the AGN. The lack of AGN in or near the hot region, however, renders this possibility somewhat remote.

3. Inverse Compton scattering by the relativistic electrons of the 3 K microwave background is also considered as the origin of the hard X-ray emission. The data cannot exclude the possibility of power-law emission from the hot component. In this case, relativistic electrons of $E \approx 2 \times 10^{-3}$ erg ($\gamma \approx 2 \times 10^3$) are needed to explain the X-ray spectrum. Another possibility is that the hard emission is produced by non-thermal bremsstrahlung due to subrelativistic, suprathermal electrons with energies grater than several keV. The total amount of the suprathermal electron in the region is estimated as $N_{\rm nt}^{\rm tot} \approx 9.0 \times 10^{68}$.

In the case 2, heating of the gas must have been occurred within $\lesssim 1$ Gyr in the past. Thermal conduction transports the heat from the hot to cold regions and the ICM will achieve an isothermal distribution over 1 Mpc scale in a time significantly longer than that. The conduction should also work in the case 1, but in this scenario the shock heating is considered to occur at present due to the subcluster merger. In the case 3, the relativistic electrons lose energy due to the inverse Compton process within $\lesssim 1$ Gyr, and subrelativistic electrons also lose their energy due to Coulomb loss within $\lesssim 0.1$ Gyr. Therefore, continuous supply of the high-energy electrons seems necessary to explain the observed features. These facts suggest that either continuous heating of the gas or acceleration of particles, most likely involving shocks in both cases, is taking place in the hot region of the intracluster space in the Virgo cluster.

The present research has raised a possibility that the ICM may contain such a hot region in other clusters. Unfortunately, no other cluster offers an opportunity for ASCA to observe the detailed structure of the ICM. Future X-ray observations with good spatial resolution in the high energy band would be very interesting to look at the detailed structure of the hard X-ray emission region in the Virgo and in other clusters.

Appendix A

The ROSAT Satellite

A.1 Overview

ROSAT (acronym for the German word *Röntgensatellit*, Trümper 1983) is a cooperative program between Germany, the USA, and the UK, launched on 1990 June. Figure A.1 shows schematic view of the ROSAT. ROSAT has two scientific payload: the X-ray telescope (XRT) with Position Sensitive Proportional Counters (PSPCs) and a High Resolution Imager (HRI) as focal plane detectors, and the Wide-Field Camera (WFC). The XRT has a 2.40 m focal-length mirror assembly consisting of four nested Wolter-I mirrors. Its mirror surfaces have a residual roughness of less than 0.3 nm, which made them the smoothest mirrors ever produced for a grazing-incidence telescope. This property is responsible for the excellent contrast of the ROSAT telescope. The PSPC provides a wide field of view ($\sim 2^\circ$ diameter), moderate energy resolution and a high spatial resolution in soft X-ray band ($0.2 - 2.5$ keV). The HRI, comprising two cascaded microchannel plates, provides a much higher spatial resolution ($\sim 2^{"}$ diameter), but a smaller field of view and no energy resolution. The WFC is an EUV telescope, consisting of 0.525 m focal-length mirror assembly of three nested Wolter-Schwarzschild mirrors and microchannel plate (MCP).

Since we utilized only the PSPC data in this thesis, we briefly describe the PSPC system. Further information on ROSAT is found in Briel et al. (1997).

A.2 Position Sensitive Proportional Counter (PSPC)

The PSPC is a multiwire proportional counter. The anode and cathode grids are contained in a gas-filled counter housing. The mutually perpendicular cathode grids determine the position of the events, while the anode grids determine the energy of the events. The entrance window consists of $\sim 1\mu$m film of polipropylen coated with carbon and lexan. Figure A.2(a) shows a window transmission of the PSPC, indicating a sharp break at 0.25 keV due to C K-edge of the window. The working gas consists of 65% argon, 20% xenon, and 15% methane. Due to a fall-off in the reflectivity of the XRT (see figure A.2(b)), the PSPC covers up to X-ray energy of 2 keV. Figure A.3(a) shows PSFs of ROSAT XRT (m_σ) and PSPC (r_σ) as a function of angle from the

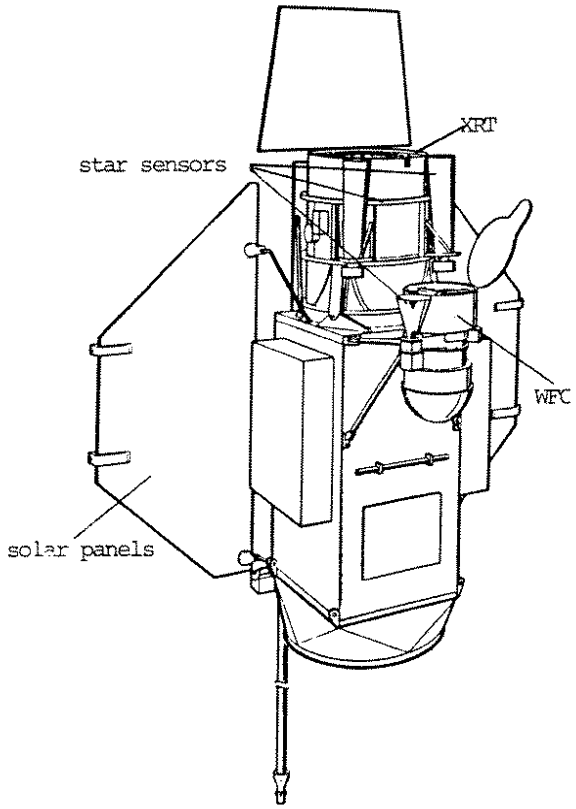

Figure A.1: Schematic view of the ROSAT spacecraft.(Briel et al., 1997).

Table A.1: Design parameters and performance of the PSPC

Energy band	$0.2 - 2$ keV (including XRT)
Energy resolution	$\Delta E/E \sim 0.43(E/0.93)^{-0.5}$
	$\sim 40\%$ at 1 keV (FWHM)
Effective area	2° deg diameter
Entrance window	$\sim 1\mu$m plastic
Positional resolution	~ 30" at on-axis (FWHM) (including XRT)

optical axis. We can see that the PSPC has a better spatial resolution (less than $1'$ arcmin within $\sim 20'$ from the optical axis) than the ASCA detectors in sort X-ray bands.

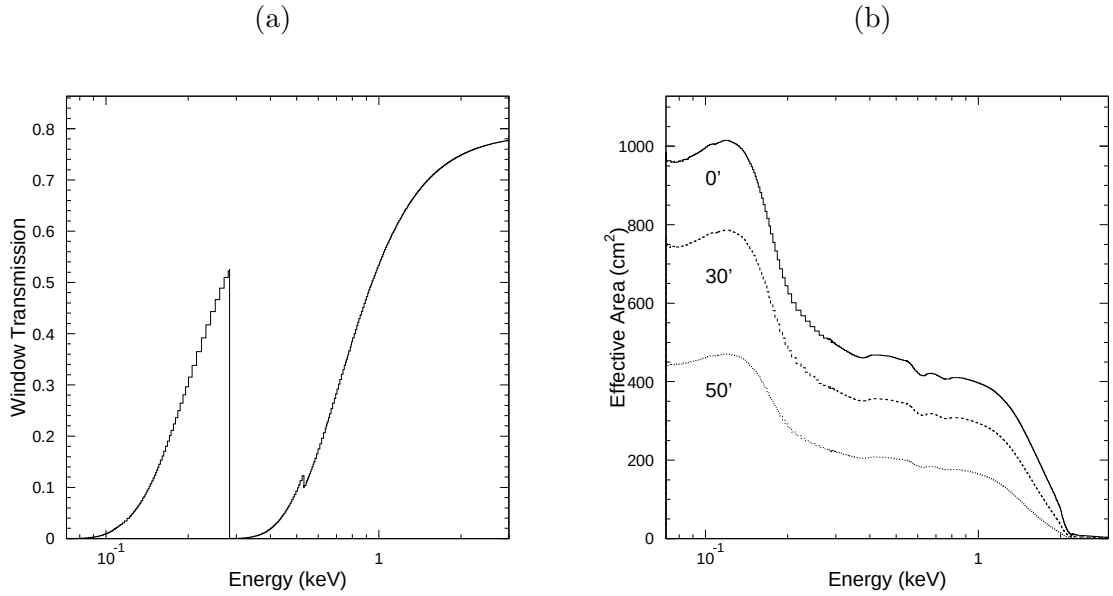

Figure A.2: (a) The ROSAT PSPC-C entrance window transmission as a function of energy. (b) The effective area of the ROSAT XRT as a function of energy for off-axis angles 0, 30 and 50 arcmin.

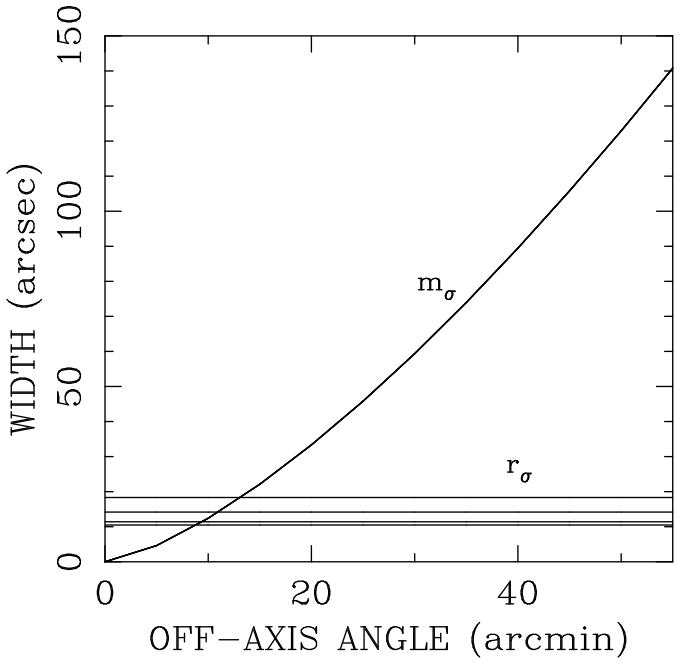

Figure A.3: The PSF of the ROSAT X-ray telescope (m_σ) and PSPC(r_σ). The 4 lines of PSPC components represent the PSF at different energy: 0.28, 0.50, 2.0 and 1.0 keV from top to bottom (Briel et al. 1997).

A.3 ROSAT All-Sky Survey

After launch in 1990, ROSAT has performed the all-sky survey using the PSPC in combination with the XRT. In the ROSAT All-Sky Survey (RASS), the Virgo cluster was observed from November 1990 to January 1991. An average exposure time of the Virgo region is about 500 seconds. Figure A.4 shows a exposure map around the Virgo cluster.

The RASS image around Virgo cluster are shown in figure A.5. The "emission bridge" structure between M87 and M49 is clearly seen, as already pointed out by Takano (1990) and Böhringer et al. (1994). As we have seen in chapter 3, Ginga found the temperature is increasing at $\sim 2 - 3^\circ$ south of M87. However, ROSAT found no evidence of the temperature increase (see figure 3.7). Böhringer et al. (1994) suggested the possibility that the Ginga result is caused by the background contamination sources which have a harder spectrum than the ICM of the Virgo cluster, such as A1553, A1541, etc.

We have performed spectrum fitting of the RASS data in the "emission bridge" region after excluding contamination of X-ray sources other than ICM. We chose the size of integrated region $\sim 1^\circ \times 2^\circ$, which corresponds to the beam size of Ginga. However, we could not obtain the ICM temperature in a reasonable error because of poor photon statistics of the RASS data (note that the temperature derived from RASS in figure 3.7 is azimuthally averaged temperature profile around M87). To study the physical condition of the ICM in this bridge-like region, we needed deeper imaging observation.

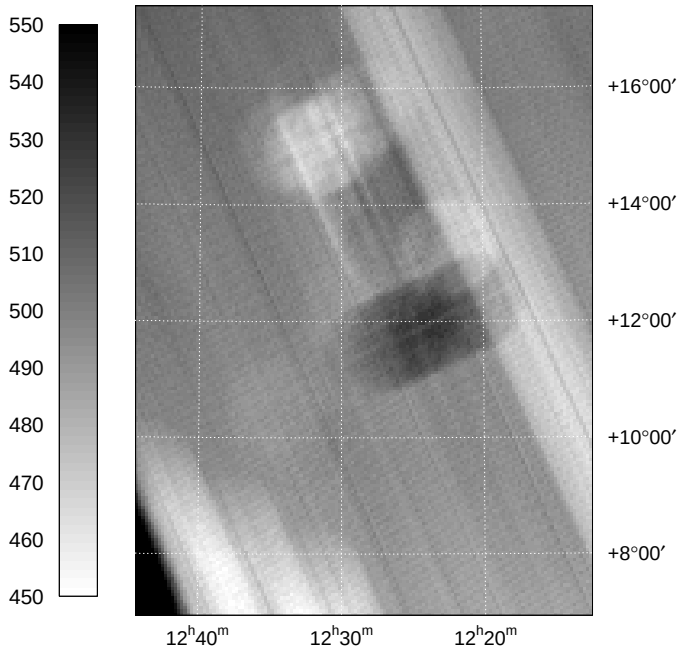

Figure A.4: The exposure map of RASS around the Virgo cluster. Left panel shows the level of the exposure time in second.

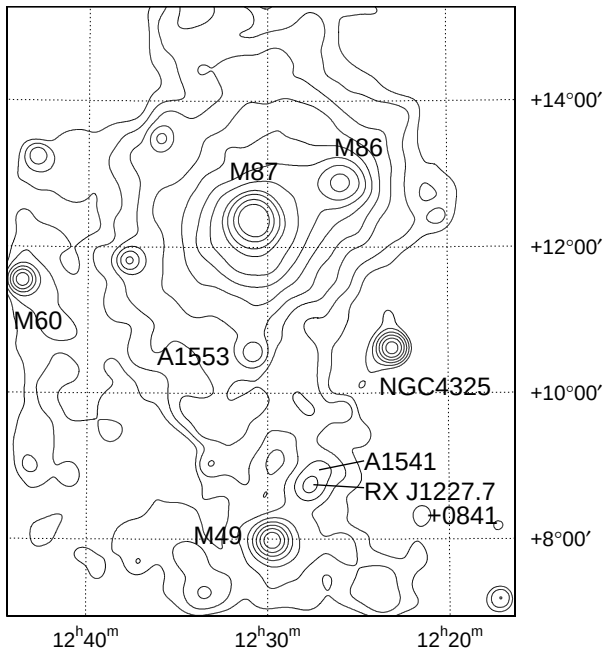

Figure A.5: RASS image of the Virgo cluster in $0.5 - 2$ keV band. The image is smoothed by a Gaussian with $\sigma = 20'$ on the faintest levels and decreasing σ value with increasing surface brightness. The contour is logarithmic scale, the lowest and highest contour line is 1.2×10^{-4} count s^{-1} arcmin^{-2} and 1.3×10^{-2} count s^{-1} arcmin^{-2}.

Appendix B

Detected Source Candidate List in the Virgo Field

The list of sources detected in the Virgo field is given in table B (see section 6.2.1). It contains the following information for each source: the source position in equinox 2000.0, the statistical significance in $0.7-7$ keV band, counting rate, photon index in the $0.7-10$ keV band, $2-10$ flux calculated from the best fit parameters of the spectrum, and source identification. The spectrum fitting is performed in the $0.7-10$ keV band, assuming a power-law with a galactic absorption indicated in table 6.1.

Table B.1: Detected Source Candidate List in the Virgo Field

Field	No.	RA, Dec[a]	Sig[b]	Rate[c]	Index[d]	Flux[e]	ID
nw_p01	1	185.9051, 13.5189	3.71	3.24	2.32	1.14	
nw_p01	2	185.6335, 13.6672	12.17	8.59	1.19	7.33	
nw_p01	3	185.5320, 13.7553	5.35	5.21	3.05	0.95	
nw_p01	4	185.6720, 13.7582	3.57	1.84	8.95	0.00	
nw_p01	5	185.8462, 13.6966	5.52	3.02	1.22	2.77	
nw_p01	6	185.5946, 13.8029	4.81	3.65	2.18	1.43	
nw_p01	7	185.9182, 13.6973	3.54	2.14	2.30	0.81	
nw_p01	8	185.6990, 13.8183	4.50	2.65	1.83	1.31	
nw_p01	9	185.7346, 13.8536	3.21	2.14	2.16	0.97	
nw_p02	1	186.0200, 12.8839	5.49	5.52	0.26	9.04	VCC 684, PGC 40298
nw_p02	2	185.7987, 13.0703	6.38	3.59	1.49	2.69	PGC 40202
nw_p02	3	186.0735, 13.0044	4.88	5.29	2.00	2.53	VCC 723
nw_p02	4	185.9649, 13.0729	5.03	2.58	1.60	1.55	
nw_p02	5	186.1178, 13.0758	3.46	3.40	2.19	1.24	
nw_p02	6	186.0764, 13.1208	4.18	3.03	1.47	2.12	
nw_p02	7	186.1312, 13.1363	3.59	3.65	2.81	0.88	
nw_p02	8	185.9802, 13.2111	3.34	1.99	2.13	0.89	
nw_p02	9	186.1875, 13.2036	3.05	5.95	1.26	5.49	
nw_p02	10	186.1459, 13.2965	4.73	4.02	1.98	1.76	
nw_p03	1	186.3875, 13.1767	3.79	50.69	2.40	17.09	
nw_p03	2	186.4014, 13.2501	3.87	5.10	2.12	2.48	VCC 810
nw_p03	3	186.3173, 13.2884	5.94	7.28	2.33	2.44	
nw_p03	4	186.3103, 13.3779	3.74	2.88	3.99	0.26	
nw_p03	5	186.5052, 13.3485	7.32	9.65	2.49	2.82	
nw_p03	6	186.4375, 13.4550	3.17	2.25	6.91	0.02	
nw_p03	7	186.5284, 13.4230	5.61	6.52	1.19	5.71	
nw_p03	8	186.3128, 13.5772	3.89	1.86	0.92	2.00	
nw_p03	9	186.2684, 13.6625	3.02	1.62	1.56	1.22	
nw_p03	10	186.5261, 13.5849	3.42	3.27	1.31	2.31	
nw_p03	11	186.5387, 13.6545	3.19	2.63	2.32	0.92	VCC 877
nw_p03	12	186.6289, 13.8360	3.86	2.93	2.13	1.18	
nw_p04	1	186.8756, 13.0750	3.42	9.42	2.97	1.88	
nw_p04	2	186.8463, 13.1287	3.15	9.16	1.29	6.91	VCC 996
nw_p04	3	186.8382, 13.1794	4.75	8.77	1.53	5.57	
nw_p04	4	186.9331, 13.1462	4.17	11.64	1.66	6.73	
nw_p04	5	186.9983, 13.2017	3.33	5.07	2.31	1.91	
nw_p04	6	187.0816, 13.1855	3.95	7.70	1.80	3.94	VCC 1101, PGC 41007
nw_p04	7	186.9311, 13.2860	3.48	3.74	2.19	1.56	
nw_p04	8	187.0620, 13.2533	3.01	4.58	2.95	0.96	
nw_p04	9	186.8432, 13.5081	3.25	3.27	2.74	0.90	
nw_p05	1	187.3704, 13.7495	8.22	9.27	1.61	5.77	RXP J122926+1345.2
nw_p05	2	187.5477, 13.6962	3.06	5.25	2.06	2.49	VCC 1265
nw_p07	1	186.1604, 14.8972	6.08	4.73	2.30	1.74	
nw_p07	2	186.2986, 14.7414	4.04	3.40	1.84	1.80	VCC 778, PGC 40477

Table B(*continued*)

Field	No.	RA, Dec[a]	Sig[b]	Rate[c]	Index[d]	Flux[e]	ID
nw_p07	3	186.0933, 14.6694	3.36	1.44	1.38	1.37	
nw_p07	4	186.0581, 14.6086	3.12	1.32	1.88	0.75	
nw_p07	5	185.9516, 14.6493	3.63	1.19	1.22	1.19	
nw_p07	6	185.8569, 14.5255	3.44	2.63	1.12	2.30	
nw_p08	1	186.3965, 14.2024	5.45	6.07	1.70	3.60	
nw_p08	2	186.2144, 14.2606	3.81	2.50	0.62	3.07	
nw_p08	3	186.2574, 14.1495	3.30	1.79	1.41	1.34	
nw_p08	4	186.0130, 14.2141	5.20	3.58	0.87	3.78	
nw_p08	5	186.1371, 14.1151	3.29	1.46	1.68	0.88	
nw_p08	6	186.2380, 13.9040	3.41	3.36	3.90	0.26	
nw_p08	7	186.2292, 13.8490	3.42	4.87	1.99	2.24	
nw_p08	8	186.1105, 13.8457	3.26	4.43	2.35	1.35	
nw_p09	1	186.8735, 14.5968	3.38	3.31	2.34	1.26	
nw_p09	2	186.6044, 14.6321	3.33	1.51	1.16	0.86	
nw_p09	3	186.6571, 14.5119	10.11	6.27	1.73	3.59	
nw_p09	4	186.5317, 14.5524	3.69	1.50	1.52	0.93	
nw_p09	5	186.4253, 14.5932	3.60	2.45	1.05	2.11	
nw_p09	6	186.4079, 14.2195	3.81	8.32	2.03	3.48	
nw_p10	1	186.7016, 13.8147	4.96	3.90	1.14	4.78	
nw_p10	2	186.6292, 13.8968	4.02	3.31	1.25	2.49	VCC 924
nw_p10	3	186.7193, 13.9217	9.53	6.39	1.95	3.03	
nw_p10	4	186.8514, 13.8793	5.17	4.35	1.71	2.46	RXP J122723+1352.8
nw_p10	5	187.0199, 13.8502	3.48	5.91	1.74	3.31	
nw_p10	6	186.8587, 13.9464	4.79	3.85	1.14	3.70	
nw_p10	7	187.0505, 14.0746	3.94	7.11	1.32	5.81	RXP J122813+1403.8
nw_p11	1	187.2144, 14.3419	3.54	1.70	2.09	0.82	
nw_p11	2	187.0873, 14.3788	4.06	1.95	2.35	0.66	
nw_p11	3	187.1855, 14.2464	5.13	3.47	1.22	2.96	
nw_p11	4	187.3250, 14.1126	3.99	7.00	1.44	4.81	RXP J122917+1405.1
nw_p11	5	187.0423, 14.0817	3.67	7.14	1.70	4.06	RXP J122813+1403.8
nw_p11	6	187.1397, 13.9951	3.70	30.29	1.54	18.69	
nw_p12	1	187.3620, 13.3335	5.81	9.11	1.99	4.37	VCC 1201, RXP J122924+1320.3
nw_p12	2	187.6805, 13.1380	5.50	9.97	1.60	6.19	
nw_p12	3	187.5879, 13.1772	3.23	4.56	2.56	1.36	
nw_p12	4	187.5387, 13.2004	4.66	5.88	1.80	3.20	
nw_p12	5	187.7487, 13.0968	7.17	22.85	2.90	4.66	
nw_p12	6	187.7016, 13.1053	4.23	11.23	1.92	5.37	
nw_p12	7	187.5827, 13.1478	4.93	9.07	1.52	5.71	
nw_p12	8	187.6061, 13.0822	8.23	18.36	2.47	5.74	
nw_p12	9	187.3866, 13.1856	3.09	4.32	2.80	1.09	VCC 1202
nw_p12	10	187.7008, 13.0193	4.33	24.88	2.64	6.25	
nw_p12	11	187.4251, 13.1220	3.73	7.12	0.84	7.70	
nw_p12	12	187.5181, 13.0555	7.95	25.96	2.63	6.60	
nw_p12	13	187.5942, 12.9832	7.80	34.50	2.72	8.44	

Table B(*continued*)

Field	No.	RA, Dec[a]	Sig[b]	Rate[c]	Index[d]	Flux[e]	ID
nw_p12	14	187.5148, 13.0207	5.34	20.63	2.15	7.09	
nw_p12	15	187.6492, 12.9436	4.08	23.35	1.92	13.37	
nw_p12	16	187.6155, 12.9323	3.33	22.62	1.28	15.79	
nw_p12	17	187.5025, 12.9583	6.89	37.91	2.65	9.17	
nw_p12	18	187.3191, 13.0401	4.42	20.40	2.03	9.36	
nw_p12	19	187.4448, 12.9173	6.77	158.88	2.33	50.34	
M87 NW	1	187.4807, 12.6349	16.44	467.82	2.14	178.67	
M87 NW	2	187.3539, 12.6723	9.25	26.70	2.10	11.05	
M87 NW	3	187.3259, 12.6820	8.05	19.23	2.49	5.79	
M87 NW	4	187.2265, 12.6821	7.27	9.54	1.83	4.84	VCC 1143 OR 1148
M87 NW	5	187.1405, 12.6984	4.48	4.14	2.69	1.27	
M87 NW	6	187.3676, 12.5219	14.43	62.46	2.68	15.50	VCC 1191
M87 NW	7	187.2430, 12.5719	13.45	24.91	2.03	11.03	
M87 NW	8	187.4037, 12.4571	3.73	47.14	1.74	23.60	
M87 NW	9	187.1697, 12.5679	9.00	11.62	2.38	3.99	VCC 1123
M87 NW	10	187.2674, 12.4854	15.81	45.41	2.31	15.69	
M87 NW	11	187.3356, 12.4273	9.42	42.44	2.74	10.14	VCC 1185, PGC 41156
M87 NW	12	187.0647, 12.5662	6.57	6.55	1.87	3.68	
M87 NW	13	187.1944, 12.4905	9.74	16.39	2.29	5.83	
M87 NW	14	187.3575, 12.3976	5.05	73.49	1.96	29.29	
M87 NW	15	187.0834, 12.4689	6.44	8.74	1.23	7.35	RXP J122821+1228.6
s_p01	1	187.7772, 12.1118	8.68	290.84	2.45	87.21	
s_p01	2	187.6650, 12.1570	3.79	188.50	2.10	76.63	
s_p01	3	187.5570, 12.1695	8.54	484.22	1.92	223.62	VCC 1264
s_p01	4	187.6613, 12.1054	9.97	92.75	2.05	39.07	
s_p01	5	187.9176, 11.9401	4.06	25.40	2.37	8.29	
s_p01	6	187.6746, 12.0293	11.25	61.78	2.21	22.52	
s_p01	7	187.5273, 12.0664	7.43	30.37	1.97	13.69	
s_p01	8	187.6928, 11.9865	8.60	38.92	1.91	18.77	
s_p01	9	187.5425, 12.0381	7.60	29.48	1.99	12.80	
s_p01	10	187.6222, 12.0016	7.10	26.87	2.85	6.24	
s_p01	11	187.8154, 11.9017	8.11	32.84	2.83	7.00	
s_p01	12	187.5778, 11.9929	7.52	25.53	1.65	14.95	
s_p01	13	187.6880, 11.8999	9.74	29.88	2.54	8.45	
s_p01	14	187.4152, 11.9610	4.26	12.86	4.33	0.78	
s_p01	15	187.6139, 11.8634	9.95	22.12	2.06	9.28	
s_p01	16	187.5408, 11.8618	6.27	12.81	2.61	3.60	
s_p01	17	187.6650, 11.7808	3.93	6.99	3.20	1.40	
s_p01	18	187.5184, 11.7868	8.34	18.00	2.73	4.43	RXP J123000+1145.8
s_p01	19	187.5716, 11.7521	9.86	20.90	2.64	5.64	
s_p01	20	187.5389, 11.7387	5.56	11.93	1.67	7.08	RXP J123012+1144.7
s_p02	1	187.2694, 11.7638	5.58	50.19	3.30	7.27	
s_p02	2	187.0779, 11.8135	7.23	37.54	2.10	14.98	VCC 1087, PGC 40985
s_p02	3	187.3866, 11.6551	3.42	61.29	2.29	21.98	

Table B(*continued*)

Field	No.	RA, Dec[a]	Sig[b]	Rate[c]	Index[d]	Flux[e]	ID
s_p02	4	187.2271, 11.7055	4.18	11.34	2.24	3.89	
s_p02	5	187.1504, 11.7272	5.48	16.38	2.54	4.27	VCC 1115
s_p02	6	187.0418, 11.7483	6.85	19.21	1.98	8.12	
s_p02	7	187.3050, 11.6215	5.38	13.01	1.98	5.94	
s_p02	8	187.2151, 11.6440	5.53	13.43	2.39	3.75	
s_p02	9	187.0647, 11.6730	5.08	8.54	2.38	2.52	VCC 1093
s_p02	10	187.4192, 11.5273	3.12	56.86	2.19	24.78	
s_p02	11	187.2395, 11.5724	4.73	7.71	1.62	4.09	
s_p02	12	187.1118, 11.6233	3.23	4.76	1.99	2.00	
s_p02	13	187.3106, 11.5264	3.27	5.99	1.42	3.99	
s_p03	1	187.6470, 11.5227	5.05	52.81	1.86	25.61	
s_p03	2	187.8084, 11.4229	4.23	16.32	1.86	7.68	
s_p03	3	187.7139, 11.4342	5.78	14.06	2.41	4.33	
s_p03	4	187.7577, 11.3769	4.46	8.53	1.75	4.97	
s_p03	5	187.8326, 11.3293	4.07	6.86	1.84	3.38	
s_p03	6	187.5736, 11.4327	3.27	6.06	2.53	1.67	
s_p03	7	187.7450, 11.3245	4.87	6.64	2.15	2.74	
s_p03	8	187.5864, 11.3658	6.28	8.76	2.81	2.07	
s_p03	9	187.6504, 11.3137	5.83	6.53	1.80	3.31	
s_p03	10	187.5071, 11.3267	5.76	7.15	1.29	5.54	RXP J122956+1120.6
s_p03	11	187.5377, 11.2703	5.27	5.17	2.40	1.74	
s_p03	12	187.5033, 11.2089	3.67	2.65	1.73	1.38	
s_p03	13	187.8426, 10.9849	3.58	7.18	2.57	1.98	
s_p03	14	187.7251, 11.0055	12.84	21.28	2.25	7.92	RXS J123053.8+110007, RXP J123055+1100.3
s_p03	15	187.3736, 11.1458	3.37	3.33	1.08	3.42	
s_p04	1	187.0012, 11.1876	3.17	7.18	6.41	0.08	
s_p04	2	187.1305, 11.0531	6.61	7.80	1.51	5.26	
s_p04	3	187.2605, 10.9754	3.49	3.69	2.37	1.22	
s_p04	4	186.9648, 11.0653	3.74	3.46	0.99	3.51	
s_p04	5	187.0738, 10.8814	3.34	1.73	1.66	1.10	VCC 1089
s_p04	6	187.0158, 10.8381	3.79	1.76	1.62	1.10	
s_p04	7	187.2640, 10.6654	3.29	4.57	2.35	1.50	
s_p05	1	186.9569, 10.4513	3.34	1.72	2.56	0.50	
s_p05	2	187.0496, 10.3927	4.50	2.21	0.42	3.54	VCC 1079
s_p05	3	187.2627, 10.2778	3.21	3.23	2.41	1.06	
s_p05	4	187.1252, 10.2042	6.67	4.83	1.02	4.42	
s_p05	5	186.9422, 10.1617	3.54	2.25	4.31	0.16	
s_p06	1	187.9226, 10.1487	3.65	7.26	2.44	2.18	
s_p06	2	187.5917, 10.2491	3.35	2.46	2.22	0.78	
s_p06	3	187.5136, 10.1786	3.21	1.88	1.06	1.75	
s_p06	4	187.7286, 10.0581	3.31	1.90	2.32	0.74	
s_p06	5	187.5819, 10.0280	14.65	8.97	2.42	2.91	
s_p06	6	187.6520, 9.9694	5.81	3.03	2.00	1.40	
s_p06	7	187.4530, 9.9865	4.21	2.21	1.02	2.13	

Table B(*continued*)

Field	No.	RA, Dec[a]	Sig[b]	Rate[c]	Index[d]	Flux[e]	ID
s_p06	8	187.7586, 9.7373	3.51	5.88	1.97	2.72	
s_p07	1	187.0335, 10.0294	4.56	3.48	2.37	1.18	
s_p07	2	186.9291, 9.9301	4.38	2.15	1.33	1.57	
s_p07	3	187.0524, 9.8491	20.14	16.95	1.73	9.36	NGC 4442(?), VCC 1062(?)
s_p07	4	186.9142, 9.8299	3.55	1.67	1.61	0.97	
s_p07	5	186.9643, 9.7565	4.47	2.44	1.98	1.22	
s_p07	6	186.8957, 9.7533	10.15	6.82	3.29	1.04	RXP J122730+0945.1
s_p07	7	187.0544, 9.6712	3.64	2.40	2.37	0.87	
s_p07	8	186.8291, 9.7228	3.78	2.88	0.26	4.52	
s_p07	9	186.8004, 9.7079	5.57	4.63	2.37	1.56	VCC 981
s_p08	1	187.7627, 9.7104	3.48	5.63	1.51	3.71	
s_p08	2	187.4821, 9.7806	4.20	3.27	1.35	3.11	
s_p08	3	187.6193, 9.7114	4.51	3.13	1.65	1.89	
s_p08	4	187.7245, 9.6197	3.10	1.90	1.21	1.76	
s_p08	5	187.4115, 9.5481	3.80	1.89	1.70	1.06	VCC 1207
s_p08	6	187.6027, 9.4258	3.33	1.43	4.32	0.09	
s_p08	7	187.3792, 9.4816	5.59	3.33	1.71	1.86	VCC 1206
s_p08	8	187.5967, 9.3043	3.73	2.08	2.76	0.52	
s_p09	1	187.0217, 9.6358	3.87	2.60	1.10	2.35	
s_p09	2	186.8908, 9.5695	9.11	7.12	1.42	5.00	VCC 1017
s_p09	3	186.9112, 9.2957	4.65	1.93	1.56	1.11	RXP J122733+0934.6
s_p09	4	186.8205, 9.2396	10.95	7.40	1.54	4.76	[HB89] 1224+095, RXP J122716+0914.2
s_p09	5	186.8301, 8.9613	8.32	6.72	2.98	1.28	RXP J122714+0858.1
s_p10	1	187.7010, 9.2750	9.60	8.81	1.86	4.45	
s_p10	2	187.3863, 9.3591	3.17	2.06	0.19	4.63	
s_p10	3	187.4774, 8.8482	3.73	1.91	0.75	2.26	
s_p10	4	187.3115, 8.8052	3.26	2.57	1.31	2.03	VCC 1172, RXP J122952+0851.5
s_p12	1	187.3148, 8.7973	3.66	5.61	0.51	8.95	
s_p12	2	187.2977, 8.6533	3.59	2.71	0.97	2.74	
s_p12	3	187.5502, 8.4980	6.60	4.25	1.89	2.08	VCC 1270, RXP J123012+0830.1
s_p12	4	187.5035, 8.4420	6.66	3.97	1.73	2.17	
s_p12	5	187.5802, 8.3696	3.52	2.25	1.05	2.07	
s_p12	6	187.4038, 8.3462	3.67	2.69	1.51	1.90	
s_p12	7	187.4022, 8.3113	3.05	2.72	1.91	1.19	
s_p12	8	187.3893, 8.2500	4.02	5.32	1.80	2.86	
s_p12	9	187.5545, 8.1536	4.45	8.55	3.00	1.56	RXP J123010+0809.9
s_p12	10	187.2394, 8.2776	3.41	3.66	1.51	2.26	
s_p14	1	186.9376, 7.7109	4.29	4.55	1.37	3.23	
s_p14	2	186.7635, 7.7442	4.63	3.38	2.23	1.28	
s_p14	3	186.8857, 7.6839	3.65	3.02	1.69	1.79	
s_p14	4	186.8073, 7.6057	4.45	2.60	1.66	1.63	
s_p14	5	186.5453, 7.6536	3.53	2.37	1.74	1.37	
s_p16	1	187.8110, 7.4355	4.65	4.66	2.94	0.86	

Table B(*continued*)

Field	No.	RA, Dec[a]	Sig[b]	Rate[c]	Index[d]	Flux[e]	ID
s_p17	1	187.8618, 8.0637	4.79	3.17	1.21	2.66	RXP J123124+0804.0
NGC 4365	1	185.9539, 7.4440	8.53	3.56	2.29	1.26	RXS J122349.4+072652, RXP J122350+0727.0
NGC 4365	2	186.3779, 7.2618	3.22	2.37	0.51	3.32	RXP J122531+0715.9
NGC 4365	3	186.1117, 7.3202	18.18	7.43	1.93	3.59	NGC 4365, VCC 731, PGC 40375, RXP J122428+0719.0
NGC 4365	4	186.0151, 7.3562	4.27	1.11	3.95	0.09	

a : Equinox 2000.0 in degree.

b : Detection significance in σ $(0.7 - 7$ keV).

c : Counting rate $(0.7 - 7$ keV) in 10^{-3} counts $\sec^{-1}$, which is normalize to the counting rate at XRTX/Y = (6, 6) mm within $r < 6$ mm assuming the photon index of 1.7.

d : Photon index in $0.7 - 10$ keV band.

e : $2 - 10$ keV band flux in 10^{-13} ergs $\sec^{-1}$ cm^{-2}

ID references: NGC = Dreyer 1888, VCC = Binggeli et al. 1985, [HB89] = Hewitt & Burbidge 1989, PGC = de Vaucouleurs et al. 1991, RXP = Voges et al. 1995, RXS = Voges et al. 1996.

Appendix C

The GIS Spectra Fitted with R-S Model

We show the 0.7–8 keV GIS spectra in the Virgo cluster regions fitted with the single-temperature R-S model. The best fit parameters are shown in section 6.4.2. Upper panel shows the GIS 2+3 data (crosses) and the model (solid line), and lower panel shows the $\Delta\chi$ for each figure. The background (CXB and NXB) and contaminating discrete sources are subtracted from the data (see section 5.2 for background subtraction, and section 6.2.1 for discrete source subtraction).

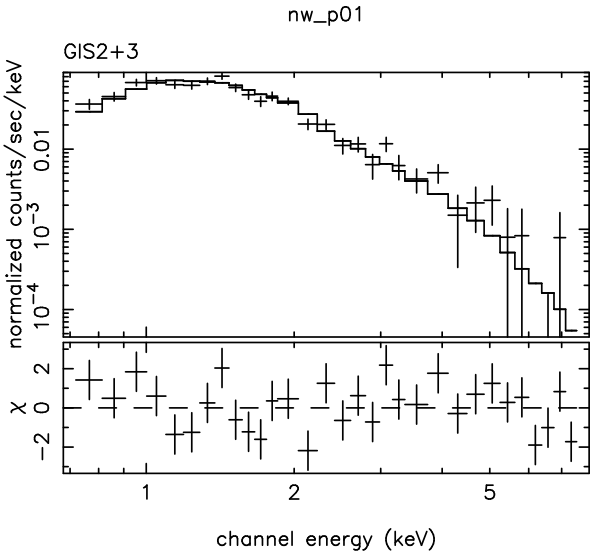
nw_p01
GIS2+3
normalized counts/sec/keV
10^{-4}
10^{-3}
0.01
χ
2
0
−2
1
2
5
channel energy (keV)

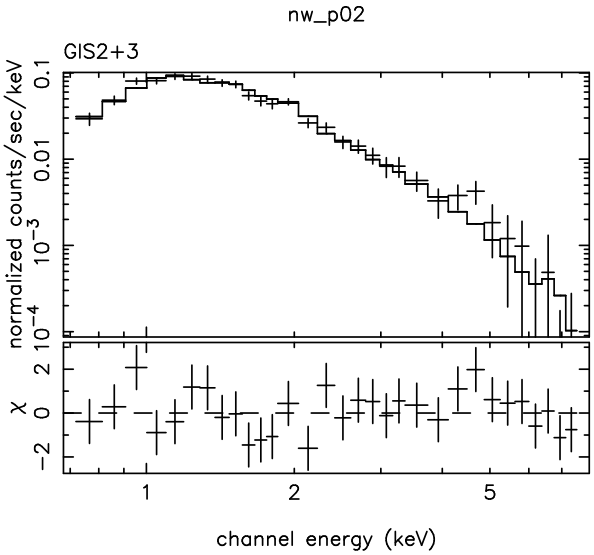
nw_p02
GIS2+3
normalized counts/sec/keV
0.1
0.01
10^{-3}
10^{-4}
χ
2
0
−2
1
2
5
channel energy (keV)

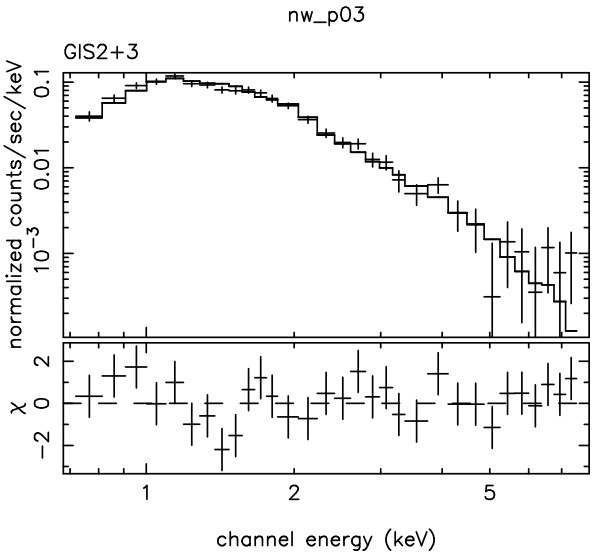
nw_p03
GIS2+3
normalized counts/sec/keV
0.1
0.01
10^{-3}
χ
2
0
−2
1
2
5
channel energy (keV)

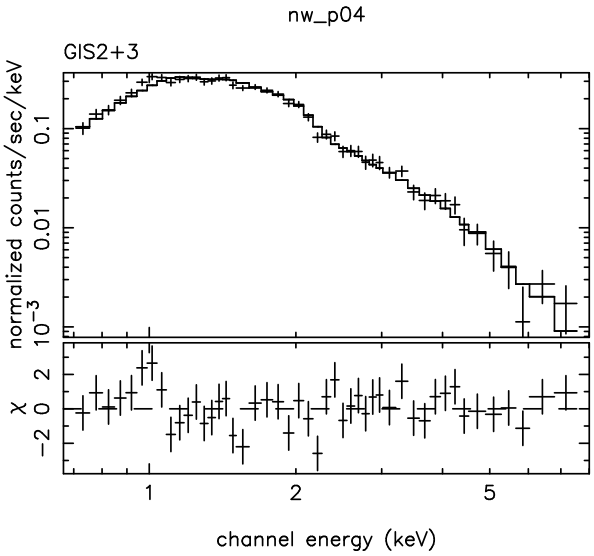
nw_p04
GIS2+3
normalized counts/sec/keV
0.1
0.01
10^{-3}
χ
2
0
−2
1
2
5
channel energy (keV)

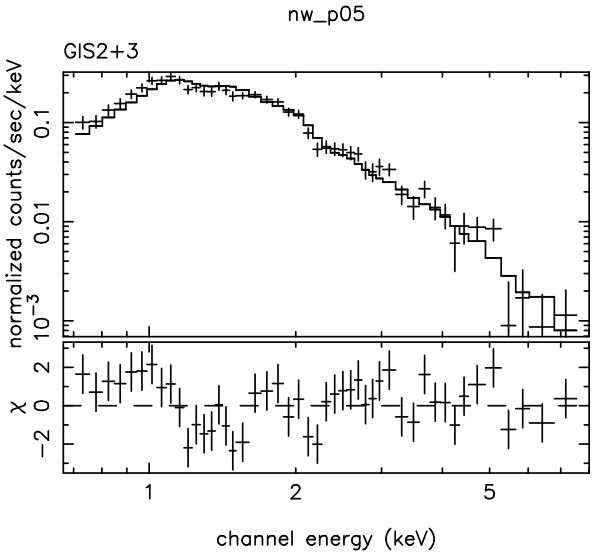
nw_p05
GIS2+3
normalized counts/sec/keV
0.1
0.01
10^{-3}
χ
2
0
−2
1
2
5
channel energy (keV)

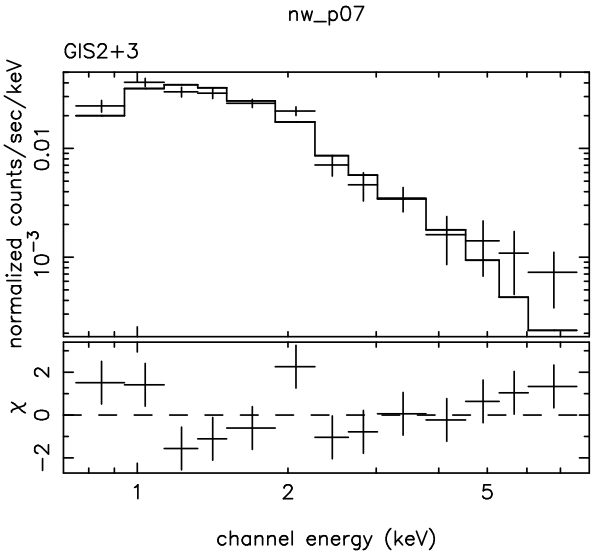
nw_p07
GIS2+3
normalized counts/sec/keV
0.01
10^{-3}
χ
2
0
−2
1
2
5
channel energy (keV)

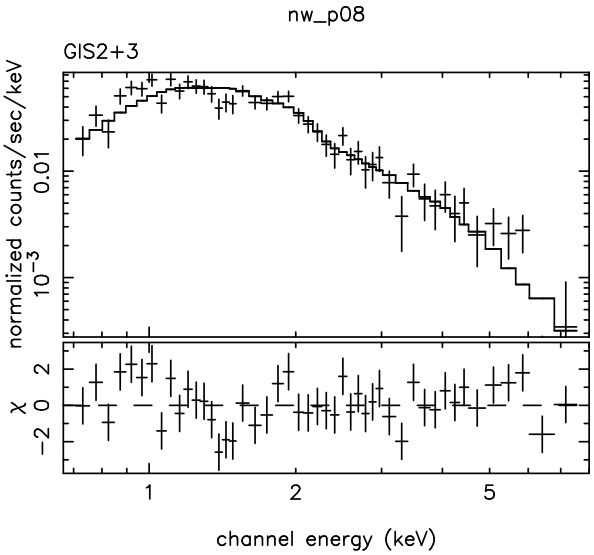
nw_p08
GIS2+3
normalized counts/sec/keV
10^{-3}
0.01
χ
channel energy (keV)

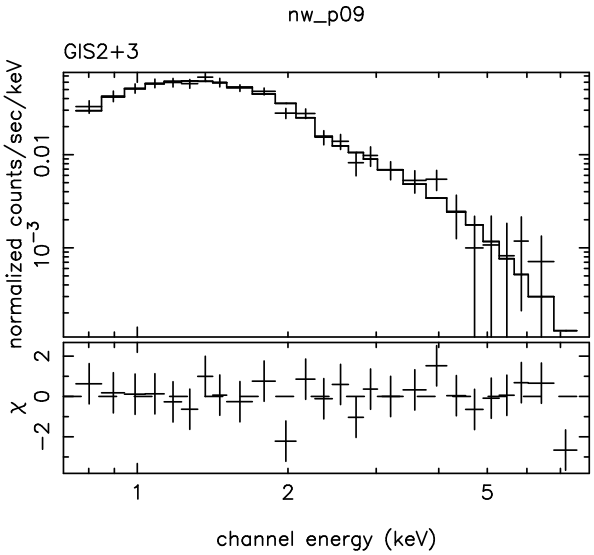
nw_p09
GIS2+3
normalized counts/sec/keV
10^{-3}
0.01
χ
channel energy (keV)

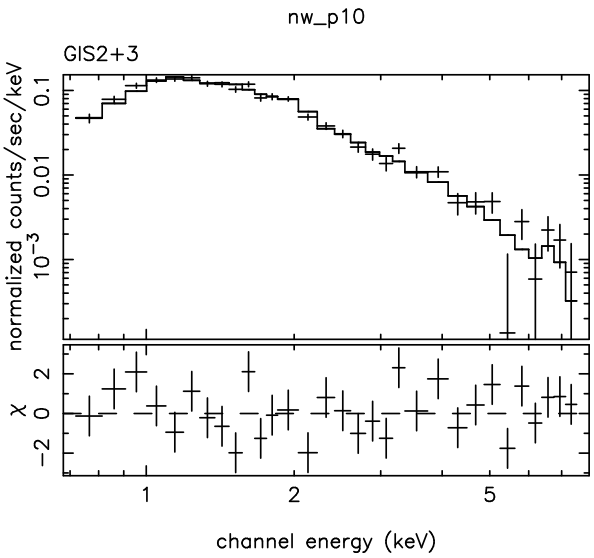
nw_p10
GIS2+3
normalized counts/sec/keV
10^{-3}
0.01
0.1
χ
channel energy (keV)

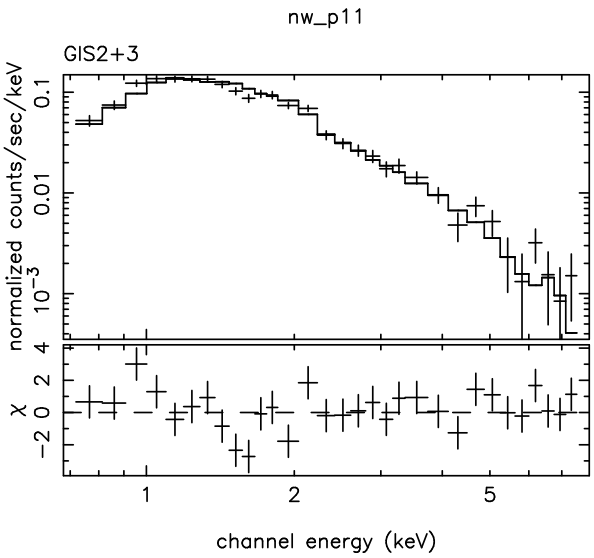
nw_p11
GIS2+3
normalized counts/sec/keV
10^{-3}
0.01
0.1
χ
channel energy (keV)

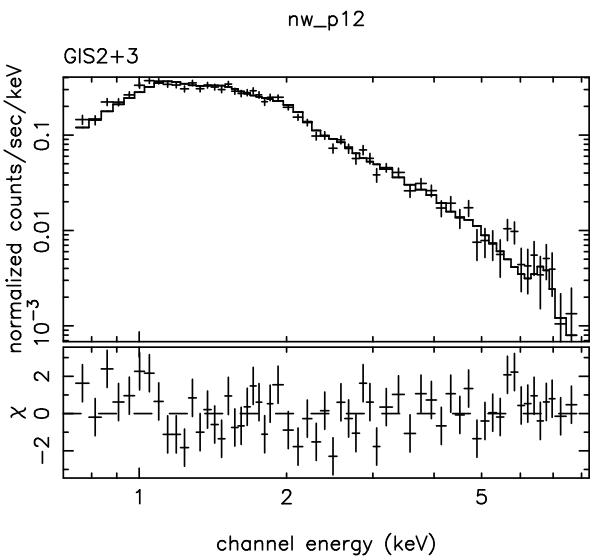
nw_p12
GIS2+3
normalized counts/sec/keV
10^{-3}
0.01
0.1
χ
channel energy (keV)

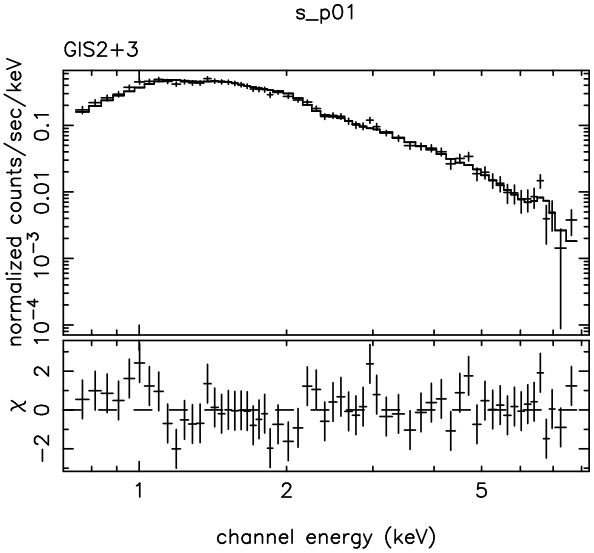
s_p01
GIS2+3
normalized counts/sec/keV
10^{-4}
10^{-3}
0.01
0.1
χ
−2
0
2
1
2
5
channel energy (keV)

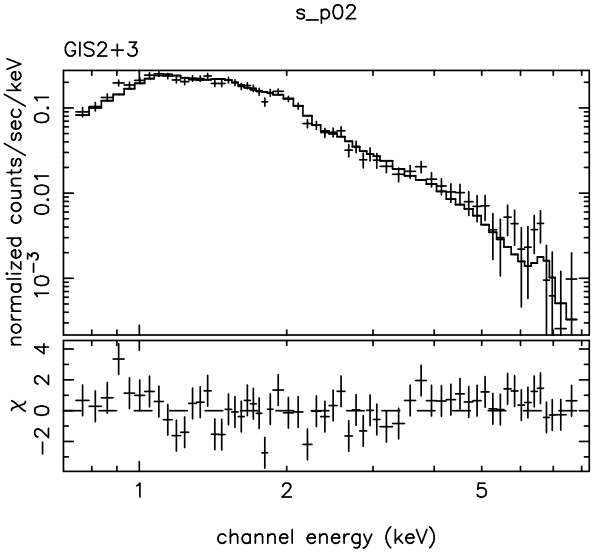
s_p02
GIS2+3
normalized counts/sec/keV
10^{-3}
0.01
0.1
χ
−2
0
2
4
1
2
5
channel energy (keV)

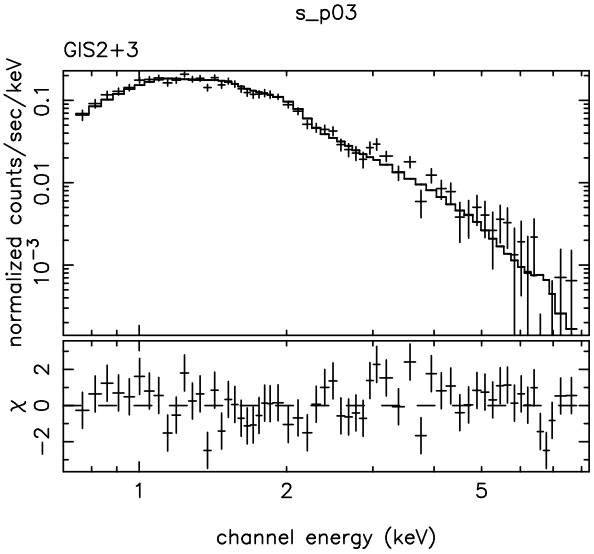
s_p03
GIS2+3
normalized counts/sec/keV
10^{-3}
0.01
0.1
χ
−2
0
2
1
2
5
channel energy (keV)

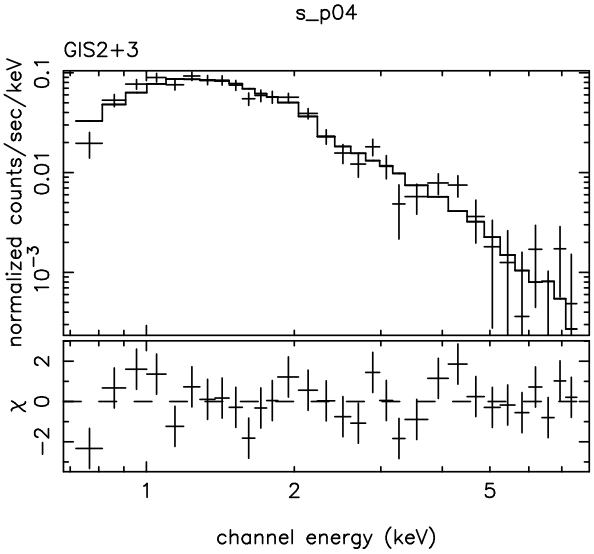
s_p04
GIS2+3
normalized counts/sec/keV
10^{-3}
0.01
0.1
χ
−2
0
2
1
2
5
channel energy (keV)

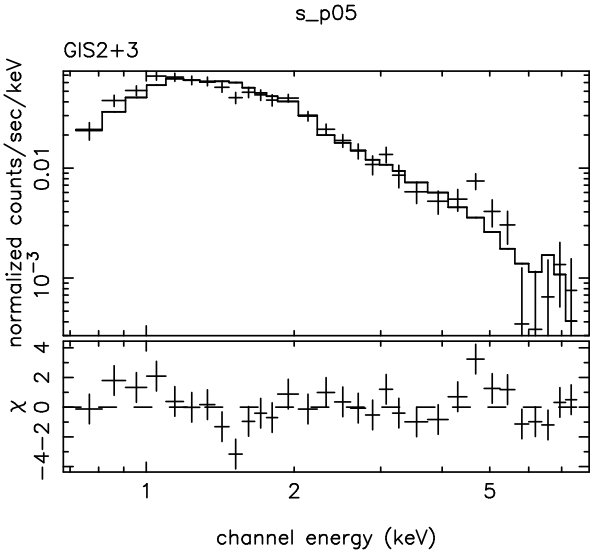
s_p05
GIS2+3
normalized counts/sec/keV
10^{-3}
0.01
χ
−4
−2
0
2
4
1
2
5
channel energy (keV)

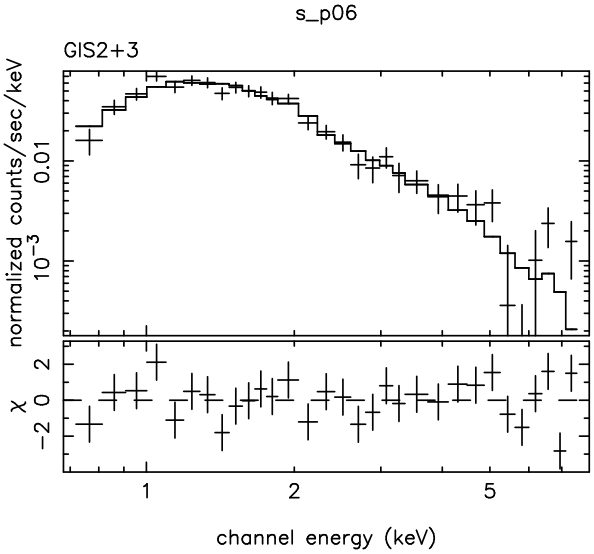
s_p06
GIS2+3
normalized counts/sec/keV
10^{-3}
0.01
χ
−2
0
2
1
2
5
channel energy (keV)

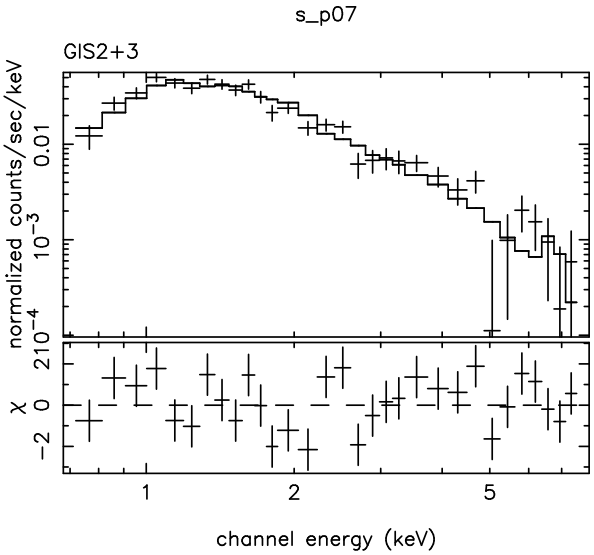
s_p07
GIS2+3
normalized counts/sec/keV
10^{-4}
10^{-3}
0.01
χ
2
0
−2
1
2
5
channel energy (keV)

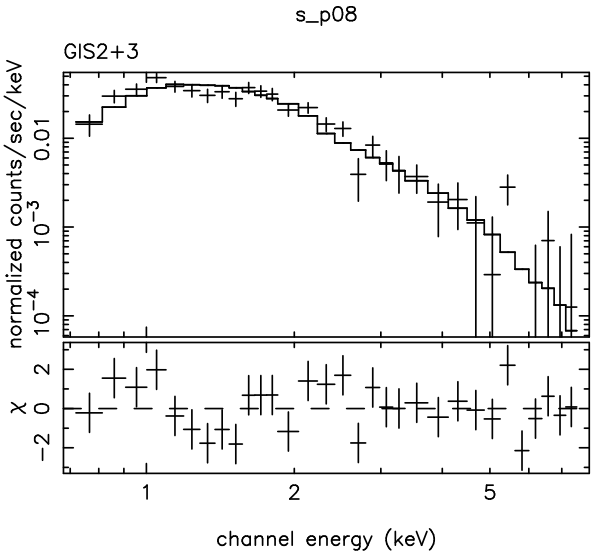
s_p08
GIS2+3
normalized counts/sec/keV
10^{-4}
10^{-3}
0.01
χ
2
0
−2
1
2
5
channel energy (keV)

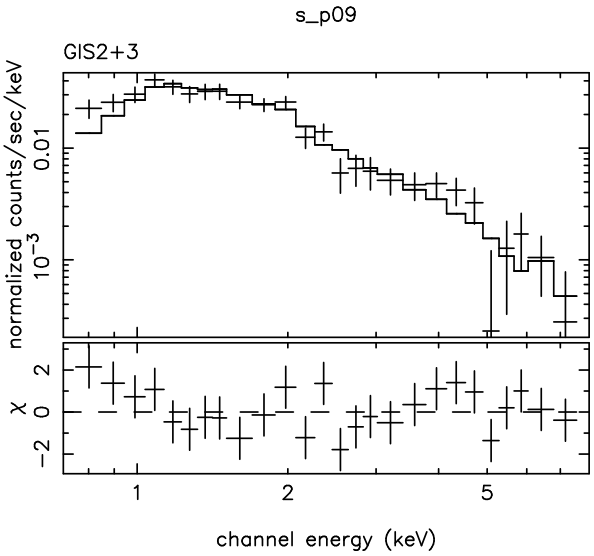
s_p09
GIS2+3
normalized counts/sec/keV
10^{-3}
0.01
χ
2
0
−2
1
2
5
channel energy (keV)

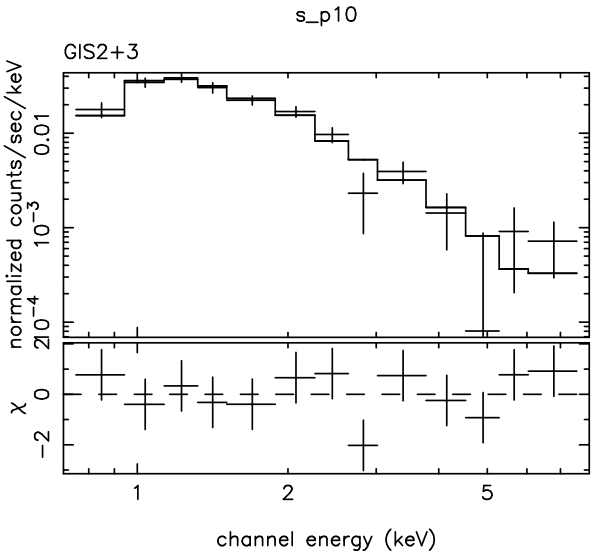
s_p10
GIS2+3
normalized counts/sec/keV
$2 10^{-4}$
10^{-3}
0.01
χ
2
0
−2
1
2
5
channel energy (keV)

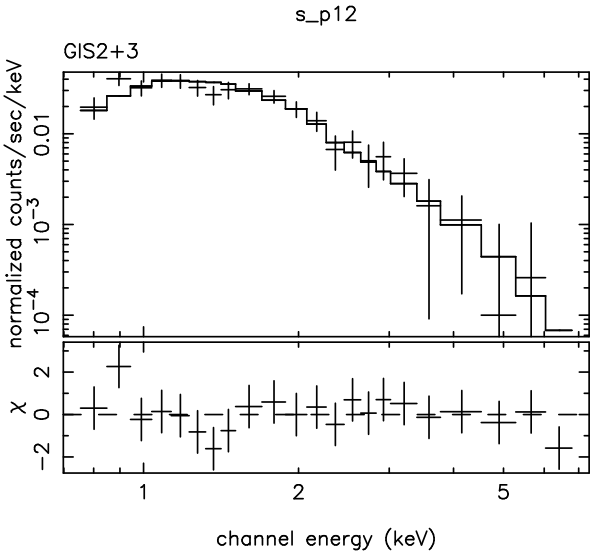
s_p12
GIS2+3
normalized counts/sec/keV
10^{-4}
10^{-3}
0.01
χ
2
0
−2
1
2
5
channel energy (keV)

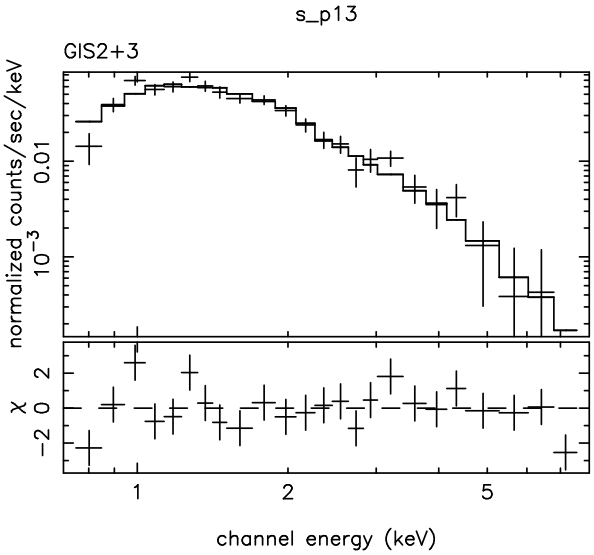
s_p13
GIS2+3
normalized counts/sec/keV
10^{-3}
0.01
χ
2
0
−2
1
2
5
channel energy (keV)

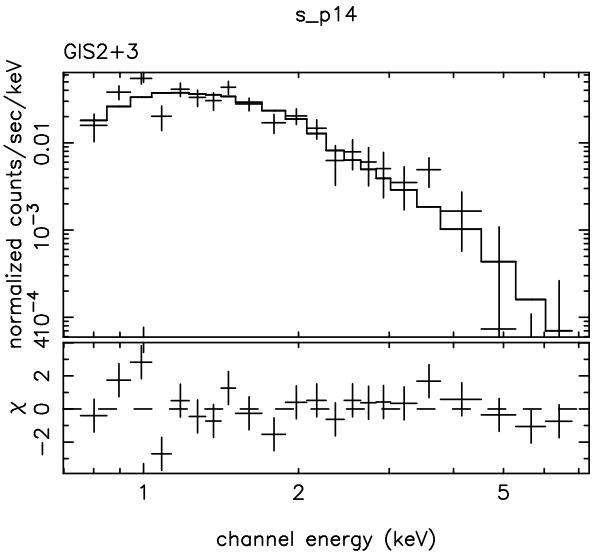
s_p14
GIS2+3
normalized counts/sec/keV
10^{-3}
0.01
$4\,10^{-4}$
χ
2
0
−2
1
2
5
channel energy (keV)

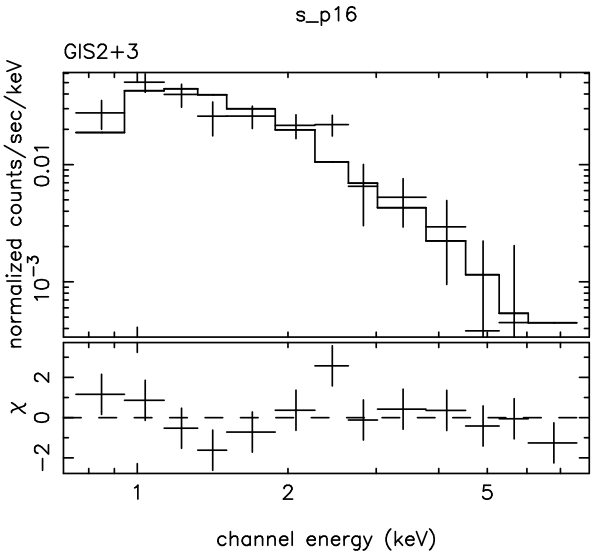
s_p16
GIS2+3
normalized counts/sec/keV
10^{-3}
0.01
χ
2
0
−2
1
2
5
channel energy (keV)

Bibliography

[1] Abell, G. O., Corwin, H. G., Jr., Olowin, R. P. 1989, ApJS, 70, 1

[2] Allen, C. W. 1973, "Astrophysical Quantities", University of London, Athlone Press, 3rd ed.

[3] Allen, S. W. & Fabian, A. C. 1998, MNRAS, 297, L62

[4] Anders, E. & Grevesse, N. 1989, Geochim. Cosmochim. Acta, 53, 197

[5] Arimoto, N., Matsushita, K., Ishimaru, Y., Ohashi, T., Renzini, A. 1997, ApJ, 477, 128

[6] Awaki, H., Koyama, K., Inoue, H., Halpern, J. P. 1991, PASJ, 43, 212

[7] Awaki, H., et al. 1994, PASJ, 46, L65

[8] Bade, N., et al. 1998, A&AS, 127, 145

[9] Bahcall, N. A. & Lubin, L. M. 1994, ApJ, 426, 513

[10] Bautz, L. P. & Morgan, W. W. 1970, ApJ, 162, L149

[11] Bazzano, A., et al. 1991, ApJ, 366, L95

[12] Bell, A. R. 1978, MNRAS, 182, 147

[13] Berkhuijsen, E. M., Haslam, C. G. T., Salter, C. J. 1971, A&A, 14, 252

[14] Binggeli, B., Sandage, A., Tammann, G. A. 1985, AJ, 90, 1681

[15] Binggeli, B., Tammann, G. A., Sandage, A. 1987, AJ, 94, 251

[16] Binggeli, B., Popescu, C. C., Tammann, G. A. 1993, A&AS, 98, 275

[17] Biretta, J. A., Stern, C. P., Harris, D. E. 1991, AJ, 101, 1646

[18] Blumenthal, G. R. & Gould, R. J. 1970, Rev. Mod. Phys., 42, 237

[19] Böhringer, H., Briel, U.G., Schwarz, R.A., Voges, W., Hartner, G., Trümper, J. 1994, Nature, 368, 828

[20] Böhringer, H. 1994b, "Cosmological Aspects of X-ray Clusters of Galaxies", ed. W. C. Seitter, NATO ASI Series C 441, Kluwer, Dordrecht, p. 123

[21] Bowyer, S., & Malina, R. F. 1991, "The Extreme Ultraviolet Explorer Mission, ed. R. F. Malina & S. Bowyer (New York: Pergamon), 397

[22] Bradt, H., Mayer, W., Naranan, S., Rappaport, S., Spade, G. 1967, ApJ, 150, L199

[23] Breitschwerdt, D., McKenzie, J. F., Völk, H. J. 1991, A&A, 245, 79

[24] Briel, U. G., Henry, J. P., Böhringer, H. 1992, A&A, 259, L31

[25] Briel, U. G. & Henry, J.P. 1994, Nature, 372, 439

[26] Briel, U. G., et al. 1997, "ROSAT User's Handbook", available from GSFC/NASA (legacy.gsfc.nasa.gov)

[27] Burke, B. E., et al. 1991, IEEE Trans. ED-39, 1069

[28] Burns, J. O., Rhee, G., Owen, F. N., Pinkney, J. 1994, ApJ, 423, 115

[29] Byram, E. T., Chubb, T. A., Friedman, H. 1966, Science, 152, 66

[30] Canizares, C. R., Fabbiano, G., Trinchieri, G. 1987, ApJ, 312, 503

[31] Cavaliere, A., Menci, N. & Tozzi, P. 1997, ApJ, 484, L21

[32] Ciardullo, R., Jacoby, G. H., Tonry, J. L. 1993, ApJ, 419, 479

[33] David, L. P., Slyz, A., Jones, C., Forman, W., Vrtilek, S. D., Arnaud, K. A. 1993, ApJ, 412, 488

[34] David, L. P., Jones, C. Forman, W. 1996, ApJ, 473, 692

[35] Davis, D. S. & White, R. E., III 1998, ApJ, 492, 57

[36] de Vaucouleurs, G., Corwin, H. G., J. 1986, AJ, 92, 722

[37] de Vaucouleurs, G., de Vaucouleurs, A., Corwin, H. G., J.., Buta, R. J., Paturel, G., Fouque, P. 1991, "Third Reference Catalogue of Bright Galaxies", Springer-Verlag, New York Press (RC3)

[38] Donnelly, R. H., Markevitch, M., Forman, W., Jones, C., David, L. P., Churazov, E., Gilfanov, M. 1998, ApJ, 500, 138

[39] Dreyer, J. L. E. 1888, MmRAS, 49, 237

[40] Ebeling, H., Voges, W., Böhringer, H., Edge, A. C., Huchra, J. P., Briel, U. G. 1996, MNRAS, 283, 1103

[41] Edge, A. C. & Stewart, G. C. 1991, MNRAS, 252, 428

[42] Egger, R. J. 1993, Ph. D. Thesis, Universität München

[43] Egger, R. J. & Aschenbach, B. 1995, A&A, 294, L25

[44] Enßlin, T. A., Lieu, R., Biermann, P. L. 1999, A&A, 344, 409

[45] Evrard, A. E., Metzler, C. A. Navarro, J. F. 1996, ApJ, 469, 494

[46] Ezawa, H., Fukazawa, Y., Makishima, K., Ohashi, T., Takahara, F., Xu, H., Yamasaki, N. Y. 1997a, ApJ, 490, L33

[47] Ezawa, H., Endo, Y., Fukazawa, Y., Kikuchi, K., Takahashi, T., the Image Analysis Working group 1997b, ASCA News No. 5, ed. ASCA Guest Observer Facility at NASA/GSFC, p. 23

[48] Ezawa, H. 1998, Ph. D. Thesis, University of Tokyo

[49] Fabbiano, G., Gioia, I. M., Trinchieri, G. 1988, ApJ, 324, 766

[50] Fabricant, D. & Gorenstein, P. 1983, ApJ, 267, 535

[51] Federspiel, M., Tammann, G. A., Sandage, A. 1998, ApJ, 495,

[52] Fouque, P., Bottinelli, L., Gouguenheim, L., Paturel, G. 1990, ApJ, 349, 1

[53] Fukazawa, Y., Ohashi, T., Fabian, A. C., Canizares, C. R., Ikebe, Y., Makishima, K., Mushotzky, R. F. Yamashita, K. 1994, PASJ, 46, L58

[54] Fukazawa, Y. 1997, Ph. D. Thesis, University of Tokyo

[55] Fukazawa, Y., Makishima, K., Tamura, T., Ezawa, H., Xu, H., Ikebe, Y., Kikuchi, K., Ohashi, T. 1998, PASJ, 50, 193

[56] Fukugita, M., Okamura, S., Yasuda, N. 1993, ApJ, 412, L13

[57] Fusco-Femiano, R., dal Fiume, D., Feretti, L., Giovannini, G., Grandi, P., Matt, G., Molendi, S., Santangelo, A. 1999, ApJ, 513, L21

[58] Gehrels, N. & Williams, E. D. 1993, ApJ, 418, L25

[59] Giacconi, R., Kellogg, E., Gorenstein, P., Gursky, H., Tananbaum H. 1971, ApJ, 165, L67

[60] Giacconi, R., et al. 1979, ApJ, 230, 540

[61] Hanisch, R. J. & Erickson, W. C. 1980, AJ, 85, 190

[62] Harris, D. E. & Romanishin, W. 1974, ApJ, 188, 216

[63] Hayakawa, S., Kato, T., Nagase, F., Yamashita, K., Murakami, T., Tanaka, Y. 1977, ApJ, 213, L109

[64] Henriksen, M. J. & Markevitch, M. L. 1996, ApJ, 466, L79

[65] Henry, J. P. & Briel, U. G. 1996, ApJ, 472, 137

[66] Hewitt, A. & Burbidge, G. 1989, ApJS, 69, 63

[67] Honda, H., et al. 1996, ApJ, 473, L71

[68] Honda, H., et al. 1997, Proc. "ASCA/ROSAT Workshop on Cluster of Galaxies", p. 153

[69] Ikebe, Y. 1994, Ph. D. Thesis, University of Tokyo

[70] Ikebe, Y., et al. 1996, Nature, 379, 429

[71] Ikebe, Y., et al. 1997, ApJ, 481, 660

[72] Inoue, H., Koyama, K., Matsuoka, M., Ohashi, T., Tanaka, Y., Tsunemi, H. 1980, ApJ, 238, 886

[73] Irwin, J. A. & Sarazin, C. L. 1996, ApJ, 471, 683

[74] Ishisaki, Y. 1995, Ph. D. Thesis, University of Tokyo

[75] Ishizaka, C., & Mineshige, S. 1996, PASJ, 48, L37

[76] Iyomoto, N., Makishima, K., Tashiro, M., Inoue, S., Kaneda, H., Matsumoto, Y., Mizuno, T. 1998, ApJ, 503, L31

[77] Jones, C. & Forman, W. 1984, ApJ, 276, 38

[78] Kaastra, J. S., Lieu, R., Mittaz, J. P. D., Bleeker, J. A. M., Mewe, R., Colafrancesco, S., Lockman, F. J. 1999, ApJ, 519, L119

[79] Kaiser, N. 1991, ApJ, 383, 111

[80] Kempner, J. C. & Sarazin, C. L. 2000, ApJ, 530, 282

[81] Kikuchi, K. & Ohashi, T. 1997, Proc. "ASCA/ROSAT Workshop on Cluster of Galaxies", p. 221

[82] Kikuchi, K., Ohashi, T., Hirayama, M., Ezawa, H., Honda, H., Shibata, R. 1998a, IAU Symposia, 188, p. 312

[83] Kikuchi, K., et al. 1998b, PASJ, submitted

[84] King, I. 1962, AJ, 67, 471

[85] Koyama, K., et al. 1984, PASJ, 36, 659

[86] Koyama, K., Takano, S., Tawara, Y. 1991, Nature, 350, 135

[87] Kraan-Korteweg, R. C., Cameron, L. M., Tammann, G. A. 1988, ApJ, 331, 620

[88] Kubo, H. 1994, Master Thesis, University of Tokyo

[89] Kunieda, H., Furuzawa, A., Watanabe, M., XRT Team 1995, ASCA News No. 3, ed. ASCA Guest Observer Facility at NASA/GSFC, p. 3

[90] Lea, S. M., Reichert, G., Mushotzky, R., Baity, W. A., Gruber, D. E., Rothschild, R., Primini, F. A. 1981, ApJ, 246, 369

[91] Lieu, R., Mittaz, J. P. D., Bowyer, S., Lockman, F. J., Hwang, C.-Y., Schmitt, J. H. M. M. 1996, ApJ, 458, L5

[92] Makino, F. & ASTRO-C Team 1987, Astrophys. Letters Commun., 25, 223

[93] Makishima, K., et al. 1989, PASJ, 41, 708

[94] Makishima, K., et al. 1996, PASJ, 48, 171

[95] Malina, R., Lampton, M., Bowyer, S. 1976, ApJ, 209, 678

[96] Markevitch, M., Forman, W. R., Sarazin, C. L., Vikhlinin, A. 1998, ApJ, 503, 77

[97] Markevitch, M. 1998b, ApJ, 504, 27

[98] Matsumoto, H., Koyama, K., Awaki, H., Tomida, H., Tsuru, T., Mushotzky, R., Hatsukade, I. 1996 PASJ, 48, 201

[99] Matsumoto, H., Koyama, K., Awaki, H., Tsuru, T., Loewenstein, M., Matsushita, K. 1997, ApJ, 482, 133

[100] Matsumoto, H. 1998, Ph. D. Thesis, University of Kyoto

[101] Matsushita, K., et al. 1994, ApJ, 436, L41

[102] Matsushita, K. 1997, Ph. D. Thesis, University of Kyoto

[103] Matsushita, K., Makishima, K., Ikebe, Y., Rokutanda, E., Yamasaki, N., Ohashi, T. 1998, ApJ, 499, 13

[104] Metzler, C. A. & Evrard, A. E. 1994, ApJ, 437, 564

[105] Mittaz, J. P. D., Lieu, R., Lockman, F. J. 1998, ApJ, 498, L17

[106] Mushotzky, R. F. 1984, Phys. Scr, 7, 162

[107] Ohashi, T., et al. 1996, PASJ, 48, 157

[108] Ohashi, T., Kikuchi, K., Matsushita, K., Yamasaki, N. Y., Kushino, A., Virgo Project Team 1998a, IAU Symposia, 188, p. 317

[109] Ohashi, T., et al. 1998b, 32nd COSPAR Scientific Assembly (submitted to Advances in Space Research)

[110] Owen, F. N. 1974, AJ, 79, 436

[111] Padovani, P., Burg, R., Edelson, R. A. 1990, ApJ, 353, 438

[112] Peterson, L. E. 1975, ARA&A, 13, 423

[113] Primini, F. A., et al. 1981, ApJ, 243, L13

[114] Rawlings, S. & Saunders, R. 1991, Nature, 349, 138

[115] Raymond, J. C. & Smith, B. W. 1977, ApJS, 35, 419

[116] Raymond, J. C. 1984, ARA&A, 22, 75

[117] Rephaeli, Y. 1979, ApJ, 227, 369

[118] Rephaeli, Y. & Gruber, D. E. 1988, ApJ, 333, 135

[119] Richstone, D., Loeb, A., Turner, E. L. 1992, ApJ, 393, 483

[120] Rocchia, R., et al. 1984, A&A, 130, 53

[121] Röttgering, H. J. A., Wieringa, M. H., Hunstead, R. W. & Ekers, R. D. 1997, MNRAS, 290, 584

[122] Roettiger, K., Burns, J., Loken, C. 1993, ApJ, 407, L53

[123] Roettiger, K., Burns, J. O., Pinkney, J. 1995, ApJ, 453, 634

[124] Rood, H. J. & Sastry, G. N. 1971, PASP, 83, 313

[125] Rybicki, G. B. & Lightman, A. P. 1979, "Radiative Processes in Astrophysics", John Wiley & Sons, Inc.

[126] Sarazin, C. L. 1988, "X-ray Emission from Clusters of Galaxies", Cambridge University Press

[127] Sarazin, C. L. & Lieu, R. 1998, ApJ, 494, L177

[128] Sarazin, C. L. 1999, ApJ, 520, 529

[129] Sarazin, C. L. & Kempner, J. C. 2000, ApJ, 533, 73

[130] Schindler, S. & Müller, E. 1993, A&A, 272, 137

[131] Schindler, S., Binggeli, B., Böhringer, H. 1999, A&A, 343, 420

[132] Schnopper, H. W., et al. 1982, ApJ, 253, 131

[133] Schombert, J. M. 1986, ApJS, 60, 603

[134] Serlemitsos, P. J., Smith, B. W., Boldt, E. A., Holt, S. S., Swank, J. H. 1977, ApJ, 211, L63

[135] Shu, F. H. 1992, "The Physics of Astrophysics volume II. Gas Dynamics", University Science Books

[136] Snowden, S. L., McCammon, D., Burrows, D. N., Mendenhall, J. A. 1994, ApJ, 424, 714

[137] Snowden, S. L., et al. 1995, ApJ, 454, 643

[138] Soker, N. & Sarazin, C. L. 1990, ApJ, 348, 84

[139] Spitzer, L. Jr. 1962, "Physics of Fully Ionized Gases Second Revised Edition", New York, Interscience

[140] Stephens, S. A. 1989, AJ, 97, 35

[141] Takahashi, T., et al. 1994, "Why we need another Cyg X-1 observation", ASCA internal report, available from ISAS (ftp.astro.isas.ac.jp: /asca/report/xrt_US.ps)

[142] Takahashi, T., et al. 1995, ASCA News No. 3, ed. ASCA Guest Observer Facility at NASA/GSFC, p. 34

[143] Takano, S. 1990, Ph. D. Thesis, University of Kyoto

[144] Tanaka, Y., et al. 1984, PASJ, 36, 641

[145] Tanaka, Y., Inoue H., Holt S.S. 1994, PASJ, 46, L37

[146] Taylor, B. G., Andresen, R. D., Peacock, A., Zobl, R. 1981, Space Science Reviews, 30, 479

[147] Tribble, P. C. 1993, MNRAS, 263, 36

[148] Trümper, J. 1983, Adv. Space Res., 2, 241

[149] Tsusaka, Y., et al. 1995, Appl. Opt., 34, 4848

[150] Tucker, W., Kellogg, E., Gursky, H., Giacconi, R., Tananbaun, H. 1973, ApJ, 180, 724

[151] Tully, R. B. 1988, Nature, 334, 209

[152] Turner, M. J. L., et al. 1989, PASJ, 41, 345

[153] Ueda, Y. 1995, Ph. D. Thesis, University of Tokyo

[154] Ueda, Y., et al. 1998, ApJ, submitted

[155] Voges, W., Gruber, R., Haberl, F., Kuerster, M., Pietsch, W., Zimmermann, H. -U. 1995, ROSAT NEWS No.32 (01-Nov-1994), ROSAT Source Catalog Version 11-May-1995 (RXP)

[156] Voges, W., et al. 1996, IAU Circ., 6420, 2

[157] White, D. A. & Fabian, A. C. 1995, MNRAS, 273, 84

[158] White, R. E., III 1991, ApJ, 367, 77

[159] Xu, H., Ezawa, H., Fukazawa, Y., Kikuchi, K., Makishima, K., Ohashi, T., Tamura, T. 1997, PASJ, 49, 16

[160] Yasuda, N., Fukugita, M. Okamura, S. 1997, ApJS, 108, 417

[161] Zel'dovich, Ya. B. & Raizer Yu. P. 1966, "Physics of Shock Waves and High-Temperature Hydrodynamic Phenomena", Academic Press

Acknowledgments

First of all, I am grateful to Prof. T. Ohashi, my supervisor, for his support and encouragement throughout my master and doctoral courses. Without his constant aid, this thesis would certainly never have been completed. I am also grateful to Dr. N. Y. Yamasaki for her continuous guidance on physical and astrophysical issues, and Dr. Y. Ishisaki for his powerful support on data analyses.

I wish to thank TERRA team members: Dr. H. Ezawa, Dr. M. Hirayama, Dr. H. Honda and Mr. R. Shibata for their technical support. I am very much obliged to Dr. K. Matsushita and Dr. H. Matsumoto for constructive discussions and cooperations. I also thank Dr. Y. Ueda, Dr. Y. Ikebe, and Dr. T. Tamura for useful advices on analysis methods.

I would like to acknowledge Prof. Trümper, Dr. H. Böhringer, Dr. S. Schindler, Dr. T. Reiprich, and other scientists at Max-Planck-Institut für extraterrestrische Physik for their useful discussions and the warm hospitality during my visit to the institute. My visit was supported by Japan Society of Promotion of Science.

I am willing to thank Prof. S. Okamura, Dr. S. Sasaki, Prof. K. Masai, and Prof. F. Takahara for valuable comments and discussions on observational and theoretical aspects of clusters of galaxies.

I wish to thank all members of our laboratory: Ms. T. Kaho, Mr. T. Kubotera, Mr. K. Mutoh, Ms. R. Arai, Mr. H. Miyazaki, Mr. S. Suzuki, Ms. M. Tsukahara, Mr. H. Kobayashi, Mr. K. Machida, Ms. E. Rokutanda, Ms. T. Furusho, Mr. T. Kurozumi, Mr. T. Minawa, Mr. T. Sato, Mr. R. Ito, Mr. A. Masuyama, Mr. R. Nakayama, Ms. M. Tanabe, Ms. C. Tokoku, Mr. N. Yokokawa, Mr. A. Kushino, Mr. Y. Michikawa, Mr. T. Toramatsu, Mr. G. Fujimoto, Ms. C. Ito, Mr. T. Ishikawa, Mr. T. Ishioroshi, Mr. H. Kameda, Mr. J. Watanabe, Mr. S. Yamamoto, and Ms. Y. Kawakami. I also owe great thanks to my friends, Mr. J. Okamoto, Mr. K. Saito, Ms. K. Wakabayashi, Mr. K. Izumi, and Mr. D. Fujikawa, who continuously encouraged me through these years.

Finally, I acknowledge ASCA team, GIS team, Virgo Cluster Mapping Project Team, SimASCA W.G., SimARF team, and ASCA_ANL W.G. for spacecraft operation, calibration, data acquisition, and analysis support. I also acknowledge support from the Japan Society for the Promotion of Science for Young Scientists.

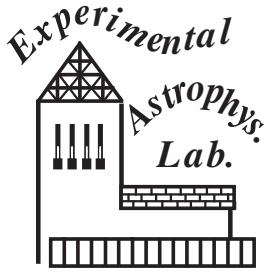
Experimental
Astrophys.
Lab.